IRPA

FS

Fachverband für Strahlenschutz e.V.

Mitgliedsgesellschaft der
International Radiation
Protection Association
(IRPA)
für die Bundesrepublik
Deutschland
und die Schweiz

Publikationsreihe
FORTSCHRITTE
IM STRAHLENSCHUTZ

Publication Series
PROGRESS IN RADIATION
PROTECTION

ION BEAMS IN BIOLOGY AND MEDICINE

39. Annual Conference of the German-Swiss Association for Radiation Protection

and

11th Workshop of Heavy Charged Particles in Biology and Medicine

Heidelberg, 26th–29th September 2007

Bandherausgeber:
J. Debus
K. Henrichs
G. Kraft

ION BEAMS IN BIOLOGY AND MEDICINE

39. Annual Conference of the
German-Swiss Association for Radiation Protection

and

11th Workshop of Heavy Charged Particles
in Biology and Medicine

Fachverband für Strahlenschutz e.V.

Mitgliedsgesellschaft der
International Radiation
Protection Association
(IRPA)
für die Bundesrepublik
Deutschland
und die Schweiz
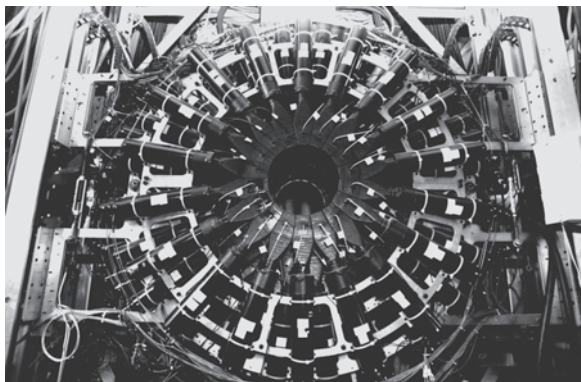
Publikationsreihe
FORTSCHRITTE
IM STRAHLENSCHUTZ

Publication Series
PROGRESS IN RADIATION
PROTECTION

ION BEAMS IN BIOLOGY AND MEDICINE

39. Annual Conference of the German-Swiss Association for Radiation Protection

and

11th Workshop of Heavy Charged Particles in Biology and Medicine

Heidelberg, 26th–29th September 2007

Bandherausgeber:
J. Debus
K. Henrichs
G. Kraft

Contents   **Page**

---

*na = contribution not available

Poster: Modeling

Particle Physics

Contents   **Page**

Contents   Page

Poster: Radiobiology 1

---

*na = contribution not available

Contents   Page

Radiobiology 2

Poster: Radiobiology 2

---

*na = contribution not available

Contents* **Page**

Contents   **Page**

_____

*na = contribution not available

Contents   **Page**

Poster: Therapy Planning

Status Reports

---

*na = contribution not available

Opening Lecture

THE IMPACT OF NEW TECHNOLOGIES ON THE INCIDENCE OF SECOND CANCERS IN RADIOTHERAPY

Eric J. Hall,
Columbia University, New York, USA

RADIATION-INDUCED CANCER; WHAT DO WE KNOW?

The data from the A-bomb survivors indicates that the incidence of all solid cancers approximates to a linear function of dose from about 100 mSv up to about 2.5 Sv.(1) The incidence data from the life span study also reveal the spectrum of malignancies that result from total body irradiation. The tumors that are induced are mostly carcinomas, arising in the cells of self-renewal tissues that line the body, such as the gastrointestinal tract, lung, breast etc. The various radiogenic tissues vary in radiosensitivity, but not by very much; the average is an ERR of 0.5/Gy.

RADIOTHERAPY PATIENTS

For the most part, it is difficult to obtain quantitative data of the incidence of radiation-induced cancer from radiotherapy patients because an appropriate and relevant control group is not available. There are a few notable exceptions. These include carcinoma of the prostate and cervix, where surgery is an option to radiotherapy, and Hodgkins lymphoma where the incidence of lung cancer, and particularly breast cancer in young women is so high that a control group is not needed. The retrospective analysis of prostate cancer patients receiving radiotherapy in the past not only provide quantitative data, about 1½% second cancers in 10 year survivors, but clearly where second cancers occur (2). Not surprisingly, many cancers occur in organs close to the prostate which receive a high dose, such as the bladder or rectum. On the other hand, about 30% of second cancers occur in the lung, far removed from the prostate and receiving a relatively low dose, largely from leakage or scattered radiation.

THE SHAPE OF THE DOSE RESPONSE RELATIONSHIP

A vital piece of information needed to assess the impact of new technology is the shape of the dose response relationship for carcinogenesis over a wide range of doses. Dr. Elaine Ron of the National Cancer Institute in Bethesda collected data for 3 tissues where induced cancer incidence at doses up to 2Gy are available from the A-bomb survivors, while data at higher doses come from radiotherapy patients.(3) While the data are limited, they show clearly that the cancer incidence which is linear with dose up to about 2 Sv in the A-bomb survivors flattens out and tends to plateau at the high doses delivered in multiple fractions that are characteristic of radiotherapy. It is also important to note that induced cancer incidence does not fall dramatically at high doses as predicted by the Gray model (4). Sachs & Brenner (5) investigated the shape of the dose response relationship for both lung and breast cancer, with low dose data coming from the A-bomb survivors and high dose data from Hodgkins lymphoma patients treated with radiotherapy. They came to a similar conclusion, namely that the induced cancer incidence, resulting from fractionated high doses tended to flatten out. They went on to model these data for lung and breast cancer and concluded that, in order to fit the data, it was necessary to assume that cells transformed by one dose fraction needed to proliferate rapidly between dose fractions in order to counter the effects of cell killing by the high doses involved. The principal overall conclusion of these studies is that at doses much higher than those experienced by the A-bomb survivors, cancer incidence depends on volume, more than on dose.

The most sophisticated method to estimate the incidence of second cancers from a given radiotherapy schedule is to obtain a detailed dose-volume histogram (DVH) and then to use the organ specific

radiation cancer risk estimates from the A-bomb survivors. There is at least one example where this methodology has been applied, namely the paper by Skoh et al (6) relating to the treatment of Hodgkins lymphoma. The authors first derived a dose-volume histogram for the treatment protocol and then used the cancer incidence data from the A-bomb survivors to assess the risk. The treatment resulted in an overall excess relative risk (ERR) of 2.2, but of great interest is the distribution of that risk. It turns out to be made up of two principal components; first a peak dose to a large volume of tissue exposed to low doses and second a peak due to a smaller volume of tissue exposed to very high doses. This illustrates an important principle.

IMRT

Several authors have applied this knowledge of radiation-induced carcinogenesis to making estimates of the increase in second malignancies that might be expected by using IMRT in place of 3D-CRT. (7, 8, 9)   The consensus seems to be that IMRT is likely to double the incidence of second cancers because (a) there is a doubling or trebling of the number of monitor units, and (b) more treatment fields lead to a larger volume of normal tissue exposed to lower doses. While a doubling of the risk may be acceptable in older patients where the risk is small, provided it is accompanied by a substantial improvement in tumor control and a reduction in acute morbidity, children are a different story. In younger patients the incidence of radiation induced cancers may be ten times higher, so that doubling is would not be acceptable.

PROTONS

Protons represent a logical step forward beyond IMRT in dose conformation. The depth-dose pattern characteristic of charged particles makes it possible for dose to be concentrated in the tumor volume without irradiating large volumes of normal tissue, remote from the target volume. However, for the full potential of protons to be realized, it is essential to adopt spot scanning technology to manipulate the size and shape of the treatment field. It is far simpler to use passive modulation in the form of a scattering fail, but this technique results in the production of secondary neutrons. Some neutron contamination in a proton beam is inevitable, generated in the collimators or in the irradiated tissues of the patient, but experiments have shown that the majority of neutrons come from the scattering foils, since neutrons are produced whenever protons lose a great deal of energy. Few data are available on neutron doses from the variety of current clinical proton facilities, but what is available indicates that the effective dose outside the treatment field is higher than for x-ray IMRT in facilities utilizing passive modulation.(7)

RBE

Neutrons are very undesirable since years of experience has shown that they have a high potential to induce carcinogenesis. RBEm for the most effective neutrons approach 100. We have much less human or animal data for the RBE of heavier ions for carcinogenesis, but it would be expedient to assume RBE values that are not less than for neutrons.

RBE – DOUBLE TROUBLE

RBE increases as dose decreases and in addition the RBE for mutation and carcinogenesis is in general larger than for cell lethality.

Consequently the RBE for carcinogenesis in remote normal tissues is much larger than for cell killing in the target volume.

Applying the lessons we know to the case of Ion therapy we can draw the following conclusions

- Minimize the volume of normal tissue around the tumor which receives the full dose – consistent with avoiding a miss.

- Avoid large volumes receiving low doses. This can be done with ion therapy and is a big plus.

- Minimize (would be nice to avoid) the generation of stray high LET particles (big RBE) that expose distant normal tissue.

REFERENCES

1. Pierce, D.A., Preston, D.L. Radiation-related cancer risks at low doses among atomic bomb survivors. Radiat Res 2000; 154: 178-186.
2. Brenner, D.J., Curtis, R.E., Hall, E.J. et al. Second malignancies in prostate patients after radiotherapy compared with surgery. Cancer 2000;88:398-406.
3. Ron, E. Personal communication, 2005.
4. Gray, L.H. Radiation biology and cancer. In: Cellular radiation biology: A symposium considering radiation effects in the cell and possible implications for cancer therapy. Baltimore: William & Wilkins: 1965. p. 8-25.
5. Sachs, R.K. and Brenner, D.J. Solid tumor risks after high doses of ionizing radiation. PNAS, 102, 13040-45, 2005.
6. Koh, Eng-Siew, Tran, T.H., Heydarian, M., Sachs, R.K., Tsang, R.W., Brenner, D.J., Pintilie, M., Xu, T, Chung, J., Paul, N., Hodgson, D.C. A comparison of mantle versus involved-field radiotherapy for Hodgkin's lymphoma: reduction in normal tissue dose and second cancer risk. Radiation Oncology, 2007http://www.ro-ournal.com/content/2/2/13.
7. Varellen, D., Vanhavere, F. Risk assessment of radiation-induced malignancies based on whole-body dose equivalent estimates for IMRT in the head and neck region. Radiother Oncol 1999;53:199-203.
8. Hall, E.J., Wuu, C. Radiation-induced second cancers: The impact of 3D-CRT and IMRT. Int J Radiat Oncol Biol Phys 2003;56:83-88.
9. Kry, S.F., Salehpour, M., Followill, D., et al. The calculated risk of fatal secondary malignancies from intensity-modulated radiation therapy. Int J Radia Oncol Biol Phys 2005;62:1195-1203.
10. Hall, E.J. Intensity-Modulated radiation therapy, protons, and the risk of second cancers. Int. J. Radiation Biol. Phys. 65:1-7, 2006.

Radiation Safety

NUCLEAR FRAGMENTS AND FAST NEUTRONS IN CARBON ION RADIATION THERAPY

D. Schardt[1,*], E. Haettner[1], H. Iwase[1] and K. Gunzert-Marx[1]

[1]Department of Biopyhsics, Gesellschaft für Schwerionenforschung (GSI), Planckstraße 1, 64291 Darmstadt, Germany

The radiation field of heavy-ion beams used for radiotherapy applications is affected by nuclear fragmentation processes along the penetration path in tissue, causing an attenuation of the primary ion beam and the build-up of light fragments including fast neutrons. In our experiments the production of secondary fragments from primary ^{12}C ions with specific energies of 200 MeV/u and 400 MeV/u delivered from the heavy-ion accelerator SIS-18 at GSI was investigated using a water absorber of variable thickness as tissue-equivalent target. Energy spectra, angular distributions and yields of fast neutrons and charged particles were investigated at various water depths by using fast scintillation detectors and time-of-flight techniques. For neutron detection a BaF$_2$-detector operated in anticoincidence with a veto detector for charged particles was used. From the resulting yield of 0.54 neutrons ($E_n>10$ MeV) per primary ^{12}C ion a neutron dose of 5.4 mSv per Cobalt Gray Equivalent (GyE) delivered to a typical medium-sized treatment volume is estimated. This value is comparable to the dose contribution of secondary neutrons in proton radiotherapy. Direct dose measurements using a wide-energy neutron detector (WENDI-II) under identical irradiation conditions were found to be in good agreement with the dose estimate based on the measured neutron fluences.

INTRODUCTION

Carbon ions offer favorable conditions for the treatment of deep-seated, localized tumors due to their physical and biological properties. Their dose profile is - in contrast to photons – inverted, the dose maximum is deposited at the end of the particle range in the so called "Bragg peak". In addition, the relative biological effectiveness (RBE) of carbon ions increases in the region of the Bragg peak by a factor of three to five. Nuclear reactions along the penetration path, however, cause a significant alteration of the radiation field.

At energies of several hundred MeV/u which are required for radiotherapy the most frequent nuclear interactions are peripheral collisions where the beam particles loose one or several nucleons. The fragments continue travelling with nearly the same velocity and direction. These nuclear reactions lead to an attenuation of the primary beam flux and a build-up of lower-Z fragments with increasing penetration depth. As the range of the particles scales with A/Z^2, the depth-dose profile of heavy-ion beams shows a characteristic fragment tail beyond the Bragg peak. The Bragg curve displayed in Fig.1 for a 330 MeV/u ^{12}C beam with the Bragg peak at about 20 cm depth of water exhibits a significant contribution of secondary fragments to the total depth-dose. In the tail behind the Bragg peak first heavier fragments like B, Be,Li-ions contribute most of the dose, while the long range tail is caused essentially by protons and α-particles.

The total reaction cross sections at high energies (> 100 MeV/u) can be well described by semi-empirical geometrical models and are almost constant over a wide energy range [1]. Typical values for various ions and the corresponding mean free paths in water are given in table 1.
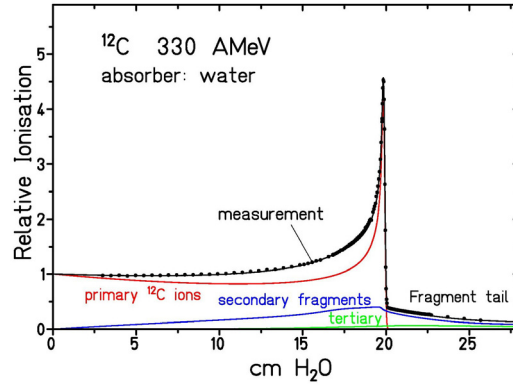
Figure 1. Bragg curve for 330 MeV/u ^{12}C ions in water measured at GSI. The data points are compared to a model calculation [1] (solid line). The calculated contributions from the primary particles (red line) and from nuclear fragments (blue line) are also shown.

Table 1: Total reaction cross section and mean-free-path in water of high-energy ions (formula by Kox et al. [2])

Ion	E [MeV/u]	σ_R [mb]	λ [cm]
p	200	350	85
^{4}He	200	770	39
^{12}C	300	1420	21
^{20}Ne	500	1580	16

SPECTRAL MEASUREMENTS

The spectral characteristics of secondary fragments as a function of penetration depth and angle with respect to the beam axis is important information required for treatment planning. Some typical features of secondary charged particles are shown in Fig.2. A pencil-like beam of 270 MeV/u ^{12}C ions passed through a 4.2 cm thick water absorber. The nuclear charge spectrum was measured with a plastic scintillator of 9 mm thickness, used as an energy loss detector, at different angles behind the absorber. Fragments of all elements from carbon down to Hydrogen can be clearly identified. The heavier fragments are sharply forward peaked as can be seen by comparing the spectra taken at 2.7° and 5.4° with respect to the beam axis, while Hydrogen and Helium fragments show broader angular distributions.
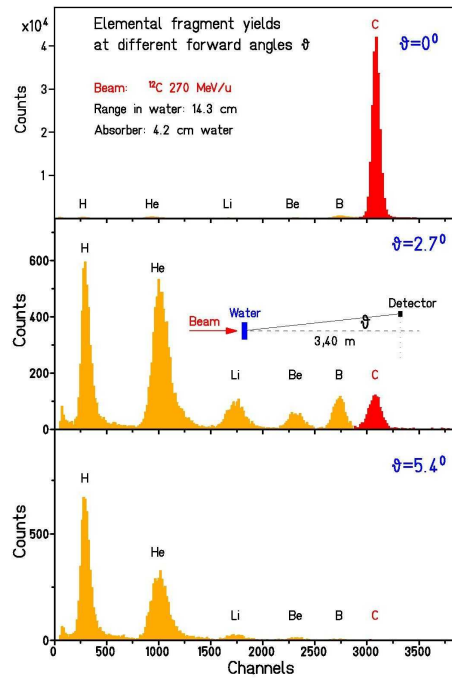
Figure 2. Relative elemental fragment yields measured at forward angles of 0°, 2.7°, and 5.4° with respect to the beam axis. Detection solid angle was 0.88 msr.

First experimental studies of the fragmentation of light ions in water or tissue-substitute materials dedicated to biomedical applications were carried out in 1971 at Princeton [3]. At LBL Berkeley detailed measurements [4] were performed on the characterization of 670 MeV/u ^{20}Ne beams which were used for patient treatments at the BEVALAC. Further investigations of nuclear fragmentation in water and tissue-substitute materials were carried out at the carbon ion treatment facilities at GSI Darmstadt [5,6] and at HIMAC in Chiba (Japan) [7].

Recent experiments at GSI [8] studying the build-up functions of secondary charged particles were performed at ^{12}C beam energies of 200 and 400 MeV/u, using a ΔE-E scintillator telescope and time-of-flight (TOF) techniques. The preliminary results include energy- and angular distributions, fragment yields and attenuation of the primary carbon projectiles at various water depths in the plateau, Bragg peak region and behind. As an example, build-up functions and angular distributions for a primary 400 MeV/u ^{12}C beam passing through a water absorber of variable thickness are shown in Figs. 3 and 4.
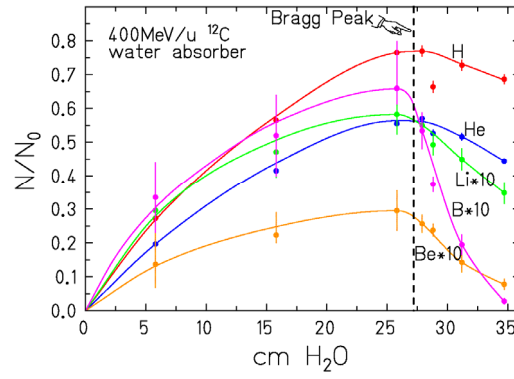
Figure 3. Build-up of secondary fragments in water. The data points were obtained by integration of the angular distributions measured at each depth.
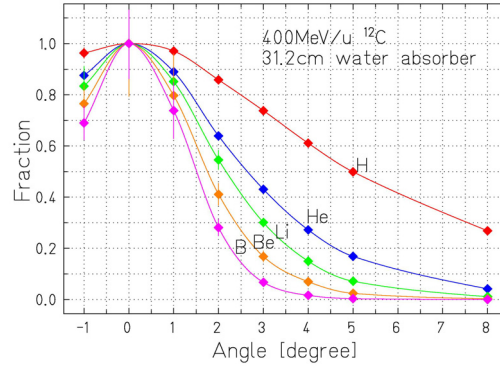
Figure 4. Normalized angular distributions of fragments of 400 MeV/u ^{12}C ions measured at a water depth of 31.2 cm, about 4 mm behind the Bragg peak.

The mean free path of ^{12}C ions in water at these energies was found to be 25.9(5) cm, i.e. about 20% larger than the calculated value given in table 1, but in agreement with our earlier results [5].

NEUTRON MEASUREMENTS

In order to study the production of fast neutrons under typical treatment conditions we used pencil-like beams of 200 AMeV ^{12}C ions with a range of 8.6 cm in water [9]. They were stopped in a water absorber with a total thickness of 12.78 cm. Secondary fragments emerging in forward direction from the water absorber (mainly protons, α-particles and neutrons) were detected by a ΔE-E-telescope in about 3 m distance from the target and at angles between 0º to 30º degrees with respect to the beam axis. The telescope consisted of a 14 cm long, hexagonally shaped BaF$_2$ scintillator and a 9 mm thick NE102 scintillator (veto detector) in front to discriminate charged particle and neutron events. Particle energies were measured by time-of-flight techniques. A thin NE102 scintillator in front of the target counted the number of incoming ^{12}C ions and delivered the start signal for the time-of flight measurement. The nuclear charge and mass of the particles were identified by the correlation of the energy loss in the veto scintillator and the energy deposited in the BaF$_2$ detector. The neutron

efficiency of the BaF$_2$ detector was obtained from separate measurements [10] using quasi-monoenergetic neutron beams at UCL Louvain (Belgium) and iThemba LABS (South Africa).

Energy spectra of fast neutrons emerging from the water target at angles of 0º, 10º, 20º and 30º are shown in Fig. 5 together with calculations performed with the Monte-Carlo code PHITS [11]. Similar data were obtained by Kurosawa et al. [12] for 180 MeV/u ^{12}C stopped in a graphite target.
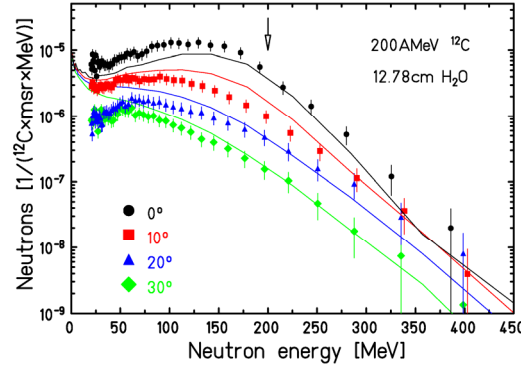
Figure 5. Neutron energy spectra measured at forward angles from 0° to 30°. The specific energy of the primary ^{12}C ions (200 MeV/u) is indicated by an arrow. PHITS calculations are shown as solid lines.

Neutrons are mainly emitted in forward direction and a broad maximum can be observed at about half of the initial beam energy at small angles (0º), indicating a strong contribution of projectile abrasion in peripheral collisions. The spectra measured at 10º, 20º and 30º have an exponential shape, which is typical for individual high energy nucleons and fragments evaporated from the hot reaction zone. From 0º to 30º a significant fraction of the neutron energy spectra extends to energies of more than 400 MeV, i.e. twice the specific energy of the incident carbon ions. This can be explained by momentum transfer of the nuclear Fermi-motion to the ejected neutrons.

In order to obtain the yields of secondary neutrons and charged fragments in the forward hemisphere the angular distributions were extrapolated to 90° and integrated. The resulting yields are 0.54(20) neutrons, 0.31(7) hydrogen fragments and 0.13(3) helium fragments per primary ^{12}C ion.

Estimation of the neutron dose in patient treatments with carbon ions

Based on the measured neutron yield for 200 MeV/u ^{12}C ions stopping in water the dose contribution of secondary fast neutrons in patient treatments with carbon ions was estimated [13] by converting the neutron fluence into kerma (kinetic energy released per mass unit). As a typical treatment volume the irradiation of a cube with the side length of 5 cm, i.e. an irradiated area of 25 cm^2, was assumed. To apply 20 Gy absorbed dose (corresponding to about 60 GyE biologically effective dose) to the given volume, a total amount of $5 \cdot 10^{10}$ carbon ions is required. This number is obtained from the computer code TRiP [14] which is used for patient treatment planning at GSI. The biologically effective dose given in units of Cobalt Gray Equivalent (GyE) includes the relative biological effectiveness (RBE) of the particles. Because of the complex composition of the particle field due to nuclear fragmentation, however, the biologically effective dose is not a simple product of absorbed dose and a mean RBE value but is evaluated by an iterative procedure using the TRiP code [15].

Taking the neutron yield of 0.54/ion, the neutron fluence 4 cm behind the irradiated volume then amounts to $(1.1 \pm 0.4) \cdot 10^9$ neutrons/cm^2. (The distance of 4 cm corresponds to the difference of target thickness and ion beam range in our measurements.) The kerma coefficient in water recommended in the ICRP 63 was extrapolated to a neutron energy of 200 MeV (k=150 pGy·cm^2) and multiplied with the fluence $\Phi(E)$ to obtain the neutron kerma. The resulting neutron dose of 8 mGy per treatment-Gy (table 2) is less then 1% of the treatment dose. This result is in good agreement with recent calculations [16] based on the Monte-Carlo code GEANT4.

Table 2: Total particle yields (E > 10 MeV/u) in the forward hemisphere and the corresponding estimated dose per treatment Gray.

	Yield (per ^{12}C ion)	Dose [mGy Gy^{-1}]
Neutrons	0.54±0.20	8±3
Protons	0.20±0.05	24±6
Hydrogen	0.31±0.07	37±8
Helium	0.13±0.03	62±14

Alternatively, the neutron dose equivalent (as defined in medical physics) can be estimated by multiplying the neutron fluence with the conversion coefficient $h_\Phi(E)$. Using a mean value of $h_\Phi = 300$ pSv·cm^2 [17] we obtain a dose value of 16 mSv per treatment-Gy or 5.4 mSv per treatment-GyE.

Using the Wide-Energy Neutron Detection Instrument (WENDI-II) [18] the neutron dose and angular distribution was obtained in independent measurements under the same experimental conditions (beam, target, geometry) as for the fluence measurements described above. The counted pulses of the WENDI-II device were converted to neutron dose by the factor 3.2×10^9 pulses/Sv. However, as discussed by Iwase et al. [19] the response of WENDI-II to high-energy protons and α-particles is negligible only below 100 MeV/u, but increases drastically at higher energies. This gives apparently higher dose values at small angles (0-10°) where high-energy charged particles dominate the radiation field. After applying this correction the neutron doses measured with WENDI-II were found to be in good agreement with those obtained from the measured neutron fluences at angles from 0-30° using the fluence-to-dose conversion factor given above [19].

Comparison of neutron doses in proton and carbon ion therapy

In table 3 dose contributions of secondary neutrons obtained from the present work with ^{12}C ions at GSI and from measurements at the proton therapy facility at PSI (Switzerland) [20] are compared. Both treatment units use scanning beam delivery systems. Although the yield of fast neutrons is much higher for ^{12}C ions than for protons the neutron doses per treatment-GyE are not very different because of the much lower number of ^{12}C ions needed to produce the same biologically effective dose as protons.

For passive beam delivery systems, where secondary neutrons are produced mainly by interactions of the primary beam with collimators, range shifters and other elements located in front of the patients, the neutron dose varies significantly with the configuration of the beam modifying equipment. This was examined experimentally by Yan et al. [21] for the medical beam line at the Harvard Cyclotron Laboratory. They found neutron dose equivalent values of typically 1-5 mSv/Gy at 50 cm distance from isocenter.

Table 3: Comparison of neutron yields and neutron doses in ^{12}C ion and proton radiotherapy for scanning beam delivery systems. The yield number given in parentheses was recalculated from the dose.

Beam [MeV/u]	Target [g/cm2]	Neutrons per primary ion	Neutron dose* [mSv per GyE]
^{12}C (200)	H$_2$O (12.78)	0.54 ± 20% (0.025)	5.4 ± 20% (scanning)
p (177)	H$_2$O (30.1)		2.3 ± 30% (scanning)

* Neutron dose expected in healthy tissue of the patient in the non-treated volume for a medium-sized target

Monte Carlo calculations performed by Agosteo et al. [22] for the proton therapy beam lines at PSI (active scanning) and at iThemba LABS South Africa (passive system) confirm the experimental results by Schneider et al. [20] and Binns et al. [23]. The calculations indicate a factor of 10 higher secondary dose for the passive beam delivery system which seems to originate predominantly from neutrons generated in the last collimator.

CONCLUSION

At energies of 100–400 MeV/u as required for irradiation of deep-seated tumors with carbon ions, nuclear fragmentation is a significant effect. The radiation field of a heavy-ion beam penetrating in tissue is rather complex due to the build-up of secondary fragments with wide energy spectra, while the flux of primary particles decreases exponentially with depth. The physical beam models included in treatment planning programs for heavy-ion irradiations of cancer patients have to take into account these effects and comparison with experimental data is indispensable for the validation process.

The present work has shown that the dose contribution caused by secondary fast neutrons in carbon ion radiotherapy is of the order of 1% of the treatment dose and much lower than the dose of secondary <u>charged</u> fragments. Further measurements as well as Monte Carlo calculations are planned to investigate the dose deposition of secondary fragments, in particular in regions outside of the planned treatment volume.

REFERENCES

1. L. Sihver, D. Schardt, T. Kanai, Japan. J. Med. Phys. 18, (1998) 1
2. S. Kox, Phys. Rev. C35 (1987) 1678
3. W. Schimmerling, K. Vosburgh, P. Todd: Science 174 (1971) 1123
4. W. Schimmerling et al., Radiat. Res. 120 (1989) 36
5. I. Schall et al., NIM B117 (1996) 221
6. M. Golovkov et al., Adv. In Hadrontherapy, Eds. U. Amaldi, B. Larsson, pp. 316-324, Elsevier Science(1997)
7. N. Matsufuji et al., Phys. Med. Biol. 48 (2003) 1605; and Phys. Med. Biol. 50 (2005) 3393
8. E. Haettner, H. Iwase, D. Schardt, Rad. Prot. Dosim. 122 (2007) 485; and E. Haettner, Master of science thesis, Stockholm, Sweden (2006)
9. K. Gunzert-Marx, PhD Thesis, TU Darmstadt (2004)
10. K. Gunzert-Marx et al., Nucl. Instrum. Meth. A536 (2005) 146
11. K. Niita, T. Sato, H. Iwase, H. Nose, H. Nakashima, L. Sihver, Proc. 2003 Symp. on Nuclear Data, Nov. 2003, JAERI-Conf-2004-005, p.33 (2004)
12. T. Kurosawa et al., Nucl. Sci. Eng. 132 (1999) 30
13. K. Gunzert-Marx et al., Rad. Prot. Dosim. 110 (2004) 595
14. M. Krämer et al., Phys. Med. Biol. 45 (2000) 3299; and Phys. Med. Biol. 45 (2000) 3319
15. M. Krämer and M. Scholz, Phys. Med. Biol. 51 (2006) 1959
16. I. Pshenichnov et al., Phys. Med. Biol. 50 (2005) 5493
17. A. Ferrari, M. Pellicioni, Rad. Prot. Dosim. 76 (1998) 215
18. R.H. Olscher et al., Health Physics 79 (2000) 170
19. H. Iwase et al., Rad. Prot. Dosim. doi:10.1093/rpd/ncm 140 (2007)
20. U. Schneider et al., Int. J. Radiation Oncology Biol. Phys. 53 (2002) 244
21. X. Yan et al., Nucl. Instrum. Meth. A476 (2002) 429
22. S. Agosteo et al., Radiother. Oncol. 48 (1998) 293
23. P.J. Binns, J.H. Hough, Rad. Prot. Dosim. 70 (1997) 441

COMPARISON OF THE SHIELDING DESIGN OF VARIOUS CARBON ION THERAPY FACILITIES IN THE COUNTRIES JAPAN, ITALY AND GERMANY

Georg Fehrenbacher[*], Gesellschaft für Schwerionenforschung mbH, Planckstr. 1, D-64291 Darmstadt, Germany

The construction of hospital based carbon ion therapy facilities concentrates presently in Japan and Europe. In this work a comparative analysis of the shielding design is given for the facilities HIMAC (Heavy Ion Medical Accelerator) in Chiba, Japan, which is operated by the NIRS (National Institute for Radiological Sciences), the facility at Gunma University, Japan, the CNAO installation (Centro Nazionale di Adroterapia Oncologica) in Pave, Italy and the HIT facility (Heidelberg Ion-Beam Therapy Centre) in Heidelberg, Germany. The basis for the radiation protection planning of the particular national radiation protection legislations is summarized. The methods for the estimation of the dose rate levels for the radiation sources – caused by ion beam interactions with target nuclei - as well as for the dose rate levels outside the shielding are presented. The calculated results for the architectural shielding designs are shown. An inter-comparison for the architectural shielding measures for the respective facilities is performed.

A Introduction

Worldwide an increasing number of - hospital based - particle therapy facilities is in operation, under construction or planned for the near future. The boom of these facilities can be explained by the very positive results of patient treatments carried out in accelerator laboratories - originally founded for fundamental research (LBL in Berkeley [1], HCL in Boston [2] or in Europe, e.g. GSI, PSI, HMI [3, 4, 5, 6] and others) – or in newer facilities, dedicated to patient treatments like the Loma Linda University Medical Centre [7]. Particle therapy installations can roughly be classified into two types of facilities, those developed only for proton treatments and those which are suitable for treatments with heavier ions like carbon. This work focuses on hospital based carbon ion treatment facilities.

Hospital based carbon ion treatment facilities were built in Japan. Several new facilities are under construction in Europe and Japan. The first facility was built by the NIRS (National Institute for Radiological Sciences) at Chiba, Japan, the Heavy Ion Medical Accelerator (HIMAC). The installation features 3 treatment places (one horizontal beam irradiation port (H); one with a vertical beam irradiation port (V) and a combined one (H&V)). Several rooms are dedicated for research. Other Japanese facilities are the HIBMC (Hyogo Ion Beam Medical Centre) at Hyogo (in operation since 2003, 3 of 5 chambers are suitable for carbon ion therapy) and an installation at Gunma University (under construction since 2006 for 3 treatment rooms, H, V, H&V). In Europe 2 facilities are under construction, the CNAO installation at Pave (Centro Nazionale di Adroterapia Oncologica, 2 H, 1 H&V rooms), Italy and the HIT facility in Heidelberg, Germany (Heidelberg Ion-Beam Therapy Centre, 2 H rooms and a carbon ion gantry). The main issue of the radiation protection of ion therapy facilities is the production of secondary radiation when parts of the ion beam or the beam as a whole is deposited in matter like the accelerator structure or in the tissue of the patient. If ions are slowed down in matter, in nucleus-nucleus interactions nuclear fragments as well as neutron and gamma radiation are released. The extent of the beam depositions (ions/sec, ion energy) determines the effort for the shielding measures. The architectural radiation protection of ion therapy facilities has to consider the expected locations of (substantial) beam losses in the synchrotron and in the beam transfer lines to the treatment chambers as well as the absolute levels of dose rates and the spatial dose patterns in the therapy chambers. The planning of the shielding walls has to take in to account the source strength of the produced radiation and the maximum tolerated dose rates in the adjacent area outside the shielding. The particular national radiation protection legislation gives the definition of radiological areas by the introduction of dose limits related to the period of exposure (in Europe one year, in Japan one week and 3 months).

---

*Corresponding author: G.Fehrenbacher@gsi.de

The planning of a facility has to consider the adequate definition of the radiological areas (as the inaccessible area for all ion beam transporting rooms, the control area, the survey area and the public area).

So far only synchrotron accelerators are in use for the acceleration of carbon ions in therapy facilities. In synchrotrons one can utilize the possibility to accelerate the ions to exact the energy which is actually needed during the treatment. In contrast to this, the passive methods use the maximum beam energy and the ions are slowed down to the needed beam energy by means of a bolus. In Japanese facilities the passive method is predominantly applied. In bolus elements, a part of the beam is lost and secondary radiation is produced. The beam forming systems are positioned near or within the therapy chamber. Therefore the shielding design must take into account that the beam forming system has to be shielded.

The aim of this work is a comparative analysis of the shielding design of different carbon ion therapy facilities in Japan, Italy and Germany which are already in operation or under construction.

B Basis of the Radiation Protection Planning of Ion Accelerator Facilities

The radiation protection planning of an ion therapy facility has to be in compliance with the requirements of the particular national radiation protection laws. Despite the fact that the specific regulations in the countries, to be considered here, give different standards for the planning of the facilities, the actual dose limits are identical in Italy and Germany. The corresponding values in Japan are higher (the values for the control and survey area). The definition of the exposure periods is different to the European ones (one week and 3 months respectively). The relevant values are given in tab. 1.

Table 1: *Classification of radiological areas in the countries Japan, Italy and Germany.*

Area (see also fig. 1)	Dose Limit		
	Japan [8]	**Italy** [9]	**Germany** [10]
Restricted	No general regulation	No general regulation (RSO[1] judgem.)	>3 mSv/h
Control	>1 mSv / week	>6 mSv/a	>6 mSv/a
Survey	>0.1 mSv / week - 1.3 mSv / 3 months <1 mSv / week	>1 mSv/a, < 6 mSv/a	>1 mSv/a, < 6 mSv/a
Public	<250 µSv / 3 months	<1 mSv/a	<1 mSv/a

[1](RSO=Radiation Safety Officer)

Figure 1: *Radiological areas of an ion treatment facility. The accelerator areas (LINAC =linear accelerator, as injector, Synchrotron) as well as the beam transfer lines are inaccessible, the patient therapy chamber is inaccessible too (except for the patient). The adjacent areas to the accelerator and the therapy chambers are partially control or survey areas. The areas adjacent to the control areas (and the LINAC here) are survey areas and the area outside the facility and parts of the clinic centre itself are classified as public areas. The dose limits for these areas are given in tab. 1 for the countries Japan, Italy and Germany.*
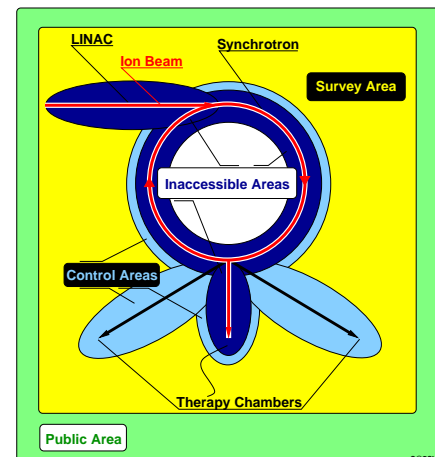
Other specific regulations defined by the responsible authorities or further internal standards can have an influence on the definition of radiological areas and their architectural shielding design.

Ion treatment facilities are designed to allow tumour irradiations with a dose rate of about Gy/min in a depth of 30 cm at maximum. This means that for carbon ion treatments the ion intensities are in the range of 3E8 ions/sec with a maximum energy of 430 AMeV.

An important issue for the shielding planning is the knowledge of the beam loss distributions in the facility. Beam losses occur during the injection from the LINAC to the synchrotron, in the synchrotron itself, near the extraction from the synchrotron to the high energy beam line and within the high energy beam line, when the ions are transported to the therapy chamber. The full beam intensity is deposited in the tumour tissue of the patient and consequently the highest radiation levels occur in the treatment chambers. Therefore the treatment chambers have the highest amount of shielding measures.

The estimation of the production of the radiation produced by light or heavy ions which are slowed down in the accelerator structure or in the patient tissue was a difficult issue in the past. The development of methods for the estimation of radiation source distributions and the attenuation in shielding walls took place in various steps. The first approach was the use of source data from proton beams with the same energy as the ion beam expressed in MeV per nucleon. The produced radiation can be transported with radiation transport programs like the Monte-Carlo (MC) codes MCNPX [11] or FLUKA [12] and the spectral radiation fluence outside the shielding can be calculated and converted in dose values using the corresponding fluence-to-dose conversion functions. The approach derived from proton source distributions (scaled up to the nucleon numbers of the nuclei of the ion beams) yields in a simplified estimation of the produced radiation dose. Over the years more and more experimental data on neutron production of light and heavier ions were available [13] for the thick target approximation and could be used for shielding calculations. In another approximation the MC radiation transport codes were extended for the calculation of specific nucleus-nucleus collisions and the derived source distributions can be transferred to other ion-target combinations. An example is given for the HETC-KFA development (intranuclear-cascade evaporation model [14]) for the calculation of neutron distributions from He-on-iron-target reactions (178 AMeV) or neutron distributions from He-on-copper-target reactions [15]. Recently further neutron data based on measurements (C ions on graphite with 400 AMeV [16]) and Monte Carlo calculations (e.g. PHITS, FLUKA [17,18]) became available and were used for the development of shielding models like that developed by Agosteo et al. [19, 20] or were directly used for shielding design calculations for CNAO [21,22], Gunma University [23] and HIT [24].

C Examples for Ion Therapy Facilities

In this work an inter-comparison for the shielding layouts of the light ion treatment facilities at HIMAC, Gunma University (both Japan), CNAO (Italy) and HIT (Germany) is presented.

HIMAC, Chiba, Japan

At HIMAC [25] a large variety of ions can be accelerated such as p, He, C, Ne, Si and Ar ions. For patient treatments carbon ions are mainly used. Near the HIMAC building a hospital was built to care the patients. The first patients were treated in the year 1994, in 2004 400 patients were treated. The accelerator installation comprises 2 synchrotrons, 3 treatment rooms, a physics and general-purpose irradiation room, a medium energy beam irradiation room and a room for biological irradiations (see fig. 2). For the patient treatments different types of rooms are available depending on the needs of the irradiation geometry. There is a room for horizontal irradiations (H), a room for vertical irradiations (V) and a room for the combination of both (H&V). The last one can be operated with two different beams from both synchrotrons (see in fig. 2 the red beam lines).

Figure 2: *Drawing of the HIMAC facility (Heavy Ion Medical Accelerator in Chiba, Japan). HIMAC is operated by the NIRS (National Institute for Radiological Sciences). The facility comprises 3 treatment rooms (H, V, H&V) and rooms for research. In the H&V treatment room, both irradiation ports can be supplied with ion beams simultaneously (red beam lines). The colours of the areas are related to the radiological areas of fig. 1.*
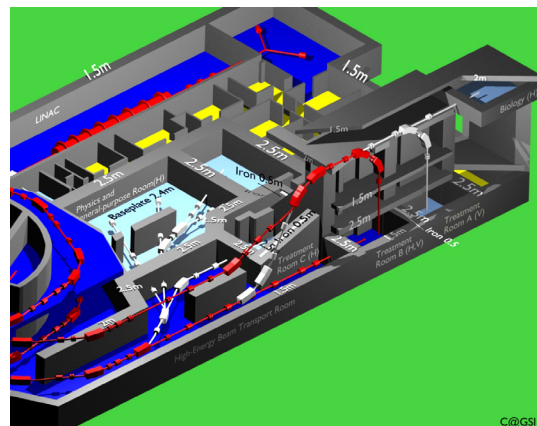
The beam extraction intensities for carbon ions in the synchrotrons amount to 2E8 pps (particles per second) [23]. For the case of He ions (500 AMeV - which is higher than for therapy irradiations actually needed) a detailed survey on beam loss distributions is given [23]. It is reported that 5% beam losses occur during the extraction, 10% beam losses during the

acceleration along the ring, 15% at the ring scrapers and 10% beam losses at the vertical beam transfer lines.

The beam loss data and the estimated period of operation per week (synchrotron 108 h/week, treatment rooms 11-18 h/week) served as a basis for the shielding calculations. The results of the HETC-KFA calculations (see above) were used for the development of an approximation formula for the calculation of the neutron fluence caused by He ions and other ion types and the possibility to compute the neutron fluence as a function of the ion energy is provided [26]. In a further step the attenuation of the neutron radiation in the bulk shield is calculated and the corresponding dose values are derived [26]. The results for the shielding calculations are given in tab. 2 for some essential areas in HIMAC as e.g. the synchrotron, the therapy chambers, the LINAC and others. The shielding walls are partially reinforced by iron layers. In tab. 2 (3rd column) the values for the thicknesses of the combined concrete-iron-shields are converted into effective values for concrete layers. The thickness of the shielding around the synchrotron amounts to 1.5 m. At the extraction area there is a 2.5 m shield in addition (fig. 2 left). The effective shield thicknesses for the therapy chambers are 3.2 m in forward direction. The value for the lateral one is 2.5 m. Values for the high energy beam transfer line, for the roof shielding as well as for the floor shield are also given in tab. 2.

Table 2: *Shielding measures of the HIMAC facilities for some areas: Synchrotron, Therapy A, B, C, Roof, Floor, HEBT and Linac. All values are given in m. In cases with combined shielding materials (concrete, iron), the effective thickness for concrete is also indicated.*

Area	Shield Thickness (m) Forward Direction / Lateral Direction	Effective Concrete Thickness (m)
Synchrotron	1.5 (Inside 2.5- also as local shield)	-
Therapy H	2.5 (0.5 Fe) / 2.5	3.22 / 2.5
Therapy H&V	2.5 (0.5 Fe) / 1.6, Maze 1.6 (0.8 Fe)	3.22 / 1.6 Maze 2.75
Therapy V	2.5 / 1.6, Maze 1.2	-
Roof	1.5	-
Floor	2.4	-
HEBT	1.5 – 2.0	-
Linac	1.5	-

Gunma University, Japan

A planning group at NIRS proposed a heavy ion treatment facility which represents a further stage to an optimized carbon ion treatment hospital [27, 28, 29, 30]. The potential of cost reduction was analyzed and following goals were defined: 1. the synchrotron circumference is reduced to a value of 61.5 m. The particle range in tissue is at most 250 mm which covers nearly all treatments performed at HIMAC. This means a beam energy of 400 AMeV at maximum is chosen, taking into account the energy degradation effects in the beam forming system. All passive systems are potential sources for the production of secondary radiation and consequently have an effect on the shielding design of the building. Here the reduction of the length of this system to 5.5 m is planned [31] which consequently reduces the total amount of the concrete shielding for the building around this area. The aim of the facility is the treatment of 600 patients per year. This will be achieved by the operation of three treatment rooms (one H-port, one V-port and a H&V-port). A fourth room (V-port) is provided for the development of new irradiation methods [27].

It is supposed that common Japanese legal standards are the basis for the shielding design for the installations (see table 1), no further specific regulations of the prefecture of Gunma are known [23]. The desired beam intensity at the irradiation port is 1.2E9 pps which yields in 3.6E8 pps for the patient

treatments [27]. An overview on beam intensities and beam loss distributions is given in table 3 at different stages of the acceleration process. For the development of the shielding design it is mentionable that abundant ion beams are decelerated in the accelerator [27] and consequently the production of neutron radiation is reduced. The planning of the shielding design was carried out by the same group responsible for the planning of HIBMC (Hyogo Ion Beam Medical Center) at Hyogo, Japan. A private architectural design office, Nikken Sekkei Ltd., was also involved in the planning (see also description of HIMAC shielding and the work of Kato [15, 32]). The methods for calculating the dose rates can be summarized as follows:

1. The source distributions of the produced neutron radiation are taken from the Kurosawa measurements [16, 23].
2. The beam loss distributions were determined by Noda et al. [27] and are listed in tab. 3.
3. The dose rates outside the shielding were computed using the ANISN code [33] and the cross sections from the JAERI [34].
4. It is also reported that single areas of the facility are designed by means of the PHITS-code [23] which was developed by Iwase et al. [17] in Japan.

The layout of the Gunma facility is shown in fig. 3. In fig. 3 the values of the shield thicknesses are indicated. At some positions the shields are reinforced by iron layers. One can see that the shielding of the synchrotron near the extraction area is considerably extended in comparison to HIMAC one with a maximum value of 5 m and a minimum shield thickness of about 3 m. The therapy chambers with H-ports are shielded with 3 m walls in forward direction (1.9 m concrete and 1.1 m iron, which results in an effective thickness of 4.6 m concrete). The lateral thicknesses of the therapy chambers range from 1.5 m to 2.5 m. The linac shielding wall amounts to 1.0 m to 2.5 m. The baseplate has a thickness of 2.5 m. The roof shielding amounts to 1.1 m to 2.2 m thickness. The wall thicknesses of the fourth irradiation room (V) are obviously reduced in comparison to the other ones due to shorter estimated irradiation periods. The wall sizes are 1.1 m to 1.7 m.

From the architectural shielding design one can derive, that the areas around the therapy chambers - within the building - are survey areas.

Figure 3: *Layout of the Gunma ion irradiation facility with the LINAC (left), the synchrotron (ring accelerator) and the therapy chambers. For the patient treatments 3 chambers are available. The fourth chamber is dedicated for the development of new irradiation methods. The values for the wall thicknesses and those for the iron reinforcements are also indicated (see also caption of fig. 2).*
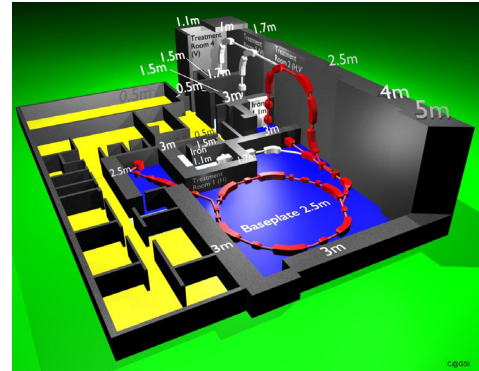
Table 3: *Beam loss distributions and absolute beam intensities for the Gunma facility, calculated by Noda et al. [27], η gives the ion beam transfer efficiency at different stages of the acceleration and transfer process. The beam intensity is given in the quantity particles per pulse (ppp) or in the quantity particles per sec (pps).*

Section	Efficiency η	Beam Intensity
Injection	0.4	2E10 ppp
Synchrotron	0.64	5E9 ppp
Extraction	0.9	1.3E9 pps
HEBT	0.95	1.2E9 pps
Chamber	0.3	3.6E8 pps

CNAO, Pave, Italy

A first layout for CNAO was developed within the framework of the TERA project [35]. Detailed shielding designs were conceived by Agosteo et al. in various investigations. In the first paper shielding calculations were carried out for a hospital based 250 MeV proton accelerator [19]. An outline is given for 400 AMeV oxygen beams. A simple approximation for the neutron yields was applied by scaling the corresponding neutron yields from proton beams to oxygen ion beams (namely $y_{Ion} = A \cdot y_{Proton}$). A line-of-sight model was developed (=estimation of the dose derived from the source strength, the distance given by the straight line source-reference-point and shield thickness). The neutron source data were used for the radiation transport using a spherical model of a concrete shield and the parameters for the 2 parameter formula were determined ($H/H_0 = r^{-2} \cdot \exp(-d \cdot \rho / \lambda)$, with the source parameter $H_0(\theta)$ and the attenuation parameter $\lambda(\theta)$, d the shield thickness and r the total distance [19]).

In a further stage of the planning of the CNAO shielding design, measured neutron spectra of Kurosawa (400 AMeV carbon beams on Cu or C [16]) were applied for the determination of the parameter values of the 2 parameter formula. The formula was used to derive the thicknesses of the shielding walls. For the input, specific assumptions for beam losses, duty factors for the accelerator operation as well as occupancy factors for the staff, which were introduced for all relevant areas in the facility, were used.

The last revision of the shielding design was done by Porta et al. [36] and Ferrarini [37]. The relevant ion beam data are 8E8 ppp (particles per pulse) for carbon ions (400 AMeV) and 2E10 ppp for proton beams (250 MeV). The total number of transported ions per year is 1E16 for both the patient treatments and for the research irradiations. The beam losses amount to 5 % at the extraction area, 5% in the whole synchrotron and 5% in single dipoles [20,37]. The first stage of the CNAO facility is shown in fig. 4 (in a second stage, 2 gantry irradiation rooms will be installed). The classification of areas around the synchrotron follows the guideline to avoid the introduction of control and – if possible - survey areas around the synchrotron (see table 1 and fig. 1). Nevertheless the technical support room used as power converters zone (room behind beam extraction area) is defined as survey area. The experiment preparation room (separated room, dark blue) is an interdicted area during the synchrotron operation. Areas as the main control room (near entrance maze to the synchrotron) as well as the outlying area accessible for the public are kept at a low annual dose level of less than 1 mSv.

Figure 4: *Overview of the CNAO facility with 3 treatment rooms (2 H, 1 V&H), an experimental room (light blue) and the synchrotron with the Linac inside. Here, the middle therapy chamber (H&V) is provided with ion beams. Indicated are also beam loss points (white stars) and the beam deposition point (red star). See also caption of fig. 2.*
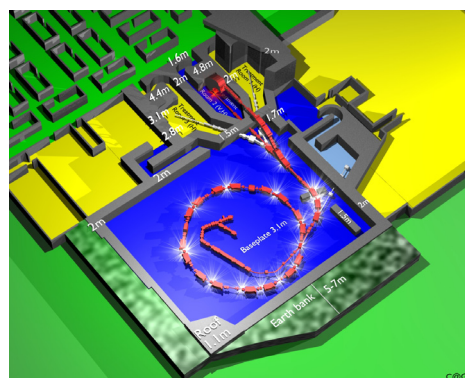
The synchrotron is shielded by a 2 m concrete wall (for the most part) which is strengthened by soil layers (5 m to 7 m to the public area). Inside the synchrotron there are additional local concrete shields. The therapy rooms are shielded to such an extent that the adjoining rooms are kept at dose rate levels lower than 0.5 µSv/h (in total 2 mSv/a including the radiation coming from the synchrotron). The lateral shield range from 2 m to 3.1 m and the forward shield walls have thicknesses of 4.4 m to 4.8 m and have an effective thickness of up to 8 m because of the oblique incidence of the neutron radiation relative to the shielding walls. It was discussed to construct the shield in the therapy chamber with heavy concrete, but it was found that the small advantage of an improved shield effect is compensated by the higher level of activation within the shield. Therefore it was decided to use only normal concrete. The floor and the roof shield have thicknesses of 3.1 m and 1.1 m to 2 m respectively.

HIT, Heidelberg, Germany

The origin of the Heidelberg heavy ion therapy facility is a design proposal of the GSI accelerator department [38]. Based on the developments of the GSI pilot project and the encouraging results of the carbon ion treatments [4] the planning of a hospital based heavy ion treatment facility was initiated [39,40]. The facility comprises 2 horizontal treatment rooms (H) and a gantry suitable for carbon ion transport (e.g. C ions with energies of 430 AMeV). In fig. 5 a part of HIT is shown. The Linac room, the synchrotron room, the therapy chambers H_1, H_2 and the gantry room are presented. Also indicated is the room for research, development and quality assurance (left). Parts of the building are covered by soil layers and other bulk materials. Some parts of the building - those containing the main accelerator components - are embedded in earth.

Figure 5: *Part of the HIT facility in Heidelberg. Shown are the LINAC, the synchrotron and the horizontal treatment chambers H_1 and H_2, each with an entrance labyrinth. Also the room for the gantry and the room for research, development and quality assurance are indicated (see also caption of fig. 2).*
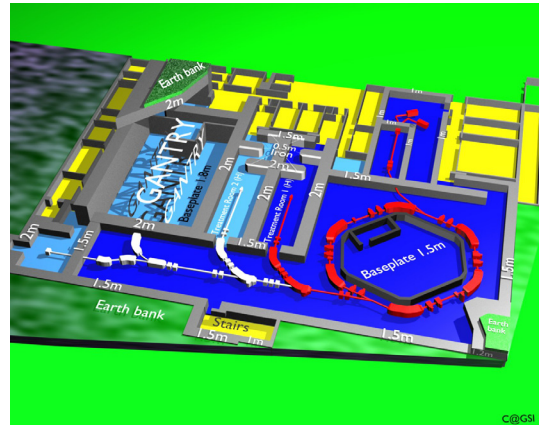
At HIT protons as well as helium ions, carbon ions and oxygen ions can be accelerated and delivered to the treatment chambers. The energies of the ions are so adapted that the maximum range in water is about 40 cm for protons and helium ions, 30 cm for carbon ions and 23 cm for oxygen ions. The beam parameters for HIT are e.g. 4E10 ppp for protons (220 MeV) or 1E9 ppp for carbon ions (430 AMeV).

The shielding design was developed on the basis of the Kurosawa neutron spectra of the 400 AMeV carbon ions [16]. A line-of-sight model was used to determine dose rates of the neutron radiation outside the shield [41]. The model considers the angular dependence of the neutron production (0°-90°), the angular dependent neutron energy distribution (E_n>5 MeV), the neutron energy dependent absorption (removal cross section) and the buildup-effect of the neutron radiation in matter. For angles greater than 90° relative to the incoming ion beam, the neutron source distribution at 90° was used. MC based radiation transport calculations were applied too. For these computations the program FLUKA (=Fluktuierende Kaskade, version of the year 2000) was applied [12]. Also for the MC calculations the Kurosawa neutron spectra were used as input. FLUKA was applied for the H_1-H_2 geometry [24] as well as for the gantry geometry [42]. For the gantry geometry calculations, the iron counterweight of 1 m thickness was taken into account which attenuates the main neutron cone substantially in the angular range +/- 25° relative to the ion beam line.

Further specific studies were performed by means of FLUKA e.g. the deepening of the floor shielding in H_1-H_2 for the installation of robots in order to estimate the effect of the dose rate level increase in the basement of the building.

In a later stage of the project the heavy ion version of FLUKA – including nucleus-nucleus collisions - was available [18]. Comparisons were performed with both calculation methods – one with the Kurosawa neutron source spectra as input for FLUKA and the other one with the complete FLUKA simulations - and results with reasonable agreement were obtained for the dose rate levels (deviations within 26 %). The shield thickness in HIT is adapted to meet the annual dose limits given in table 1. Furthermore the responsible authority for HIT gave the guideline to limit the dose rate levels outside the interlocked area particular for 10-min-irradiation periods. The limit here is 3 μSv/h. The planning is based on assumptions on beam losses at local (specific) areas with about 10 % of the beam intensity, e.g. at the beam extraction point and 10 % beam losses in the beam deflection elements (dipoles). Because of the incomplete knowledge on the beam loss distributions in the synchrotron and the beam transfer lines, it was decided to install in cases of increased beam losses additional local shielding elements e.g. a stack of concrete blocks. In HIT the radiological areas are defined as follows:

- All areas where the ion beam is transported are inaccessible.
- The adjacent therapy chambers are control areas.
- Other adjacent areas to the accelerator and therapy rooms are survey areas.
- Accelerator areas with interrupted beam operation are control areas because of probable radioactive activation.

For the treatment chambers H_1, H_2 the crosswise shield walls (altogether 3 per chamber) in the entrance maze have in forward direction total thicknesses of 5.5 m, 3 steel layers (each 0.5 m) improve the shielding effect (total effective concrete thickness of 7.66 m). The lateral shield amounts to 2 m thickness. The building of the gantry room has a wall thickness of 2 m. The shield effect is improved by the iron counterweight of 1 m thickness. Here the shielding calculations can take advantage of the fact that the main direction of the produced radiation varies according to the alternating irradiation position of the gantry (dose reduction factor of 10 at most, see also DIN6847-2 [43]). Also the roof shields (2 m) of the H_1 -H_2 therapy chambers are partially reinforced by steel layers (0.5 m, which results in an effective concrete thickness of 2.72 m). The synchrotron is shielded by a 1.5 m concrete wall and partially by additional soil layers to the outside area. It is expected that outside the building of the synchrotron the measurable dose rate will be negligible. Soil layers (and other bulk materials) cover the roof shield of the synchrotron and H_1, H_2 respectively as well as parts of the building for the gantry treatments. The baseplate amounts to 1.5 m to 1.8 m. The shield to the ground reduces the activation of soil and ground water.

D Summary

The planning of ion therapy facilities has to consider that the operation of an accelerator and the therapy units are unavoidably associated with the production of secondary radiation (mainly neutron radiation) by the nuclear interaction of the ion beam nuclei with the target nuclei in matter.
The accelerators of the ion therapy facilities – considered in this work - are designed to enable beams which ensure that the therapy dose rate for the tumour tissue is in the range of about one Gy per minute or higher. This means that the beam intensities for carbon ions are in the range of a few 1E8 particles per second (pps). The maximum carbon ion beam intensities of the facilities vary from 1E8 pps (HIMAC) to 3.6E8 pps (Gunma). The values of these intensities and the maximum carbon ion energies (in the range from 380 AMeV to 430 AMeV) served as a basis for the shielding design calculations. The shielding designs are mainly based on the carbon ion operation although for ions lighter than carbon ions other characteristics of the corresponding source strength and angular distributions of the secondary radiation are expected. The dose limits of the national radiation protection legislations for Italy and Germany are equivalent. The Japanese laws give dose assessment standards for one week periods and 3 months periods, but they give higher dose levels for survey and control areas extrapolated for a whole year (see tab. 1).

The applied methods for the calculation of the dose rate levels are based on data from specific nucleus-nucleus collisions (defined by ion type, ion-target-combination and ion energy) in thick target approximations. These were partially derived from MC codes, e.g. the HETC-KFA code [14]. These (older) codes were extended for the modelling of some specific nucleus-nucleus collisions. The produced source distributions – essentially for neutron radiation – were adapted to other ion-target combinations. The attenuation of the produced neutron radiation in the shielding was computed by application of exponential laws with parameters which were derived for the specific energy distributions of the neutron radiation. Meanwhile measured neutron source data became available for carbon ions [16]. These are used as input distributions for radiation transport calculations and for the determination of the source and attenuation parameters for the line-of-sight models. Recently complete MC models (PHITS [17] and FLUKA [18]) were applied for both the source distribution calculations and the transport of the produced radiation through the geometrical models of the accelerators and the therapy chambers. For the shielding, following materials are mainly used (the corresponding values for λ – in the formulation

$H/H_0 = \exp(-d \cdot \rho / \lambda)$ - for high energy hadrons are also indicated, see Sullivan [44]): Normal concrete, ($\lambda=100$ g/cm^2), earth ($\lambda=100$ g/cm^2) and iron ($\lambda=132$ g/cm^2).

For the inter-comparison of various carbon ion therapy facilities in different countries following tendencies can be stated:

The shielding of the synchrotron of the Gunma facility was increased in comparison to that of the HIMAC facility (from 1.5 m to at least 3 m and 5 m at most). The CNAO facility has shields for the synchrotron with thicknesses of 2 m concrete (for the most part) and soil layers in addition. The HIT facility has 1.5 m concrete walls for the synchrotron. The building of HIT is partially embedded in earth. Therefore the shielding effect is improved by soil layers. The shielding of the therapy chambers has to consider different irradiation geometries and different concepts for the access to the chamber. First, the different geometries of the horizontal treatment chambers (H) are assessed. The most challenging design is given for the HIT facility where the main neutron cone affects directly the entrance maze. Here the radiation is attenuated by 3 cross walls which are reinforced by steel layers (in total 4.0 m concrete and 1.5 m steel = 7.66 m effective concrete). At CNAO only the middle therapy chamber has a comparable design to HIT, but the beam here is shared between vertical and horizontal irradiations. In forward direction there is a shield thickness of 4.8 m (+1.6 m maze wall) concrete, in total 6.4 m. At HIMAC and Gunma University there is a 2.0 m (+0.5 m Fe, 3.2 m effective concrete in total) and a 2 m (+ 1.1 m Fe, 4.7 m effective concrete in total) shield respectively for the forward direction. At HIMAC and Gunma University the access to the chamber is lateral to the beam line, which is an advantage for the reduction of the radiation levels in the entrance maze. The lateral shielding of the therapy chambers range from 1.5 m (Gunma), 2 m -2.5 m (HIT, HIMAC) to 3.1 m (CNAO) for the chamber with H-port. For the others (combined H&V, V) the corresponding thickness values are lower and reach from 1.5 m to 2 m at most. A characteristic of HIT is the installation of a carbon ion gantry. Here the shielding effect must be guaranteed by an iron 1-m-counterweight and a 2 m concrete shield of the building. In all facilities roof shields (1.1 m to 2.2 m at least) are installed to reduce the radiation propagation into the vicinity of the facility by the skyshine effect. Floor shields (2 m to 3.2 m) are installed in the basement of the buildings to reduce the activation of the soil and groundwater.

All facilities – considered in this work - are essentially designed for the operation of carbon ions. For lighter particles than carbon ions, the shielding layout has to take into account the altered source distributions for the produced neutron radiation (higher dose rate levels for larger angles, but lower mean neutron energies). Consequently the layout of the installation is for the most part conservative for the beam (loss) depositions in forward direction, but not necessarily for larger angles ($\theta > 25°$) relative to the primary beam due to higher intensities. Nevertheless no substantially increased dose rate levels outside the shielding are expected for the operation of e.g. protons. This can be confirmed by the fact that for ions lighter than carbon, the mean energy of the produced neutron radiation is substantially lowered and the effectiveness of the shielding is improved.

For the inter-comparison of the shielding design of the ion therapy facilities one can conclude, that from the first facility in Japan to the recent facilities in Europe, the amount of shielding measures and the degree of radiological protection of the architectural layout increased with the comparatively safest shielding design for CNAO.

Acknowledgement

References

1. Castro J. *Results of Heavy Ion Radiotherapy*, Radiat. Environ. Biophys. 34, 45-48 (1995).
2. Munzenrider J. *Proton Therapy at Harvard*, Strahlentherapie 161, 756-763 (1985).

3. Kraft G. *Tumortherapie mit schweren Ionen, physikalische und biologische Grundlagen; Technische Realisierung an der GSI, Klinische Ergebnisse*; Verein zur Förderung der Tumortherapie mit schweren Ionen e.V., Darmstadt, ISBN: 3-00-017833-3 (2005).
4. Schultz-Ertner D. et al. *Results of Carbon Ion Radiotherapy in 152 Patients*, Int. J. Radiation Onc. Biol. Phys., Vol. 58, No. 2, 631-640, (2004).
5. Pedroni, E. *The 200-MeV Proton Therapy Project at the Paul Scherrer Institute: Conceptual Design and Practical Realization*, Med.Phys. 22 1, 37-53 (1995).
6. Heufelder J. et al. *Fünf Jahre Protonentherapie von Augentumoren am Hahn-Meitner-Institut Berlin*, Z.Med.Phys. 14, 64-71 (2004).
7. Slater J.M. et al. *The Proton Treatment Center at Loma Linda University Medical Center: Rationale for and Description of its Development*, Int. J. Radiat. Oncol. Biol. Phys. 22, 383-389 (1992).
8. Japanese Radiation Protection Laws (Prevention Law): *Law concerning Prevention from Radiation Hazards due to Radioisotopes etc.*, No. 167, 10 June 1957 and as amended on June 2004.
9. The Italian Radiation Protection Laws: *Decreto Legislativo del Governo n° 230/1995 modificato dal 187/2000 e dal 241/2000 "Attuazione delle direttive 89/618/Euratom, 90/641/Euratom, 92/3/Euratom e 96/29/Euratom in materia di radiazioni ionizzanti."*
10. The German Radiation Protection Ordinance: *Verordnung über den Schutz vor Schäden durch ionisierende Strahlen (Strahlenschutzverordnung – StrlSchV) vom 20. Juli 2001, zuletzt geändert durch die Artikel 2 der Gesetze vom 12. August 2005 (BGBl. I. S. 2365) und 1.September 2005 (BGBl. I. S. 2618).
11. Waters L.S. (Editor) MCNPX^{TM} User's manual, Los Alamos Report TPO-E83-G-UG-X-00001 (1999).
12. Fasso A. et al. *FLUKA: New Developments in FLUKA, Modelling Hadronic and EM Interactions*, Proceedings of the 3rd Workshop on Simulating Accelerator Radiation Environments, KEK, Tsukuba, Japan, 7-9 May 1997, Ed. H. Hirayama, KEK Proc. 97-5, 32-43 (1997).
13. Nakamura T., Heilbronn L. *Handbook on Secondary Particle Production and Transport by High-Energy Heavy Ions*, ISBN 981-256-558-2, World Scientific (2006).
14. Cloth P. et al. *The KFA-Version of the High-Energy Transport Code HETC and the generalized Evaluation Code SIMPEL* Jül-Spez-196, March 1983, Kernforschungsanlage Jülich GmbH (1981).
15. Kato T., Nakamura T. *Estimation of Neutron Yields from thick Targets by high-energy ^{4}He Ions for the Design of Shielding for a heavy Ion Medical Accelerator* Nucl. Instr. and Meth. in Phys. Res.A 311, 548-557 (1992).
16. Kurosawa T., Nakao N., Nakamura T., Uwamino, Y., Shibata T., Nakanishi N., Fukumura A. Murakami K. *Measurements of secondary Neutrons produced from thick Targets bombarded by high-energy Helium and Carbon Ions*, Nucl. Sc. Eng., 132, 30-57 (1999).
17. Iwase H., Niita K., Nakamura T. *Development of General-Purpose Particle and heavy Ion Transport Monte Carlo Code*, Journ. Nucl. Sci tech., 39, 1142-1151 (2002).
18. Fasso A., Ferrari, A., Ranft, J., and Sala, P.R. *FLUKA: A Multi-Particle Transport Code,* CERN-2005-10, INFN/TC_05/11, SLAC-R-773 (2005).
19. Agosteo S. et al. *Shielding Calculations for a 250 MeV Hospital-based Proton Accelerator* Nucl. Instr. and Meth. in Phys. Res. A 374, 254-268 (1996).
20. Agosteo S. *Radiation Protection at Medical Accelerators* Rad.Prot.Dosim., Vol. 96, No. 4, 393-406 (2001).
21. Porta A., Agosteo S., Campi F. *Monte Carlo Simulations for the Design of the Treatment Rooms and Synchrotron Access Mazes in the CNAO Hadrontherapy Facility* Rad.Prot.Dosim. Vol. 113, N0.3, 266-274 (2005).
22. Ferrarini M., PHD thesis *Construction and Calibration of a REM Counter and of an extended Range Bonner Sphere System based on CR39 Detectors for Environmental Monitoring of medical Accelerators*, Polytechnico di Milano, (2007).
23. Uwamino Y., RIKEN, personal communication *Information on Shielding Design Studies for Japanese Carbon Ion Therapy Facilities (2007).*
24. Fehrenbacher G., Gutermuth F., Radon T. *Calculation of Dose Rates near the Horizontal Treatment Places of the heavy Ion Therapy Clinic in Heidelberg by means of Monte-Carlo-Methods* GSI, internal note (unpublished) (2002).
25. Hirao Y. et al. *Heavy Ion Medical Accelerator in Chiba – A Design Summary and Update –* Division of Accelerator Research, Report NIRS-M-89, HIMAC-001, National Institute of Radiological Sciences (1992).
26. Ban S. *Shielding Study on high-energy Proton Synchrotron*, PHD Thesis, Faculty of Engineering, Kyoto University (1982).
27. Noda K. et al. *Development for new Carbon Cancer-Therapy Facility and future Plan of HIMAC*, Proceedings of EPAC 2006, Applications of Accelerators, Technology Transfer and Industrial Relations, Edinburgh, Scotland, 955-957 (2006).
28. Noda K. et al. *Design of Carbon Therapy Facility based on 10 Years Experience at HIMAC*, Nucl. Instr. and Meth. in Phys. Res. A 562, 1038-1041 (2006).

29. Noda K. et al. *HIMAC and new Facility Design for wide spread Use of Carbon Cancer Therapy*, Proceedings of APAC 2004, Gyeongju, 552-556, Korea (2004).
30. Furukawa T. et al. *Design of Synchrotron and Transport Line for Carbon Therapy Facility and related Machine Study at HIMAC*, Nucl. Instr. and Meth. in Phys. Res.A 562 1050-1053 (2006).
31. M. Komori et al. *Design of compact Irradiation Port for Carbon Radiotherapy Facility*, Proceedings of APAC 2004, Gyeongju, Korea (2004).
32. Kato T., Nakamura T. *Analytical Method for Calculating Neutron Bulk Shielding in a Medium-Energy Accelerator Facility*, Nucl. Instr. and Meth. in Phys. Res. B 174 482-490 (2001).
33. Engle W.A. Jr. *A User's Manual for ANISN, A one-dimensional discrete Ordinates Transport Code with anisotropic Scattering*, USAEC report K-1693, (1967).
34. Kotegawa H. et al. JAERI-M 93-020, Japan Atomic Energy Research Institute (1993).
35. Amaldi U., Silari M. (editors) *The TERA Project and the Centre for Oncological Hadrontherapy*, The TERA Foundation, (INFN, Frascati, II Ed.) (1995).
36. Porta A., Agosteo S., Campi F. *Monte Carlo Simulations for the Design of the Treatment Rooms and Synchrotron Access Mazes in the CNAO Hadrontherapy Facility* Rad.Prot.Dosim. Vol. 113, N0.3, 266-274 (2005).
37. Ferrarini M., *Personal Communication*, Politecnico di Milano, Dipartimento di Ingegneria Nucleare, Via Ponzio 34/3, 20133, Milano (2007).
38. Debus J., (Groß K.D., Pavlovic M., Editors) *Proposal for a dedicated Ion Beam Facility for Cancer Therapy*, GSI (1998).
39. Eickhoff H., Haberer T., Schlitt B., Weinrich U. *HICAT – The German Hospital-based light Ion Cancer Therapy Project*, Conference Proceedings, PAC03 (2003).
40. Heeg P., Eickhoff H., Haberer T. *Die Konzeption der Heidelberger Ionentherapieanlage HICAT*, Z.Med.Phys. 14, 17-24 (2004).
41. Fehrenbacher G., Gutermuth F., Radon T. *Neutron Dose Assessments for the Shielding of the planned heavy Ion Cancer Therapy Facility in Heidelberg*, GSI Report 2001-05, GSI (2001).
42. Fehrenbacher G., Gutermuth F., Radon T. *Estimation of Carbon-Ion caused Radiation Levels by Calculating the Transport of the produced Neutrons through Shielding Layers*, GSI Scientific Report 2001, 205 (2002).
43. DIN 6847 Part 2, German Technical Standards, *Medical Electron Accelerators – Part 2: Radiation Protection Rules for Installatio*n, DIN Deutsches Institut für Normung e.V., Berlin, No. DIN 6847-2:2003-12, (2003).
44. Sullivan A.H. *A Guide to Radiation and Radioactivity Levels near high-energy Particle Accelerators*, Nuclear Technology Publishing, Ashford, Kent (1992).

Poster: Dosimetry, Radiation Protection

DOES RADIOBIOLOGICAL EFFECTIVENESS CHANGE IN LASER DRIVEN ION THERAPY?

Günther Dollinger[1], Anna A. Friedl[2], Christoph Greubel[1*], Volker Hable[1*], Guido A. Drexler[2]
[1]Universität der Bundeswehr München, LRT2, D-85579 Neubiberg, Germany
[2]Ludwig-Maximilians-Universität München, Strahlenbiologisches Institut, D-80336 München, Germany

Intense femtosecond laser light is proposed as an alternative accelerator for future proton or heavy ion tumor therapy installations. The main difference to conventional ion therapy will arise from the short ion pulses which deposit their energy in tissue within a time span of about a nanosecond. We discuss the potential effects on the biological response of these pulsed beams in comparison to conventional proton or heavy ion beam treatment where a certain voxel of the tumor is irradiated within milliseconds to seconds. A difference may occur from short time chemistry in the cells only since combined dose effects in the physical dose delivery as well as on complex biological reactions are not envisaged to change. The magnitude of changes and their effect on the radio biological response cannot be foreseen at today´s knowledge. We, therefore, plan to elucidate potential differences by a pulsed beam irradiation setup installed at the microprobe SNAKE at the Munich tandem accelerator.

IMPROVED RADIATION PROTECTION FOR MANUAL TASKS BY THE USE OF AN IMMERSIVE CAMERA SYSTEM

G. Reinhart[1], A. Eursch[1,*]

[1]Institute for Machine Tools and Industrial Management (*iwb*), Technische Universität München, Boltzmannstr. 15, 85748 Garching, Germany

This paper presents a support system as a solution for the often unfavourable working conditions for manual tasks in the field of nuclear science. Its main goal is to improve the radiation protection for the operators and to reduce the permanent threat of nuclear radiation. The support system consists of a steerable camera system with intuitive control in combination with the information technology Augmented Reality that supplies the user with necessary data, required details and even working instructions. Versatile additional features are possible that ease the work and create further benefit.

The work with radioactive material implicates potentially high health and safety hazards for operators due to frequent contact to nuclear radiation. Particularly as manual labour is still required e.g. in medical research and manufacturing. At present no support system is available to deal with the permanent threat of nuclear radiation and to assist the operators to perform their mostly stressful, complex and demanding tasks.

INITIAL SITUATION

Unfavourable working conditions make the performing of tasks even more difficult: The required shielding hinders the operators by limiting the free moving space and leads to a non-ergonomic operating position. An example is a shielded glovebox for the production of radioisotopes in larger amounts [2]. The lead glass window (see Fig 1, left hand side) delimitates the field of vision and causes a lot of drawbacks like an inadequate reaching area of the hands, a bothering discrepancy between the kinaesthetic sense of the hand and the visual perception because of the refraction and a high price.

SOLUTION

The authors propose the promising information technology of augmented reality (AR) in combination with an immersive camera system as an excellent solution for this challenge [3].

Camera System

The camera system consists of a pan-tilt-zoom (ptz)-camera inside the shielded area, e.g. a semi hotcell, and a head-mounted display for the operator (see Fig 1, right hand side). An intuitive input device guarantees easy operation. The camera substitutes the lead glass window and offers a series of additional advantages: The activities inside the box can be recorded easily e.g. for documentation. Remote monitoring is possible and supporting staff can watch the operator's actions. But the main benefit is the enabling of the use of AR since the camera system is the required technical basis for information visualization.

*Corresponding author:
andreas.eursch@iwb.tum.de
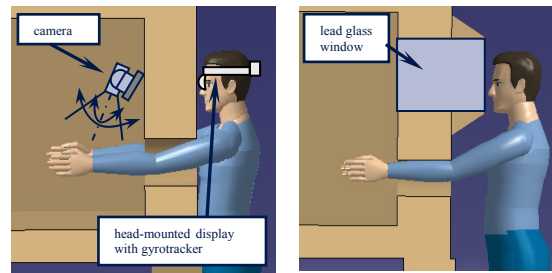
Figure 1. The lead glass window, e.g. of a shielded glovebox, creates severe drawbacks and constricts the work of the operators (left hand side). The camera system replaces the lead glass. It consists of a ptz-camera in the radioactive area and a head-mounted display for the operators in combination with an intuitive control, e.g. a gyrotracker (right hand side).

Augmented Reality Support

AR offers the possibility to superimpose important auxiliary information directly into the operator's view of the working environment, related to the aimed task and its location. This feature serves to increase safety by implementing an appropriate safety strategy including visualization of possible emitters of nuclear radiation, giving warnings and highlighting dangerous areas. An AR system supplies the operators with necessary information to cope with their assignment, support decision making and thus lower stress and increase comfort, advancing complete and accelerated task fulfilment (see Fig. 2). As a consequence, spurious presence in the radioactive environment can be reduced to a minimum, diminishing the time of exposure to the harmful radiation and thus improving operational safety. AR offers numerous further possibilities like guidance, flexibility and protection that can change the work with radioactive material.

APPLICATION

To gain experience and for validation purposes a prototype system was developed and implemented in collaboration with preferential users, especially radiochemists and technicians. It was designed for an exemplary case: the production of radioisotopes for medical research in order to enable new applications. The interviewed operators looked upon the camera system favourably. They also confirmed the benefit of the AR support for their work. The results of the special use case can be easily transferred to other tasks in the field of nuclear science since the difficulties and the requirements are quite similar. AR is a potent basic technology with numerous possibilities [1]. It only has to be adapted to the specific application and the required tasks in the field of nuclear science.

REFERENCES

1. Azuma, R.; Baillot, Y.; Behringer, R.; Feiner, S.; Julier, S.; MacIntyre, B.: Recent advances in augmented reality. IEEE Computer Graphics and Applications 21 (2001) 6, pp. 34-47.
2. Harfensteller, M.; Eursch, A.; Zaeh, M. F.; Moreno, J.; Kabai, E.; Henkelmann, R.; Türler, A.; Huenges, E.; Mentler, M.: Automated Target Processing in Radioactive Environments. In: Westkämper, E. (Ed.): The 1st CIRP-International Seminar on Assembly Systems. Stuttgart: 2006, pp. 277 - 281. ISBN: 978-3-8167-7213-2.
3. Reinhart, G.; Eursch, A.; Zeilinger, T.: Augmented Reality-Unterstützung für die Produktion von radioaktiven Stoffen in abgeschirmten Handschuhboxen. In: Gausemeier, J. et al. (Eds.): 6. Paderborner Workshop Augmented & Virtual Reality in der Produktentstehung, Vol. 209. Paderborn: HNI-Verlagsschriftenreihe 2007, pp. 129-144. ISBN: 978-3-939350-28-6.
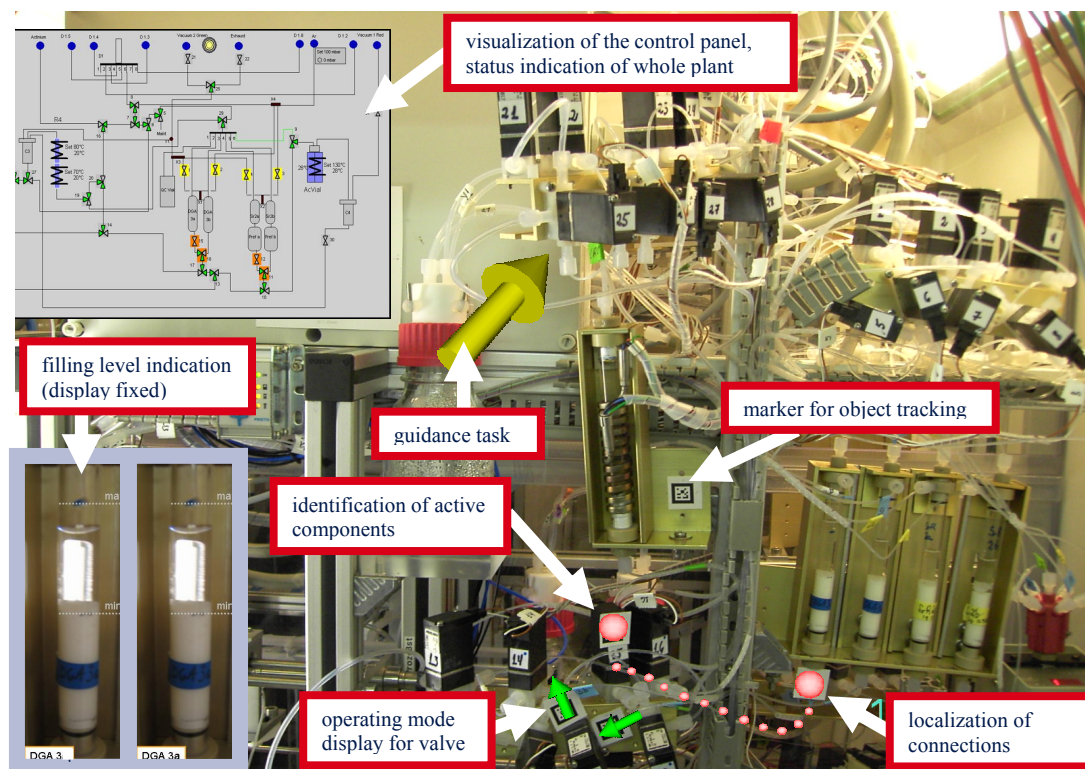
Figure 2. AR support for the operators. Examples of possible features

SHIELDING CALCULATIONS FOR THE LIGHT ION THERAPY FACILITY HIT

G. Fehrenbacher[1,*], F. Gutermuth[1,2], and T. Radon[1]

[1]Gesellschaft für Schwerionenforschung mbH Planckstr. 1 D-64291 Darmstadt, Germany
[2]now at ENBW, Kernkraft GmbH, Rheinschanzinsel, D-76661 Philippsburg, Germany

The successful carbon ion therapy project at GSI motivated the planning of a hospital-based carbon ion therapy facility in Heidelberg (HIT=Heidelberg Ion-Beam Therapy Centre)[1]. The shielding planning of the facility was based on line-of-sight-models and Monte Carlo (MC) radiation transport calculations. In this work some of the results of the MC calculations are presented i.e. the shielding of the gantry and the horizontal irradiation chambers. Different approaches concerning the source terms and a comparison between protons and heavy ions are discussed

A SIMULATION TOOL

The dose rate assessments are based on Monte-Carlo simulations performed with the FLUKA[2] code. FLUKA is a radiation transport program capable of simulating with high accuracy the interaction and propagation in matter of about 60 different particles, e.g. gammas of any energy, hadrons of energies up to several TeV, and neutrons down to thermal energies. In 2004 the transport of heavy ions has been added employing the RQMD[3] and the DPMJET[4] models.

B TYPE OF SIMULATION

The major component of potential radiation exposure in this work is neutron radiation which is produced near the treatment units and near areas with losses of the primary beam. The production of neutrons by a 400 AMeV carbon beam in tissue-equivalent material as it is used in carbon therapy has been measured at HIMAC in Chiba[5]. Due to the lack of MC codes capable of propagating heavy ions through matter at that time, these neutron spectra were used for the first shielding investigation of HIT.

C SHIELDING OF THE GANTRY

With FLUKA, neutrons based on the above mentioned measured spectra, were transported through a 1m thick iron block representing the beam catcher and another concrete wall with a thickness of 2m. For the sake of computing power the set up was simplified using cylinder geometry (see Fig.1a). The dose rate was scored directly after the first shielding wall. A second wall was then introduced to study the Albedo effect from close lying walls. Fig. 1b) shows that for large angles the dose can become considerably higher when a second wall is included. The blue line demonstrates that the gamma dose is 2 orders of magnitude lower than the neutron dose and can thus be neglected in this case.

*Corresponding author: G.Fehrenbacher@gsi.de
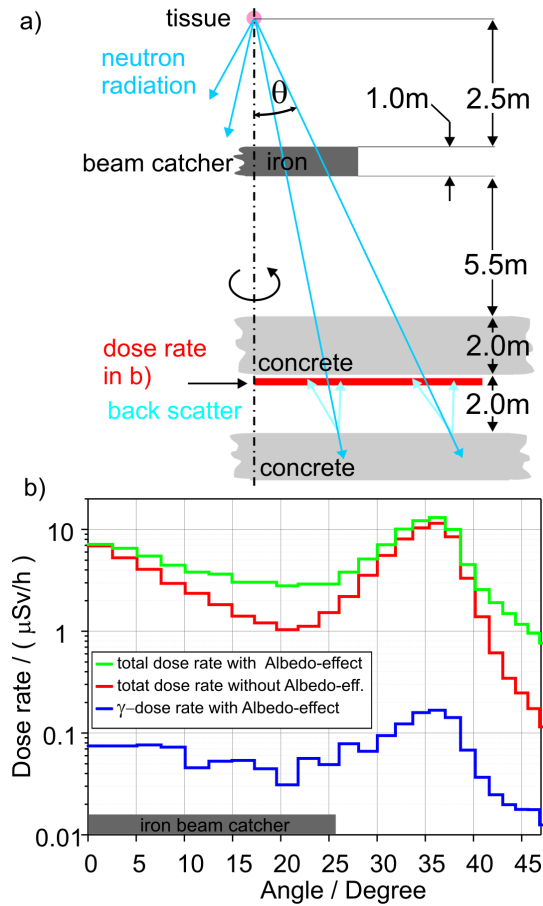
Figure 1. Monte Carlo Simulation of the gantry. Panel a) shows the cylindrical geometry used. Panel b) displays the dose neutron and gamma dose rates after the first concrete wall.

D SHIELDING OF THE HORIZONTAL IRRADIATION CHAMBERS

The horizontal treatment chambers were simulated in a very realistic 3-dimensional geometry. Fig. 2 shows a top view of a treatment room including the entrance maze on the level of the primary beam. A color map is super-positioned, allowing a reading of the dose rates at any position. Due to the entrance in forward direction opposing the primary beam the corresponding maze had to be designed in an extensive way. Many of the walls facing the primary beam or the harder and direct component of the neutron radiation were equipped with thick iron layers in order to induce spallation reactions which shift the neutron spectrum to lower energies and in addition provide a shorter radiation length.
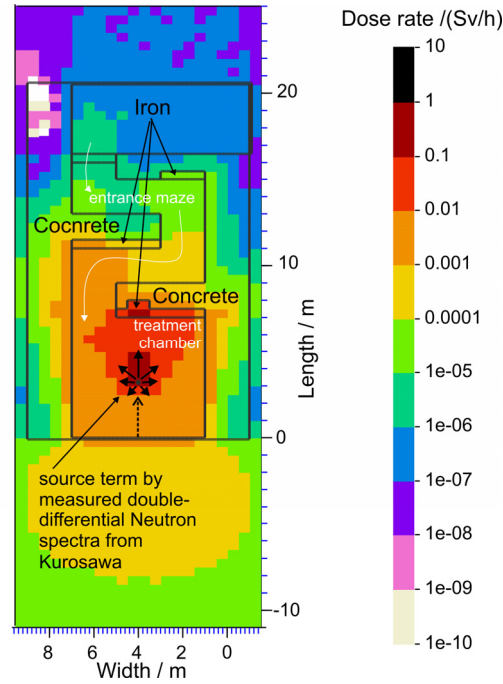
Figure 2. Dose-map of a horizontal treatment place. Measured neutron spectra induced by a 400 AMeV C-12 beam on a graphite target were used as a source term.

Fig. 3 shows for the geometry of Fig. 2 a comparison of the results of a MC simulation with heavy ions and a simulation with protons. Both parameter sets of the beams are used for clinical particle therapy. It is worthwhile to note that the simulation which uses ab initio heavy ions (left panel of Fig. 3) agrees well with the simulation using the measured neutron spectra shown in Fig. 2. The dose rates due to the measured neutron spectra show roughly 25% higher values at most. Finally it can be stated that FLUKA is an ideal tool for shielding calculations of particle therapy facilities. All calculation approaches shown provide a consistent impression of an authentic shielding. In a recent project, dose measurements have been performed at GSI with beam and target parameters adapted to particle therapy conditions. The aim was to verify the measured dose values with the ones derived by MC codes like FLUKA. Preliminary results point out relative differences of roughly 30%.
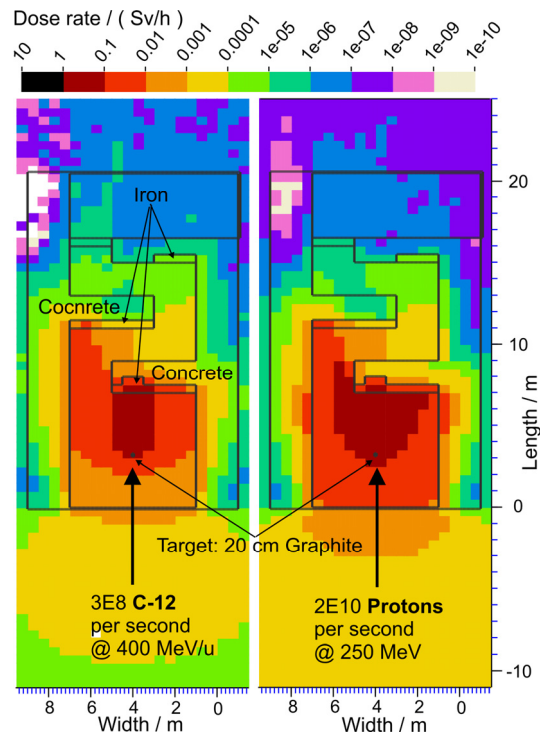
Figure 3. Comparsion of the dose rates for heavy ions and protons used at the horizontal irradiation facility. The intensities of both beams are adapted to result in similar therapy doses.

REFERENCES

1. Debus J., (Groß K.D., Pavlovic M., Editors) Proposal for a dedicated Ion Beam Facility for Cancer Therapy , (1998).

2. A. Fassò, A. Ferrari, J. Ranft and P.R. Sala, FLUKA: status and prospective for hadronic applications, in: A. Kling, F. Barao, M. Nakagawa, L. Tavora, P. Vaz (Eds.), Proceedings of the Monte Carlo 2000 Conference, Lisbon, 23-26 October 2000, Springer-Verlag Berlin (2001) p. 955.

3. H. Sorge, Flavor production in Pb(160A GeV) on Pb collisions: Effect of color   ropes   and   hadronic rescattering, Physical Review C 52 (1995) 3291-3314.

4. J. Ranft, Phys. Rev. D51 (1995) p.64; New features in DPMJET version II.5, hep-   ph/9911213   and DPMJET version II.5, code manual, hep-ph/9911232

5. T. Kurosawa et al. Measurements of secondary Neutrons produced from thick Targets bombarded by high-energy Helium and Carbon Ions, Nucl. Sc. Eng.,132,30-57 (1999).

MONTE CARLO DEPTH-DOSE CALCULATIONS FOR DIFFERENT I-VALUES IN HEAVY ION THERAPY

Katrin Henkner[1], Oliver Jäkel[1]

[1] Department of Medical Physics in Radiation Oncology, Heavy Ion Group; German Cancer Research Center, Im Neuenheimer Feld 280, 69120 Heidelberg, Germany

In carbon ion radiotherapy the ion range in water is of great importance for beneficial treatment. The range of ions is mainly determined by the mean ionization potential, the I-value, of the corresponding medium. For current stopping power and range tables an I-value for water of 67.2 eV according to ICRU 73 [5] is used. In the earlier report ICRU 49 [3] an I-value of 75 ± 3 eV was recommended shifting the ranges to higher depth as compared to 67.2 eV. According to experimental data this low I-value did not represent the experimental Bragg peak positions. Following Paul [1] we determined the range of carbon ion depth dose curves in water. For carbon ions we calculated an average shift of the Bragg peak position of 4 mm between the calculations using an I-value of 67.2 eV and the experimental data by Sihver [2]. The best I-value describing the experimental data was in the region of 81 eV.

Introduction

In therapy with heavy ions the range of ions is very important in order to calculate correct depth dose curves, LET, fluence and energy distributions during treatment planning. Traveling through media, a monoenergetic heavy ion beam slows down according to its energy loss per unit path length, known as stopping power. It forms a depth dose curve having a plateau at the entrance region and rises towards the Bragg peak near the end of the ion range where the particles stop. So the stopping power is responsible for the shape of the curve and the position of the Bragg peak. The stopping power is depending on the particle characteristics (charge and velocity) and on properties of the target medium, like the mean ionization potential, or the I-value, which is a geometric mean value of all ionization and excitation potentials of an atom of the absorbing media. It enters logarithmically in the stopping power and is proportional to the atomic number. Obtaining I-values by calculating them from experimental stopping power data is the most frequently method. For gases it can also be obtained from the oscillator strength functions. I-values of compounds can be calculated by the additivity rule [4] from the elemental values. In ICRU Report 37 [6] I-values for all elements were based on stopping power measurements, oscillator strength distributions and dielectric response functions. In this work we calculated stopping power values from the ICRU data and determined the Bragg peak position, which was then compared to experimental data by Sihver [2].

Methodology

Ranges of heavy ions were extracted by calculating depth dose curves by dose D, particle fluence ϕ and mass stopping power S/ρ at energy E by

$$D(x) = \int_{E_{min}}^{E_{max}} \phi(E, x) * \frac{S}{\rho}(E, x) * dE(x) \tag{1}$$

The stopping power S=-dE/dx was calculated by the Bethe-Bloch equation

$$-\frac{dE}{dx} = 0.307 \rho \frac{Z}{A} \frac{z^2}{\beta^2} \left(\frac{1}{2} \ln \frac{2 m_e c^2 \beta^2 W_{max}}{1 - \beta^2} - \beta^2 - \ln I - \frac{C}{Z} - \frac{\delta}{2} \right) \tag{2}$$

with ρ density of the medium, Z atomic number and A atomic mass of the target, z charge of the projectile, $\beta = v/c$, m_e electron mass, I mean ionization potential, W_{max} maximum energy transfer in a single collision, C shell corrections and δ density correction.

The modified value from equation (2) in this work was the mean ionization potential I of the medium. The I-values for elements are tabulated in ICRU Report 49 [3] and for compounds the values were calculated by Bragg's additivity rule [4] by

$$\ln I = \frac{\left[\sum_i w_i (Z_i / A_i) \ln I_i \right]}{\sum_i w_i (Z_i / A_i)} \tag{3}$$

Thus, the fraction by weight w_i, the atomic mass A_i and the atomic number Z_i of element i were used to calculate the mean I and thus the stopping power.

The calculations were done with the Monte Carlo Code SHIELD-HIT v2, which uses the exclusive approach for nuclear reactions and the Bethe-Bloch and Lindhard-Scharff formula for stopping power calculations down to 25 keV/u.

We calculated depth dose curves in water of monoenergetic pencil beams of 270 MeV/u and 330 MeV/u carbon ions. The target medium was shaped by a cylinder of length 30cm and radius 10cm. In the Bragg peak region the resolution was 0.01cm.

Determining the change in stopping power and Bragg peak position for media we calculated stopping power values with Bethe-Bloch and Lindhard-Scharff formula for ICRU given I-values and their uncertainties described in ICRU 37 [6] for 270MeV/u carbon ions.

Results

Comparing calculated and measured depth dose curves for carbon ion beams of 270MeV/u and 330 MeV/u showed an increase in ion range by increasing I-value. As seen in Figure 1, for example, the Bragg peak position of the adopted I-value I=67.2 eV by ICRU 73 did not fit to the experimental data measured at GSI. The same behavior was resulting at 330 MeV.
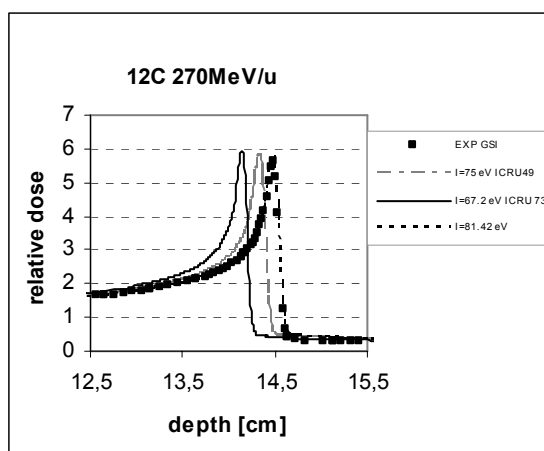
Figure 1. Depth dose curves (dose was standardized to the entrance dose) of a 270MeV/u carbon pencil beam with I-values of 67.2 eV (line black), 75 eV (dashed dotted grey) and 81.42 eV (dotted black) were compared to experimental data measured at GSI (Darmstadt).

The uncertainties of I-values of 5% to 10% stated by the ICRU for compounds were also affecting the Bragg peak position by shifting it forwards or backwards according to the appointed I-value in the data table of ICRU 37.

Discussion

The ion range of experimental results was larger than the Monte Carlo calculated results for ICRU 73. If the I-value was fitted according to the experimental data, the resulting value was higher than the ICRU I-value. The ICRU 73 adopted I-value of 67.2 eV seemed to be too small compared to experimental data. An I-value of around 81eV represented the measured curve in shape and Bragg peak position of carbon ions for 270MeV/u and 330MeV/u very good.

The shift in the Bragg peak compared to ICRU calculated Bragg peak increased with increasing energy of the incident particle.

The uncertainties of the listed I-values in ICRU 49 resulted in a displacement of the depth dose curve. This limits the precision of calculated ranges based on the ICRU data.

Conclusion

The calculation of I-values is very complex and must be done very carefully, because the calculation of correct stopping powers, Bragg peak positions and nuclear fragments are of great importance for dosimetry and treatment planning. A consistent single I-value for the whole range of ions (from proton up to argon) is needed and will increase accuracy of the stopping power. For this value one has to collect measured and Monte Carlo calculated stopping power data for several particles, energies and materials.

Acknowledgements

REFERENCES

1. Paul, H. The mean ionization potential of water, and its connection to the range of energetic carbon ions in water. Nuclear Instruments and Methods in Physics Research B 255 (2007) 435-437
2. Sihver, L., Schardt, D., Kanai. T. Depth-Dose Distributions of High-Energy Carbon, Oxygen and Neon Beams in water. Jpn J Med Phys 18 (1)
3. Stopping Powers and ranges for Protons and Alpha Particles. Vol. 49. International Comission of Radiation units and Measurements. Bethesda, Maryland. 1993
4. Stopping Powers and ranges for Protons and Alpha Particles. Vol. 49. International Comission of Radiation units and Measurements. Bethesda, Maryland. 1993 page 15
5. Stopping of Ions heavier than Helium. Journal of the ICRU Vol 5 No 1 (2005) Report 73. Oxford University Press
6. Stopping Powers for Electros and Positions. Vol. 37. International Comission of Radiation units and Measurements. Bethesda, Maryland. 1984

SECONDARY DOSES TO PATIENT IN LIGHT ION THERAPY – MONTE CARLO STUDIES COUPLED WITH ANTHROPOMORPHICAL PHANTOMS.

Martha Hultquist and Irena Gudowska
Medical Radiation Physics, Karolinska Institutet and Stockholm University, Stockholm, Sweden

Abstract

Secondary particles like neutrons, protons and heavier ions produced in light ion therapeutic beams contribute to the dose delivered to tumor and healthy tissues outside the treated volume. These particles are characterized by a wide range of LET (Linear Energy Transfer) and are a source of undesirable dose to critical organs of the patient. Production of neutrons and secondary protons in therapeutic ion beams requires special concern since they possess high energies and are easily transported long distances through the patient and can generate damage in healthy tissues. As a consequence, this damage can result in the occurrence of secondary tumors. These issues are especially critical for paediatric patients since their tissues are still in rapid development and a curative treatment may result in very long survival times.

Due to the very complex interaction pathways of high energy and heavy charged ions transported in the patient, 3-D Monte Carlo (MC) particle transport codes provide a unique and very useful tool in the prediction of the physical radiation doses to organs.
In this work calculations of absorbed dose delivered to the treatment volume and to the patient's organs exposed only to secondary particles, produced in proton and heavier ion beams, were performed with the MC code SHIELD-HIT. SHIELD-HIT simulates the interactions of hadrons and atomic nuclei of arbitrary mass number (Z, A) with complex extended targets. Simplified versions of the mathematical anthropomorphical phantoms EVA (female), ADAM (male) and a child phantom, based on the MIRD geometry, were applied in the SHIELD-HIT calculations. Calculations were also performed for a cylindrical homogeneous water phantom. The incident ion beam was simulated as a quasi-monoenergetic beam with an energy spread, σ_E, and a Gaussian spatial distribution. The studies were also performed for parallel monoenergetic beams and for a more clinically relevant case with a spread out Bragg peak (SOBP).

RADIATION SHIELDING PROPERTIES OF KEVLAR AND NEXTEL IN HUMAN SPACE INFRASTRUCTURES

M. Pugliese[1], F. Ballarini[2], T. Berger[3], M. Briccarello[5], M. Casolino[4], R. Destefanis[5], M. Faraud[5], G. Gialanella[1], G. Givone[6], G. Grossi[1], V. Guarnieri[5], C. Lobascio[5], L. Manti[1], A. Nagamatsu[7], A. Ottolenghi[2], P. Piccozza[4],G. Reitz[3], A. Rusek[8], P. Scampoli[1], A.Zanini[6] and M. Durante[1]

[1]Department of Physics and INFN, University Federico II, Naples, Italy. [2] Department of Physics, University of Pavia, Italy. [3]DLR, Koln, Germany. [4]INFN Tor Vergata Section, Rome, Italy. [5]Thales Alenia Space, Turin, Italy. [6]INFN, Turin section, Turin, Italy. [7]JAXA, Japan, and [8]NASA Space Radiation Laboratory, Brookhaven National Laboratory, Upton, NY, USA

INTRODUCTION

Shielding is the only practical countermeasure to exposure to cosmic radiation during space travel. It is well known that light, hydrogenated materials provide the best shielding against space radiation. Kevlar® and Nextel® are two materials of great interest for spacecraft shielding because of their known ability to protect human space infrastructures from meteoroids and debris. Nextel is a woven ceramic fabric manufactured by 3M, while Kevlar, well-known for its use in bullet-proof vests, is an aromatic polyamide (aramid) manufactured by DuPont. Thales Alenia Space has designed and integrated a number of rigid pressurized modules for the International Space Station using specific combinations of Nextel and Kevlar, in addition to aluminium, to protect against hypervelocity impacts of man-made debris or naturally occurring meteorites. The same materials are candidates for the protection of inflatable space modules, currently under study for future exploration missions. The radiation shielding properties of these materials are, however, unknown. In this study, we measured space radiation hardness of these shielding materials and compared to polyethylene, a highly effective space radiation shield.

METHODS

Full characterization of Kevlar and Nextel vis-à-vis ionizing radiation was achieved with the following tests:

Ground-based physics tests

Bragg curves of 1 GeV/n Fe-ions were measured at the NASA Space Radiation Laboratory at the Brookhaven National Laboratory (USA) using a calibrated egg-ionization chamber. Bragg curves in Kevlar and Nextel were compared to those in polyethylene. Beam fragmentation behind thick Kevlar shields was measured using CR-39 solid state nuclear track detectors and compared to polyethylene and aluminium.

Ground-based biology tests

Human peripheral blood lymphocytes were exposed to 1 GeV/n Ti-ions behind shields in Kevlar, aluminium, lucite (PMMA) of 20 g/cm^{2}areal thickness. Chromosomal aberrations were measured using FISH-painting combined to premature chromosome condensation in lymphocytes at the 1st post-irradiation mitosis.

International Space Station (ISS) tests

TLD dosimeters were exposed on ISS behind shields in Kevlar, Nextel and, for comparison, polyethylene and low-density foam (simulating absence of shielding). Shielding blocks were also attached on the active detector ALTEINO on ISS to measure the relative attenuation of the different components of the cosmic radiation spectrum.

Modelling

Radiation properties of Kevlar and Nextel were modelled using the FLUKA fully integrated particle physics Monte Carlo simulation package. In particular, Bragg curves of 1 GeV/n Fe-ions in different materials were simulated and compared to experimental data.

RESULTS

The results of all different tests performed show that Kevlar, which is rich in carbon atoms (about 50% in number), has an effectiveness in reducing dose delivered by heavy ions close (80-90%) to that of polyethylene. Biology data suggest that it can reduce the chromosomal damage more efficiently than PMMA. Nextel is a worst radiation shielding material than Kevlar, and the expected reduction on dose is roughly ½ than that provided by the same mass of polyethylene.

GEANT4BASED SIMULATION OF CARBON BEAM IRRADIATION INSIDE CT IMAGE VALIDATION WITH RADIOCHROMIC FILMS

N. Zahra[1,2], P. Lautesse[2], L. Guigues[3], T. Frisson[3,1] and D. Sarrut[1,3]

[1]Leon Berard anticancer center, 28 rue Laenec, 69373 Lyon cedex 08, France

[2]Nuclear Physics Institute of Lyon, Claude Bernard University, National Institute of Nuclear Physics and Particle Physics (IN2P3CNRS), DOUA rue Enrico Fermi, 69622 Villeurbanne cedex, France

[3]CREATIS laboratory (UMR CNRS 5220, Inserm U 630), INSA, Bât. Blaise Pascal, av. Jean Capelle, 69621 Villeurbanne cedex, France

We developed a Geant4based simulation framework for hadrontherapy allowing to compute 3D dose distribution inside a CT image. A specific particle navigation algorithm has been developed to decrease computational time. We obtained speed up between 4 and 16 according to different image material description. An experience was made at GANIL accelerator (France) using a ^{13}C beam. The detectors used as dosimeter were radiochromic films. Dose was measured in different phantom configuration. Homogeneous phantoms were used for the calibration part and heterogeneous phantoms for dose deposit validation. Preliminary result show good agreement with the simulation.

Introduction

Our purpose is to develop a MonteCarlo simulation framework to compute the dose distribution obtained from different particle beams in a complete patient description (CT image[1]). To validate this simulation we compared MonteCarlo results to the deposited energy obtained by irradiation of radiochromic films in different (homogeneous or inhomogeneous) materials.

Materials and methods

Monte Carlo method:

The proposed framework, called Therapeutic Irradiation Simulator "ThIS" [1], is based on Geant4 [2]. The physics list includes Geant4standard nuclear processes [3]. Data from CT patient description (Dicom[2]) can be easily included with macro commands. We developed a specific navigation algorithm to improve the computational time by suppressing unnecessary geometrical steps occurring at boundaries of voxels with same material. Dose and deposited energy distribution can be computed with any resolution independently of the voxel size.

GANIL experience:

We have made phantoms composed of inhomogeneous materials to represent human tissues (soft tissues, bone and lung). Phantoms were composed of several slices of polycarbonate resin (Lexan, 1.2 g.cm^3), epoxy and polyester resin (Delmat, 2.2 g.cm^3) and polystyrene (0.05 g.cm^3). In each phantom, radiochromic films (Gafchromic MD 55) [4] were placed between materials slices at different depth (between each inhomogeneity, near the Bragg peak). Films were digitalized with an EPSON scanner (636 nm wave length) and analyzed. Phantoms were irradiated at GANIL (Grand Accelerateur National des Ions Lourds, France) using 76 MeV/u 13C ion beam. The experiments were performed with different irradiation time duration.

Results

We obtained the 3D dose distribution in a 2x2x2 mm^3 resolution (Fig 1) corresponding to a 192 MeV/u carbon ion beam in a 6 million voxels patient description with 26 different materials. Speedup obtained with our navigation technique can reach a factor between 4 and 16 according to the accuracy needed in the scene materials description.
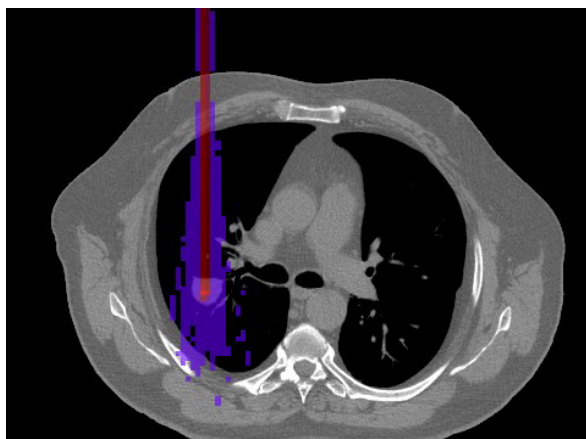
Fig.1 2D illustration of a 3D dose distribution in thorax, simulated with ThIS.

_____

1. CT:Computerized Tomography
2. DICOM: Digital Imaging and Communications in Medicine

Data obtained from the films irradiation is currently being analyzed. A calibration curve was obtained using a flat ionization chamber PTW 23344 placed at 14 mm (estimation of Bragg peak position) in a homogeneous phantom of polycarbonate resin. Fig 2 shows the calibration curve of the radiochromic films. Preliminary results show good agreement between experimental data and Monte Carlo ThIS simulations (Fig. 3). The depthdose plot was normalized according to the dose obtained from the film at depth=0 mm. The experimental data point at 14 mm in Fig. 3 shows a little shift in relation to the Monte Carlo simulation. This could be due to the minimal material slice thickness of 2 mm. The film was placed 1.5 mm before the Bragg peak.
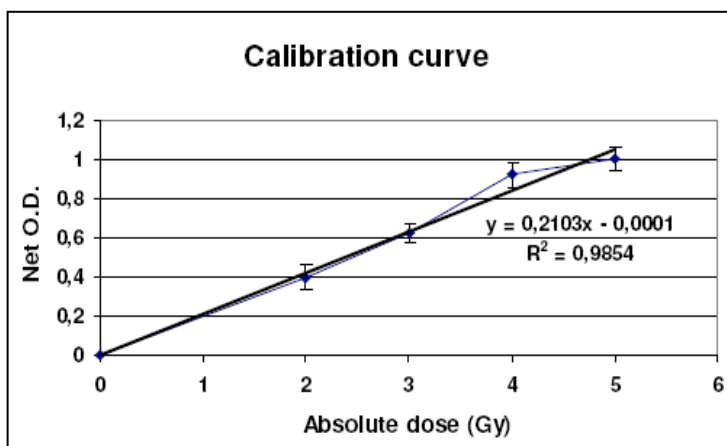
Fig. 2 Calibration curve obtained using a flat ionization chamber PTW 23344 placed at 14 mm (estimation of Bragg peak position) in a homogenous phantom of polycarbonate resin.
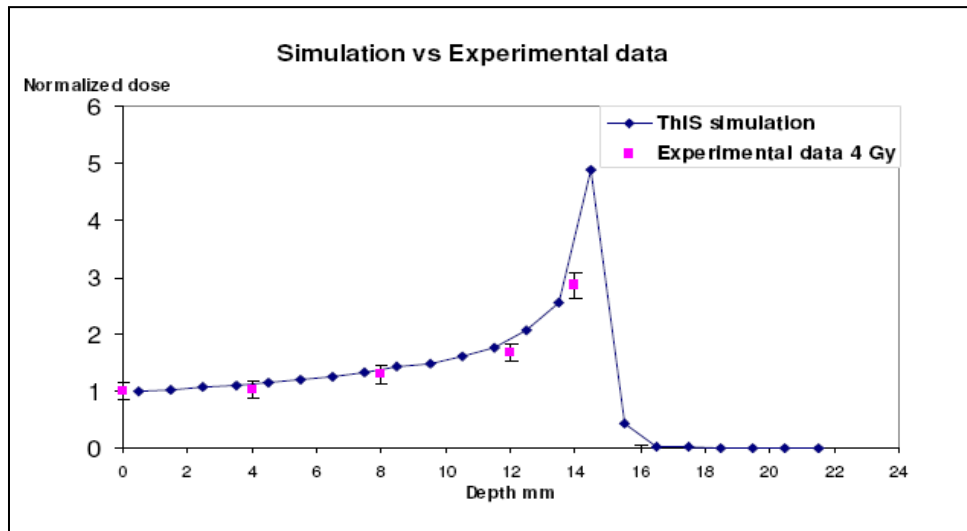
Fig. 3 Comparison between experimental data obtained with a homogenous phantom irradiated at 4 Gy and a ThIS simulation.

Conclusion

ThIS framework is available at http://www.creatis.insalyon.fr/rio/ThIS. However, such code will be merge in the GATE [5] software within next two years according to the fGate project funded by the ANR (National Research Agency). Radiochromic films seem to be an interesting way to measure dose distribution with carbon ion beams. Lower thickness materials should be anticipated for the next experience.

Acknowledgment

The authors want to thank all people making possible the GANIL run, particularly M. Bajard and Joel Hérault.

REFERENCES

[1] See http://www.creatis.insalyon.fr/rio/ThIS
[2] J. Allison et al. "*Geant4 developments and applications*". Nuclear Science, IEEE Transactions on, 53(1):270–278, 2006.
[3] I. Pshenichnov, I. Mishustin, and W. Greiner. "*Neutrons from fragmentation of light nuclei in tissuelike media: a study with the geant4 toolkit*". Phys Med Biol, 50(23):5493–507, 2005.
[4] *Radiochromic Film Dosimetry* Recommendations of AAPM Radiation Therapy Committee Task Group No. 55, AAPM Report No. 63, Medical Physics, Vol. 25(11), 1998
[5] S. Jan et al. "*Gate: a simulation toolkit for PET and SPECT*". Phys Med Biol, 49(19):4543–2004

Poster: Modeling

A COMPARISON OF RADIOBIOLOGICAL MODELS FOR LIGHT ION THERAPY

M. Hollmark[1,*], M. Beuve[2], M. R. Edgren[1], T. Elsaesser[3], P. Kundrát[4], A. E. Meijer[1], C. Rodriguez-Lafrasse[5], M. Scholz[3], M. P. R. Waligórski[6,7] and I. Gudowska[1]

[1] Karolinska Institutet-Stockholm University, Department of Oncology and Pathology, Medical Radiation Physics, Box 260, SE-171 76 Stockholm, Sweden

[2] UMR 5205, LIRIS ; UMR5822 IPNL ; Université de Lyon, Lyon, F-69003, France ; université Lyon 1, Lyon, F-69003, France

[3] GSI, Biophysics, 64291 Darmstadt, Germany

[4] Institute of Physics, Academy of Sciences of the Czech Republic, Na Slovance 2, CZ-182 21 Praha 8, Czech Republic

[5] Department of Biochemistry, INSERM U189, Lyon-Sud Medical School, Oullins, France

[6] The Marie-Skłodowska-Curie Centre of Oncology, Kraków Division, Garncarska 11, 31-115 Kraków, Poland

[7] Institute of Nuclear Physics, Polish Academy of Sciences, Radzikowskiego 152, 31-342, Kraków, Poland

Treatment planning for light-ion therapy requires radiobiological models describing the effects of light-ion irradiation on cellular survival. The aim of this work is to compare some of the radiobiological models currently in use. The cell line used in these studies is an AA human melanoma cell line, irradiated *in vitro* by ^{60}Co and ^{10}B^{5+} ions of different values of linear energy transfer. The models used to analyze the data are the linear-quadratic model, the repairable-conditionally repairable model, the probabilistic two-stage model, Katz's cellular track structure theory, and the local effect model.

There is an increasing interest in hadron radiotherapy around the world. When compared to conventional therapy with electrons and photons beams, the improved accuracy of dose conformity and the increased biological efficacy of light ion beams are the main advantages ultimately enhancing the eradication of a tumor while sparing the surrounding normal tissues. Treatment planning for light ion therapy requires not only accurate knowledge of the physical processes of energy deposition but also of the likely response of tumor and normal cells following irradiation by ions. This necessitates development of models describing the effects of light ion irradiation on cellular survival. These radiobiological models are very complex in view of the fact that the cellular and subcellular mechanisms of damaged cells are extremely intricate. The objective of the present collaborative study is to indicate the possible correlations or counter-indications of some of these radiobiological models currently in use, hopefully to facilitate the prospect to develop more rigid and precise models for application in hadron radiotherapy planning. Alternatively, the result of our comparison should demonstrate whether these models can complement each other. To accomplish these goals, undoubtedly, larger sets of cell survival data for other ion species and different linear energy transfer (LET) will be required.

METHODS AND MATERIALS

The benchmark cell line used in these studies is the AA human melanoma cell line, irradiated under aerobic conditions by ^{60}Co and ^{10}B^{5+} ions of different values of LET (40, 80, 125 and 160 keV μm^{-1}) [1, 2]. The irradiations were performed at the The Svedberg Laboratory in Uppsala, Sweden. The models used to analyze the data are the standard linear-quadratic (LQ) model, the repairable-conditionally repairable (RCR) model, and the probabilistic two-stage (P2S) model. Two further parametric models studied are Katz's cellular track structure theory (TST) and the local effect model (LEM) in use at GSI in Darmstadt.

---

*Corresponding author: malin.hollmark@ki.se

Descriptive models

LQ model

The most common approach in modeling cell survival *in vitro* is to express survival curves through the linear-quadratic (LQ) model [3], where the probability of survival is expressed as

$$S(D) = \exp(-(\alpha D + \beta D^2)) \qquad (1)$$

The LQ-model has been in extensive use in radiobiology for the last decades and it agrees reasonably well with experimental data at clinically relevant doses. Some disadvantages of this model are the continuous bending of the curve at high doses and the incapacity to account for low-dose hypersensitivity at doses below approximately 1 Gy.

RCR model

The recently developed repairable-conditionally repairable damage (RCR) model has been proposed to solve both the low- and high-dose responses [4, 2]. The model is based on the interaction between two Poisson processes with a separation of damages into two types of lesions: a potentially repairable but also potentially lethal lesion if non-repaired or misrepaired and a conditionally repairable lesion, which for example might lead to an apoptotic response. The induction of damages can be approximated by a simple bi-exponential cell survival expression:

$$S(D) = \exp(-aD) + bD \exp(-cD) \qquad (2)$$

P2S model

Also the probabilistic two-stage model [5, 6] takes into account two classes of DNA damage with different severity. Lethal lesions are assumed to be formed either through the single-track mechanism or through at least pair-wise combinations of less severe lesions. The outcome of cellular repair processes is represented explicitly through the corresponding repair success probabilities. Based on the interplay of damage induction and repair processes, the general model scheme enables to describe a large variety of survival curves, including, e.g., linear and shouldered curves or those including hypersensitivity to low doses of radiation. If the repair success probability of a single lesion is independent of the outcome of repair and total number of other lesions, or if only the residual damage is considered, the model prediction for the cell survival curve takes the form of [7]

$$S(D) = \exp(-\theta_1 D)\,(1+\theta_2 D) \qquad (3)$$

with the parameters θ_1, θ_2 related to damage induction and repair probabilities.

Predictive models

TST model

The cellular track structure theory developed by Katz *et al* is a parametric phenomenological model which describes and predicts RBE for cellular survival *in vitro* after heavy ion irradiation [8, 9]. The target response is described using four model parameters: m, D_0, σ_0 and κ. The first two parameters are used to calculate the probability of cell survival, Π_γ, after a dose D_γ of X-, γ- or δ-rays. The third and fourth parameter apply in calculating the probability Π_i of cell survival after exposure to a beam of ions, of charge Z, speed β, LET(Z, β) = LET$_\infty$ and fluence, F. These probabilities contribute to cell survival, $S = \Pi_i \times \Pi_\gamma$. The model also applies to mixed-field irradiation and supplies parameters to represent cells irradiated in aerobic or anoxic conditions.

LEM model

The local effect model is used for treatment planning for $^{12}C^{6+}$ ion beam radiotherapy at GSI. It is based on the assumption that the biological effect is entirely determined by the spatial local dose distribution inside the cell nucleus, and that there is no principal difference between the action of local

dose depositions of X-rays and that of charged particles [10, 11]. The average number of lethal events after ion irradiation is expressed as

$$N_{ion} = -\int_V dV \frac{\ln S_x[d(x,y,z)]}{V} \qquad (4)$$

where V is the volume of the sensitive site, S_x is the survival after X irradiation, and $d(x,y,z)$ is the local ion dose deposition.

REFERENCES

1. Meijer, *et al.*, Dose and time dependent apoptotic response in a human melanoma cell line exposed to accelerated boron ions at four different LET. *Int J Radiat Biol*, 2005. **81**(4): p. 261-72.
2. Persson, *et al.*, Relative biological effectiveness of boron ions on human melanoma cells. *Int J Radiat Biol*, 2002. **78**(8): p. 743-8.
3. Sinclair, W.K. The shape of radiation survival curves of mammalian cells cultured *in vitro*, in *Biophysical aspects of radiation quality*. 1966, Technical Reports series No. 58: (Lyon: IAEA). p. 21-43.
4. Lind, *et al.*, Repairable-conditionally repairable damage model based on dual Poisson processes. *Radiat Res*, 2003. **160**(3): p. 366-75.
5. Kundrat and P., Detailed analysis of the cell-inactivation mechanism by accelerated protons and light ions. *Phys Med Biol*, 2006. **51**(5): p. 1185-99.
6. Kundrat, *et al.*, Probabilistic two-stage model of cell inactivation by ionizing particles. *Phys Med Biol*, 2005. **50**(7): p. 1433-47.
7. Kundrat, P., *submitted to Appl. Radiat. Tracks*, 2007.
8. Katz, *et al.*, Survey of cellular radiosensitivity parameters. *Radiat Res*, 1994. **140**(3): p. 356-65.
9. Katz, *et al.*, Inactivation of cells by heavy ion bombardment. *Radiat Res*, 1971. **47**(2): p. 402-25.
10. Elsasser, *et al.*, Cluster effects within the local effect model. *Radiat Res*, 2007. **167**(3): p. 319-29.
11. Scholz, *et al.*, Track structure and the calculation of biological effects of heavy charged particles. *Adv Space Res*, 1996. **18**(1-2): p. 5-14.

PROBABILISTIC TWO-STAGE MODEL OF CELL KILLING BY IONIZING RADIATION: THE MODEL, ITS INTERPRETATION AND RELATION TO OTHER RADIOBIOLOGICAL MODELS, AND APPLICATIONS IN TREATMENT PLANNING IN HADRONTHERAPY

Pavel Kundrat

Institute of Physics, Academy of Sciences of the Czech Republic, Na Slovance 2, 18221 Praha 8, Czech Republic

Cell killing by ionizing radiation strongly depends both on the biological properties of a given cell line and on the radiation quality. The probabilistic two-stage model takes into account the induction of damage to DNA by radiations of different qualities and also the outcome of subsequent repair processes, strongly varying among different cell lines. Based on the interplay of damage induction and repair processes, the model enables to describe a large variety of experimental survival curves, including linear, parabolic, or upward-bended curves as well as those exhibiting the low-dose hypersensitivity phenomena. In a simplified case, the model can be viewed as a solution to the kinetic models of radiation effects, such as the repair-misrepair, lethal-potentially lethal, or saturable repair models. Linear-quadratic approximations in the medium-dose ranges can be formulated, too, while a linear behavior is predicted for very high doses.

From analyzing published survival data after proton and light ion irradiation, per-track damage probabilities in dependence on ion species and energy have been derived. Comparisons with Monte Carlo simulations of specific classes of DNA damage indicate a potential interpretation of lethal lesions in terms of clustered DNA damage.

A simple physical model of light ions' Bragg peaks has been used with the given radiobiological module to estimate the biological effectiveness of therapeutic ion beams along their penetration depth in tissue. Model predictions for CHO cells irradiated by carbon beams have been in excellent agreement with measured data. Although further work is necessary to increase the predictive power of the given model scheme, already the present results indicate its possible applications in light ion radiotherapy.

MODELING THE BIOLOGICAL EFFECTIVENESS OF RADIATIONS OF DIFFERENT QUALITIES: LETHAL DAMAGE INDUCED BY LOW-ENERGY PROTONS IN V79 CELLS AND CORRELATIONS WITH ENERGY DEPOSITION, RADICAL DISTRIBUTION, AND SPECIFIC DNA DAMAGE

P. Kundrat[1], M. Davidkova[2], V. Stepan[2,3], Z. Palajova[2], L. Judas[1,4]

[1]Institute of Physics AS CR, Prague, Czech Republic

[2]Nuclear Physics Institute AS CR, Prague, Czech Republic

[3]Faculty of Nuclear Sciences and Physical Engineering, Czech Technical University, Prague, Czech Republic

[4]Dept. of Radiation Protection, General Teaching Hospital, Prague, Czech Republic

A semi-analytical scheme of the probabilistic two-stage radiobiological model used in conjunction with a simple model of light ions' Bragg peaks has predicted biological effectiveness in terms of the survival of CHO cells along penetration depth of therapeutic carbon beams in excellent agreement with measured data (Kundrat P., 2006, Radiat. Prot. Dosim. 122, 480-482). However, some input data to the radiobiological module, namely the per-track damage probabilities, have been derived directly from corresponding experiments under monoenergetic (track-segment) conditions. This seriously limits the predictive power of the given scheme. To overcome this issue, a detailed microscopic radiobiological module has to be formulated, predicting the biological efficiency of radiations of different qualities. As a first step towards this goal, we have analyzed in detail the mechanism of V79 cell killing by protons with LET values from 5 to 40 keV/μm (energies from 0.5 to 7 MeV), for which ample sets of experimental data exist. Per-track probabilities of residual (unrepaired) damage induction have been derived using the probabilistic two-stage model, and their correlations with distribution patterns of deposited energy, radical concentrations and specific classes of DNA damage predicted by detailed Monte Carlo simulations have been studied. Proton tracks in liquid water have been simulated with the code TRIOL (Bigildeev E.A., Michalik V., 1996, Radiat. Phys. Chem. 47, 197-207). Water radiolysis has been modeled by the STOCHECO code (Michalik V., Begusova M., Bigildeev E.A., 1998, Radiat. Res. 149, 224-236), enabling to explicitly respect the influence of oxygen concentration on the initial and time-dependent yields and radial profiles of radiolytic species. Combined direct and indirect damage to DNA has been modeled by folding the mentioned simulations with molecular structures of DNA oligonucleotides. Correlations between the per-track yields of lethal damage in V79 cells and the track structure in terms of energy deposition, spatial distribution of radicals, and the spectra of DNA damage, in particular clustered DNA lesions, have been studied. The reported studies provide new information regarding the biophysical interpretation of initial events leading to cell inactivation. These studies open the way towards detailed biophysical modeling of cell killing effects by radiations of different qualities, including applications in treatment planning in hadron radiotherapy.

MONTE CARLO SIMULATION OF WATER RADICAL CHEMISTRY IN FAST ION TRACKS

Max Kreipl, Werner Friedland, Herwig G. Paretzke

GSF - Institute of Radiation Protection, Ingolstädter Landstraße 1, 85764 Neuherberg, Germany

Monte Carlo simulation calculations have been started investigating possible differences in the effects of a very short (> 1 ps) pulsed ion beam as compared to a more random distribution of ion tracks in time and space as presently often used for tumour therapy. Such effects could arise from interactions between two or more tracks correlated to each other in short temporal and spatial distances. Radiation damage to DNA results from direct (non-scavengable) effects due to ionising events within the DNA constituents as well as from indirect (scavengable) effects due to chemical interaction primarily with OH• radicals produced in the surrounding water shell. Within these two pathways possible inter-track effects at the total doses of interest here are supposed to occur primarily due to indirect effects. Therefore, the Monte Carlo simulation of water radical chemistry in the biophysical charged particle track structure code PARTRAC [1] has been re-assessed. Among other parameters, the thermalisation distance between generation and hydration of sub-excitation electrons turned out to be a critical input parameter for calculated radical yields; using increased values from [2] resulted in a better agreement of our calculations with other experimental and modelling results.

Calculations of the time development of the yield of the principle radicals have been performed for protons, helium and carbon ions in comparison to 60Co γ-irradiation. Whereas initial yields (in terms of new species produced per energy deposited) are almost independent on radiation quality (e.g. LET), a pronounced dependence on LET is found for the yields of OH• radicals and hydrated electrons with a slightly higher yield for heavier ions at the same LET at the end of the chemicals stage after about 1 μs. The simulation results are in accord with data from the literature, also for H2 and H2O2.

Furthermore, the history of water radicals due to pairs of ion tracks with a small spatial and/or temporal distance in-between has been determined and compared with the condition of two completely independent tracks. For spatial distances of up to 10 nm and time intervals up to 10 ns, the inter-track effects lead to a rather similar time course of radical yields corresponding to the results for a radiation quality with twice the LET. Further investigations are underway to analyse the resulting impact on radiation damage to DNA.

References

[1] Ballarini et al., Radiat. Environ. Biophys. 39, 179 (2000)

[2] Meesungnoen et al., Radiat. Res. 158, 657 (2002)

Particle Physics

VERIFICATION OF THE MULTIPLE SCATTERING AND ENERGY LOSS STRAGGLING ALGORITHMS FOR THERAPEUTIC LIGHT ION BEAMS IMPLEMENTED IN A SEMI-ANALYTICAL PENCIL BEAM MODEL AND THE MC CODE SHIELD-HIT; BENCHMARK WITH EXPERIMENTS

I. Gudowska[1], M. Hollmark[1], F. Di Rosa[2], G. A. P. Cirrone[2], G. Cuttone[2], P. Kimstrand[3], E. Traneus[4] and N. Tilly[3,4]

[1]Karolinska Institutet-Stockholm University, Department of Medical Radiation Physics, Stockholm, Sweden

[2]Istituto Nazionale di Fisica Nucleare, Laboratori Nazionali del Sud, Catania, Italy

[3]UppsalaUniversity, Department of Oncology, Uppsala, Sweden

[4]Nucletron Scandinavia AB, Uppsala, Sweden

A semi-analytical algorithm, developed for calculation of narrow ion beams for radiation therapy, and a Monte Carlo code *SHIELD-HIT* are verified against experimental data. Radial dose profiles of 62 MeV and 180 MeV protons have been measured at CATANA facility in Italy and at TSL in Sweden, respectively. The scattering properties of primary carbon beams and their secondaries are studied with *SHIELD-HIT* and compared with experiments performed at HIMAC, Chiba (290 MeV/u) and at GSI, Darmstadt (400 MeV/u).

The accuracy achievable in current radiation therapy with light ions calls for improved precision in the calculation of the energy deposition distribution of narrow charged particle beams. In order to correctly calculate the energy deposition and biological effectiveness of light ions in matter, a physical beam model has to be set up. This model should describe the multiple scattering processes, the stopping power and the nuclear reactions of the ions with adequate precision. Monte Carlo techniques are often used for accurate calculations of the energy deposition of charged particles in media, and are especially suitable for transport in heterogeneous media. For many practical treatment-planning problems, the combination of fast analytical calculations and the accurate calculations of energy deposition kernels by Monte Carlo codes is a very useful approach to achieve precise dose distributions for both photon and proton radiation therapy. The aim of the present study is to verify a semi-analytical method developed for fast calculation of dose distributions for light ion therapy [1, 2] and the Monte Carlo code *SHIELD-HIT* [3, 4] against experimental data.

MATERIALS AND METHODS

Monte Carlo code *SHIELD-HIT*

The ion transport code used in this work is the Monte Carlo code *SHIELD-HIT*, a program well suited for simulations in the field of ion therapy. *SHIELD-HIT* simulates the interactions of hadrons and atomic nuclei of arbitrary charge and mass number with complex extended targets in a wide energy range, from 10 GeV/u down to 25 keV/u, and to thermal energies in the case of neutrons. The *SHIELD-HIT* code extends the original hadron transport code *SHIELD* [5] and was developed for heavy ion therapy. All versions of *SHIELD/SHIELD-HIT* codes apply an exclusive approach and the Russian nuclear models [5-7] to describe hadron-nucleus and nucleus-nucleus inelastic interactions. *SHIELD/SHIELD-HIT* have been benchmarked extensively [3, 4, 7, 8], showing good agreement with the available experimental data. The ionization energy loss of heavy charged particles in the media is calculated using the data from [9, 10]. The energy loss straggling and multiple scattering processes are described by gaussian distributions.

Analytical calculations

A fast semi-analytical model used for calculation of energy deposition of narrow ion beams in water has been developed. The model applies the Fermi-Eyges theory for calculation of multiple scattering of light ion beams traversing water. The developed semi-analytical algorithm incorporates the energy deposition kernels calculated by the Monte Carlo transport code *SHIELD-HIT*, in which ion scattering and energy straggling processes are suppressed. The analytical dose distributions are calculated by weighting the *SHIELD-HIT* calculated dose with analytical Gaussian multiple scattering and straggling distributions. Both primary and secondary particles are considered in this study. To evaluate the influence of the lightest secondary particles (nuclear charges $Z=1$ and $Z=2$) on the total lateral dose distribution, primary and secondary dose distributions are calculated separately.

Experiments

The first Italian proton therapy facility, Centro di AdroTerapia e Applicazioni Nucleari Avanzate (CATANA), with a 62 MeV proton beam, was realized in Catania, at the Istituto Nazionale di Fisica Nucleare-Laboratori Nazionali del Sud (INFN-LNS) in Catania. The proton beam is delivered by a superconducting cyclotron installed and working since 1995. A beam treatment line in air has been assembled together with a dedicated positioning patient system. The beam is ideal for treatment of shallow tumors in the ocular region, such as uveal melanoma [11]. The experiments presented here were designed exclusively for the present collaboration in order to produce well defined lateral dose profiles for the verification of *SHIELD-HIT*. The dose profiles of a 62 MeV proton beam (25 mm in diameter) were measured at different depths in PMMA and air using gafchromic detectors.

A proton beam scanning system with a beam energy of 180 MeV is under development at the The Svedberg Laboratory (TSL) in Uppsala, Sweden [12, 13]. The radial dose profile of a stationary pencil beam at different depths in water has been measured with a Hi-pSi diode mounted on a 3D-servo. The calculations of the 180 MeV protons use input from Kimstrand *et al* [14]. The results of these experiments are used in this work for the verification of both *SHIELD-HIT* and the semi-analytical model.

RESULTS

The multiple scattering and radial energy deposition of fragments produced along the ion path are calculated analytically as well as simulated by *SHIELD-HIT*. The results are verified against experimental data of the transverse energy deposition for clinical proton beams of 62 MeV and 180 MeV, respectively. The scattering properties of primary carbon beams and their secondaries are studied with *SHIELD-HIT* and compared with experiments performed at HIMAC, Chiba (290 MeV/u) [15] and at GSI, Darmstadt (400 MeV/u) [16].

REFERENCES

1. Hollmark, M*., et al.*, Influence of multiple scattering and energy loss straggling on the absorbed dose distributions of therapeutic light ion beams: II. Semi-analytical beam model. *manuscript*, 2007.
2. Hollmark*, et al.*, Influence of multiple scattering and energy loss straggling on the absorbed dose distributions of therapeutic light ion beams: I. Analytical pencil beam model. *Phys Med Biol*, 2004. **49**(14): p. 3247-65.
3. Geithner, O*., et al.*, Calculation of stopping power ratios for carbon ion dosimetry. *Phys Med Biol*, 2006. **51**(9): p. 2279-92.
4. Gudowska, I*., et al.*, Ion beam transport in tissue-like media using the Monte Carlo code SHIELD-HIT. *Phys Med Biol*, 2004. **49**(10): p. 1933-58.
5. Dementyev, A.V. and N.M. Sobolevsky. SHIELD – Universal Monte Carlo hadron transport code: scope and applications. in *Third workshop on simulating accelerator radiation environments (SARE 3)*. 1997. KEK, Tsukuba, Japan)
6. Botvina, A.S*., et al.*, MSDM – Multy-Stage Dynamical Model, in *International codes and model intercomparison for intermediate energy activation yields. NSC/DOC(97)-1, NEA/P&T No 14, OECD*, R. Michael and P. Nagel, Editors. 1997: Paris. p. 307-312.
7. Sobolevsky, N.M. The SHIELD Transport Code: a Tool for Computer Study of Interaction of Particles and Nuclei with Complex Media. in *Proc of the 3rd Yugoslav Nuclear Society International Conference YUNSC 2000. The VINCA Institute*. 2001. Belgrade).

8. Dementyev, A.V. and N.M. Sobolevsky, SHIELD - Universal Monte Carlo hadron transport code: scope and applications. *Radiation Measurements*, 1999. **30**: p. 553-557.

9. ICRU Stopping powers and ranges for protons and alpha particles, in *International Commission on Radiation Units and Measurements. Report 49*. 1993, MD, ICRU: Bethesda.

10. ICRU Stopping of Ions Heavier Than Helium, in *International Commission on Radiation Units and Measurements. Report 73*. 2005, MD, ICRU: Bethesda. p. 253.

11. DeNardo, L.*, et al.*, Microdosimetric investigation at the therapeutic proton beam facility of CATANA. *Radiat Prot Dosimetry*, 2004. **110**(1-4): p. 681-6.

12. Tilly*, et al.*, Development and verification of the pulsed scanned proton beam at The Svedberg Laboratory in Uppsala. *Phys Med Biol*, 2007. **52**(10): p. 2741-54.

13. Lorin*, et al.*, Development of a compact proton scanning system in Uppsala with a moveable second magnet. *Phys Med Biol*, 2000. **45**(5): p. 1151-63.

14. Kimstrand, P.*, et al.*, A beam source model for scanned proton beams. *Phys Med Biol*, 2007. **52**(11): p. 3151-68.

15. Matsufuji*, et al.*, Influence of fragment reaction of relativistic heavy charged particles on heavy-ion radiotherapy. *Phys Med Biol*, 2003. **48**(11): p. 1605-23.

16. Haettner*, et al.*, Experimental fragmentation studies with 12C therapy beams. *Radiat Prot Dosimetry*, 2006. **122**(1-4): p. 485-7.

SPECTROMETRY OF LET USING TRACK-ETCH DETECTORS – FRAGMENTATION STUDIES AND RADIOBIOLOGICAL EFFECTIVENESS IN HEAVIER ION BEAMS

I. Jadrníčková*, F. Spurný, M. Davídková
Nuclear Physics Institute, ASCR, Prague, Czech Republic

The therapy using light ions has started to assert in treatment of tumor diseases, so it is necessary to investigate the behavior of these particles. When particles pass through the matter, they can interact with nuclei and some fragments may be produced. The contribution describes some experimental studies performed in several heavier ion beams using a spectrometer of linear energy transfer (LET) based on chemically etched track detectors. It is able to register particles with LET above around 10 keV/μm. During last years, the detectors were exposed by C, O, Ar, and Fe ions with energies from about 130 to 1000 MeV/amu, in bare beams and behind absorbers. The spectra of linear energy transfer measured with track-etch detectors are compared with those obtained by PHITS code. We made an attempt to quantitatively distinguish the contribution of primary particles and of fragments. From the LET spectra, some dose characteristics, such as absorbed dose, dose equivalent, or quantity characterizing radiobiological effectiveness can be calculated. The radiobiological effectiveness increases with increasing LET of a particle up to about 70 keV/μm, then it decreases.

INTRODUCTION

When heavier ions to be used for radiotherapy pass through the matter, they can interact with nuclei and some fragments may be produced. The fragments diminish the number of primary ions and also produce additional ionization in front of and also behind the Bragg peak. One of quantities used to characterize energy deposition in a matter is linear energy transfer (LET). Experimental studies performed in several heavier ion beams, bare and/or behind a shield, using a spectrometer of linear energy transfer (LET) based on chemically etched track detectors are described in this paper. The spectrometer is able to register particles (both primary and secondary) with LET above around 10 keV/μm. The spectra of linear energy transfer measured with track-etch detectors are also compared with those obtained by means of theoretical calculation using PHITS code [6]. From the LET spectra absorbed dose, dose equivalent, or quantity characterizing radiobiological effectiveness can be then calculated.

METHODS

LET spectrometer, irradiations

The spectrometer of linear energy transfer is based on the chemically etched polyallyldiglycolcarbonate (PADC) track-etch detector. In this study, the material Page (Page Moulgings Ltd, England) 0.5 mm thick has been used. Before etching, one corner of each sample used is irradiated with ^{252}Cf fission fragments and another one with alpha particles from ^{241}Am to check the exact etching conditions. After irradiation, the detectors are etched in 5 N NaOH at 70°C during 18 hours, (removed layer about 17 μm thick on each side of the detector). To determine the LET value of a particle, the etching rate ratio V ($V=v_T/v_B$; where v_B is bulk etching rate and v_T is track etching rate) is established through the determination of track parameters. They are measured by means of an automatic optical image analyzer LUCIA G. The obtained V-spectra are then corrected for the critical angle of detection and they are transformed into the LET spectra using the calibration curves. This LET spectrometer enables determining LET of particles approximately from 10 to 700 keV/μm [1]. The L distributions of track numbers allow to calculate the integral values of dose, D_L,

---

dose equivalent H_L corresponding to particles with L above ~10 keV/μm and, also, integral values of the "biological weighted effective dose", BWE_L, due to these particles. These integral values are obtained as:

$D_L = \sum(dN/dL) \, L \, dL,$ (1)

$H_L = k. \sum(dN / dL) . L . Q(L) . dL ,$ (2)

$BWE_L = \sum(dN/dL) \, L \, r(L) \, dL,$ (3)

where dN/dL is track density in the interval dL, L is the LET of a particle, $Q(L)$ is the ICRP 60 [2] quality factor, and $r(L)$ is the biological weighting function generally characterising the survival of cells exposed to radiation with various L values [3]. If L is expressed in MeV.cm^2.g^{-1}, D_L is obtained in Gy when constant k is equal to 1.6×10^{-10}.

The detectors were during few last years exposed in high energy heavy charged particle beams at:

- HIMAC installation (NIRS Chiba, Japan) in the frame of the ICCHIBAN programs [4],
- NASA Space Radiation Laboratory (BNL) program, and
- Nuclotron of the Laboratory of High Energies, JINR, Dubna [5].

RESULTS

Fragmentation processes in heavy ion beams

The contribution of fragments to the absorbed dose by means of the LET spectrometer have been already investigated in previous studies; some of results for 480 meV/amu ^{12}C ions in various depths in plexiglass and for 1 GeV/amu ^{16}O and ^{56}Fe before and behind the aluminum absorbers have already been presented [7,8], new results are described below.

In Figure 1 there are presented spectra of absorbed dose before and behind the polymethylmethacrylate (PMMA) absorbers for three types of ions (^{16}O, ^{40}Ar, and ^{56}Fe) used in ICCHIBAN 8 run; the uncertainties are omitted for better lucidity.

One can see that with the decreasing energy of the ions (as particles pass through the matter) the spectra are shifted towards higher values of LET. In the spectra, one can also distinguish the main peak and contribution of fragments and other particles.
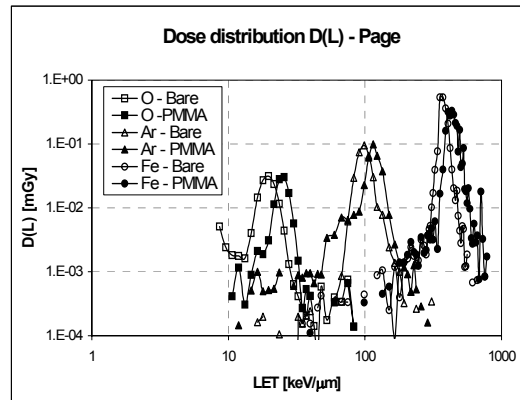
Figure 1.   Dose distributions in LET in some heavier ion beams, bare and/or behind a shield.

We made an attempt to distinguish the contribution of primary ions and of fragments to the absorbed dose; the results for Page are summarized in Table 1, together for ICCHIBAN 8 and also for some data from foregoing ICHIBANs.

Without the absorbers there would be theoretically no secondary particles, nevertheless, we measured that the fragments and secondary particles contribute with few percents (3 − 9 %) to the absorbed dose. These particles may originate from the fragmentation and nuclear reactions in the air or in the ion-conduit. Behind the absorbers the contribution of fragments increases with the increasing depth in the beam up to the depth before the Bragg peak; for 480 MeV/amu ^{12}C ions the maximum of fragment contribution was found at 0.93 of the particle's range [8].

The measured data are compared with the ones, obtained by means of simulation (for broad monoenergetic beams) using the PHITS code; only particles with LET above 10 keV/μm and new calibration curves for Page material were considered.

Most of the data are in a quite good agreement (when the uncertainties are taken into account), nevertheless in some cases (for 1000 MeV/amu [16]O ions behind aluminum and for 130 MeV/amu [56]Fe ions behind the PMMA) we measured higher values. Some discrepancies may be caused by simplification in the simulations (e.g. simpler geometry of the experiments).

The production of fragments depends on the material of the absorber. From Table 1 one can see that for iron ions the contribution to the absorbed dose is higher behind the water than behind the aluminum absorber, both with the thickness of 5 g/cm2. This is in agreement with results published in [9] where the fragmentation of 1 GeV/amu iron ions was investigated in lead, aluminum, and PMMA target; the highest fragmentation was observed for the PMMA target, the lowest one for lead target.

An example of comparison of relative measured and simulated spectra for 440 MeV/amu [40]Ar behind 9 g/cm^2 is shown in Fig. 2.

Figure 2. Comparison of measured (Page) and simulated (PHITS) spectra (in relative units)
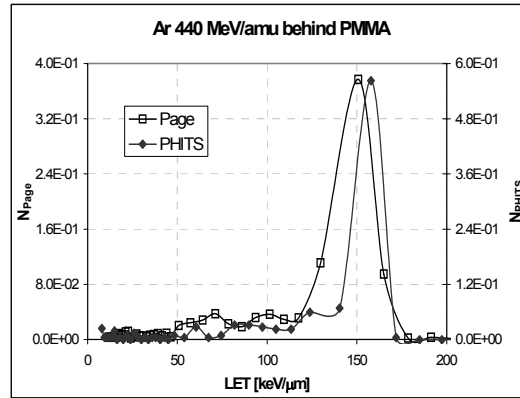
Table 1. Relative contribution from fragments to the absorbed dose

ions and primary energies [MeV/amu]	depths [g/cm^2]	dose from fragments	
		PHITS	Page
[16]O 395 MeV/amu [1]	10.01	17.1	16.8 ± 1.2
[16]O 1000 MeV/amu [2]	54.00 (Al)	16.2	36.3 ± 1.4
[40]Ar 440 MeV/amu [1]	5.25	25.1	31.2 ± 1.7
[40]Ar 500 MeV/amu [3]	9.00	40.5	34.5 ± 2.2
[56]Fe 130 MeV/amu [1]	0.35	5.7	11.5 ± 0.7
[56]Fe 450 MeV/amu [4]	5.00 (H2O)	35.4	34.2 ± 2.1
[56]Fe 450 MeV/amu [4]	5.00 (Al)	12.2	13.3 ± 1.5
[56]Fe 1000 MeV/amu [2]	10.00 (Al)	20.9	21.2 ± 1.8

[1]ICCHIBAN 8, [2]ICCHIBAN BNL, [3]ICCHIBAN 6, [4]ICCHIBAN 4

Relative biological effectiveness

Finally, we have tried, using LET spectra measured, to estimate relative biology effectiveness in heavy ion beams studied during several last years. It was calculated through the equation (3), on the base of data measured in beams of C, O, Ar, and Fe ions, bare and/or behind different shieldings. LET of primary particles used covered the range from about 10 up to about 500 keV/μm. RBWE have been

calculated separately for primary ions and total values, including the influence of fragments and other secondary particles. The results obtained are presented in the Figure 3. One can see there that:

1. There is only limited difference in the RBWEs corresponding to primary particles and total ones, including fragments and secondary particles.
2. Maximum value of RBWE is situated at LET about 70 keV/µm, with increasing LET, it decreases. It should be considered when a particle treatment is to be chosen.

CONCLUSIONS

1. It was found that the spectrometer of linear energy transfer (LET) based on chemically etched track detectors developed in our laboratory and recently upgraded permits an independent estimation of the contribution of fragments and other secondary particles in heavier ion beams considered to be used in radiotherapy. It permits to consider particles with LET higher than about 10 keV/µm.
2. Experimental results obtained have been compared with the results of calculations performed by means of PHITS code, generally, a good agreement can be stated, taking into account the differences between experimental and theoretically chosen irradiation geometries.
3. The RBWE values obtained for beam studied exhibits a maximum 100 keV/µm, as it could be expected from the LET dependence of the general the biological weighting function. Relatively low importance of fragments on the values of RBWEs has been observed, it should be however reminded that the studies have been mostly performed well before the Bragg peak region.
4. Further experimental studies and theoretical calculations are prepared to enlarge the knowledge on the importance of secondary particles in heavier ion therapy beams, particularly along the range as complete as possible..
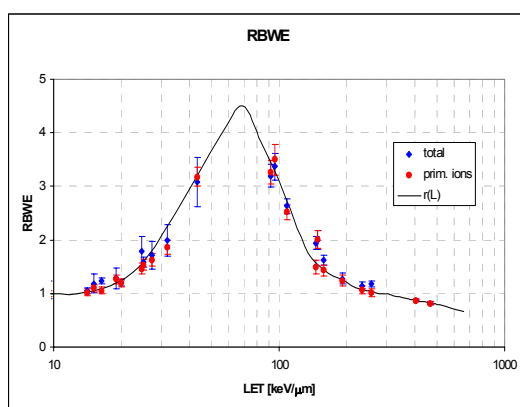
Figure 3.   RBWE in heavier ion beams.

REFERENCES

1. Spurný F., Jadrníčková I., Molokanov A.G., Bamblevski V.P., 2005. Upgrading of LET track-etch spectrometer: Calibration and uncertainty analysis. Radiat. Meas. 40, 343-346.
2. ICRP Publication 60 Recommendations; Annals of ICRP No. 1-3, (1991).
3. Loncol, T., Cosgrove, V., Denis, J. M., Gueulette, J., Mazal, A., Menzel, H.G., Pihet, P. and Sabattier, R. Radiobiological effectiveness of radiation beams with broad LET spectra: microdosimetric analysis using biological weighting functions. Radiat. Prot. Dos. 52, 347- 352 (1994).
4. Uchihori Y., Benton E.R., (Eds.), 2004. Results from the first two intercomparisons of dosimetric instruments for cosmic radiation with heavy ions beams at NIRS (ICCHIBAN–1&2) experiments. HIMAC–078, NIRS Chiba, Japan, February 2004.
5. JINR Basic facilities (2006) [online] www.jinr.ru/facil.
6. Iwase H., Niita K., Nakamura T., 2002. Development of a general-purpose particle and heavy ion transport Monte Carlo code. J. Nuc. Sci. Technol. 39, 1142-1151.

7. Jadrníčková I., Molokanov A.G., Spurný F., 2006. Doses and LET spectra in the beam of 12C with energy 500 MeV/amu. Radiat. Prot. Dos. 122, 488-490.

8. Jadrníčková, I., Spurný, F. and Molokanov, A.G. (2007) Contribution of secondary particles to the dose in 12C radiotherapy and other heavy ion beams. Radiat. Prot. Dosim., DOI:10.1093/rpd/ncm133.

9. La Tessa C., Guetersloh S., Heilbronn L., Miller J., Sihver L., Zeitlin C., 2005. Fragmentation of 1 GeV/nucleon iron ions in thick targets relevant for space exploration. Advances Space Research 35, 223-229.

STUDYING THE SECONDARY ELECTRON FLUENCE IN ^{12}C ION BEAMS BY MEANS OF AN EXTRAPOLATION CHAMBER

Ö. Kartal[1,2,*], O. Jäkel[1], J.Breckow[2], G.Hartmann[1], B.Ackermann[1]

1 Deutsches Krebsforschungszentrum(DKFZ), Heidelberg, Germany

2 Institut für Medizinische Physik und Strahlenschutz(IMPS),Fachhochschule-Gießen-Friedberg, Gießen,Germany

In clinical radiation dosimetry, ionization chambers are used to determine the absorbed dose in water under the condition that the Bragg-Gray cavity theory is fulfilled. This theory requires that the gas in the chamber volume does not disturb the fluence and the energy spectrum of the electrons that pass through the cavity and the contribution of the energy originating from the photon interactions in the cavity to the absorbed dose is negligible. By means of an extrapolation chamber, which has a variable air-volume it can be studied, how well these conditions are fulfilled when measuring the absorbed dose in water in ^{12}C ion beam. The measurements carried out in GSI Heavy Ion Facility, Darmstadt, Germany with an extrapolation chamber showed that the electrode separation of an air-filled plane-parallel chamber is a significant factor affecting the electron fluence in the chamber sensitive volume and therefore the measured absorbed dose in the surrounding medium.

INTRODUCTION

Radiation dosimetry in radiotherapy makes use of air-filled plane-parallel ionization chambers not only in conventional irradiation with ^{60}Co gamma rays, and high-energy photon and electron beams but also in heavy ion beams. Calibrated commercial chambers are recommended by the IAEA-TRS 398 [1] as reference instruments in clinical heavy ion beams. Plane-parallel chambers are especially recommended for the measurement of depth dose distributions. An absorbed dose measurement in a phantom with such a plane-parallel chamber is valid under the assumption that the Bragg-Gray conditions are satisfied. Since these conditions are not adequately met, the readings are corrected for perturbations causing a deviation from an ideal Bragg-Gray cavity. In the same report of IAEA [1] the perturbation factor p_Q that is used to calculate the correction factor k_Q is taken to be unity for heavy ions which implies that there is no perturbation of the electron fluence in the chamber cavity at all, provided that the chamber operates at charged particle equilibrium (CPE). This topic was also discussed by Hartmann et al. [2]. They concluded that the uncertainty of p_Q=1 is not greater than 1%. In this work an extrapolation ionization chamber is used to study the effect of the secondary electron fluence in dosimetry of heavy ion beams.

THEORETICAL BACKGROUND

Both the Bragg-Gray cavity theory and the Spencer-Attix relation, which may be considered as a supplement of the former theory, require that the fluence and energy spectrum of the electrons passing through the phantom and the chamber cavity must be the same and the contribution of photon interactions in the cavity to the absorbed dose is negligible. Assuming that the cavity satisfies these conditions, the absorbed dose in the cavity is the quotient of the charge collected in the cavity by the effective mass of air multiplied by the mean energy required to produce an ion-pair in the gas (Eq.1).

$$D_{air} = \frac{dQ}{dm} \cdot \overline{W}_{air} \qquad \text{(Eq. 1)}$$

$\overline{W}_{air}$ is given to be 34.50J/C [1]. Replacing the mass of air by the product of density of air ρ, effective area of measuring electrode A and the electrode seperation z, it is possible to express the dose as a function of the ionization gradient dQ/dz for a small cavity.

---

*Corresponding author: o.kartal@gmx.de ,
o.kartal@dkfz.de

$$D_{air} = \frac{dQ}{dz} \cdot \frac{1}{\rho \cdot A} \cdot \overline{W}_{air} \qquad\qquad \text{(Eq. 2)}$$

Having measured the capacitance C of the chamber and plotted the reciprocal of the capacitance as a function of the electrode separation, the effective area of the measuring electrode can be determined. The slope of this linear relation is the inverse of the product of the effective area A and the dielectric constant for vacuum ε_0. Since the air density ρ for measuring conditions would also be known, the absorbed dose in the cavity can easily be calculated if dQ/dz is determined. Absorbed dose in the surrounding medium can be reached by multiplying the absorbed dose in the cavity by the ratio of restricted mass collision stopping powers of medium and air (Eq.3).

$$\frac{D_{med}}{D_{air}} = \left(\frac{L}{\rho}\right)^{med}_{air} \qquad\qquad \text{(Eq. 3)}$$

By means of an extrapolation ionization chamber it is quite simple to determine the ionization gradient dQ/dz because it is a type of plane-parallel chamber the electrode separation of which can be varied. For dose calculation not the absolute electrode separation is required, but just the relative increments of electrode separations. For that reason this chamber is also called the gradient chamber [3]. In this work however, the ionization gradient through the chamber cavity is going to be observed to see how it behaves through the entire cavity, therefore it is essential to know the absolute electrode separations which are measured with an accuracy of ±0.05mm.

MATERIAL AND METHODS

The extrapolation ionization chamber used in this work has a fixed measuring electrode (Ø2.200±0.025cm) made of graphite that is surrounded by a guard ring (Ø13.420±0.025cm) of same material which are separated by a 0.2mm thick teflon ring. Polarizing electrode is a 14µm thin polycarbonate based foil. The electric field in the chamber at every electrode separation was chosen to be approximately 1100V/cm to make sure that the chamber operates at a region very close to the saturation. Though all readings were corrected for ion recombination losses using the two-voltage method [4]. The extrapolation chamber is equipped with a steering device developed in DKFZ, Heidelberg to vary the electrode separation, which is connected with a cable to the chamber via an RS232 interface. The polarizing electrode can be moved in the beam axis by means of this steering device in a range of approximately 1 to 9 mm in steps of 1mm. The electrode separation can also be varied manually in a range of 0.3mm to 9mm in steps of 0.05mm. The collected charge in the chamber was measured by an electrometer (Unidos-Webline, PTW) and the required high-voltage was provided by another power supply (NHQ-102M, Struck).

Measurements were carried out in GSI,Darmstadt in ^{12}C ion beam of 300MeV/u energy. Two special made plates (119mg/cm² thick PMMA and 170mg/cm² thick graphite) were used as phantom materials placed in front of the entrance window of the chamber (polarizing electrode). Thus the effective point of measurement for the chamber lies at a depth of approximately 3mmH$_2$O corresponding the plateau region in the depth dose distribution instead of SOBP (Spread out Bragg-Peak) in order to avoid the dose fluctuations. The collected charge was measured three times at each electrode separation in the range of 1mm to 8mm and at two different voltages. The measurement was repeated after exchanging the positions of the plates.

RESULTS AND DISCUSSION

Using the two-voltage method, the saturation charge is determined at each separation of electrodes and is represented as a function of electrode separation (Fig.1). Saturation charge has an almost perfect linear relation to the electrode separation. A least-squares fit gives a straight line with a very high correlation coefficient (R=0.996), which would imply that the ionization gradient is almost constant through the cavity. Nevertheless, to analyze this more closely the ionization gradients dQ/dz, that are normalized over the average are plotted as a function of electrode separation (Fig.2).
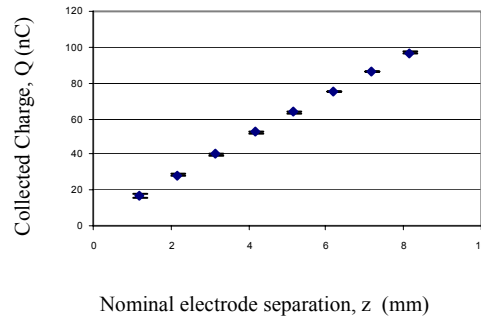
Figure 1. Saturation charge collected in the extrapolation chamber in ^{12}C ion beam of 300 MeV/u energy as a function of the electrode separation.
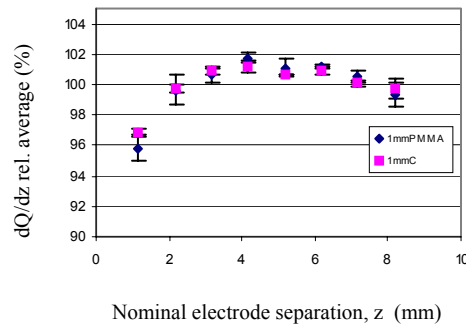
Figure 2. Ionization gradients for two different phantom combinations normalized over the average plotted as a function of electrode separation in 300 MeV/u energy ^{12}C ion beam.

The measured slopes in fig.2 vary by about 4-5% through the entire air cavity. These measurements were later on also carried out in ^{60}Co gamma rays and in high-energy photon and electron beams, which led to similar results. Zankowski et al. [4] studied the same effect in conventional beams. They analyzed the curve in three regions; namely z<1mm, 1mm≤z≤2mm and z>2mm and concluded that the second region is the true Bragg-Gray region for these irradiation types. The measurements done in this work with the extrapolation chamber in ^{60}Co gamma rays and in high energy photon and electron beams confirm their results to a great extent. However, the so-called true Bragg-Gray region in ^{60}Co gamma rays and in megavolt photons seems to be a bit larger (1-2.6mm) than in electron beams. In ^{12}C ion beam on the other hand, this region lies deeper in the cavity and is larger (3-6mm) than in above mentioned beam types. The ionization gradient at 2mm (typical electrode seperation of commercial plane-paralle chambers) electrode separation is ~1% less than at 3mm where it can be interpreted as the true Bragg-Gray region. Krießbach studied the influence of the chamber wall (polarizing electrode) in radiation dosimetry of ^{12}C ion beams by means of a Monte-Carlo simulation software [6]. He concluded that the secondary electron fluence at the boundary wall to air is ~4% less than it would be at CPE (charged particle equilibrium) in air. The smallest electrode spacing used here in ^{12}C ion beam was 1mm. The ionization gradient at this separation is about 4.5% less than the mid-region (3-6mm) where it is interpreted as the region of CPE.

Analyzing the curve (fig.2) in three distinct regions like Zankowski et al. did in their work [5], we can discuss the reasons of the variations of the secondary electron fluence through the cavity. In the first region (z<3mm), the cavity is so small that relatively few ionizations are caused by the electrons generated in the cavity. In ^{12}C ion beams 90% of the total ionizations are caused by the ions and by the secondary electrons generated in the cavity [6]. Besides, in this region the uncertainty of the slope is relatively larger than in larger separations due to the uncertainty in the electrode separation. The second region (3mm≤ z ≤ 6mm) can be referred as the true Bragg-Gray region, which at the same time should correspond to the range of the secondary electrons generated in the phantom and in the wall. In

the last region (z>6mm) the ionization gradient is ~2% less than the mid-region. It can be caused by the light fall in the mass stopping powers of the electrons and/or can also be caused by the predominating of the out-scattered electrons by air over the in-scattered electrons by the surrounding.

REFERENCES

1. International Atomic Energy Agency, Technical Report Series-398, "Absorbed dose determination in external beam radiotherapy", (2000)
2. Hartmann, Jäkel, Heeg, Karger, Krießbach, "Determination of water absorbed dose in a carbon ion beam using thimble ionization chambers", Phys.Med.Biol.44 (1999)
3. S.C. Klevenhagen, "Determination of absorbed dose in high-energy electron and photon radiation by means of an uncalibrated ionization chamber", (1990)
4. Käse, Bjärngard, Attix, "The Dosimetry of Ionizing Radiation", Vol.II (1987)
5. C.E. Zankowski, E.B. Podgorsak, "Calibration of photon and electron beam with an extrapolation chamber", (1996)
6. A. Krießbach, "Untersuchung des Wandeffektes von Ionisationskammern bei der Bestrahlung mit ^{12}C Ionen" , (1999)
7. U. Müller, "Eine extrapolationskammer zur dosimetrie niederenergetischer röntgenstrahlung" Göttingen, (1979)

Radiobiology 1

DYNAMICS OF DNA DOUBLE STRAND BREAKS DETECTED BY LIVE CELL MICROSCOPY INDICATES ONLY LIMITED CLUSTER FORMATION AFTER HIGH LET IONIZING RADIATION.

Burkhard Jakob, Jörn Splinter, Yvonne Schweinfurth and Gisela Taucher-Scholz,

GSI Biophysik, Planckstr.1, 64291 Darmstadt, Germany

DSBs are believed to occur in higher number and proximity after irradiation with densely ionizing radiation.Connections between wrong DNA ends can lead to loss of genetic information, chromosomal translocations and ultimately, to cellular transformation or tumorigenesis. To analyse the mobility of DSB-containing chromosomal domains in mammalian cells, we took advantage of the extremely localized dose deposition of low energy particle beams. In comparison to laser irradiation, that is commonly used to introduce localized damage, heavy ion (HI) beams offer the possibility to control and determine the deposited dose. As well, they avoid the usage of DNA interacting photosensitizer, which might influence the observed repair processes. Mechanistically HI act as an ionizing radiation by the production of δ-electrons. Thus HI are supposed to lead to a similar spectrum of DNA lesions as γ- or X-rays, but with differences in respect to the geometrical dose/lesion distribution (Fig.1).
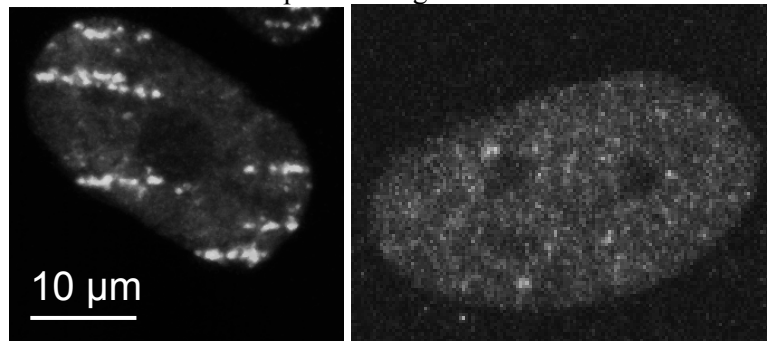
Fig.1: Distribution of DSBs in nuclei of human fibroblasts (AG1522) indicated by γ-H2AX immunostaining 15 min after irradiation with low energy carbon ions (E: 9.6 MeV/u LET: 175 keV/μm) under a small angle (left) or 10 Gy x-rays (right), respectively.

With our beamline microscope, we are able to measure the fast accumulation of early repair-related proteins immediately after the ion impact. As an example, in Fig. 2 the recruitment kinetics of aprataxin_GFP [3] a SSB repair related protein is shown after the irradiation with low energy uranium ions, showing the sub-second temporal resolution of the current setup (insert Fig.2). Fig. 3 shows the actual irradiation chamber (left) allowing the irradiation and observation with the cells kept in cell culture medium during observation, avoiding artefacts generated by osmotical or pH-dependent stress responses. In Fig. 3 (right) the temperature controlled chamber mounted on the beamline microscope is displayed. The image was taken from the direction of the beam.. Using this beamline-microscope, we could demonstrate that the irradiation-induced foci appear at the distinct sites of ion traversals [Jakob] and do not move in a range exceeding 1 μm in the first minutes. Long term observations using live cell microscopy (Fig.4) revealed a certain degree of constrained motion of chromosomal domains containing DSBs and geometrical changes of the focal structures. Up to now, we have no indication of a massive clustering of individual domains to form higher level repair centres as observed in yeast [1], or an active roaming of damaged chromatin in the search for homology [2].
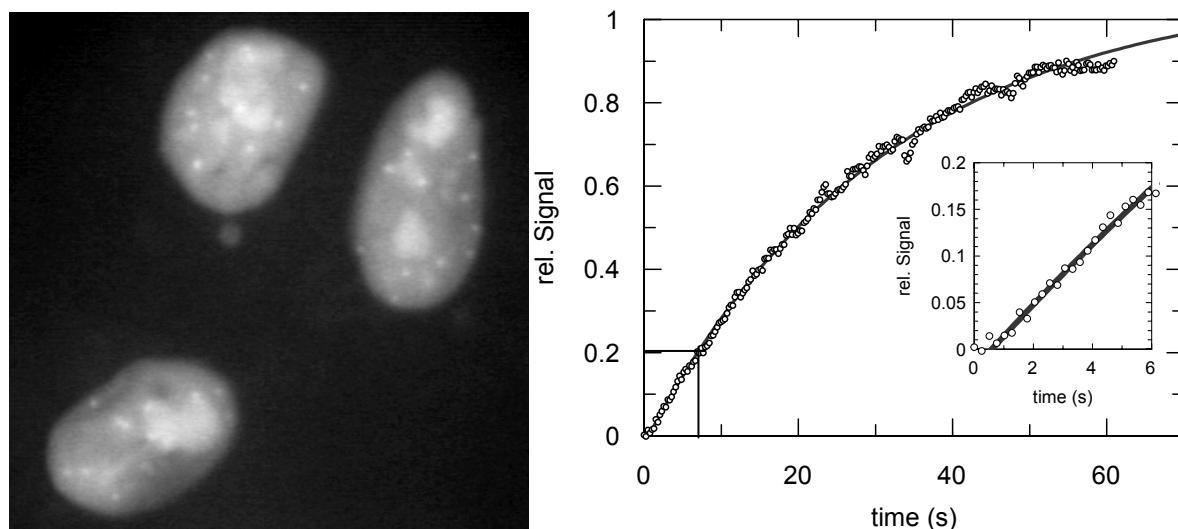
Fig.2:Measuring recruitment kinetics after Heavy ion irradiation. left: Sample image taken from a sequence showing the accumulation of aprataxin-GFP (white dots) in the nuclei of Hela-cells after irradiation with low energy uranium ions (E: 4.2 MeV/u LET: 14300 keV/µm) obtained at the beamline microscope. Right: Kinetic of the aprataxin accumulation at sites of ion traversal allowing the calculation of recruitment constants. The insert illustrates the temporal resolution of the current setup.
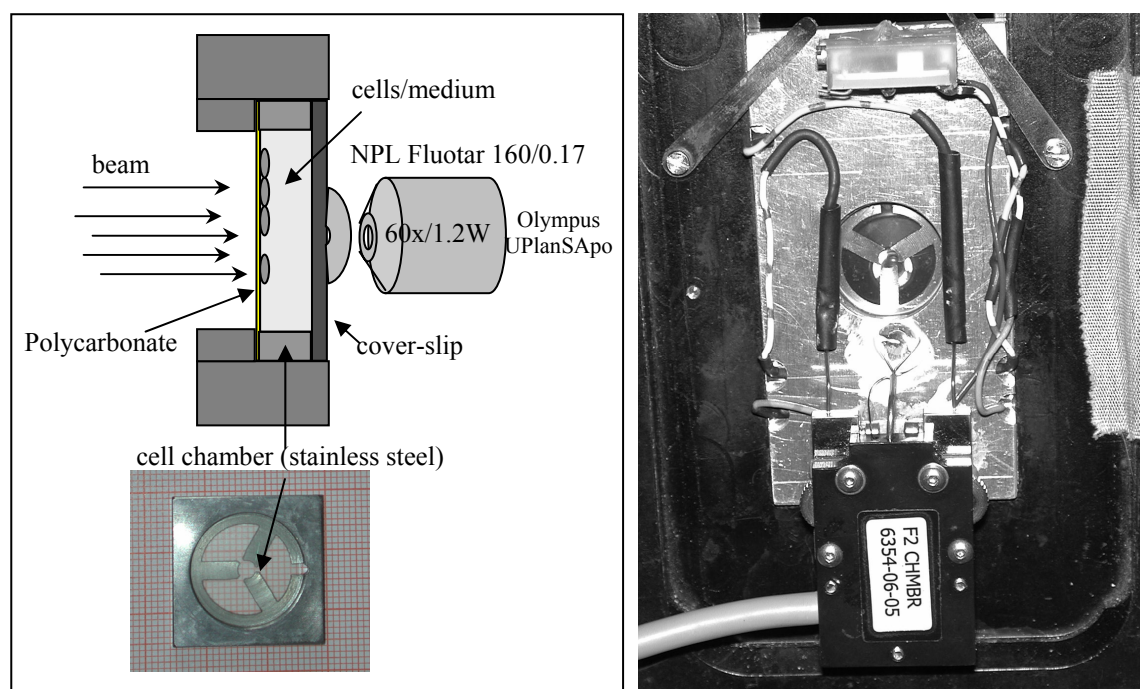
Fig.3. left: Setup of the microscopical conditions allowing the irradiation with low energy ions and the microscopy in cell culture medium. Right: Modified temperature controllable cell chamber mounted on the beamline microscope.
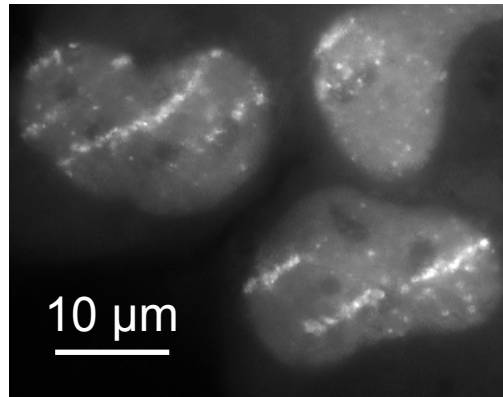
Fig. 4: Time-lapse microscopy after heavy-ion irradiation: Living cells can be observed and the behaviour of repair related proteins studied over several hours in a fluorescence microscope equipped with a Focht-chamber (FCS2, Bioptech). Example image of U2OS nuclei expressing NBS1-GFP (kindly provided by Claudia Lukas, Copenhagen) after the irradiation with low energy Ca ions (low angle; E: : 7.4 MeV/u LET: 1850 keV/µm).

We compared the spatiotemporal behaviour of macro- and microfoci forming proteins after irradiation with HI. In most cases, there is a one to one correlation between γ-H2AX stained macrofoci (megabasepair-domain) and internal microfoci, pointing that they do not represent the sites of individual lesions (Fig. 5). These microfoci might either represent a lesion processing complex inside every γ-H2AX stainable domain, requiring only a short range movement of damaged DNA. Alternatively at a given time only a sub-fraction of lesions might be processed as indicated by the formation of a microfocus. However, considering passive protein diffusion and binding to DNA lesions, the serial processing by translocation of the DNA repair machinery seems highly improbable.
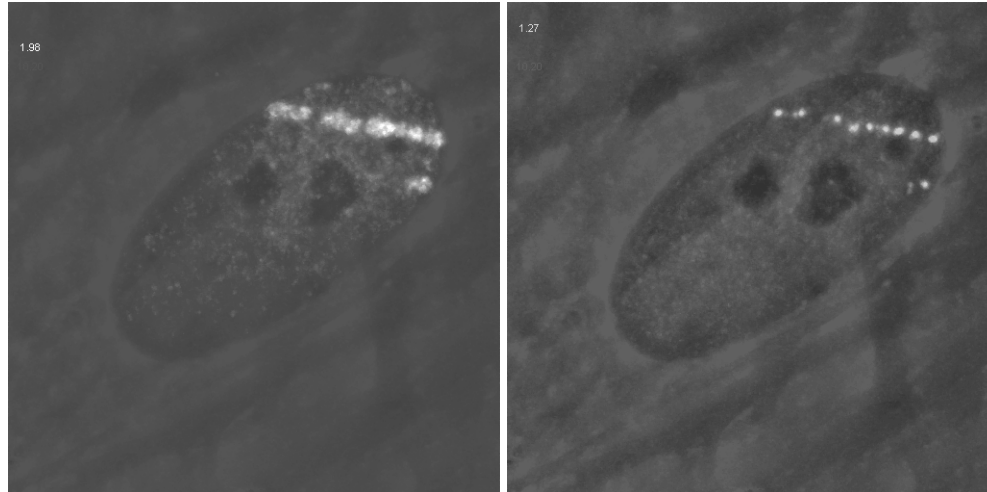
Fig. 5: Example of a double-immuno-staining experiment showing the two classes of foci in human AG-fubroblasts after irradiation with low energy chromium ions (low angle; E: : 6.5 MeV/u LET: 2630 keV/µm). left: γ-H2AX representing the macrofocus-type. Right: XRCC1 representing the microfocus-type. Both fluorescence signals overlayed by a phase contrast image showing the whole nucleus.

In summery, our data using localized densely ionizing irradiation lead to a hypothesis of a quite localized processing of DNA lesions. The repair might occur in repair centres associated with each megabasepair-domain. In the timescale of hours, only constrained and random migration of damaged chromatin domains could be observed. So far, the results do not support the idea of wide-range homology search or formation of repair clusters from different chromatin domains.

[1] Lisby et al., Nat. Cell Biol. (2003), 5, 572-7.
[2] Aten et al., Nat. Cell Biol. (2003), 5, 572-7.

IRRADIATION OF LIVING CELLS AT SNAKE

V. Hable[1,*], C. Greubel[1], G. Dollinger[1], A. Hauptner[2], R. Krücken[2], H. Strickfaden[3], S. Dietzel[3], T. Cremer[3], G.A. Drexler[4], A.A. Friedl[4]

[1]Angewandte Physik und Messtechnik LRT2, UniBw-München, 85577 Neubiberg, Germany
[2]Physik Department E12, TU-München, 85748 Garching, Germany
[3]Department Biologie II, LMU-München, 82152 Martinsried, Germany
[4]Strahlenbiologisches Institut, LMU-München, 80336 München, Germany

The ion microprobe SNAKE, (Superconducting Nanoprobe for Applied nuclear (Kern-) physics Experiments) at the Munich 14MV Tandem accelerator is capable to focus an ion beam to a spot size of about 0.5µm (FWHM). This allows, in combination with a single ion preparation, the accurate application of an arbitrary dose to a defined cell nucleus or a substructure of it. By irradiating arbitrary patterns dynamics and kinetics of several proteins involved in double strand break (DSB) repair have been investigated by using immunofluorescence methods and, recently, also by live cell imaging of GFP tagged proteins.

The ion microprobe SNAKE is designed to focus a beam of protons or heavy ions to a submicrometer size by means of a superconducting quadrupole lens doublet and a specially developed slit system [1]. The submicrometer beam resolution in combination with the wide spectrum of ion sorts and energies available makes SNAKE an ideal tool to study irradiation induced DNA damages [2].

SNAKE SETUP

A schematic drawing of SNAKE can be seen in fig. 1. The beam generated in the ion source is accelerated by the 14MV Tandem accelerator. A broad spectrum of ions is possible. By varying the ion sort and the acceleration voltage, the dose applied to one cell nucleus by a single ion can be adjusted by about four orders of magnitude from a few mGy up to about 10Gy (see fig. 2). A 90° analyzing magnet makes sure that only ions of the wanted magnetic rigidity (and therefore mass and velocity) can pass. Behind this magnet specially developed slits are located, which cut the beam to a diameter of about 10-20µm. These slits serve as an object, which is demagnified by a factor of 1/88 in x and 1/24 in y using the superconducting multipole lens that is situated in a helium bath cryostat. Cells, which are nurtured on a Mylar foil in specially designed cell containers, are placed on the table of an optical microscope (see the CAD drawing figure 3) at the focal plane of SNAKE.

As the cells have to be under atmospheric pressure, the beam leaves the vacuum through a 7.5µm Kapton foil at the exit nozzle. To limit beam broadening by scattering in the foil, the exit nozzle can be moved by a step motor on contact to the Mylar foil, on which the cells grow under live conditions during irradiation.
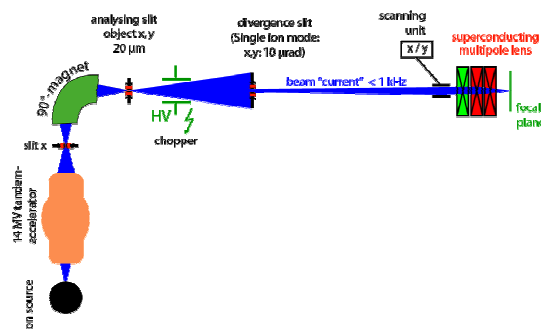
Figure 1. Schematic drawing of the essential devices of SNAKE.
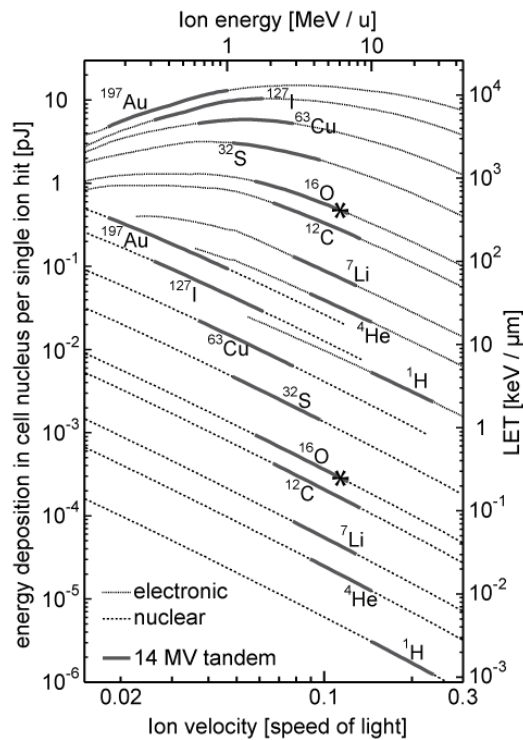
Figure 2. LET and energy deposition in a single 75µm thick cell nucleus from nuclear and electronic interaction for various ions. The solid segments of the lines show the energy range which can be used at SNAKE. [1]

To be able to take advantage of the well defined dose applied by a single ion, one must be able to define the number of ions hitting the cell nucleus as well. For this purpose a single ion preparation is implemented. The device consists of a high voltage chopper shown in fig. 1, which deflects the beam in order to inhibit the beam. The high voltage can be switched off by a trigger signal from the user, so that irradiation takes place. Every ion that hits the cell sample is detected by a photomultiplier tube behind the cell container. If the desired number of ions, e.g. one ion, has arrived, the high voltage is switched on, so that no more ions reach the cell. If wanted, e.g. for irradiation of patterns or a selected number of cells, the beam is moved to the next irradiation position by an electrostatic scanning unit and the procedure starts again.

In this single ion mode we reach a beam resolution on air of about 0.55µm in x- and 0.40µm in y-direction [3].

Figure 3. CAD drawing of the SNAKE
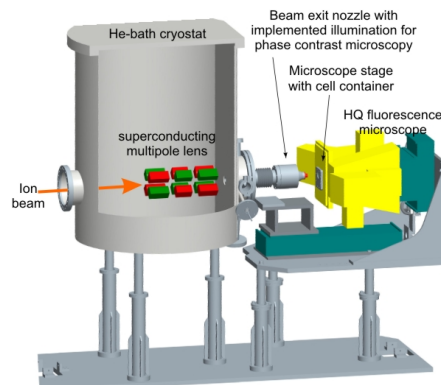
The small beam diameter enables targeted irradiation of cell nuclei or even substructures of it. But it also allows irradiating the cells with highly defined geometric patterns. These are helpful to evaluate protein dynamics in fixed cells using immunofluorescence techniques.

Figure 4. a) γ-H2AX foci of cells irradiated in a line pattern fixed 0.5h after irradiation. b) The irradiation pattern on a nuclear track detector (1 ion per spot). c) 15h after irradiation the lines look more dispersed.
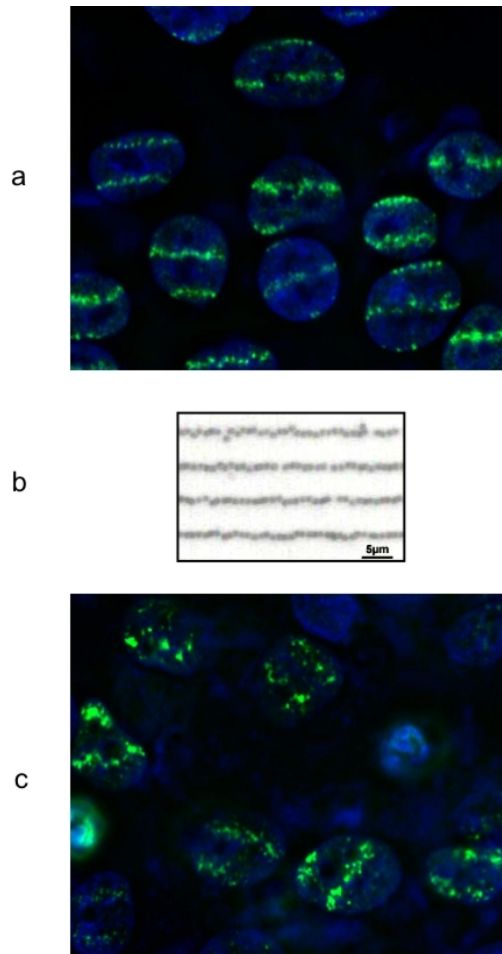
Figure 4 shows line patterns of foci built by the phosphorylated histone γ-H2AX, which acts as a DSB indicator. The lines are formed by single 100MeV oxygen ions separated 1μm each, while the distance between the lines is 6μm. The fluorescence image of immuno-stained γ-H2AX in fig. 4a was taken 30min after irradiation. It shows the detailed point-wise structures of the irradiation well represented. In contrast, fig. 4c was taken 15h after irradiation. Some of the nuclei have rotated and the spread in the lines is significantly enhanced. The behavior reveals at first glance dynamics within the irradiated cell nuclei [4]. The deviation of the foci around the irradiation line increases with time. When evaluating the dynamics quantitatively the line pattern has advantages, too: The best fit straight line through a row of foci in the cell nucleus represents the irradiation line. Thus, one can evaluate the deviation σ of the foci around the best fit straight line which is a relative measure being independent to movements of the whole cell nucleus (such as the rotations in fig. 4c) [4].
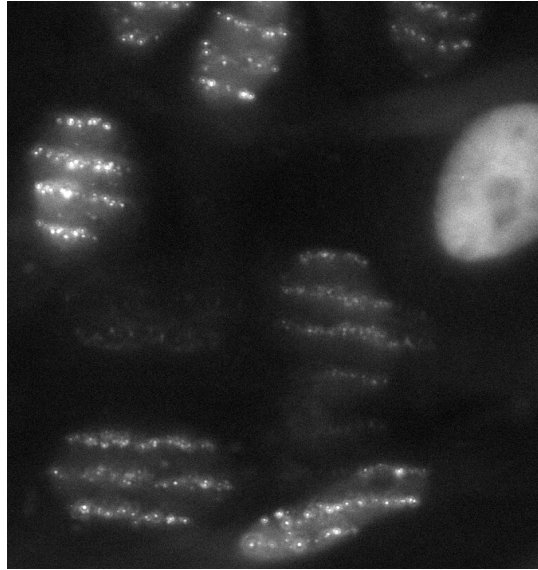
FOCI ALONG AN ION TRACK

In the microscopic data used for the evaluations described before the picture plane is perpendicular to the flight direction of the ion beam. But we also have a setup for inclined irradiations, where the ions hit the cells under an angle of 10°. So we can investigate protein dispersion along the ion tracks in the cell nuclei (see fig. 5). The most interesting question related to these experiments is to compare the densities of DSB induced foci along the track for lower LET ions (e.g. 30MeV Lithium shown here) with that of higher LET ions (e.g. 100 MeV oxygen). Measured differences in focus density between both ion sorts are not as drastic as simple models predict [5]. Naively, one expects the density to be proportional to the LET. But this assumption neglects chromatin structure in the nucleus.

LIVE CELL IMAGING

The optical microscopy performed on irradiated cells, as shown before, requires killing the cells at a certain time after irradiation in order to perform the immuno-staining of various repair proteins. Thus, only one point in time is investigated. In order to get the time course of a reaction of the cell we have recently set up live cell imaging of cells by GFP tagged repair proteins. For this purpose a high quality fluorescence microscope is mounted to the beam line (see fig. 3). Also phase contrast microscopy (e. g. for targeting purposes) is implemented. To provide the cells good terms during the irradiation and observation period, the newly developed LCI cell containers can be heated to 37°C and the cells are surrounded by cell culture medium.

First time series of the repair proteins Rad 52 (fig. 6) and Mdc1 in the living cell have already been taken using this new setup.
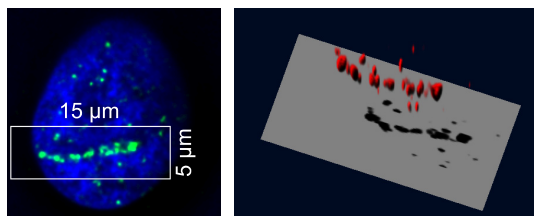
Figure 5. Track of a single ion through a cell nucleus. Left: One slice of a z-stack from 3D-optical fluorescence microscopy. Right: 3D-reconstruction from the whole stack.

Figure 6. GFP tagged protein Rad52 in living cells is imaged by online fluorescence microscopy at SNAKE. It shows line-wise foci arrangement 6h after irradiation with 100MeV oxygen ions. Protein unbound to irradiation foci shows the form of cell nuclei.

REFERENCES

1. O. Schmelmer, G. Dollinger, G. Datzmann, C. Goeden, H.-J. Körner, Nucl. Instr. and Meth. B 158/1-4 (1999) 107.
2. A. Hauptner, S. Dietzel, G. A. Drexler, P. Reichart, R. Krücken, T. Cremer, A. A. Friedl and G. Dollinger; Radiat Environ Biophys 42 (2004) 237-245.
3. G. Dollinger, V. Hable, A. Hauptner, R. Krücken, P. Reichart, A.A. Friedl, G. Drexler, T. Cremer, S. Dietzel; Nucl. Instr. and Meth. B 231 (2005) 195-201.
4. V. Hable, G. Dollinger, C. Greubel, A. Hauptner, R. Krücken, S. Dietzel, T. Cremer, G.A. Drexler, A.A. Friedl and R. Löwe; Nucl. Instr. and Meth. B 245 (2006) 298-301.
5. A. Hauptner, R. Krücken, C. Greubel, V. Hable, G. Dollinger, G. A. Drexler, M. Deutsch, R. Löwe, A. A. Friedl, S. Dietzel, H. Strickfaden, T. Cremer; Radiation Protection Dosimetry 122 (2006) 147.

HEAVY IONS VS. LASER MICROIRRADIATION – TWO SYSTEMS TO INDUCE LOCALIZED DNA LESIONS IN LIVING CELLS

J. Splinter[1,*], B. Jakob[1] and G. Taucher-Scholz[1]

[1]Gesellschaft fuer Schwerionenforschung, Department of Biophysics, Planckstraße 1, 64291 Darmstadt, Germany

Ion beams offer the advantage to generate strictly localized DNA lesions in cell nuclei, thus facilitating the analysis of spatiotemporal dynamics of DNA damage response processes following ionizing irradiation. Immediately after the ion impact, a fast accumulation of early repair-related proteins can be observed by our newly developed beamline microscope. In addition to our beamline microscope, we established a Laser Microdissection system for localized generation of DSBs after the method of Limoli and Ward (1993) to look for differences in the recruitment and spatiotemporal behaviour of repair related proteins due to differences in the radiation quality. Here, we compared UV laser and HI irradiation induced DNA damages on two distinct levels. Using immunocytochemical staining methods we visualized the DSB marker γH2AX and compared the spreading of the γH2AX signals induced by both irradiation types, respectively. Furthermore, by additionally staining of single-strand breaks (SSBs), cyclobutan pyrimidine dimers (CPDs) or (6-4) photoproducts, respectively, the damage spectra of both irradiation systems could be characterized. According to our data the comparison of the UV laser and HI as alternative methods to produce strictly localized DNA damage revealed differences in the observed damage spectra. A resulting influence on e.g. the kinetics of repair proteins will be a topic of further investigation.

In the research context of DNA repair heavy ions (HI) are used as a tool to induce strictly localized DNA lesions. Due to the characteristic dose distribution of HI, the regions of DNA damage show a radial symmetry and are restricted to a few cubic micrometers (1). In terms of cellular dimensions this allows to distinguish between regions of damaged and undamaged DNA within a single cell nucleus. Research groups using HI for DNA damage induction take advantage of this attribute to investigate the spatio-temporal behavior of the DNA repair machinery.

In recent years more and more publications can be found in which UV laser microirradiation (UVLM) is used to generate regions of DNA damage similar in their sharp localization to ionizing radiation induced foci (IRIF) (2,3). Furthermore, due to the laser-microscope-hybrid assembling, laser microirradiation systems offer the possibility of high irradiation precision and allow the observation of the recruitment of early repair proteins (4). These advantages combined with the low costs compared to HI experiments make laser microirradiation systems a tempting choice in the research field of DNA repair.

In this work we will compare heavy ions and a nitrogen laser system (337nm) as DNA damaging systems by characterizing the types of induced damages and their spatial distribution. Therefore we visualized the regions of DNA damage by immunocytochemical staining of γH2AX, the phosphorylated form of the histone variant H2AX. The histone γH2AX is a well established marker for DNA double-strand breaks (2). The comparison between γH2AX signals induced by UVLM and HI irradiation has been carried out on the level of the width, the intensity and the structure of the induced γH2AX signal.

An immunocytochemical staining method was also used to visualize different types of classical UV damages as cyclobutane pyrimidine dimers (CPD) and pyrimidine (6-4) pyrimidone photoproducts (6-4 PP) whereas oxidative base damages like 8-oxo-7,8-dihydro-2'-deoxyguanosine (8-oxodGuo) were detected by observing one of the proteins responsible for their repair. The human 8-oxoguanine DNA glycosylase-1 (hOGG1) is sensitive to oxidative damages, especially 8-oxodGuo, and initiates the base excision repair (BER) pathway (5). In a live cell experiment we monitored the response of GFP tagged hOGG1 in transiently transfected osteo sarcoma cells (U2OS) to UVLM and HI irradiation.

---

*Corresponding author: J.Splinter@gsi.de

MATERIALS AND METHODS

Cell culture

Confluent normal human foreskin fibroblasts (AG1522D, Coriell Cell Respository, Camden, NJ; passage 13 to 16) and osteo sarcoma cells (U2OS) were used for experiments. The fibroblast cells were grown on coverslips (24 x 24 mm² and 30 mm in diameter, respectively) at 37°C, 100% humidity and 95% air/5% CO_2 in EMEM (Biochrom AG, Berlin, Germany) containing 1% glutamine, 1% penicillin/streptomycin and 15% fetal calf serum. The osteosarcoma cells were grown on coverslips (40 mm in diameter) under the same incubation conditions but in DMEM (Cambrex, East Rutherford, NJ) containing 4,5 g/l glucose Na-pyruvat, 1% penicillin/streptomycin and 10% fetal calf serum. Cells were checked regularly and were found to be free of mycoplasma contamination.

In some UVLM experiments fibroblast cells were UV sensitized by incubation (48h) with 1µM BrdU.

hOGG1-GFP transfection

The hOGG1-GFP containing plasmid was kindly provided by K. O. Greulich. For transfection one million osteo sarcoma cells (U2OS) were resuspended in corresponding nucleofector solution. Cells and 4 µg of plasmid DNA were mixed in the Amaxa cuvette und directly placed DM the nucleofector device (Amaxa AG, Cologne, Germany). Cells were treated with program X-01. Cell suspension was removed immediately from the cuvette by adding prewarmed medium with the Amaxa pipette and added on the previously described coverslips for further incubation.

Cell irradiation

Heavy ion irradiation

Irradiation was performed under low angle conditions as previously described (1). The experimental procedure of online microscopy is described in detail by Jakob et al. (6).

UV laser irradiation

Immediately before irradiation cell samples were loaded in a Focht chamber (FCS2, Bioptechs, Butler, PA) and mounted in the UV laser system (Leica AS LMD Microdissection System; Leica, Wetzlar, Germany). Per sample 25 to 40 cells were irradiated with different amounts of irradiation energy (0,2 – 10µJ per cell).

UVC irradiation

Normal human fibroblast cells were irradiated under a Reprostar II (Camag, Muttenz, Switzerland) with UVC settings and an irradiance of 10 W/m². The irradiation took ten seconds and was partially shielded by a polycarbonate micropore filter.

Cell fixation and immunocytochemical staining

If not recorded under live cell conditions cells were fixed 1h after irradiation with 2% paraformaldehyde as described previously (7). Anti-phospho-H2AX primary antibody (mouse monoclonal IgG; Upstate Technology, Hamburg, Germany) was used in a dilution of 1:400 in 0,2% BSA in PBS and counterststaining of the DNA was performed with 1µM ToPro3 (Molecular Probes, Leiden, Netherlands). Anti-CPD and anti-6-4-photoproduct primary antibodies (MBL International, Woburn, MA) were used in a dilution of 1:3000 and 1:400, respectively, after denaturation of DNA in 2M HCl. Staining of the cells with secondary antibodies is described previously (1).

Microscopy

Microscopic analysis was done on a Leica TCS confocal system equipped with a DM IRBE inverted microscope (lens: HCX PlanApo 63x/1.32) and an argon-krypton laser. Images were taken as

previously described (1). In the case of UV laser irradiation the irradiated cells were relocalized by using reference marks and a coordinate transformation procedure.

Computational analysis of γH2AX signals

In cooperation with the University of Applied Science Darmstadt, a computer algorithm was developed in IDL to analyze confocal image stacks of irradiated cell nuclei showing streak shaped damage signals (1).

RESULTS

Comparison between HI and UV laser induced γH2AX signals

For a better resolution of the ion traversal and the resulting γH2AX signal HI irradiation was performed under a low irradiation angle as previously described (1). Thus we obtain streak shaped signals which increases the number of parameters the comparative analysis is based on. The parameters can be divided into two groups; the first describing the rough structure of the induced γH2AX signals, the latter give information about the fine structure. In figure 1 the parameter of «inter cluster range» and of «foci area» as members of the rough structure and fine structure parameters, respectively, are shown as representative examples for different repair time points and different irradiation types. The optical impression of similar looking γH2AX signals independent of the used DNA damaging system is verified by the corresponding values in the rough structure analysis (fig. 1, top). The distance between damage clusters are similar comparing Carbon ion irradiation with low laser energies (below 50nJ per pulse) and Uranium ion irradiation with higher laser energies (50 – 150nJ per pulse) combined with the usage of BrdU as a DNA sensitizing reagent. A closer look on the induced damages shows the fine structure of the γH2AX signal – here the foci area – and thereby reveals discrepancies between both irradiation types (fig. 1, bottom). The most probable explanation for the shown variations in the area of induced γH2AX foci are the differences in the irradiation geometry. While a single ion forms a

Figure 1. Results of the computational streak analysis. The rough structure parameter « inter cluster range » and the fine structure parameter « foci area » are shown for different repair time points in the case of HI irradiation (Carbon: 256 keV/μm; Uranium: 14.350 keV/μm) and for different laser energies (A: below 50 nJ/pulse; B: 50 – 150 nJ/pulse) in the case of UVLM (after one hour of repair). Additionally, UVLM was performed with and without the DNA sensitizing effect of BrdU.
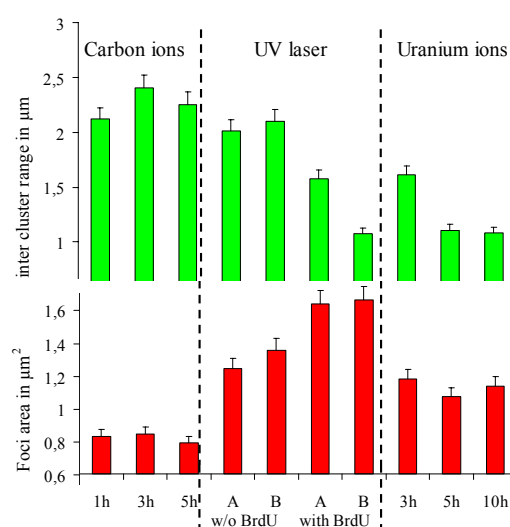
streak shaped region of damage, several laser pulses are needed to irradiate the same area due to the perpendicular irradiation geometry of the laser microirradiation system (fig. 2). This leads to radial symmetrical damage structures in the case of HI irradiation and to wall shaped damage regions after

laser microirradiation (fig. 2A). Thus, in projections of the image stacks of the irradiated cell nuclei the fine structure of the induced γH2AX signals seems less distinct due to the wider spreading of the γH2AX in the z-direction. This result indicates that a comparison between HI and UVLM on a structural level is difficult to perform as long as the problem of different irradiation geometries isn't solved.
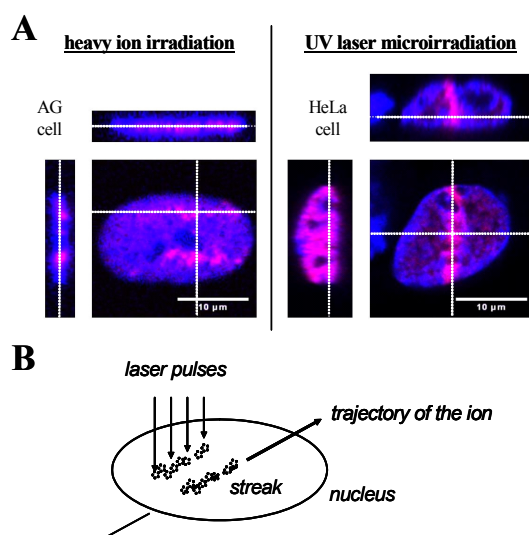
Figure 2. (A) Induced γH2AX signals (red) in irradiated nuclei. The distance between the slices is 365nm. After heavy ion irradiation ionization events induce DNA double-strand breaks in a radial symmetrical shape (AG-1522-D cell, left). In contrast the large-volume region of UV laser induced DNA damages is shown in a cervix carcinoma cell (HeLa, right). The DNA was stained with ToPro3 (blue). (B) A schematic representation of both irradiation geometries: an ion traversal and an alignment of adjacent laser pulses.

Comparison between the different types of HI and UV laser induced damages

A further attempt for a quantitative comparison of HI irradiation and UVLM is based on the detection of different types of DNA damages. Therefore, we investigated the induction of UV damages (CPDs and 6-4 photoproducts) by immunocytochemical staining methods and compare their amount after different types of irradiation. 6-4 photoproducts can only be seen in UVC micropore irradiated samples but neither in heavy ion irradiated samples nor in UV laser irradiated nuclei (fig. 3A). Comparable data for CPDs are not shown. Thus, no difference could be found between heavy ion irradiation and UVLM on the level of CPD and 6-4 photoproduct induction.

The last type of the three major UV damages is the oxidized base damage, especially the 8-oxodGuo, which is reported to be dominantly induced after irradiation with UVA wavelengths. To get additional information about the fast kinetics of repair proteins related to these type of damage we used a live cell imaging approach. This allowed us to monitor the damage response of transiently transfected osteo sarcoma cells (U2OS) with hOGG1-GFP fusion protein which is sensitive to 8-oxodGuo and initiates the BER pathway. A early and fast recruitment of hOGG1-GFP could be observed to sites of UVLM (fig. 3B). In contrast, an irradiation with Uranium ions did not induce the recruitment of hOGG1-GFP.

CONCLUSION

Usage of computational streak analysis made it possible to identify differences in the fine structure of heavy ion and UV laser irradiation induced γH2AX signals (fig. 1A). Looking at the different

irradiation geometries used to induce streak shaped regions of DNA damage (fig. 2) a possible explanation of the

Figure 3. (A) Induced 6-4 PP signals (green) in human fibroblast nuclei after different types of irradiation. The weak signals of the counterstaining (blue: ToPro3; red: 53bP1, γH2AX and XRCC1, respectively) are due to the denaturation of DNA in the course of the 6-4 PP staining protocol. (B) Recruitment of hOGG1-GFP to sites of UVLM. The transiently transfected U2OS cells are shown immediately before irradiation (0 sec), during the irradiation (9 sec) and 28 seconds after the first laser pulse.
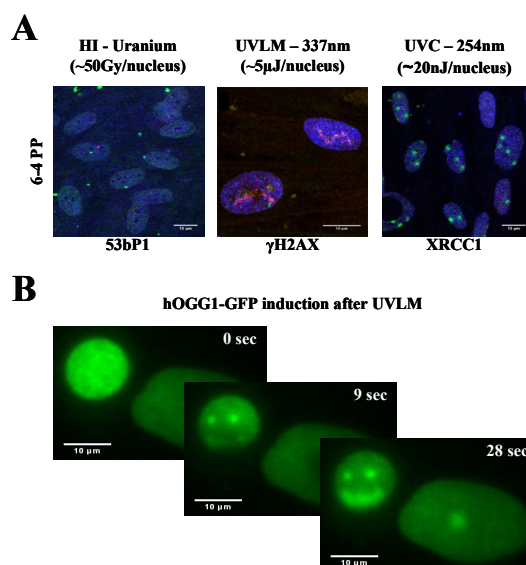
observed discrepancies is found. The impact of this result on approaches of a laser dosimetry based on the structural comparison with sparsely ionizing radiation (8) has to be a topic of further investigation.

The structural approach to compare HI and UV laser irradiation was motivated by the question whether UVLM is as localized as HI irradiation and does it induce a comparable amount of DSBs? Though both questions have to be answered with yes, the structural approach failed as a tool for a quantitative comparison of both irradiation types. Hence, we continue the comparison and characterize the different types of damages induced by UVLM or HI irradiation, respectively. Starting with classical UV damages like CPDs, 6-4 PPs and 8-oxodGuos, we've chosen the types of damage differences are most probable to be found. An induction of CPDs and 6-4 PPs could not be observed after UVLM, thus indicating that the amount of these damages isn't high enough to be detected by fluorescent microscopy (fig. 3A). While the high photon fluxes of the UVLM are able to produce highly increased amounts of DSBs compared to the classical UVA bulb irradiation, that phenomenon can't be observed in the case of CPDs and 6-4 PPs.

The induction of 8-oxodGuo was observed indirectly under live cell imaging conditions. Therefore, the 8-oxodGuo sensitive glycosylase hOGG1 was used as a marker for BER which is the repair pathway responsible for the repair of 8-oxodGuo. The fast recruitment of the GFP tagged hOGG1 fusion proteins could be monitored to sites of UVA laser microirradiation (fig. 3B) suggesting a high BER activity at these sites.

In comparison, after HI irradiation neither CPDs or 6-4 photoproducts nor the recruitment of hOGG1-GFP could be observed in the irradiated cell nuclei. According to these observations the distribution of the involved repair pathways after UVLM and HI irradiation shows differences in the observed BER activity. The most probable explanation for the existing BER activity after UVLM is the increased amount of oxidative base damages which seems to be missing after HI irradiation. Whether the simultaneously working repair mechanisms have an influence on each other can't be excluded, but the very fast and transient recruitment of hOGG1-GFP to regions of UVLM suggests a very weak influence.

REFERENCES

1. B. Jakob, M. Scholz and G. Taucher-Scholz, Biological imaging of heavy charged-particle tracks. Radiat. Res. 159, 676-684 (2003).
2. Rogakou, E.P., C. Boon, C. Redon, and W.M. Bonner, Megabase chromatin domains involved in DNA double-strand breaks in vivo. J. Cell Biol. 146, 905–916 (1999).
3. Tashiro, S., J. Walter, A. Shinohara, N. Kamada, and T. Cremer, Rad51 accumulation at sites of DNA damage and in postreplicative chromatin. J. Cell Biol. 150, 283–291 (2000).
4. C. Lukas, F. Melander, M. Stucki, J. Falck, S. Bekker-Jensen, M. Goldberg, Y. Lerenthal, S.P. Jackson, J. Bartek, and J. Lukas, Mdc1 couples DNA double-strand break recognition by Nbs1 with its H2AX-dependent chromatin retention. EMBO J. 23, 2674–2683 (2004).
5. K. J. Kim, I. Chakrabarty, G.-Z. Li, S. Grösch, B. Kaina and T. M. Rünger, Modulation of base excision repair alters cellular sensitivity to UVA1 but not to UVB. Photochem. Photobiol. 75, 507-512 (2002).
6. B. Jakob, J. H. Rudolph, N. Gueven, M. F. Lavin and G. Taucher-Scholz, Live cell imaging of heavy-ion-induced radiation responses by beamline microscopy. Radiat. Res. 163, 681-690 (2005).
7. B. Jakob, M. Scholz and G. Taucher-Scholz, Characterization of CDKN1A (p21) binding to sites of heavy ion induced damage: colocalization with proteins involved in DNA repair. Int. J. Radiat. Biol. 78, 75-88 (2002).
8. S. Bekker-Jensen, C. Lukas, R. Kitagawa, F. Melander, M. B. Kastan, J. Bartek and J. Lukas, Spatial organization of the mammalian genome surveillance machinery in response to DNA strand breaks. J. Cell Biol. 173, 195-206 (2006).

MEASUREMENTS OF DNA-DOUBLE STRAND BREAKS AFTER TUMOUR THERAPY-RELATED CARBON IRRADIATION AND COMPARISON WITH ΓH2AX ANALYSIS AFTER INDUCTION OF HIGHLY COMPLEX DNA- LESIONS

Yvonne E. Schweinfurth, Jana Topsch, Philippe Barberet, Burkhard Jakob, and Gisela Taucher-Scholz
Gesellschaft fuer Schwerionenforschung, Biophysics, Darmstadt, Germany

Radiotherapy with carbon beams is characterised by an inverse dose profile, extreme precision of irradiation and enhanced relative biological effectiveness (RBE) in the tumour. The increased RBE is assumed to be due to the clustered DNA double strand breaks (DSBs).

To study DSBs under conditions mimicking therapeutical ion irradiation, cells were exposed to high energy carbon ions in a water phantom. Human fibroblasts (AG 1522), hamster cells (CHO-K1) or prostate tumour cells (R-AT1) were placed in the entrance channel (healthy tissue) and in the extended Bragg-Peak (tumour) region. The γH2AX signals were analysed semi-automatically from confocal images. This foci counting was complemented by flow cytometry to account for overlapping foci and multiple DSBs produced along the ion tracks. Both methods indicate a dose-dependent induction of DSBs in the Bragg peak as well as in the entrance channel shortly after irradiation of AG and CHO cells. A clear reduction of γH2AX (both foci and mean fluorescence) was observed with time, reflecting an efficient repair even of ion-induced DSBs. However, the level of residual DSBs was slightly but consistently increased after exposure to Bragg peak ions. Prostate cancer cells showed no differences between the entrance channel and Bragg peak region in the amount of γH2AX foci but clearly in the induction of micronuclei in Bragg peak.

Additionally, we used carbon and lead ions to observe γH2AX during processing of complex DNA-lesions. Irradiation with ions under standard and microbeam conditions induced distinct γH2AX foci. For the later time points (> 1 h) after irradiation we observed splitting of the primary γH2AX foci in sub-compartments or small foci. The generated secondary foci were localized in different layers of the nucleus. The secondary foci disappeared after carbon irradiation or persisted for several days (for very heavy lead ions). Colocalization with 53BP1, Mre11, PML and p53 was analysed. The dispersion and splitting of ion induced foci was also detected in live cell imaging experiments with U2OS 53BP1-GFP cells. Furthermore, the localisation of the residual γH2AX signals within the nuclear chromatin structure in HeLa-H2B GFP cells was strongly influenced by chromatin structure.

The data obtained contribute to a better understanding of the spatial "reorganisation" of nuclear lesion processing after induction of DSBs.

GENOTOXICITY OF HEAVY IONS IN RECOMBINANT BACTERIA

C. Baumstark-Khan[1], C. E. Hellweg[1], I. Testard[2] and G. Reitz[1]

[1] Division of Radiation Biology, Institute of Aerospace Medicine, German Aerospace Center (DLR), Linder Hoehe, D-51147 Koeln, Germany

[2]LARIA, Grande Accelerateur National des Iones Lourdes (GANIL), Boulevard Henri Bequerelle BP 55027, F- 14076 Caen, France

The mutagenic potential of the heavy ion component of the galactic cosmic radiation of space environment is of major concern for astronauts in terms of tumor induction as radiation late effects. The recombinant SWITCH test is based on TA1535 Salmonella typhimurium cells transformed with a bi-cistronic vector harbouring (a) the genes for bioluminescence production from Photobacterium leiognathi under the control of a DNA-damage inducible promoter and (b) the gene for green fluorescent protein from the jellyfish Aequorea victoria under the control of a constitutive promoter. Suchlike genetically modified organism report on the presence of genotoxic conditions by dose dependent increase of bioluminescence induction and on the presence of cytotoxic conditions by dose dependent decrease in GFP fluorescence. By this, it is possible to analyse bacterial inactivation and mutation induction by ionizing radiation in parallel in the same cell within short time. Experiments with heavy ions have been performed with the SWITCH test at GANIL with 75 MeV/A carbon, 95 MeV/A argon, and 29 MeV/A lead. The results obtained clearly show that the numbers of hits (particles per cm^2) necessary to inactivate the bacteria (cytotoxicity) depend on LET. The higher the ionisation capacity of the accelerated ion, the less hits resulted in the same test effect, e.g. 37 % survival. For genotoxicity induction it can be seen, that for very high LET radiation the number of hits required is much less then for lower LET radiation (e.g. 1.4×10^6/cm^2 hits for lead versus 1.3×10^7/cm^2 hits for carbon). The power of the genotoxic response seems to be inversely related to LET. While carbon radiation results in a maximal induction of 72.6x, argon radiation leads to a 29.4x value and lead results in only a factor of 4.8. From the experiments with 3 different ions cross sections σ were calculated. Inactivation cross sections (σ_{RCP}) rise over the whole LET range under investigation. The same is true for genotoxicity cross sections (σ_{RGP}). Cross sections for maximal luminescence emission (σ_{RGP} for peak response) differ by a factor of about 10 from cross sections for inactivation; cross sections for doubling the response from untreated cells (σ_{RGP} for 2x) are about 3 orders of magnitude higher.

INTRODUCTION

Along with the long-term space exploration come various potential health risks due to unique physical factors of the space environment. Space radiation is one of the primary environmental hazards associated with space flight. For radiation protection purpose of astronauts, the biological response to the complex radiation field in Space has to be known. In order to deal with space-related risk radiation exposure must be properly characterized and quantified, and biological effects of charged particles have to be analyzed in ground based research, especially as astronauts are subjected to a differing radiation quality in space than they receive on Earth. For risk assessment, the mutagenic potential of the heavy ion component of the galactic cosmic radiation is of major concern for tumor induction as radiation late effects.

Heavy ion accelerators are valuable tools for simulating single components of the Space radiation and for performing ground based research in Space radiation biology. Accelerated heavy ions represent an important tool to study the dependence of biological radiation action on the radiation quality.

Adverse biological effects induced by densely ionizing radiation on eukaryotic cells include cell killing, cell cycle perturbations, genetic instability, cell transformations and mutations. In mammalian cell systems, survival and the induction of HPRT mutations have been studied by various authors. Such mammalian tests are costly and labor-intensive. Bacterial tests are suitable to uncover overall

---

mechanistic reactions. They are relative cheap and results can be obtained in short times. The SWITCH test (SWITCH: Salmonella Weighting of Induced Toxicity (Genotoxicity) and Cytotoxicity for Human Health), developed by the Cellular Biodiagnostic group at the German Aerospace Centre (DLR), is such a bacterial short-term assay for parallel determination of genotoxicity and cytotoxicity [1]. Genotoxicity is measured by SOS-dependent induction of bioluminescence [2] and cytotoxicity by dose-dependent reduction in constitutive expressed GFP-fluorescence [3].

The SWITCH test has shown its validity for a series of scientific questions and environmental applications. It has been used so far for determination of the genotoxic potency of more than 100 chemical agents and a series of environmental applications. The SWITCH test has been shown to be sensitive towards the effects of ultraviolet radiation (UVA, UVB and UVC) and to ionizing radiation (150 kV X-rays) as well. The test will also be performed as one of the first German experiments to be performed on the International Space Station ISS [4].

MATERIAL AND METHODS

Plasmid, bacterial strain and growth conditions

The construction of the plasmid pSWITCH carrying (i) the luxCDABFE genes downstream a strong SOS-dependent promoter and (ii) the optimized "cycle 3" variant of GFP in frame with the lacZ initiation codon was described elsewhere. The strain Salmonella choleraesuis subsp. choleraesuis TA1535, one of the tester strains in the most often used bacterial test for mutagenicity, the Ames test, was transformed with the plasmid pSWITCH. Transformed bacteria (TA1535-pSWITCH) were selected and cultivated at 37 °C in LB-medium supplemented with 50 μg ml^{-1} ampicillin.

Irradiation procedures

Log phase cultures of strain TA1535-p*SWITCH* were incubated in pre-warmed double concentrated LB-medium containing 100 μg ml^{-1} ampicillin until absorption at 600 nm (A_{600}) reached 0.2 ($\sim 2 \times 10^8$ CFU ml^{-1}). 500 μl of such exponentially growing cells were transferred into suitable vessels and exposed to either X-rays (Müller Typ MG 150, Germany, 50 kV, 16 mA, 5 Gy min^{-1} dose rate) or heavy ions of various LETs (carbon, 75 MeV/A, 37 keV μm^{-1}; argon, 95 MeV/A, 377 keV μm^{-1}; lead, 29 MeV/A, 10238 keV μm^{-1}) at the French heavy ion accelerator GANIL, (Caen, France). Bacteria were exposed to high LET heavy ion particles at room temperature with dose rates adjusted to achieve irradiation within 2 minutes. Dosimetry was performed by the GANIL dosimetry group.

Testing of genotoxicity and cytotoxicity with the SWITCH-Test

75 μl of irradiated recombinant bacterial culture were added per well of a white microplate with a transparent bottom (LB96P-CMP Mikro Lumat Plates, PerkinElmer Life Sciences) already containing 75 μl water. The plate was immediately placed into the microplate reader (Multilabel Counter 1420 Victor^2 form PerkinElmer Life Sciences, Waltham, MA, USA) with a controlled temperature of the plate of 30 °C. The reader was programmed to repeat the measurement cycle of 2 min orbital shaking, luminescence reading without filter for 0.2 s/well, followed by absorbance measurement for 0.1 s/well at 490 nm (20 nm band width) and by fluorescence reading for 0.1 s/well at 510 nm after excitation at 405 nm, every 10 min for 50 cycles resulting in eight hours of measurements.

Numerical analysis

For each well, luminescence output, optical density and fluorescence output was measured for 50 time points. For each irradiated sample 6 replicate measurements and 2 background measurements were done. These raw data were transferred into an Excel macro sheet; here a time-resolved background-correction for each measurement well was performed. To determine dose-effect relationships the following calculations were done:

Relative luminescence Lux$_{rel}$ was calculated for the genotoxic potential of the applied samples according to equation 1 with background-corrected light emission data for peak luminescence outputs of the untreated culture (Lux$_0$), and of the culture treated with the test samples (Lux$_i$).

$$Lux_{rel} = Lux_i / Lux_0 \qquad\qquad (1)$$

For determination of cytotoxicity relative absorbance Abs_{rel} was calculated according to equation 2 with background-corrected absorbance data for absorbance measured after 6 hours of incubation of the untreated culture (Abs_0) and of the cultures treated with the samples (Abs_r). An analogous calculation (equation 3) was performed to compute relative fluorescence (Flu_{rel}) with background-corrected fluorescence data for fluorescence yields measured after 6 hours of incubation of the untreated culture (Flu_0) and of the cultures treated with the samples (Flu_r).

$$Abs_{rel} = Abs_r / Abs_0 \qquad\qquad (2)$$

$$Flu_{rel} = Flu_r / Flu_0 \qquad\qquad (3)$$

The statistical analyses of the data from each of these parameters were carried out according to standard protocols. Means and standard errors were derived from at least three experimental plates, each replicate having 6 parallel samples of each of the dose groups. Means and standard errors were determined for each dose for the different exposure schedules. Lux_{rel}, Abs_{rel} and Flu_{rel} values were plotted as a function of dose or fluence. Analysis of variance and t-statistics were used to determine significance ($2p < 0.05$) of these data.

The factor of SOS induction F_i was calculated according to equation 4 from relative light emission data (Lux_{rel}) and relative cell growth (Abs_{rel}). This was done in order to correct for cell concentration effects due to impairment in total light emission of the culture by substance related associated cytotoxicity.

$$F_i = Lux_{rel} / Flu_{rel} \qquad\qquad (4)$$

The threshold for a sample to be genotoxic was defined as a twofold increase of the luminescence induction factor F_i, whereas a relative fluorescence of less than 0.5 is determined to be a signal for cytotoxicity in this test.

RESULTS AND DISCUSSION

The recombinant SWITCH test is based on TA1535 Salmonella typhimurium cells transformed with a bi-cistronic vector harboring (a) the genes for bioluminescence production from Photobacterium leiognathi under the control of a DNA-damage inducible promoter and (b) the gene for green fluorescent protein from the jellyfish Aequorea victoria under the control of a constitutive promoter. Suchlike genetically modified organism report on the presence of genotoxic conditions by dose dependent increase of bioluminescence induction and on the presence of cytotoxic conditions by dose dependent decrease in GFP fluorescence. By this, it is possible to analyze bacterial inactivation and mutation induction by ionizing radiation in parallel in the same cell within short time.

Upon exposure to genotoxic agents or environmental conditions, the bacteria were cultivated for 8 hours in a multi-label counter with regular measurements of bioluminescence, optical density and fluorescence. From the kinetics of light output, optical density and fluorescence, Relative Genotoxic Potential (RGP) and Relative Cytotoxic Potential (RCP) of the treatment conditions can be determined (see Fig. 1). RCP can be described in terms of the dose necessary to inactivate 37 percent of the bacterial cells (D_0); RGP can be given either as the dose required to double (2x level, dotted line) the ground level of luminescence from untreated cells (1x level, dashed line) or to determine the dose achieving maximal light output (peak dose) and the power of genotoxicity measured as luminescence value for the peak dose (Lux_{max}).

Experiments with heavy ions have been performed with the SWITCH test at GANIL during the beam time period 2006 (P708) with 75 MeV/A carbon, 95 MeV/A argon, and 29 MeV/A lead. The results are shown in Fig. 2. The results obtained clearly show that the numbers of hits (particles per cm^2) necessary to inactivate the bacteria (cytotoxicity) depend on LET. The higher the ionization capacity of the accelerated ion, the less hits resulted in the same test effect, e.g. 37 % survival. This could be verified for measurements of relative absorbance (optical density at 490 nm) as well as for measurements of relative fluorescence (GFP yields). For genotoxicity, it can be seen, that for very high LET radiation, the number of hits required to double the luminescence output of non-treated cells is much less then for lower LET radiation (e.g. 1.4×10^6 cm^{-2} hits for lead versus 1.3×10^7 cm^{-2} hits for

carbon). The power of the genotoxic response (peak height) seems to be inversely related to LET. While carbon radiation results in a maximal light output of 72.6x, argon radiation leads to a 29.4x value and lead results in only a factor of 4.8.
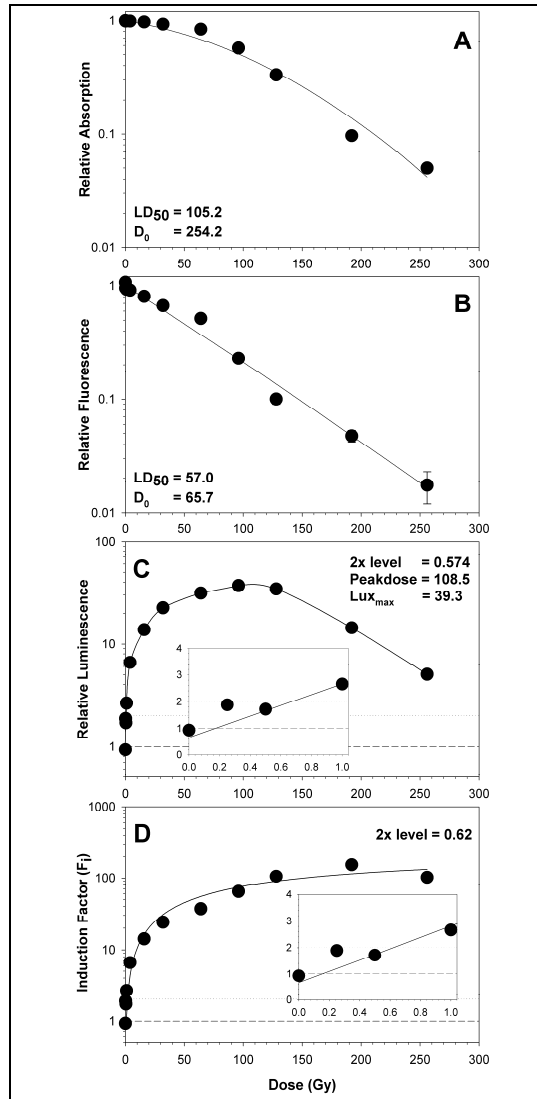
Figure 1. Responses of the SWITCH test system to 150 kV X-rays. Cytotoxicity is determined as the decrease of Relative absorbtion (A) or Relative fluorescence (B), genotoxicity is shown as Relative luminescence (C). The Induction factor (D) results from light output data (C) corrected for cell killing (A).

From the experiments with 3 different ions cross sections σ were calculated and plotted versus LET (Fig. 3). Inactivation cross sections (σ_{RCP}, calculated as $1/D_0$) rise over the whole LET range under investigation. The same is true for Genotoxicity cross sections (σ_{RGP}, calculated as $1/D_{2x}$ or as $1/D_{Peak}$). While cross sections for maximal luminescence emission (σ_{RGP} for peak luminescence) differ by a factor of about 10 from cross sections for inactivation, cross sections for doubling the luminescence emission from untreated cells (σ_{RGP} for 2x luminescence) are about 3 orders of magnitude higher.
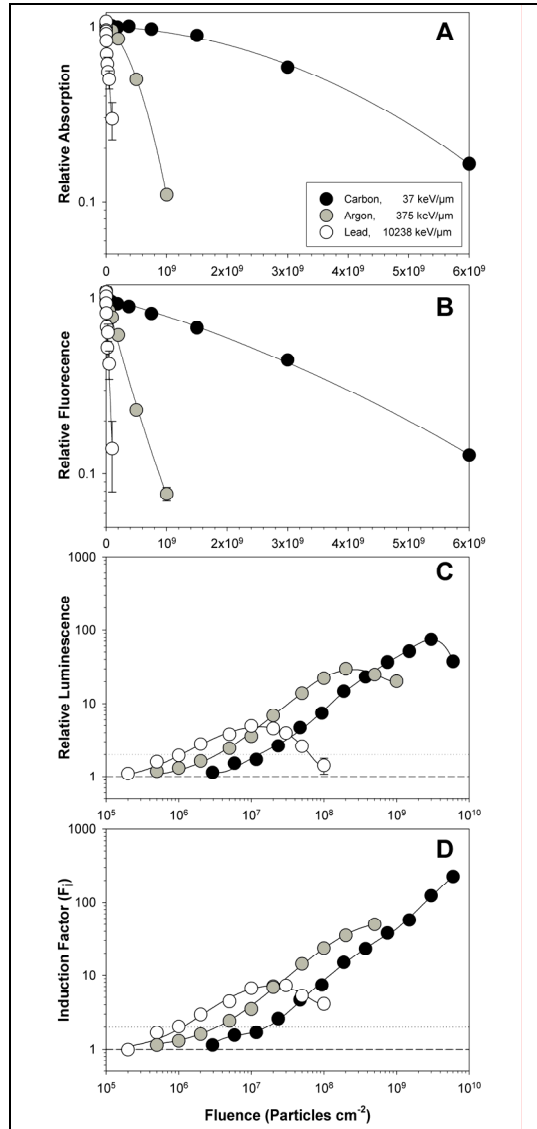
Figure 2. Responses of the SWITCH test system to accelerated heavy ion exposure. Cytotoxicity and genotoxicity are shown as described for Figure 1. Luminescence data and Induction factors are displayed on a double logarithmic scale in order to show the wide dynamic range of the test system.

From the experiments with 3 different ions cross sections σ were calculated and plotted versus LET (Fig. 3). Inactivation cross sections (σRCP, calculated as $1/D_0$) rise over the whole LET range under investigation. The same is true for Genotoxicity cross sections (σ_{RGP}, calculated as $1/D_{2x}$ or as $1/D_{Peak}$). While cross sections for maximal luminescence emission (σ_{RGP} for peak luminescence) differ by a factor of about 10 from cross sections for inactivation, cross sections for doubling the luminescence emission from untreated cells (σ_{RGP} for 2x luminescence) are about 3 orders of magnitude higher.

The main reason for the investigation was to understand the relationship between genotoxicity and cellular inactivation brought about by components of space radiation. Thereby, radiation risk considerations can gain profit from better knowledge on relative biological effectiveness and quality factors for densely ionizing radiation. Accordingly, more data are to be obtained for radiation types covering the spectrum of LET values important for the space environment.
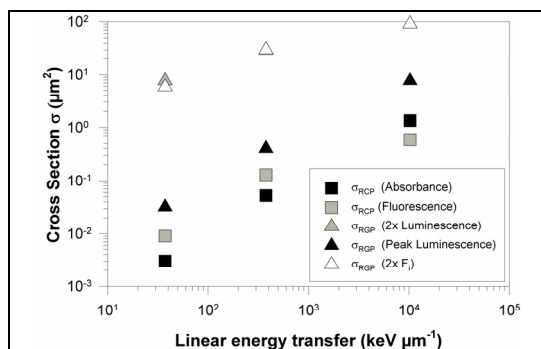
Figure 3. LET dependency of cross sections σ for Relative Genotoxic Potential (RGP) and Relative Cytotoxic Potential (RCP).

REFERENCES

1. Baumstark-Khan C, Cioara K, Rettberg P, and Horneck G. (2005) Determination of Geno- and Cyto-Toxicity of Groundwater and Sediments Using the Recombinant SWITCH-Test, Journal of Environmental Science and Health, Part A: &Toxic/Hazardous Substances & Environmental Engineering 40 245-263.
2. Ptitsyn, L. R.; Horneck, G.; Komova, O.; Kozubek, S.; Krasavin, E. A.; Bonev, M.; Rettberg, P. A biosensor for environmental genotoxin screening based on an SOS lux assay in recombinant Escherichia coli cells. Appl. Environ. Microbiol. 1997, 63, 4377-4384
3. Baumstark-Khan, C.; Rode, A.; Rettberg, P.; Horneck, G. Application of the Lux-Fluoro test as bioassay for combined genotoxicity and cytotoxicity measurements by means of recombinant Salmonella typhimurium TA1535 cells Anal. Chim. Acta. 2001, 437, 23-30.
4. Rabbow E, Stojicic N, Walrafen D, Baumstark-Khan C, Rettberg P, Schulze-Varnholt D, Franz M, and Reitz G. (2006) SOS-Lux toxicity test on the International Space Station. Research in Microbiology, 157: 30-36.

CYTOGENETIC DAMAGE INDUCED IN VIVO BY HIGH AND LOW LET RADIATION: FOLLOW-UP OF RADIOTHERAPY PATIENTS

S. Ritter[1,*], C. Hartel[1], E. Nasonova[1,2], S. Sommer[1], C. Fournier, [1] P. Hessel[1], J. Debus[3], and D. Schulz-Ertner[3]

[1]Gesellschaft für Schwerionenforschung, Biophysik, 64291 Darmstadt, Germany
[2]Joint Institute for Nuclear Research, 141980 Dubna, Russia
[3]Clinical Radiology, 69120 Heidelberg, Germany

To gain more insights into the *in vivo* formation of aberrations following high and low LET radiation, we currently perform a cytogenetic follow up of prostate cancer patients (intermediate risk). In 2006 a clinical phase I/II trial combing photon intensity-modulated radiotherapy (IMRT) and C-ion boost (6x3 GyE) has been started in Germany. In parallel to this clinical trial the yields and the types of radiation-induced chromosome aberrations are investigated in peripheral blood lymphocytes of patients.

INTRODUCTION

Since the start of C-ion therapy at GSI, Darmstadt, in December 1997 about 340 patients have been treated. Most patients had chordoma or low grade chondrosarcoma of the skull base. Based on the promising clinical results, namely high local control rates and mild side effects [1], the application has been recently extended to intermediate risk prostate cancer. A clinical phase I/II trial combining photon intensity-modulated radiotherapy (IMRT) and C-ion boost has been started in 2006. In parallel to this clinical trial the yields and the types of radiation-induced chromosome aberrations are investigated in peripheral blood lymphocytes of prostate cancer patients.

Aberrations are believed to be the most accurate and sensitive indicator of genetic damage and are commonly used for estimating absorbed dose and to assess possible health risks such as cancer induction ([2-3] and references therein). Furthermore, *in vitro* experiments as well as modelling studies suggest that specific alterations in the aberration spectrum might be used as fingerprints to determine whether the initial exposure was to high or low LET radiation. In particular, densely ionizing radiation has been found to be much more effective than sparsely ionizing radiation in inducing complex chromosomal rearrangements (e.g. [4] and references therein).

MATERIALS AND METHODS

For cytogenetic analysis blood samples (8 ml) are taken before, during and at the end of therapy (78 GyE) as well as 1 year after the treatment. Lymphocytes are isolated, cultivated *in vitro* for 48h and chromosome spreads are prepared according to standard techniques [5]. Cytogenetic damage is visualised in first generation metaphases by solid staining to identify unstable aberrations and by multiplex fluorescence in situ hybridisation (mFISH) to reveal chromosomal exchanges induced within the whole genome. Examples are shown in figure 1. Additionally, to gain information on differences in individual radiosensitivity, an aliquot of the pre-treatment blood sample is exposed *in vitro* to 3 Gy X-rays.

RESULTS

To date, 5 patients treated with IMRT and a C-ion boost (6x3 GyE) and one patient treated solely with IMRT entered the study. The data obtained so far by Giemsa-staining and mFISH reveal a low level of aberrations (0.01-0.02/cell) in lymphocytes before therapy. After *in vitro* exposure slight individual differences in the radiation response have been observed, but these differences are not significant. As expected, cytogenetic damage increases during the radiotherapy course (figure 2). One year after the treatment the aberration yield is still as high as at the end of the therapy (data not shown). Although complex aberrations are discussed as a fingerprint of high LET exposure, their numbers are low in patients treated with C-ion boost. When these results are compared to data generated for a patient

treated solely with IMRT, no significant differences are observed. Thus, despite applying high-resolution mFISH staining, the cytogenetic data obtained so far reflect only the effect of dose, but do not provide information on the applied radiation quality as observed in other *in vivo* studies (e.g. [6]).
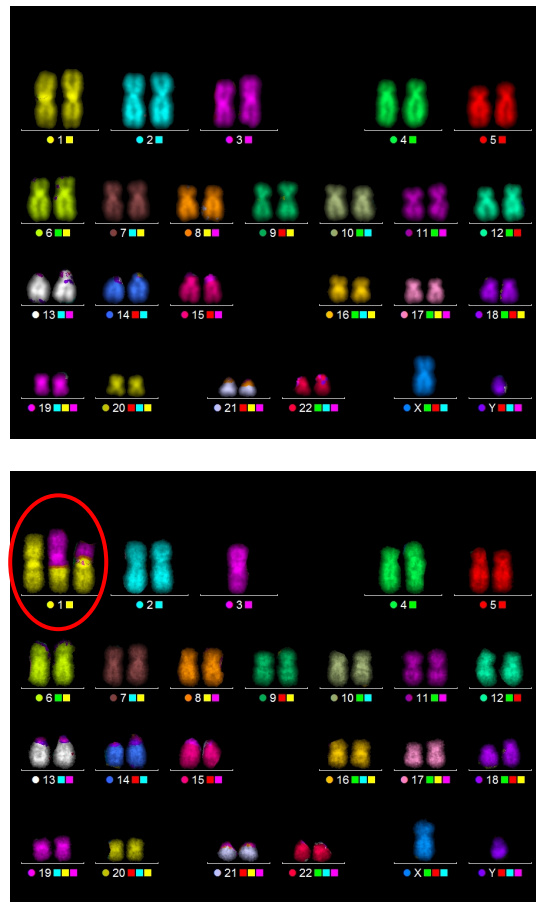
Figure 1. Examples for mFISH karyotypes from peripheral blood lymphocytes taken from prostate cancer patients. Upper panel: undamaged lymphocyte; lower panel: lymphocyte with a reciprocal translocation between chromosome 1 and 3 detected at the end of radiotherapy.
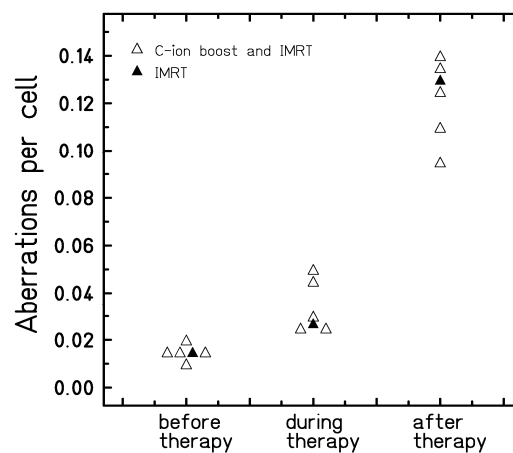
Figure 2. Yield of aberrations in lymphocytes of prostate cancer patients measured following solid staining. Cells were analysed before therapy, during therapy (i.e. after 6 fractions) and at the end of therapy.

REFERENCES

1. Schulz-Ertner D. et al. (2004) Int. J. Radiat. Oncol. Biol. Phys. 58, 631-640
2. IAEA (2001) Cytogenetic analysis for radiation dose assessment. Technical Report Series no. 405. Vienna.
3. Bonassi S. and Au W.W. (2002) Mutat Res. 511:73-86.
4. Anderson R.M. et al. (2003) Radiat. Res. 159, 40-48.
5. Nasonova E. and Ritter S. (2004) Cytogenet. Genome Res. 104, 216-220.
6. Durante M. et al. (2004) Cytogenet. Genome Res. 104, 240-244.

Physics and Dosimetry

THERAPY MONITORING WITH PET TECHNIQUES

J. Pawelke[1,*], T. Bortfeld[2], F. Fiedler[1], T. Kluge[1], D. Möckel[1], K. Parodi[3], F. Pönisch[1,4], G. Shakirin[1], W. Enghardt[1,4]

[1]Institute of Radiation Physics, Forschungszentrum Dresden-Rossendorf, PO Box 510119, 01314 Dresden, Germany

[2]Department of Radiation Oncology, Massachusetts General Hospital, 30 Fruit Street, Boston, Massachusetts 02114, USA

[3]Heidelberg Ion Therapy – HIT, Im Neuenheimer Feld 400, 69120 Heidelberg, Germany

[4]Radiation Research in Oncology – OncoRay, University Hospital and Medical Faculty C.G. Carus, Technische Universität Dresden, Fetscherstraße 74, PO Box 86, 01307 Dresden, Germany

Abstract: The technique of positron emission tomography is the only known method to monitor the dose delivery precision of ion beam radiotherapy three-dimensionally, in-vivo and non-invasively. The different approaches of PET therapy monitoring and their clinical impact are described. In addition, the feasibility of extending the method of in-beam PET for hard photon beams is discussed.

A INTRODUCTION

The favourable physical and radiobiological properties of light ion beams (e.g. carbon) offer improved conformality for the delivery of the dose to the tumour and better sparing of surrounding healthy tissues than conventional electron and photon radiation therapy. However, to exploit this advantage, in particular for very delicate therapeutic cases as e.g. the treatment of compact, deep-seated, radioresistant tumours growing in close vicinity to organs at risk, in-vivo confirmation of the actual dose delivery would be highly desirable. Positron emission tomography (PET) is the only known technique which provides an opportunity for monitoring the treatment delivery three-dimensionally and non-invasively.

B PET BASED MONITORING APPROACHES

The basis of PET therapy monitoring is the detection of the annihilation γ-rays following the decay of positron (β^+) emitting nuclei by a positron camera. Several approaches are feasible which may differ in (i) the way of inducing β^+-activity in the patient, (ii) the method of detecting this activity and (iii) the modes of applying PET monitoring to quality assurance in ion therapy [1].

B.1 Induction of β^+-activity

Beams of β^+-active ions (e.g. ^{11}C) can be used to measure the ion range in the patient, as pioneered at the Lawrence Berkeley Laboratory [2] and investigated also at the Heavy Ion Medical Accelerator in Chiba (HIMAC) [3] as well as at the Forschungszentrum Dresden-Rossendorf and the Gesellschaft für Schwerionenforschung (GSI) in Darmstadt [4]. A pronounced activity maximum at the position corresponding to the ion range is obtained by injecting a β^+-active beam [4]. However, the production and shielding of β^+-active beams result in greater expense and, therefore, beams of stable ions (e.g. ^{12}C) are preferred for radiotherapy. The incoming stable ions undergo nuclear fragmentation reactions by interaction with the atomic nuclei of the irradiated tissue leading to a minor amount of β^+-emitting nuclei (autoactivation). This irradiation-induced activity distribution is correlated to the therapeutically relevant dose distribution, but not directly matching it due to different physical processes underlying positron emitter production and energy deposition (Fig. 1). Therefore, therapy monitoring has to be performed by comparing the measured β^+-activity distribution with an expected pattern which is calculated on the basis of the treatment plan, the patient anatomy and the time course of irradiation and

---

*Corresponding author: J.Pawelke@fzd.de

imaging [5].

B.2 Detection of β⁺-activity

There are two ways for routine three-dimensionally imaging the β^+-activity distribution. In-beam (i.e. during the irradiation) PET allows in-situ therapy monitoring but requires the integration of the tomograph into the treatment site. In order to avoid interferences with the beam and restrictions to the patient positioning, dedicated solutions for detector geometry [6], e.g. a double-head positron camera (Fig. 2), and, consequentially, data processing methods are necessary.

In contrast, off-line (i.e. after the irradiation) PET allows for the direct use of commercial ring tomographs as widely used for PET tracer imaging. However, the applicability and usefulness of off-line PET monitoring is limited to the detection of long-lived isotopes. Furthermore, the moving of the patient from the treatment site to the PET scanner after irradiation may introduce additional position uncertainties. Hence, new off-line strategies are investigated, e.g. using PET/CT instead of PET imaging alone [7], using the same patient positioning system for irradiation and PET measurement and moving the patient without release from the positioning system to a scanner installed as close as possible to the treatment site.

C CLINICAL IMPACT ON ION THERAPY

C.1 Monitoring of carbon therapy at GSI

Routine clinical application of in-beam PET is performed at the experimental carbon ion therapy facility at GSI Darmstadt. The technological basis for it is a double head positron camera [8] integrated into the therapy unit (Fig. 2). The device detects during the therapeutic irradiation the decay of minor amounts of positron emitting nuclei (predominantly ^{11}C and ^{15}O), which are produced via irradiation. Sophisticated algorithms of tomographic reconstruction deliver the spatial distribution of positron emitters in vivo. They are related to the dose distribution by means of a precise Monte Carlo simulation [5] of the production of positron emitters and the detection of annihilation γ-rays (Fig. 3). Comparing these with the measured PET images, deviations between the planned and actually delivered dose distributions are revealed, can be quantified [9] and compensated for in the further course of the fractionated treatment. Reasons for such deviations are ion range modifications due to minor patient positioning errors in combination with large tissue density gradients or due to changes of the tissue density distribution within the irradiated volume (e.g. radiation induced tumour shrinking) during the three weeks of fractionated radiotherapy. At the carbon ion therapy facility of GSI more than 370 cancer patients, most of them with tumours in the head and neck region, have been treated since 1997; all these treatments were monitored by means of in-beam PET for quality assurance.

C.2 Monitoring of other ion species

For radiobiological reasons it is highly desirable to have not only carbon beams, but a large variety of ion species with atomic numbers between 1 (hydrogen) and 8 (oxygen), available for therapy. Thus, novel ion therapy accelerators, e.g. at the Heidelberg Ion Therapy (HIT), are capable of delivering beams of all these ions with therapeutically relevant energy values. Since in-beam PET offers the unique possibility to measure particle ranges in-vivo, it allows for sensitively testing the physical beam model underlying the dose calculation algorithms for treatment planning. This is of high relevance in the commissioning of new ion species for therapeutic application. Therefore, the in-beam PET scanner at the GSI therapy facility is used to measure with very high precision physical data being necessary for extending in-beam PET to other ion beams like proton [10], helium [11] and oxygen [12] (Fig. 1). Moreover, in-beam PET phantom studies with protons at GSI [10] triggered research on post-radiation PET/CT imaging at Massachusetts General Hospital, Boston (Fig. 4). First clinical results [13] confirm the predicted positive impact.

D MONITORING OF HARD PHOTON BEAMS

The successful application of PET for monitoring radiation therapy with ions motivated investigations on the feasibility of the method for hard photon beams. This is studied with the aim to proof the feasibility for combining an in-beam PET scanner with an extremely compact 50 MeV electron accelerator delivering a pencil like beam of ultrahard bremsstrahlung photons. In this case positron emitters are generated by (γ, n) photonuclear reactions in the tissue at photon energy values above 20 MeV. The in-beam PET experiments are carried out at 20 – 40 MV bremsstrahlung beams of the ELBE radiation source at the Forschungszentrum Dresden-Rossendorf (FZD). In a first step it has been shown by means of Monte Carlo calculations [14] that for electron beam energies beyond 30 MeV the induced dose related activity density is comparable with that obtained during irradiation with carbon ions. This has been successfully confirmed in the second step [15], where the ^{11}C activity generated in plastic phantoms during photon irradiation at ELBE has been measured and quantified by means of the human PET scanner (Fig. 5). Just recently bremsstrahlung induced positron emitters (^{11}C and ^{15}O) has been imaged in-beam for the first time worldwide by means of a small limited angle positron camera installed at the ELBE beam, with the encouraging results that dosimetry as well as the control of patient positioning on the basis of in-beam PET appear feasible (Fig. 5).

Fig. 1: The depth distributions of calculated dose (blue, dashed) and measured β^+-activity (red, solid) induced by beams of protons as well as ^{3}He, ^{12}C and ^{16}O ions in thick targets of polymethyl methacrylate. The prominent maxima in the cases of ^{12}C and ^{16}O are formed by positron radioactive projectile fragments, whereas the pedestals as well as the distributions generated by ^{1}H and ^{3}He are due to target fragments.

Fig. 2: The double-head positron camera at the treatment site at GSI Darmstadt. The horizontal carbon ion beam leaves the beam pipe through a 20×20 cm^2 window visible in the centre of the picture. To provide sufficient space for patient positioning, the PET scanner can be moved on rails parallel to the beam between the measuring position displayed and the parking position upbeam.

Fig. 3: Clinical application of in-beam PET at the carbon ion therapy facility at GSI Darmstadt. As an example, the irradiation of a chondrosarcoma of the skull base with a lateral portal coming from the left side of the patient, i.e. right side in the picture, (maximal dose: 0.63 Gy) is displayed. As indicated by the dose distribution superimposed onto the computed tomogram (left) the carbon ions must not penetrate the brain stem as an organ at risk. The comparison of the predicted (middle) with the measured (right) β^+-activity distributions shows that this was fulfilled during the treatment. The isodose and isoactivity lines are decoded in rainbow colours and denote 5, 15, … 95 % of the maxima.

Fig. 4: Monte Carlo calculated (left) and measured (right) activity distribution after proton irradiation of a clivus chordoma patient at Massachusetts General Hospital, Boston. Images reprint from [13].

Fig. 5: Two-dimensional β^+-activity distributions generated by ultrahard bremsstrahlung (coming from the left) in an inhomogeneous phantom consisting of 2 cm thick slabs of polymethyl methacrylate (PMMA), polyethylene (PE) and different tissue equivalent materials (lung, adipose and bone). Upper image: in-beam PET result measured during 34 MV photon irradiation showing the distribution of ^{11}C (half-life: 20 min) and ^{15}O (half-life: 2 min) from the photonuclear reactions ^{12}C(γ, n) and ^{16}O(γ, n), respectively. Lower image: result of the PET measurement at the human scanner. This measurement started 30 min after finishing the 30 MV photon irradiation. Therefore, it shows only the ^{11}C distribution (^{15}O has been nearly completely decayed during 30 min.), leading to a reduced contrast between PE, PMMA, adipose tissue and bone compared to the in-beam image.

E ACKNOWLEDGMENT

REFERENCES

1. J. Pawelke, W. Enghardt, B.G. Hasch, R. Hinz, K. Lauckner, M. Sobiella: Positron emission tomography for quality assurance of heavy ion therapy, GSI Report **97-09**, H5 (1997)
2. J. Llacer: Positron emission medical measurements with accelerated radioactive ion beams. Nucl. Sci. Appl. **3**, 111 (1988)

3. M. Kanazawa, A. Kitagawa, S. Kouda, T. Nishio, M. Torikoshi, K. Noda, T. Murakami, M. Suda, T. Tomitani, T. Kanai, Y. Futami, M. Shinbo, E. Urakabe, Y. Iseki: Application of an RI-beam for cancer therapy – In-vivo verification of the ion-beam range by means of positron imaging, Nucl. Phys. A **701**, 244c (2002)

4. J. Pawelke, L. Byars, W. Enghardt, W.D. Fromm, H. Geissel, B.G. Hasch, K. Lauckner, P. Manfraß, D. Schardt, M. Sobiella: The investigation of different cameras for in-beam PET imaging, Phys. Med. Biol. **41**, 279 (1996)

5. F. Pönisch, K. Parodi, B.G. Hasch, W. Enghardt: The modelling of positron emitter production and PET imaging during carbon ion therapy, Phys. Med. Biol. **49**, 5217 (2004)

6. P. Crespo, G. Shakirin, W. Enghardt: On the detector arrangement for in-beam PET for hadron therapy monitoring, Phys. Med. Biol. **51**, 2143 (2006)

7. K. Parodi, H. Paganetti, E. Cascio, J.B. Flanz, A.A. Bonab, N.M. Alpert, K. Lohmann, T. Bortfeld: PET/CT imaging for treatment verification after proton therapy – A study with plastic phantoms and metallic implants. Med. Phys. **34**, 419 (2007)

8. W. Enghardt, P. Crespo, F. Fiedler, R. Hinz, K. Parodi, J. Pawelke, F. Pönisch: Charged hadron tumour therapy monitoring by means of PET, Nucl. Instrum. and Meth. in Phys. Res. A **525**, 284 (2004)

9. W. Enghardt, K. Parodi, P. Crespo, F. Fiedler, J. Pawelke, F. Pönisch: Dose quantification from in-beam positron emission tomography, Radiother. Oncol. **73**, S96 (2004)

10. K. Parodi, F. Pönisch, W. Enghardt: Experimental study on the feasibility of in-beam PET for accurate monitoring of proton therapy, IEEE Trans. Nucl. Sci. **52**, 778 (2005)

11. F. Fiedler, P. Crespo, K. Parodi, M. Sellesk, W. Enghardt: The feasibility of in-beam PET for therapeutic beams of ^{3}He. IEEE Trans. Nucl. Sci. **53**, 2252(2006)

12. F. Sommerer et al: Experiments and simulations for in-beam PET monitoring with oxygen beams, in this contribution, (2007)

13. K. Parodi, H. Paganetti, H. Shih, S. Michaud, J. Loeffler, T. DeLaney, N. Liebsch, J. Munzenrider, A. Fischman, A. Knopf, T. Bortfeld: Patient study of in-vivo verification of beam delivery and range using positron emission tomography and computed tomography imaging after proton therapy, Int. J. Radiat. Oncol. Biol. Phys. **68**, 920 (2007)

14. H. Müller and W. Enghardt: In-beam PET at high-energy photon beams – a feasibility study, Phys. Med. Biol. **51**, 1779 (2006)

15. D. Möckel, H. Müller, J. Pawelke, M. Sommer, E. Will and W. Enghardt: Quantification of β^+ activity generated by hard photons by means of PET, Phys. Med. Biol. **52**, 2515 (2007)

Fig. 1: The depth distributions of calculated dose (blue, dashed) and measured β^+-activity (red, solid) induced by beams of protons as well as ^{3}He, ^{12}C and ^{16}O ions in thick targets of polymethyl methacrylate. The prominent maxima in the cases of ^{12}C and ^{16}O are formed by positron radioactive projectile fragments, whereas the pedestals as well as the distributions generated by ^{1}H and ^{3}He are due to target fragments.

Fig. 2: The double-head positron camera at the treatment site at GSI Darmstadt. The horizontal carbon ion beam leaves the beam pipe through a 20×20 cm^2 window visible in the centre of the picture. To provide sufficient space for patient positioning, the PET scanner can be moved on rails parallel to the beam between the measuring position displayed and the parking position upbeam.

Fig. 3: Clinical application of in-beam PET at the carbon ion therapy facility at GSI Darmstadt. As an example, the irradiation of a chondrosarcoma of the skull base with a lateral portal coming from the left side of the patient, i.e. right side in the picture, (maximal dose: 0.63 Gy) is displayed. As indicated by the dose distribution superimposed onto the computed tomogram (left) the carbon ions must not penetrate the brain stem as an organ at risk. The comparison of the predicted (middle) with the measured (right) β^+-activity distributions shows that this was fulfilled during the treatment. The isodose and isoactivity lines are decoded in rainbow colours and denote 5, 15, … 95 % of the maxima.

Monte Carlo calculated (left) and measured (right) activity distribution after proton irradiation of a clivus chordoma patient at Massachusetts General Hospital, Boston. Images reprint from [13].

Fig. 5: Two-dimensional β^+-activity distributions generated by ultrahard bremsstrahlung (coming from the left) in an inhomogeneous phantom consisting of 2 cm thick slabs of polymethyl methacrylate (PMMA), polyethylene (PE) and different tissue equivalent materials (lung, adipose and bone). Upper image: in-beam PET result measured during 34 MV photon irradiation showing the distribution of ^{11}C (half-life: 20 min) and ^{15}O (half-life: 2 min) from the photonuclear reactions ^{12}C(γ, n) and ^{16}O(γ, n), respectively. Lower image: result of the PET measurement at the human scanner. This measurement started 30 min after finishing the 30 MV photon irradiation. Therefore, it shows only the ^{11}C distribution (^{15}O has been nearly completely decayed during 30 min.), leading to a reduced contrast between PE, PMMA, adipose tissue and bone compared to the in-beam image.

EXPERIMENTS AND SIMULATIONS FOR IN-BEAM PET MONITORING WITH OXYGEN BEAMS

F. Sommerer[1,2,*], F. Cerutti[1], W. Enghardt[3], A. Ferrari[1], K. Parodi[4]
[1]CERN, Geneva, Switzerland
[2]Atominstitut of the Austrian Universities, Vienna, Austria
[3]TU Dresden and Forschungszentrum Dresden-Rossendorf, Dresden, Germany
[4]Heidelberg Ion Therapy, Heidelberg, Germany

In-beam PET is presently used for monitoring tumor treatments with ^{12}C ions at the experimental ion therapy facility at GSI, Darmstadt, Germany. The basic principle of this technique is a comparison between the measured and simulated β^+-activity spatial distributions. In future ion therapy centers besides ^{12}C also ^{16}O, ^{3}He and protons will be used for treatment. To enable monitoring of treatments delivered by all possible therapeutic ion beams, a general purpose simulation code capable to predict the irradiation induced β^+-activity is needed. The code presently used at GSI for simulating the activity is dedicated to ^{12}C ions and cannot be extended in a straightforward way. We have chosen the FLUKA Monte Carlo transport code for simulating the activity created by ^{16}O beams. In-beam PET experiments with ^{16}O of different energies on various targets were performed at the treatment place at GSI and compared with the simulations.

Introduction

When ions travel in matter they undergo nuclear reactions with the nuclei of the target. Some of the produced residues are β^+-active and can be measured by means of positron emission tomography (PET). This offers the possibility to monitor ion therapy.

At the experimental heavy ion therapy facility at GSI, Darmstadt, Germany a PET scanner is fully integrated into the treatment site and the treatment of more than 350 patients has been monitored this way since 1997. This method is called in-beam PET and it is presently the only feasible non-invasive method to monitor ion therapy. To enable patient positioning and to not interfere with the beam, the scanner is designed in double head geometry covering only a small part of the solid angle.

The basic principle of in-beam PET monitoring is a comparison between the measured β^+-activity and a simulated one [1]. At GSI the treatment is only done with ^{12}C ions and the dedicated code [2] used for simulating the β^+-activity is not extendable to other ions in an easy way.

At HIT (Heavy Ion Therapy) in Heidelberg, Germany apart from ^{12}C also ^{16}O, ^{3}He and protons will be used and monitoring by means of in-beam PET is planned.

To enable in-beam PET monitoring a code capable to predict the β^+-activity is needed. Our choice is the FLUKA Monte Carlo transport and interaction code [3, 4].

FLUKA

FLUKA is a multi purpose particle transport code with applications in many fields. The main reasons for choosing it for these investigations are:

- good results in predicting the β^+-activity induced by proton beams [5]
- its ability to read and handle computed tomography (CT) data
- good results for calculating dose in ion therapy [6]
- its recently added interface with a module which is capable to handle nuclear reactions at low energies

*Corresponding author:
florian.sommerer@cern.ch

In FLUKA nucleus-nucleus interactions at therapeutic energies are treated by an interface to a Relativistic Quantum Molecular Dynamics code (RQMD) which can handle interactions down to about 100 AMeV. For simulations like the ones presented here it is necessary to include also reactions at lower energies, otherwise one would miss β^+-activity especially in vicinity of the maximum dose delivery (Bragg peak).

In the development version of FLUKA a model based on the Boltzmann Master Equation theory (BME) [7] is available, which handles nucleus-nucleus interactions at energies below 100 AMeV down to the Coulomb barrier.

Experiments

In-beam PET experiments with ^{16}O beams on homogeneous targets of PMMA, water (with a small amount of gelatine added to avoid convection) and graphite were performed. The data were stored in list mode (i.e. with time information) to enable back projections at different time intervals.

In this experimental run the raster scanner could not be used and, therefore, a small instability of the beam in lateral position could not be corrected for.

For each experiment two back projections were done. The first one uses events decayed in the pauses of the irradiation because during the beam extractions (spills) the signal is corrupted by prompt gamma rays. The second one was done 10 minutes after irradiation end for 10 minutes, thus all short lived nuclei are already decayed and, therefore, the activity distribution is different from the first one.

Simulations

For the simulations the development version of FLUKA was used, which allows to cover the whole energy range for nucleus-nucleus reactions by using both RQMD and BME.

The experimental pulsed beam delivery (i.e. on/off) was carefully modeled. However, there was not enough information to model also the lateral instability of the beam.

First straightforward simulations needed roughly 100 days of computing time and still produced results with high statistical errors. The reason for this was twofold:

(1) β^+-active residual nuclei which do not decay during the measuring time do not contribute to the activity distribution and are, therefore, lost

(2) because of the limited solid angle of the double head PET detector most annihilation photons do not reach the detector and do not contribute either

Both problems could be solved by using biasing techniques. The first biasing method repeats the decay of every residual nucleus 250 times. To compensate for the unphysical replication each particle gets a weight assigned which is 1/250 in that case. The weight has to be taken into account in the post processing.

This biasing technique has positive impact on both of the above mentioned problems because each of the 250 replicas is decaying at different times and the annihilation photons have different directions. But still a lot of CPU time is wasted because of photons which do not reach the detectors. However, with this biasing alone the simulations were still too slow to produce results of satisfying statistics in reasonable computing time. Because only a small part of the computing time is used for transport, nuclear interaction length biasing, a standard biasing tool of FLUKA, did not further accelerate the results.

To further improve the simulation speed decay-direction-biasing for annihilation photons was implemented especially for these simulations (it is not available in the official FLUKA distribution). The principle is the following: when annihilation photons are created their directions are isotropically distributed. Decay-direction-biasing forces one photon to be emitted in a given direction. To compensate for the unphysical direction change one of the two photons gets a different weight according to the angle between the original direction and the forced direction. The second annihilation photon gets the same weight as the first one and points in the opposite direction. After assigning the weight and the new direction the photons are transported normally.

For these simulations none of the FLUKA standard scoring methods could be used. Instead for each pair of annihilation photons the position where the photons leave the target, their direction cosines, the time, the weight and some additional information were stored in a file.

To make the activity distributions of the FLUKA simulations comparable to the measured ones, the detection process and the back projection have to be modeled carefully. Instead of modeling the detector in FLUKA, the code presently used at GSI for simulating the activity during treatment was used for this purpose [2]. The part that creates the annihilation photons was removed and it was modified to take the output of FLUKA as input. Furthermore, this code was modified to be able to deal with the different weights of the photons.
All detector properties are taken into account and the result is a list mode data file that can be processed by the back projection routines exactly the same way than the experimental data.

Results and discussion

Because of limited space only the case of 350 AMeV ^{16}O-beam on a block of PMMA ($40 \times 9 \times 9$cm^3, $\rho = 1.18$ g/cm^3) is presented here. First preliminary results are shown in the figures 1 and 2.
Figure 1 shows a comparison of the back projections of the β^+-activity during irradiation (i.e. only during spill pauses) between FLUKA (solid line) and the experiment (dotted line). Figure 2 shows a back projection of the activity 10 minutes after irradiation end for 10 minutes.
In the entrance region one can see that some activity is found outside of the target (target starts at 0 cm). This is an effect of the back projection and is the same in the experiment and in the simulation.
A total of $4 \cdot 10^6$ primaries were simulated which gave, because of the biasing used, $5.56 \cdot 10^7$ pairs of annihilation photons. About $1.4 \cdot 10^6$ annihilation pairs were found for the time interval starting at 10 minutes after irradiation end and ending 10 minutes later. During the 119 spill pauses each of about 2 s length $2.6 \cdot 10^6$ annihilation pairs were found.
The simulations were performed in 20 parallel runs of about 5.5 hours each therefore a total CPU time of 110 hours was used. This is about 22 times faster than the initial simulations without biasing and still gives much better results in terms of statistics.
In both figures one can see that the position of the experimental peak is closer to the entrance than the simulated one. The reason for that can be that in this preliminary simulations the geometry of the experiment was modeled in a very simple way and all material in the beam (i.e. ionization chambers and the air) was neglected. It is planned to add this material in future simulations and it is expected that then the position of the simulated activity peak will come closer to the experimental one. Taking into account the material in the beam line could have also an effect on the height of the peak, because a part of the beam particles is already fragmented and therefore the peak to plateau ratio could be different.
The lack of activity just before the peak in figure 2 occurs where the energy of beam particles decreased down to the threshold between the two event generators in FLUKA (100 AMeV. At now the implemented BME model underestimates the yield of products close in mass and charge to the projectile and the target nucleus. That is the case of ^{11}C (the main responsible for the activity profile in figure 2) produced by the interaction between an incoming ^{16}O nucleus and a ^{12}C nucleus belonging to PMMA.
The presented preliminary results prove that FLUKA is capable of predicting the activity distribution created by ^{16}O, however further refinements are needed. The material in the beam path has to be modeled to bring more accurate results.
The BME modeling of inelastic scattering and of few nucleon transfer has to be improved in order to provide a better account for products close in mass and charge to the projectile and the target nucleus.
The presented simulations also show the power of the biasing techniques of FLUKA which can, if used properly, save considerable amounts of computing time.
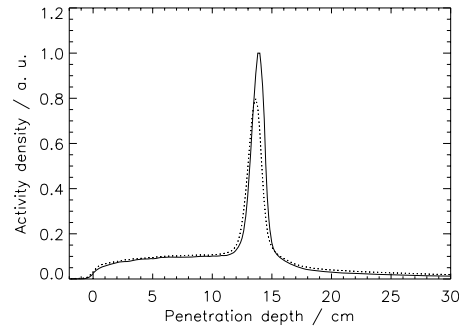
Figure 1 Activity profile during spill pauses for a 350 *A*MeV [16]O beam on PMMA. The solid line is the result of the FLUKA simulation, the dotted line shows the experimental result
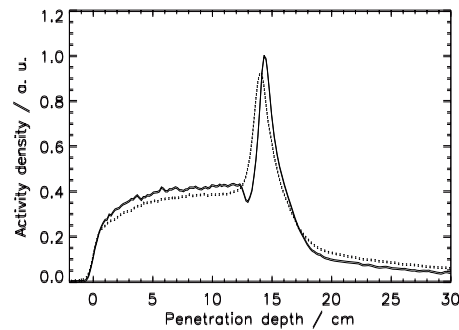
Figure 2 As Figure 1, but measured for 10 minutes, starting 10 minutes after finishing the irradiation

REFERENCES

1. Charged hadron tumor therapy monitorting by means of PET, W. Enghardt etal., *Nucl. Instrum. Meth.* **A 525** (2004) 284-288
2. The modelling of positron emitter production and PET imaging during carbon ion therapy, F. Pönisch etal., *Phys. Med. Biol.* **49** (2004) 5217-5232
3. FLUKA: a multi-particle transport code, A. Fassò etal. *CERN-2005-10 (2005), INFN/TC_05/11, SLAC-R-773*
4. The physics models of FLUKA: status and recent developments, A. Fassò etal. *Computing in High Energy and Nuclear Physics 2003 Conference (CHEP2003)*
5. Clinical CT-based calculations of dose and positron emitter distributions in proton therapy using the FLUKA Monte Carlo code, K. Parodi etal., *Phys. Med. Biol.* **52** (2007) 3369-3387
6. Investigating the accuracy of the FLUKA code for transport of therapeutic ion beams, F. Sommerer etal., *Phys. Med. Biol.* **51** (2006) 4385-4398
7. Low energy nucleus-nucleus reactions: the BME approach and its interface with FLUKA, F. Cerutti etal., *Proc. 11th Int. Conf. on Nuclear Reaction Mechanisms, Varenna (Italy) E. Gadioli ed., Ric. Scient. ed Educ. Perm.* **S 126** (2006) 507

ABSORBED DOSE AND QUALITY DISTRIBUTION IN LIGHT ION RADIATION THERAPY WITH β^+ EMITTERS

Author: Johanna Kempe

Department of Medical Radiation Physics, Karolinska Institutet and Stockholm University, Stockholm, Sweden

The use of radioactive ion beams in light ion radiation therapy is of special interest for clinical range and dose determination using *in vivo* PET imaging. The radiation quality in terms of depths absorbed dose and LET distribution of positron emitting particles such as ^{8}B , ^{9}C ^{10}C and ^{11}C has been investigated using the Monte Carlo code SHIELD-HIT. The absorbed dose distributions of the primary and secondary particles, produced by the fragmentation processes of the primary beam and secondary target fragments, are calculated and discussed with regard to their contributions to low-and high- LET components. The absorbed dose in the plateau region and the fragmentation tail beyond the Bragg peak of the primary particles and the main secondary particles, i.e protons and alphas, in a ^{8}B beam of energy 329 MeV/u is comprised mainly of low LET components. The high LET components, mainly caused by the primaries, appear in the Bragg peak region and are characterized by a quasi-Gaussian distribution.
A fundamental understanding of the radiation quality of radioactive ion beams is of greatest importance in biological optimized radiation therapy.

DOSIMETRY AND INSTRUMENTATION FOR CARBON ION RT

C. P. Karger[1,*], P. Heeg[2], O. Jäkel[1,2]
[1]Dept. Medical Physics in Radiation Oncology, German Cancer Research Center (DKFZ), Heidelberg, Germany
[2]Heidelberg Ion Therapy (HIT), Heidelberg, Germany

Due to the increased biological effectiveness of Carbon ions, dose prescription is performed in terms of biologically effective rather than absorbed dose. Nevertheless, the operational quantity for dosimetry is still absorbed dose to water, which can be measured accurately using ionization chambers. At the Gesellschaft für Schwerionenforschung (GSI), an actively scanned Carbon ion beam was applied for patient treatments over the past ten years. As a prerequisite, Carbon ion dosimetry has been established and introduced into clinical routine. In the following, instrumentation and clinical application of Carbon ion dosimetry is summarized.

Introduction

Although dose prescription in heavy ion radiotherapy is performed in terms of biologically effective dose, the operational quantity for dosimetry is still absorbed dose to water. The reason for this is that absorbed dose can be accurately measured with standard dosimetric equipment like ionization chambers and no reference to a model for the relative biological effectiveness (RBE) or any specific biological system is necessary. Here, the dosimetric instrumentation and applications as applied at the Carbon ion therapy project at GSI are described.

MATERIALS AND METHODS

Detectors

In principle, the same detectors as for photons and electrons may be used in carbon ion radiotherapy. In this context, the most important detector types are:

- Thimble ionization chambers
- Plane-parallel ionization chambers
- Films
- Solid state and other detectors

Thimble ionization chambers

Thimble ionization chambers define the gold standard for dose measurements in ion beams. They are especially applied in situations where absolute dose measurements are performed, i.e. for the calibration of the beam monitor, validation of the dose calculation and verification of beam delivery and some quality assurance tests. Depending on the application either ionization chambers with rather large volumes (e.g. a Farmer chamber) or small volumes (pin point chamber) are used.

Plane-parallel ionization chambers

In contrast to thimble ionization chambers, plane-parallel chambers are mostly applied for relative dose measurements, especially for the determination of depth dose profiles used as base date in treatment planning. For this, the signal of the plane-parallel chamber has to be normalized to the fluence of the beam, which may be measured either by a second chamber or by the beam monitor. The cross section of plane-parallel chambers may be relatively small (e.g. in the case of a Roos chamber) or may have a large extensions (e.g. in the case of the beam monitor. While in the first case, the parallel chamber may at least in principal be used for absolute dose measurements, as long as the measured

field in homogeneous and larger than the extension of the chamber, this is not possible for larger area chambers used as beam monitor. Large area chambers, on the other hand, integrate the signal over the complete beam and the signal is not sensitive to beam broadening caused by scattering.

Films

In contrast to photon therapy, the use of films for heavy ion beams is more difficult. Due to the dependence of the film response on linear energy transfer (LET), there is no unique relation between optical density and dose. Measurement of absolute dose is therefore only possible for defined LET-conditions (e.g. at a fixed depth of a monoenergetic beam), for which a calibration curve (optical density vs. dose) must be available. For superposition of beams of different energies (e.g. a clinical treatment field), the expected optical density can be predicted, however, the calculation of the absorbed dose from the optical density is generally not possible as this would require the knowledge of the contributions of the different energy and LET components. Films are therefore mainly used for the test of geometrical beam alignments, dose homogeneity checks of monoenergetic beams and qualitative verification of the lateral shape of treatment fields.

Solid state and other detectors

Other detector types such as TLDs, Diodes, diamond detectors or water calorimeters are only occasionally applied for dosimetry in heavy ion beams. Similar to films, the response of solid state detectors is LET-dependent and unless the specific energy and LET-characteristics are not additionally used these detector types may only be used for measurements with fixed energy and LET-conditions (e.g. for measuring lateral dose profiles). The use of water calorimeters aims to determine absolute dose by measuring temperature differences. This technique, however, is still under development and its application requires substantial efforts.

Phantoms

Dosimetric measurements may be performed in homogeneous as well as in inhomogeneous phantom materials. Water phantoms, solid water slabs or PMMA may be used for measurements in homogeneous material. PMMA phantoms are often preferred due to the cheapness and availability of PMMA. It has to be considered that the range of Carbon ions in PMMA is reduced by a factor of 1.165 as compared to that in water. Moreover the range may not be correctly calculated by the empirical relation between CT-Hounsfield numbers and water-equivalent range, which is used to calculate dose distributions on the patient-CT. Inhomogeneous phantoms are used for integral checks of the irradiation system including the range of particles in structures not equivalent to water. Inhomogeneous phantoms usually consist of water-equivalent material with inserts of tissue-equivalent material. Alternatively, anthropomorphic phantoms (e.g. an Alderson phantom) may be used.

Dosimetric applications

In heavy ion radiotherapy, the following types of dosimetric measurement may be identified:

- Absolute dose
- Beam monitoring
- Base data
- Validation of dose calculation
- Quality assurance
- Verification of beam delivery

Absolute dose

For absolute dose measurements thimble ionization chambers calibrated in terms of absorbed dose in water in a ^{60}Co-beam are state of the art. The absorbed dose in water at the effective point of meas-

*Corresponding author: c.karger@dkfz.de

urement P_{eff} is given by [1,2,3]

$$D_w(P_{eff}) = M_{Corr} N_W^{Co-60} k_Q \quad (1a)$$

with

$$k_Q = \frac{W^{C-12}}{W^{Co-60}} \cdot \frac{\bar{s}_{w,a}^{C-12}}{(\bar{L}/\rho)_{w,a}^{Co-60}} \cdot \frac{p^{C-12}}{p^{Co-60}} \quad (1b)$$

where M_{corr} is the electrometer reading corrected for deviations from reference conditions, N_w is the calibration factor of the chamber in the ^{60}Co-field and k_Q corrects for the for the beam quality. k_Q, is calculated from several radiation specific parameters for Carbon ions (numerator) and [60]Co (denominator). W denotes the average energy required to produce an ion, $\bar{s}$ and $(\bar{L}/\rho)$ are the mean and restricted stopping power ratios between water and air, respectively, and ⠀⠀⠀are the chamber specific perturbation factors.

Beam monitoring

Monitoring of beam delivery is performed with large area ionization chambers. According to the code of practice TRS-398 issued by the IAEA [1], a calibration of the beam monitor is to be done in terms of dose per monitor unit. To do so, the dose has to be measured in the middle of the physical dose distribution of each spread-out Bragg peak and the dose has to be related to the number of applied monitor units. This procedure, however, is only feasible for passive beam delivery systems [4], where the number of spread-out Bragg peaks with different extensions in depth is basically limited by the available number of modulator wheels. For a scanning beam delivery, this procedure is no longer feasible as the extension of the spread-out Bragg peak may be different for each patient. Moreover, the extension may be different at different points within the treatment fields. This results in a practically infinite number of beam configurations, for which the beam monitor would have to be calibrated.

For the active scanning system used at GSI, the calibration factor (CF) of beam monitor is therefore determined in terms of particle number (N_{C-12}) per monitor unit (N_{MU}) rather than dose per monitor unit. This is done for each monoenergetic Bragg-peak of initial energy E according to [2,3]

$$(2a),$$

where the determination of the number of ions is reduced to a measurement of the absorbed dose to water:

$$N_{C-12}(E) = D_w(z) \frac{\Delta x \Delta y}{S^{C-12}(z)/\rho} \quad (2b).$$

In eq. 2b, D is the dose and S/r is the mass stopping power at the measurement depth z, respectively. Δx and Δy are the step sizes of the scanning system in x- and y-direction, respectively. For each treatment field, the number of particles at each energy and scan position is calculated by the treatment planning system.

Base data

For treatment planning, the relative depth dose profiles of either the spread-out Bragg-peaks (for passive beam delivery systems) or monoenergetic Bragg-peaks have to be measured. For this plane-parallel ionization chambers are used, preferably in combination with an adjustable water column, which makes measurements more efficient. In addition, the relation between the CT-Hounsfield units and the relative water-equivalent range has to be established, which may be done by measuring the peak posi-

tion of a monoenergetic Bragg-curve with and without inserting either tissue equivalent substitutes of samples of real tissues of defined thickness into the beam.

Validation of dose calculation

Correct dose calculation has to be checked during commissioning by the treatment planning system as well as after significant changes of the dose calculation algorithm. For this absolute dose measurements are required. Examples for such measurements are:

- Check of monitor calibration by measurements in the middle of spread-out Bragg-peaks. Especially for active systems, it is important to check the correct superposition of energies.
- Measurements of treatment fields planned for homogeneous phantoms,
- Measurements of treatment fields planned for inhomogeneous or anthropomorphic phantoms.

Quality assurance

To check the constancy of the beam delivery system, dosimetric measurements have to be performed within the framework of quality assurance protocols. These measurements may consist of repeating measurements of validation of dose calculation with focus on constancy of the obtained results, but also of depth dose distributions, of testing the constancy of the monitor calibration and its dependency on fluence, flux and asymmetric beams.

Verification of beam delivery

Especially for scanned beams, the correct superposition of all beams should be verified by comparing measured and calculated doses for the individual patient. For a dynamic delivery of the dose measured and calculated doses may agree at one point while they do not at another. Therefore a sufficiently large and representative sample of measurement points has to be measured. The sample should contain different measurement positions in depth as well as across the beam. To be efficient, simultaneous measurements at many points together with an online evaluation should be feasible.

RESULTS AND DISCUSSION

Although different dosimetric detectors are available for application in Carbon ion radiotherapy, ionization chambers are mostly used due to their accuracy and their ability of electronic read-out. Solid state detectors generally are more sensitive to variation of the LET in the radiation field. Measurements are mostly performed in homogeneous water or PMMA phantoms. If the relation between CT-Hounsfield units and water-equivalent range is to be checked, inhomogeneous or anthropomorphic phantoms are used. The measurement techniques described above are routinely applied at GSI since 1997, where the treatment of patients started.

Absolute dose

The combined standard uncertainty in the determination of absolute dose in water for a clinical Carbon ion beam is currently 3.0% for thimble and 3.4% for plane-parallel ionization chambers [1]. The main contribution to this uncertainty results from the uncertainty of the stopping power ratio and the W-value of Carbon ion beams used to calculate the beam quality correction k_Q (eq. 1b). Recent investigations quantify the uncertainty of the stopping power ratio outside the Bragg-peak position to be less than 1% [5].

Beam monitoring

At GSI, the monitor calibration is performed in a thin slab of water-equivalent material [2,3]. As the effective point of measurement lies in a depth of only a few millimeters, projectile fragmentation can be neglected. Practically, the calibration is performed for a representative set of six energies, and the calibration factor at the other energies is obtained by interpolation. Day-by day variation is considered by a scaling factor.

To achieve a higher and faster electronic signal, the monitor chambers are floated by a constant rate of a Carbogen/Krypton-mixture. To obtain a stable calibration of the monitor, the flow of both gases as well as the mixing ration must be kept within narrow tolerances. In addition to the monitor chambers, multi-wire chambers are used to monitor the position of the scanned beam.

Base data

The Bragg curves required for dose calculation are calculated by the beam model, which was adjusted to measured depth dose curves at several energies [6]. The resulting curves are stored in a table in steps of 10 MeV/u in the range from 50 to 500 MeV/u. For energies in between, the curves are linearly interpolated.

To calculate the range of the particles in inhomogeneous tissue, a relation between CT-Hounsfield units and water-equivalent range of tissue-equivalent substitutes has been established [7]. It is important to note that the measured Hounsfield units may depend on parameters of the CT-protocol (e.g. beam energy, slice size, reconstruction filter). The CT-protocol was therefore fixed for heavy ion treatment planning.

Validation of dose calculation

Validation of dose calculation is performed in homogeneous and inhomogeneous phantoms using cubic, geometrically shaped and patient-typical treatment plans [8,9]. Due to some uncertainties in the currently applied beam model, we typically see a slight negative deviation between measured and calculated dose, which increases for small target volumes in large depths. Currently, work is done, to improve the quality of the beam model. It is important to note that the uncertainty in the determination of the absolute dose does not affect the comparison of measured and calculated dose as this uncertainty is involved in both, the dose measurement as well as in the monitor calibration, and therefore cancels out.

Quality assurance

All dosimetric measurements as well as all geometrical checks are laid down in a written quality assurance document, which served together with the acceptance measurements as the basis of the governmental approval [8,9]. All tests are regularly performed since 1997, where the treatment of patients started at GSI. As treatments at GSI takes place only during three blocks of 4 weeks per year, the frequency of the quality assurance measurements is daily, per treatment block and annually.

Verification of beam delivery

Prior to treatment, each treatment plan is verified using a water phantom with a stack of ionization chambers, which are red out remotely [10]. Each treatment field is measured in the center of the dose distribution as well as at the distal edge. Deviations between measured and planned doses normalized to the maximum doses are calculated. Currently applied acceptance criteria are 5% for the mean deviation of all measured points and 5% for the standard deviation of all deviations. Measurement points in large dose gradients are not considered. The measured mean deviations are in the range of -2 to -3% of the maximum dose. The verification of a treatment plan currently takes about 45 min. This time may be reduced significantly if a faster beam delivery and an automated setup of the phantom is available.

CONCLUSION

The principal methods of Carbon ion dosimetry have already been developed, although the uncertainty in the determination of the absolute dose in water is larger than for photons. Further investigations are necessary to reduce the uncertainties of the parameters needed to calculate the beam quality factor k_Q. Monte Carlo simulations may also help to determine k_Q more accurately. In the future, water calorimeters might be an alternative to ionization chambers calibrated in ^{60}Co for reference dosimetry.

*Corresponding author: c.karger@dkfz.de

Other detector types such as diodes or diamond detectors may be of interest for special applications. For this, however, the LET dependence of their response has to be thoroughly investigated. To improve the compliance of measured and calculated doses, the uncertainty of the input data required by the beam model has to be reduced. This includes accurate measurements of the amount of fragments produced in the beam as well as well as their angular distributions. For efficient clinical application of Carbon ion therapy, dosimetric measurements should be automated as far as possible. This especially holds for dose verification measurements, which currently require a substantial amount of time.

REFERENCES

1. IAEA (International Atomic Energy Agency) Absorbed dose determination in photon and Electron beams – an international code of practice. Technical report series No. 277 (1987) IAEA, Wien.
2. Hartmann G.H., Jäkel O., Heeg P., Karger C.P., Krießbach A.: Determination of water absorbed dose in a carbon ion beam using thimble ionization chambers. Physics in Medicine and Biology 44, 1193-1206, 1999.
3. Karger C.P., Jäkel O., Heeg P., Hartmann G.H.: Klinische Dosimetrie für schwere geladene Teilchen. Zeitschrift für Medizinische Physik 12, 159-169, 2002.
4. Jäkel O., Hartmann G.H., Karger C.P., Heeg P., Vatnitsky S.: A calibration procedure for beam monitors in a scanned beam of heavy charged particles. Medical Physics 31, 1009-1013, 2004.
5. Geithner O., Andreo P. Sobolevski N., Hartmann G., Jäkel O.: Calculation of stopping power ratios for carbon ion dosimetry. Physics in Medicine and Biology 51, 2279-2292, 2006.
6. Krämer M., Jäkel O., Haberer T., Kraft G., Schardt D., Weber U.: Threatment planning for heavy ion radiotherapy: physical beam model and dose optimization. Physics in Medicine and Biology 45, 3299-3317, 2000
7. Jäkel O., Jacob C., Schardt D., Karger C.P., Hartmann G.H.: Relation between carbon ion ranges and X-ray CT numbers for tissue equivalent phantom materials. Medical Physics 28, 701-703, 2001
8. Karger C.P., Hartmann G.H., Jäkel O., Heeg P.: Quality management of medical physics issues at the German heavy ion therapy project. Medical Physics 27, 725-736, 2000.
9. Jäkel O., Hartmann G.H., Karger C.P., Heeg P., Rassow J.: Quality assurance for a treatment planning system in scanned ion beam therapy. Medical Physics 27, 1588-1600, 2000.
10. Karger C.P., Jäkel O., Hartmann G.H., Heeg P.: A system for three-dimensional dosimetric verification of treatment plans in intensity-modulated radiotherapy with heavy ions. Medical Physics 26, 2125-2132, 1999.

ANTIPROTON RADIATION DOSIMETRY

Niels Bassler[1, 2,*], Michael H. Holzscheiter[3], Jørgen B. Petersen[4] and the AD-4/ACE Collaboration[†]

[1]Deutsches Krebsforschungszentrum, D-70191 Heidelberg, Germany
[2]Dept. of Experimental Clinical Oncology, Aarhus University Hospital, DK-8000 Aarhus, Denmark
[3]Dept. of Physics and Astronomy, University of New Mexico, Albuquerque, NM, USA
[4]Dept. of Medical Physics, Aarhus University Hospital, DK-8000 Aarhus, Denmark

The AD-4/ACE collaboration at CERN is investigating the anticipated benefit of antiproton radiotherapy. The experimental tasks have been twofold: 1) To quantify the radiobiological properties of the antiproton beam. 2) Perform absolute dosimetry on a pulsed antiproton beam. In order to do define the biological properties of antiprotons it is inevitable that we have adequate dosimetry of the antiproton beam. This is complicated in the peak-region by the mixed particle field from the antiproton annihilation. A beam of antiprotons will behave similar as a proton beam at high velocities, but when the antiprotons stop, they annihilate on a nuclei of the target material, producing high energy gamma's, pions, neutrons, and recoil ions. A portion of the annihilation energy released hereby is observed as an augmentation of the well known proton Bragg peak.

We have performed dosimetry experiments and investigated the radiobiological properties using antiprotons at 50 and 125 MeV from the Antiproton Decelerator (AD) at CERN. Dosimetry experiments were carried out with ionization chambers, alanine pellets and radiochromic film. Radiobiological experiments were done with Chinese V79 WNRE hamster cells.

Monte Carlo particle transport codes were investigated and compared with results obtained from the ionization chambers and alanine pellets. A track structure model have been applied on the calculated particle spectrum, and have been used to predict the LET-dependent response of the alanine pellets.

The particle transport program FLUKA produced data which were in excellent agreement with our ionization chamber measurements, and in good agreement with our alanine measurements. FLUKA is now being used to generate a wide range of depth dose data at several energies, including secondary particle–energy spectra, which will be used as base data for a treatment planning software such as TRiP for further studies of expected clinical consequences. This can also be used to compare antiprotons to carbon ions and protons in realistic treatment situations.

[*] Corresponding author: n.bassler@dkfz.de

[†] Michael H. Holzscheiter[1], Niels Bassler[2,3], Jan Alsner[2], Gerd Beyer[4], John J. DeMarco[5], Michael Doser[6], Dragan Hajdukovic[7], Oliver Hartley[4], Keisuke S. Iwamoto[5], Oliver Jäkel[3], Helge V. Knudsen[8], Sandra Kovacevic[7], Søren Pape Møller[9], Jens Overgaard[2], Jørgen B. Petersen[2], Osman Ratib[4], Timothy D. Solberg[10], Sanja Vranjes[11], Bradly G. Wouters[12].

1. University of New Mexico, Albuquerque, NM, USA; 2. Dept. of Medical Physics and Experimental Clinical Oncology, Aarhus University Hospital, Aarhus, Denmark; 3. Deutsches Krebsforschungszentrum, Heidelberg, Germany; 4. Hospital Universitaire de Geneve, Geneva, Switzerland; 5. David Geffen School of Medicine, UCLA, Los Angeles, CA, USA; 6. CERN, Geneva, Switzerland; 7. University of Montenegro, Podgorica, Montenegro; 8. Dept. of Physics & Astronomy, University of Aarhus, Aarhus, Denmark; 9. ISA, University of Aarhus, Aarhus Denmark; 10. University of Nebraska Medical Center, Omaha, NE, USA; 11. VINCA Institute for Nuclear Sciences, Belgrade, Serbia; 12. University of Maastricht, Res. Institute Growth and Development, The Netherlands;

INTRODUCTION

Antiprotons were suggested as a new beam modality for radiotherapy [1], as these have some dosimetric and radiobiological properties which may result in significant reduction of dose deposited to the normal tissue, beyond that achievable with proton therapy.

A beam of fast antiprotons will traverse matter in a similar way as protons do. The stopping powers are equal, straggling and in-flight annihilation only differ a little from that of protons [2]. At the end of the trajectory, antiprotons will mainly annihilate on a high-Z nucleus, releasing 1.88 GeV of energy. A part of this energy is found in form of 4 or 5 pions. From solid angle arguments, 1 or 2 pions may hit the nucleus, introducing a nuclear cascade which in the end causes the nucleus to fragment. These fragments consist mainly of lighter nuclei [3]. Compared to protons, the depth dose curve of antiprotons is similar in the plateau region, but exhibits a dramatic increase of dose in the peak region, created by the secondary particles from the annihilation process. In terms of radiobiology, antiprotons have similar RBE as protons in the plateau region, but the RBE is again increasing in the peak region due to the radiobiological properties of the nuclear fragments. In the ACE/AD-4 group we have investigated the radiobiological and dosimetric properties of the antiproton beam [4-7].

Antiprotons at relevant energies are currently only available at CERN. Unfortunately, apart from the mixed particle field, the dosimetry of this beam is further complicated by the compact shape of the beam, as well as the low fluence and the pulsed time structure.

THE ACE/AD-4 EXPERIMENT AT CERN

50 or 125 MeV antiprotons are extracted from the antiproton decelerator (AD) at CERN using the DEM beam line. Usually, about 3×10^7 antiprotons can be extracted every 90 seconds. The beam has a Gaussian shape with a FWHM of roughly 1 cm. The number of antiprotons is measured from shot to shot with a beam current transformer, mounted upstream of the target in the beam line. Depending on the experiment, the beam structure was verified with radiochromic films inserted in the beam. Some online monitoring of the beam is possible via a CCD camera, which is focused on a thin scintillator foil and can provide images of single beam shots.

The biological experiments consisted of irradiation of Chinese Hamster Cells VRNE. The results for a ~50 MeV beam are published in [6].

Alanine Detectors

L-α-Alanine is an amino-acid which forms a radical electron pair when subjected to ionizing radiation. The amount of formation of radicals can be measured non-destructively by electron spin resonance (ESR) spectroscopy, which gives a signal that is proportional to some extent to the received dose. The LET dependence of alanine has intensively been investigated in [8-10]. A model for predicting the response of the LET behaviour of alanine is presented in [11]. We here use the alanine model in conjunction with the calculated mixed particle spectrum from FLUKA 2006.3 [12, 13]. In this manner we are able to predict a response which we then can compare with our measured responses.

The alanine stack is placed into a PMMA phantom, and the incoming beam is degraded with polystyrene disks, producing a 1 cm spread-out Bragg peak. Radiochromic films are used for verifying the beam position. The pellets are ~2 mm thick, except for those located in the Bragg peak, where we use thinner 0.5 mm pellets instead for better spatial resolution.

Results:
We found good agreement between the calculated and measured alanine responses, which are shown in figure 1. Our data are in good agreement in the plateau region, though there seems to be a slight overestimation of the response in the peak region.

*Corresponding author: n.bassler@dkfz.de
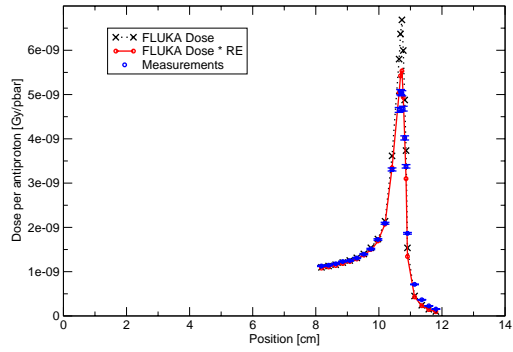
Figure 1: Alanine pellets irradiated with 126 MeV antiprotons. Measurements compared with Monte Carlo calculations.

Ionization Chambers

Ionization chambers cannot be applied directly due to the pulsed structure of the antiproton beam. The 3×10^7 antiprotons exit the AD within 300 ns, which produces a large transient dose rate. Volume recombination becomes significant and a correction factor must be applied. Here we used Boag's two voltage method [14] in order to determine the magnitude of this correction factor. In order to measure a depth dose curve, we placed two Advanced Roos type ionization chamber in the beam. The ionization chambers had a diameter of ~ 4 cm, thereby effectively integrating the entire beam. One ionization chamber was fixed at a position in the entry region, and served as a fluence monitor. The other ionization chamber was immersed in water and mounted on a caliper. This caliper could be moved and provided position readings of sub-mm precision. The acquired charge was translated to dose using a gamma ray calibration factor. This was cross-calibrated towards another Roos chamber, which again was calibrated at a secondary standard laboratory [15]. The charge correction quality factor between ^{60}Co and antiprotons was set to unity. Boag's correction factor was determined at several positions along the depth dose curve using several voltage settings for the ionization chamber, and was interpolated in those positions where the charge only was recorded at one voltage.

Results:
We found excellent agreement between FLUKA calculations and the ionization chamber measurements, after applying Boag's theorem. Results have been submitted for publication.
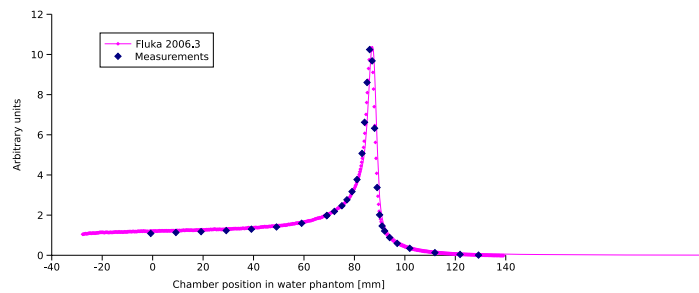
Figure 2 Ionization chamber measurements in a water phantom.

Thermoluminescent Detectors (TLDs)

Stacks of LiF:Mg,Ti were irradiated with antiprotons, attempting to characterize the average LET spectrum in the peak. The pellets were obtained by TLD Poland and were Harshaw equivalent TLD-700 and TLD-600, partially based on ^{7}LiF and ^{6}LiF, respectively, where the latter is also sensitive to

thermal neutrons. The pellets were individually calibrated with gamma rays using a gamma beam from a 6 MV medical accelerator. Relative effectiveness for monochromatic ion beams were found in literature and model calculations were done using the ECLaT model [16].

Results:

Thermoluminescent detectors do not only show a strong LET dependence [17], but do also have a significant dependence on fluence [18], particle type and particle energy [19]. In addition, hysteresis effects are introduced depending on how the pellets are handled [20]. Other handling procedure dependent parameters such as heating rate, annealing procedure, and TL glow curve deconvolution, make it almost impossible for intercomparison of results obtained at other laboratories. This combined with the lack of adequate models which can predict the response, even for monochromatic ion-beams, leaves us to the conclusion that these detectors are too complicated to use in a mixed-particle environment.

DISCUSSION AND CONCLUSION

The results obtained encourage the use of ionization chambers and alanine pellets as redundant dosimeters. After identifying a Monte Carlo transportation code matching our results, we are now able to simulate the dose distribution of various experimental set-ups. Experimental measurements with ionization chambers and alanine pellets can be used to cross check the Monte Carlo calculations. Combining the knowledge of the physical dose with radiobiological experiments, we can extract an RBE for antiprotons. Additionally, we can now use FLUKA to calculate particle-energy spectra along the depth dose line. These data have been extracted and converted to a format for the treatment planning software TRiP. TRiP will then be able to handle antiprotons and will be used for antiproton planning studies. This will possibly lead to a clearer picture of the anticipated clinical benefits.

ACKNOWLEDGEMENTS

REFERENCES

1.   L. Gray and T. E. Kalogeropoulos. Possible biomedical applications of antiproton beams: Focused radiation transfer. *Radiation Research*, **97**:246–252, (1984).
2.   N. Bassler, M. Holzscheiter, H. Knudsen, and the AD4/ACE Collaboration. Cancer therapy with antiprotons. *Low Energy Antiproton Physics-LEAP '05*, *AIP Conference Proceedings*, **CP796**:423–430. American Institute of Physics, (2005).
3.   D. Polster, D. Hilscher, H. Rossner, T. von Egidy, F. J. Harmann, J. Hoffmann, W. Schmid, I. A. Pshenichnov, A. S. Iljinov, Ye. S. Golubeva, H. Machner, H. S. Plendl, A. Grouchulska, J. Jastrzebski, W. Kurcewiz, P. Lubinski, J. Eades, and S. Neumaier. Light particle emission induced by stopped antiprotons in nuclei: Energy dissipation and neutron-to-proton ratio. *Physical Review C*, **51**:1167–1180, (1995).
4.   Michael H. Holzscheiter, Nzhde Agazarayan, Niels Bassler, Gern Beyer, John J. DeMarco, Michael Doser, Toshiyasu Ichioka, Keisuke S. Iwamoto, Helge V. Knudsen, and Bradly G. Wouters. Biological effectiveness of antiproton annihilation. *NIM B*, **221**:210–214, (2004).
5.   Carl Maggiore, Nzhde Agazarayan, Niels Bassler, Ewart Blackmore, Gerd Beyer, John J. DeMarco, Michael Doser, Charles R. Gruhn, Michael H. Holzscheiter and Bradly G.Wouters. Biological effectiveness of antiproton annihilation. *NIM B*, **214**:181–185, (2004).
6.   Michael H. Holzscheiter, Niels Bassler, Nzhde Agazaryan, Gerd Beyer, Ewart Blackmore, John J. DeMarco, Michael Doser, Ralph E. Durand, Oliver Hartley and Bradly G. Wouters. The biological effectiveness of antiproton irradiation. *Radiotherapy and Oncology*, **81**:233–242, (2006).

7. Niels Bassler. *Experimental Studies Relevant for Antiproton Cancer Therapy*. PhD thesis, Aarhus University, (2006).
8. J. W. Hansen and K. J. Olsen. Theoretical and experimental radiation effectiveness of the free radical dosimeter alanine to irradiation with heavy charged particles. *Radiation Research*, **104**:15–27, (1985).
9. K. J. Olsen and J. W. Hansen. The response of the alanine dosemeter to low energy protons and high energy heavy charged particles. *Radiation Protection Dosimetry*, **31**:81–84, (1990).
10. J.W. Hansen and K. J. Olsen. Predicting decay in free-radical concentration in L-α-Alanine following high-LET radiation exposures. *Appl. Radiat. Isot.,* **40**:935–939, (1989).
11. J. W. Hansen. *Experimental Investigation of the Suitability of the Track Structure Theory in Describing the Relative Effectiveness of High-LET Irradiation of Physical Radiation Detectors*. PhD thesis, Risø National Laboratory, DK-4000 Roskilde, (1984).
12. A. Fasso', A. Ferrari, J. Ranft, and P. R. Sala. FLUKA: a multi-particle transport code. CERN-2005-10, INFN/TC 05/11, SLAC-R-773, (2005)
13. The physics models of FLUKA: status and recent developments, La Jolla, CA, USA, March 24-28 (2003). (paper MOMT005), eConf C0303241 (2003), arXiv:hep-ph/0306267
14. J. W. Boag and J. Currant. Current collection and ionic recombination in small cylindrical ionization chambers exposed to pulsed radiation. *British Journal of Radiology*, **53**:471–478, (1980).
15. Özgür M. Kartal. *Cross-calibration of ionization chambers for heavy ion beams*. Institut f`ur Medizinische Physik und Strahlenschutz, FH Giessen, Germany, June 2007. Bachelor's Thesis.
16. O. B. Geiß, M. Krämer, and G. Kraft. Efficiency of thermoluminescent detectors to heavy charged particles. *NIM B*, **142**:592–598, (1998).
17. W. Schöner, N. Vana, and M. Fugger. The LET dependence of LiF:Mg,Ti dosemeters and its applications for LET measurements in mixed radiation fields. Radiation Protoection Dosimetry, **85:**:263–266, (1999).
18. I. Gamboa-deBuen, P. Avilés, M. Rodríguez-Villafuerte, A. E. Buenfil, C. Ruiz-Trejo, and M. E. Brandan. Supralinear response and efficiency of LiF:Mg,Ti to 0.7, 1.5 and 3 MeV protons. *NIM B*, **183**:487–496, (2001).
19. Y. S. Horowitz, D. Satinger, E. Fuks, L. Oster, and L. Podpalov. On the use of LiF:Mg,Ti thermoluminescence dosemeters in space - a critical review. *Radiation Protection Dosimetry*, **106**, (2003).
20. O. Ávila, M. Rodríguez-Villafuerte, I. Gamboa-deBuen, P. Avilés, A. E. Buenfil, C. Ruiz-Trejoand P. Gonzáles, M. E. Brandan, and Y. S. Horowitz. On the correct measurement of relative heavy charged particles to gamma thermoluminescent efficiencies. *Radiation Protection Dosimetry*, **100**:87–90, 2002.

HEAVY-ION RADIOBIOLOGY FOR SPACE RESEARCH

Marco Durante
Dipartimento di Scienze Fisiche, Università Federico II, Napoli, Italy

Cosmic radiation represents one of the main health risks for a safe colonization of the Solar system. The high uncertainty on the biological effectiveness of energetic heavy ions and the lack of simple and effective countermeasures represent the main problems. A large international research effort is currently under way to gather experimental data on the long-term risk caused by exposure to galactic heavy ions. Ongoing experiments focus on late effects in cell cultures or animals exposed to heavy ions at energy below 1 GeV/n. However, most of the dose equivalent in deep space is delivered by heavy nuclei at energies between 1 and 30 GeV/n. Besides, charged particles at energies >1 GeV/n provide a reasonable proxy of the heavy component of the galactic cosmic rays for quantitative assessment of shielding material. The biological effectiveness of these ultrarelativistic ions should be assessed to provide sound health risk estimates for long-term exploratory class space missions.

A. INTRODUCTION

Current programs of space agencies focus on exploration of the colonization of the Solar system, and in particular on manned missions to the moon and Mars. Outside of the shield provided by the Earth's geomagnetic field, crews will be exposed to high-Z and energy (HZE) particles from galactic cosmic radiation (GCR). Each cell nucleus in an astronaut's body during an interplanetary trip would be hit by a HZE particle approximately once a month. HZE particles are very energetic and produce secondary fragments when they interact with target atomic nuclei in the spacecraft walls. Therefore, shielding of GCR can only partly reduce the exposure and, within our current knowledge of heavy-ion risk, does not provide a solution of the problem. Heavy ions are generally considered more effective than sparsely ionizing radiation for the induction of late effects, including cancer, but the uncertainty is very high. Using standard methods for cancer risks projections based on the double detriment life table for an average population and a radiation induced cancer mortality rate scaled to the data from Atomic bomb survivors, radiation risks for extended missions to the moon and the Mars exploration mission are shown in Table I [1]. In this Table, 95% confidence intervals are reported that take into account the uncertainties in space environments, biological effectiveness factors and dose-rate effects. Acceptable levels of risks for astronauts are typically set at 3% fatal risk, however the large uncertainties in projections and the likelihood of other fatal or morbidity risks for degenerative diseases precludes a go no-go decision for Mars exploration at this time.

B. GROUND-BASED STUDIES

Uncertainty in risk estimates can only be reduced by increasing our scientific knowledge of the biological effects of HZE particles. Radiobiology spaceflight experiments are difficult, expensive, and hardly reproducible. Dose rate in low-Earth orbit is relatively low (below 1 mSv/day), and it is therefore very difficult to assess radiation effects and to separate them from stress response to launch and spaceflight conditions. Most of our knowledge on the risk from exposure to HZE ions comes indeed form accelerator experiments [2]. To undertake ground-based space radiation research special facilities are needed to accelerate ions from protons to iron to relativistic energies. Only a few such facilities exist in the world, and NASA has invested in a new facility at Brookhaven National Laboratory on Long Island, NY [3]. Results flowing from the NASA Space Radiation Laboratory (NSRL) are certainly improving our knowledge of biological effects of HZE nuclei and therefore reducing the uncertainty on health risk. Similarly, the European Space Agency (ESA) is preparing a

Corresponding author: Marco.Durante@na.infn.it

ground-based space radiobiology program exploiting European high-energy accelerators [4].

C. GALACTIC COSMIC RADIATION

GCR originate outside the solar system and impinge isotropically on Earth. Because of their high energies up to 10^{20} eV they most probably originate from supernova explosions, neutron stars, pulsars or other sources where high energetic phenomena are involved. Detected particles consist of 98% baryons and 2% electrons. The baryonic component is composed of 85% protons (hydrogen nuclei), with the remainder being alpha particles (14%) and heavier nuclei (about 1%). Figure 1 shows the abundances of these elements up to cobalt relatively to silicon. Although iron ions are one-tenth as abundant as carbon or oxygen their contribution to the GCR dose is substantial, since dose is proportional to the square of the charge. This is also indicated in Figure 1 [5].
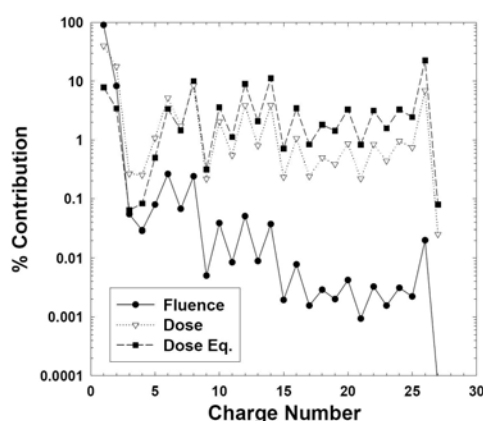
Figure 1. Elemental composition of GCR and relative contribution in dose and dose equivalent [5].

Cosmic ray flux varies between two extremes which correspond in time with the maximum and minimum solar activity. Solar activity and cosmic ray fluxes are anticorrelated. The slope of the energy spectra in Figure 2 for energies below some GeV/nucleon is affected by this modulation of the cosmic ray flux [6]. It is caused by the solar magnetic field, which is coupled to the solar wind. During the minimum of the 11-year solar cycle the solar wind has a minimum strength and its effect on the energy spectra is smaller than at maximum solar activity. Cosmic rays incident on the solar system interact with the solar magnetic field and thus lose energy. This leads to flattened energy spectra at lower energies. With increasing solar activity the maximum of the energy spectrum is shifted to higher energies. At 100 MeV per nucleon the particle fluxes differ by a factor of about 10 between maximum and minimum solar activity conditions, whereas at about 4 GeV per nucleon only a variation of about 20% is observed.

D. PARTICLES FOR SPACE RADIOBIOLOGY

Figure 1 suggests that very heavy ions, especially ^{56}Fe, are of particular interest for space radioprotection, along with lighter nuclei such as carbon, oxygen, and silicon. These particles are indeed currently tested in most space radiobiology experiments [2]. Tests are carried out at high-energy accelerators able to provide biology/medical facilities. Energy is generally below 400 MeV/n when medical accelerators (such as HIMAC in Japan) are used, and up to 1 GeV/n at NSRL. Very few experiments have so far used HZE ions at energies above 1 GeV/n, notwithstanding their abundance in the GCR (Figure 2). In fact, NASA has calculated the contribution in energy to the dose equivalent for different ions in the GCR. Differential spectra are shown in Figure 3 at the solar minimum. Dose from hydrogen and helium display a large fraction at low energy, caused by slow protons and α-particles produced by target fragmentation. For very heavy nuclei, the main contribution comes from energies between 1 and 30 GeV.
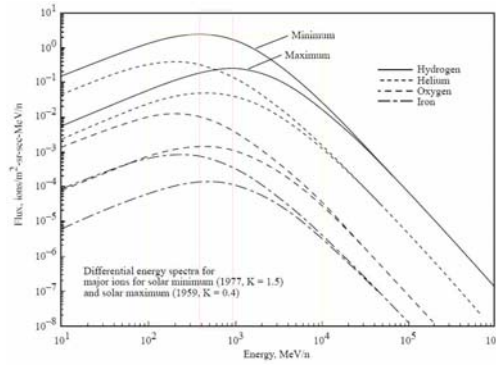
Figure 2.   GCR particle spectra and their modification by solar activity of galactic heavy ion energy spectra at 1 AU as relevant for radiation protection [6].
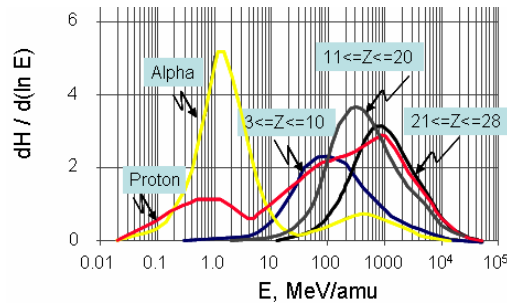
Figure 3.   Annual dose to blood forming organs at solar minimum behind 5 g/cm^2 Al. The differential energy spectrum is broken down for particles of different atomic number. Calculation by HZETRN courtesy of John W. Wilson (NASA Langley).

The contribution of ultrarelativistic (1<E<30 GeV/n; 0.88<β<0.99) particles to the equivalent dose would be even higher at solar maximum, when the energy peaks is shifted to about 2 GeV/n for all ions (Figure 2).

E. BIOLOGICAL EFFECTIVENESS OF ULTRA-RELATIVISTIC HZE PARTICLES

Biological effects of charged particles depends on both the particle LET and atomic number [7]. For iron, the minimum ionization potential is reached around 2 GeV/n, and LET slowly increases at higher energy (Figure 4). Particles with the same charge and LET but different energy will have different track size.
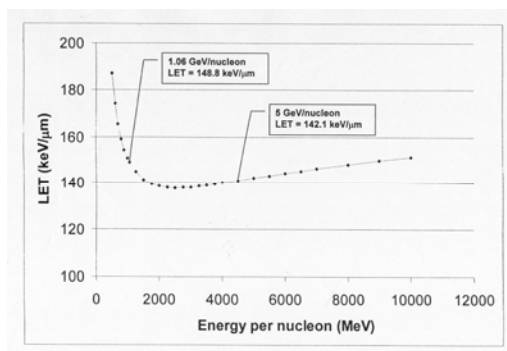
Figure 4. LET in water of iron ions as a function of the energy per nucleon. Plot courtesy of J. Miller (LBL, USA).
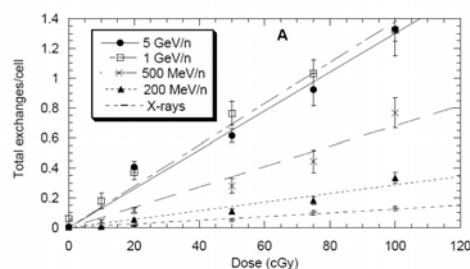
Figure 5. Dose-response curve for the induction of exchanges involving chromosomes 1 and 2 from human lymphocytes exposed to Fe-ions of different energies. High energy ions were accelerated at the Brookhaven National Laboratory (NY, USA), while low energy beams were produced at the HIMAC (Chiba, Japan). Total exchanges were measured by FISH-painting. Plot form ref. [8].

Very few measurements of biological effects of heavy ions at energies above 1 GeV/n are available. Figure 5 reports the induction of chromosomal aberrations, measured by FISH-painting in human peripheral blood lymphocytes exposed to Fe-ions at energies from 0.2 to 5 GeV/n [8]. The effectiveness was the highest for 1 and 5 GeV/n, whose LET is between 140 and 150 keV/μm (Figure 4).

F. SHIELDING STUDIES

Accelerator studies are also important for testing of shielding materials to be used in space. Figure 6 shows Bragg curves of 1 GeV/n Fe-ions produced at NSRL in different materials: polyethylene, considered one of the best shielding material for space radiation, due to its high hydrogen content; aluminum, an essential structural material, but a poor shield for cosmic rays; and two new materials used in inflatable modules, Kevlar and Nextel.

Figure 6. Bragg curves of Fe-ions in different materials. Thickness is expressed in g/cm^2.
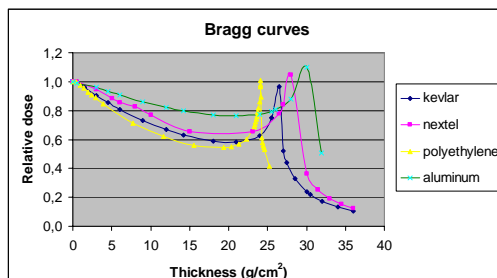
The reduction in dose at thin shields, caused by projectile fragmentation, can be used to compare the effectiveness of the different materials. A comprehensive study using iron at 1 GeV/n has been carried out by Miller and co-workers of the Lawrence Berkeley Laboratory (LBL) and results are shown in Figure 7 [9]. These results beg the question of whether the accelerator tests are limited to a qualitative intercomparison of the shielding materials, or can provide a quantitative estimate of the dose reduction expected in deep space for a given thickness of the shielding material. The LBL group has recently proposed that a good quantitative estimate can be achieved by using ions at energies higher than 1 GeV/n [10]. In fact, Figure 8 shows measurements of dose reduction per unit thickness (areal denisity) using ^{56}Fe ions at different energies on polyethylene. Experimental data are from ref. [8] and [9] and total GCR dose reduction or HZE (Z≥3) only dose reduction in space were calculated by the Monte Carlo code BBFRAG as described in ref. [10].
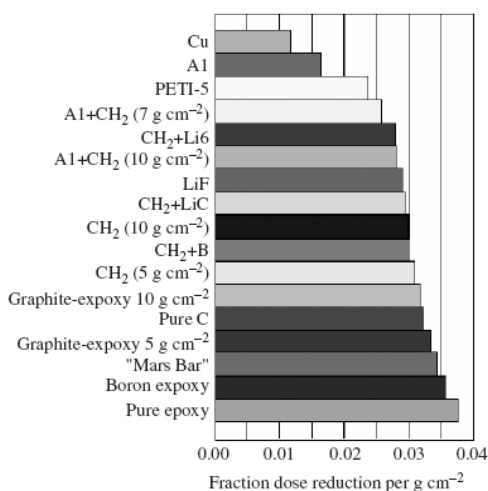
Figure 7. Dose reduction properties of a variety of shielding materials exposed to Fe 1 GeV/n accelerated at NSRL. The fraction of dose reduction per unit mass thickness is derived from the initial slopes of the Bragg curves (see Figure 5). As expected from calculations, lighter hydrogenous materials induce a greater dose reduction. Plot form ref. [9].
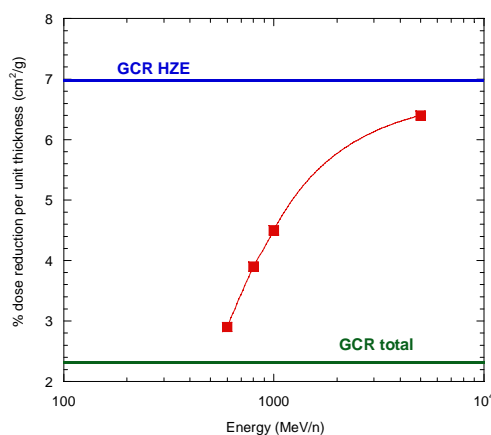
Figure 8. Percent of dose reduction per g/cm^2 of Fe ions in thin polyethylene shields. Data points are measured from Bragg curves in ref. [8] and [9]. Lines are Monte Carlo calculations of the GCR dose reduction in space [10]. The green line includes total GCR, while the blue line is limited to the heavy ion component.

The percent dose reduction per unit target thickness increases by increasing the energy, and it is always higher than the value calculated for total GCR. In fact, over 50% of the dose delivered by the GCR is deposited by H and He (Figure 1), and these light charged particles are almost not affected by thin shields. On the other hand, the calculations relative to heavy ions only in the GCR leads to values slightly higher than those measured. Here indeed the contribution of very high energy ions is relevant (Figure 3), especially because the simulation in ref. [10] assumed conditions close to the solar maximum. The results suggest that heavy ions at energies around 5-10 GeV/n represent an excellent proxy of total heavy ions in the GCR, and can be used to provide quantitative estimates of dose reduction induced by a given shielding material in spacecrafts or planetary habitat modules, at least for thin shields.

G.CONCLUSIONS

Ground-based radiation biophysics studies are necessary for risk assessment in human space exploration. The experiments should exploit heavy ions at high energy to mimic the most hazardous, and less known, component of the space radiation field. Models and measurements suggest that the energy range 1-10 GeV/n should be carefully explored, because most of the equivalent dose to the crews will be deposited by particles in this very high energy range. In addition, heavy ions at this energy represent a reasonable proxy of total HZE in the GCR for ground-based tests of thin shields. At the moment, medical accelerators designed for hadrontherapy (e.g. HIMAC) can cover the range up to 500 MeV/n, while the NASA Space Radiation Laboratory at the Brookhaven National Laboratory can reach 1 GeV/n. An exceptional opportunity to boost research in this field in Europe comes from the construction of the new Facility for Antiproton and Ion Research (FAIR) at GSI in Darmstadt (Germany) [4]. This novel accelerator will result from a combined effort of Germany and several other countries, and will present unique opportunities for space radiation research, including the ability to produce ions with energies up to 45 GeV/n together with a raster scanning system for the delivery of the dose in selected fields. Fully operative in 2015, FAIR is potentially a formidable tool for research in space radiation. A program in space radiation research (BIOMAT, also including heavy-ion radiobiology and material research) has been approved by the FAIR steering committee [11]. This program involves a large international collaboration, including users from Europe, USA, and Japan with different experimental proposal in the field of space radiation biology and physics.

REFERENCES

1. Cucinotta FA, Durante M. Cancer risk from exposure to galactic cosmic rays: implications for space exploration by human beings. *Lancet Oncol.* 7, 431-435, 2006.
2. Durante M, Kronenberg A. Ground-based research with heavy ions for space radiation protection. *Adv. Space Res.* 35, 180-184, 2005.
3. Lowenstein DI, Rusek A. Technical developments at the NASA Space Radiation Laboratory. *Radiat Environ Biophys* 46, 91-94, 2007.
4. Durante M, Kraft G, O'Neill P, Reitz G, Sabatier L, Schneider U. Preparatory study of a ground-base space radiobiology program in Europe. *Adv. Space Res.* 39, 1082-1086, 2007.
5. Schimmerling W, Cucinotta FA, Wilson JW. Radiation risk and human space exploration. *Adv. Space Res.* 31, 27–34, 2003.
6. Badhwar GD. The radiation environment in Low Earth Orbit. *Radiat. Res.* 148, S3-S10, 1997.
7. Scholz M, Kraft G. Calculation of heavy ion inactivation probabilities based on track structure, X-ray sensitivity and target size. *Radiat. Prot. Dosim.* 52, 29-33, 1994.
8. Durante M, George K, Gialanella G, Grossi G, La Tessa C, Manti L, Miller J, Pugliese M, Scampoli P, Cucinotta FA. Cytogenetic effects of high-energy iron ions: dependence on shielding thickness and material. *Radiat Res* 164, 571-576, 2005.

9. Zeitlin C, Guetersloh S, Heilbronn L, Miller J. Shielding and fragmentation studies. *Radiat Prot Dosim* 116, 123-124, 2005.
10. Guetersloh S, Zeitlin C, Heilbronn L, Miller J, Komiyama T, Fukumura A, Iwata Y, Murakami T, Bhattacharya M. Polyethylene as a radiation shielding standard in simulated cosmic-ray environments. *Nucl Instr Meth* B252, 319-332, 2006.
11. Durante M. BIOMAT. Biophysics collaboration: applications of relativistic heavy ions in radiobiology and space radiation protection. *FAIR Newsletter* 3, 11-13, 2006.

Table 1. Calculations of effective doses, % risk of death from fatal cancer, and 95% CI for lunar or Mars missions. Calculations are at solar minimum where GCR fluence is highest for a 5-g/cm^2 aluminum shield. The absorbed dose, D and Effective dose, E are averaged over tissues prominent for cancer risk[2], and competing causes of death are treated in the risk calculation, compressing the distribution of risk probabilities at larger values (>5%). Adapted from ref. [1]

Exploration mission	D, Gy	E, Sv	Fatal Risk(%)	95% CI
Males (40 y)				
Lunar (180 d)	0.06	0.17	0.68	[0.20, 2.4]
Mars swingby (600 d)	0.37	1.03	4.0	[1.0, 13.5]
Mars exploration (1000 d)	0.42	1.07	4.2	[1.3, 13.6]
Females (40 y)				
Lunar (180 d)	0.06	0.17	0.82	[0.24, 3.0]
Mars swingby (600 d)	0.37	1.03	4.9	[1.4, 16.2]
Mars exploration (1000 d)	0.42	1.07	5.1	[1.6, 16.4]

PARTICLE-INDUCED PHOSPHENE STIMULATION IN HEAVY-ION TUMOR THERAPY

O. Kavatsyuk[1,2,*], D. Schardt[1] and M. Krämer[1]
[1]Gesellschaft für Schwerionenforschung (GSI), Darmstadt, Germany
[2]National Taras Shevchenko University of Kyiv, Ukraine

Many patients with tumours located in the skull base reported visual sensations ("phosphenes") during radiation therapy with ^{12}C ions at GSI Darmstadt. These effects, mostly described as streaks moving through the field of vision, occur only during well-defined time-phases of the raster-scan irradiation and they are related to the actual position and stopping range of the pencil-like ion beam. An attempt was made to correlate the phosphene observations with temporary local dose deposition near the eyes or sensitive structures of the visual system. First results based on a pushbutton study with a total of 39 patients indicate that phosphenes are mainly stimulated by local dose deposition in the eye or substructures in the eye (presumably the retina). No phosphenes were observed in a number of cases, where the optic nerves were located partly in the treatment volume but the eyes were clearly outside the radiation field,.

INTRODUCTION

The phenomenon of visual sensations (phosphenes) induced by energetic particles in the cosmic radiation was reported for the first time by astronauts of the Apollo-11 mission in 1969 and then in later space flights. These light effects were usually described as flashes, streaks or dots. Under terrestrial conditions similar effects were observed by volunteers in accelerator experiments but also by patients undergoing radiation therapy with photons or particle beams.

An experiment by McNulty *et al.* in 1978 [1] using carbon ions with energies above and below Cherenkov threshold showed that large diffuse flashes appear due to Cherenkov radiation, whereas points and streaks seemed to be caused by direct ionisation (without photons) of the retina. In 1978 Gramenitsky and Fetisov [2] performed an experiment with protons of different energies and arrived at the conclusion that the Cherenkov radiation in the human eye is the predominant effect.

Many of the patients with skull base tumours (chordomas and chondrosarcomas) treated with carbon ions at GSI-Darmstadt reported bright visual sensations during irradiation which seem to be similar to phosphene observations in space. Typical patterns of phosphenes sketched by the patients are shown in Fig.1.

The present study attempts to establish correlations of phosphene stimulation with local dose deposition near sensitive structures of the visual system, e.g. retina, optic pathways or visual cortex. The raster-scanning system with a pencil-like beam used in the heavy-ion therapy unit at GSI offers unique conditions for such investigations as the dose is delivered dynamically point-by-point and the beam position and penetration depth can be traced in real-time. The beam energies used in patient irradiations are in the range of $80 - 400$ MeV/u and are well below the threshold (≈ 480 MeV/u) for production of Cherenkov light in the vitreous body of the eye, which was reported in previous studies with relativistic carbon ions and protons as a dominating effect [1-3]. Apparently, in our studies other mechanisms of radiation phosphene stimulation such as direct retina stimulation, effects in optical pathways or in the visual cortex are involved. Up to now the phosphene study at GSI includes a total of 39 patients.

*Corresponding author: o.kavatsyuk@gsi.de
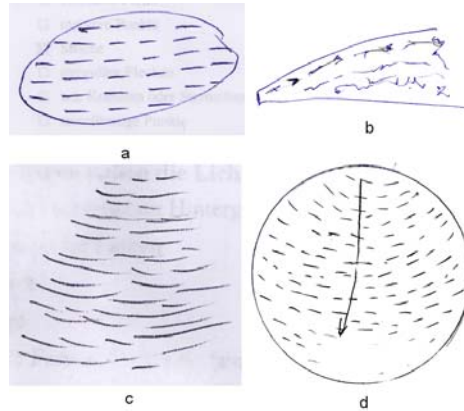
Figure 1.Examples of phosphene observations sketched by the patients in their questionnaires. Most candidates describe phosphenes as streaks, moving quickly in lateral or vertical direction. The quick movement is caused by the scanning motion of the carbon beams.

EXPERIMENTAL SET-UP

For the present studies at GSI selected patients were asked to press a pushbutton instantly at the moment of phosphene observation. The pushbutton events were recorded by a CAMAC data acquisition system in listmode with 10 ms time tagging together with all relevant data of the irradiation in this instant. This included the actual scan point position, energy, intensity and focus setting of the carbon beam. One treatment field has typically 10,000 – 20,000 scan point positions. As most patients were treated with 20 fractions (1 fraction per day) it was possible to repeat the phosphene measurements at different treatment days.

DATA ANALYSIS

Pushbutton results

As a first step in the analysis it was checked whether the phosphene observation was time-correlated with the beam pulses. The carbon beam is delivered by slow extraction of the bunches circulating in the GSI synchrotron. One complete extraction takes about 2 s, followed by a pause of 3 s until the next spill arrives. In addition, the therapy control system includes a fast beam interrupt device that is activated each time when the irradiation of one slice of the target volume is completed.

The patients were asked to press the button once at the first moment of a phosphene sensation. This seemed to be the most practical way in view of the short beam pulses. The data analysis showed that in most cases all signals of the patients occur either within a beam pulse or (in case of very short beam pulses) shortly after, reflecting the patient's reaction time (see Fig.2).
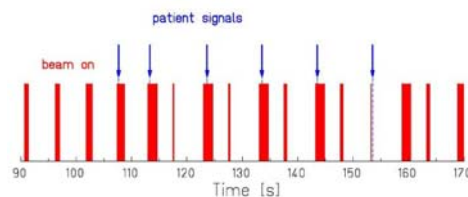
Figure 2. Time correlation of phosphene observation and beam pulses.

In the next step the correlation of phosphene observation and energy steps, corresponding to iso-range slices in tissue, was examined. Each slice corresponds to a pre-defined specific energy of the ^{12}C ions. In the example shown in Fig.3, the irradiation included 25 different beam energies from 150 to 250 MeV/u. The pushbutton events indicating phosphene observation occur only in those slices with

local dose deposition near the eyes. Repeated measurements at seven different treatment days (patient irradiation with the same treatment plan) show good reproducibility of the pushbutton measurements.
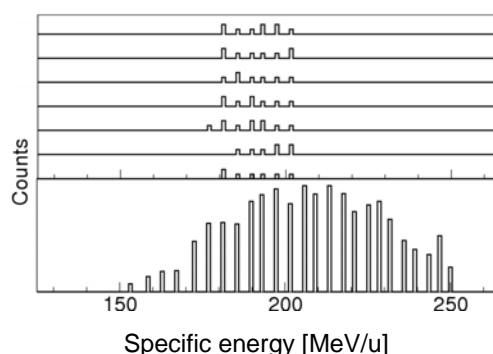
Figure 3. Correlation of phosphene observation for *Patient A* with carbon ion energy steps, obtained from pushbutton measurements performed at seven different treatment days (upper histograms). Each energy step corresponds to a well-defined depth in tissue of the Bragg peak. Counts displayed in the upper histograms indicate phosphene observation during the corresponding treatment slice. The height of the bars is not relevant here.

In Fig.4 an example of the beam scanning path for one energy/depth for *Patient A* is shown (view perpendicular to the beam direction). Preliminary analysis taking into account human reaction time leads to the conclusion that *Patient A* observes phosphenes during the first scan points in this slice. These upper points correspond to anatomical locations near the eyes of the patient.
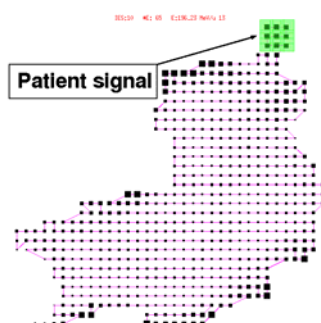
Figure 4. Beam scanning path for one slice of carbon ion irradiation of *Patient A*. The area marked in green is correlated with phosphene stimulation, based on pushbutton time analysis.

The treatment plans (two fields) for the same patient are shown in Fig.5 superimposed to the corresponding transversal CT slices. The target volume is indicated by a red contour line. The colours correspond to 90% (orange), 75% (yellow), 50% (green), 30%(light blue) and 10%(blue) of the target dose.
Patient A reported phosphenes only for the treatment field in Fig.5a where a small dose was located in the left eye (probably affecting the retina). This region corresponds to the green area marked in Fig.4. There was no phosphene observation when the dose covered the optical nerves but not the eye directly (Fig.5b). Note that the optical nerves are located close to the target volume at a dose level of 50- 75%.
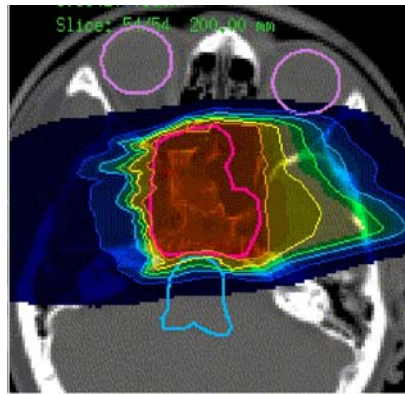
a) *Patient A*: Phosphenes
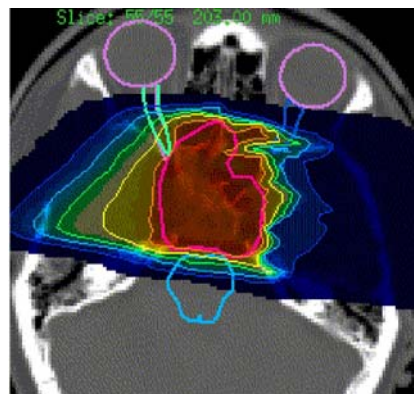
b) *Patient A*: No phosphenes

Figure 5. Planned physical dose distributions for a two-field treatment for *Patient A*. The beam enters from left in plan (a) and from right in plan (b). Phosphenes were observed for field (a) only.

Questionnaire results

In addition to the pushbutton recordings, the candidates were asked to fill in a questionnaire with detailed information of the phosphene observations, indicating the form (dots, strikes, streaks etc.), colour, behaviour and position in the visual field. 78% of the patients describe phosphenes as streaks and 22% as comets or stardust. 83% report white colour on black background, 17% light-yellow and 17% see different colours. Nearly all patients who answered the question about phosphene motion (70%) report quickly moving streaks/lights. Decreasing brightness of the phosphenes in the course of the RT (normally 20 days) is reported by most patients. Moreover, 26% of patients reported other sensations (mostly smell or taste) during irradiation.

CONCLUSION

First results of correlation measurements using a pushbutton method to record the time of phosphene observation by the patient together with detailed data of the dynamic scanning beam delivery system at GSI indicate that phosphenes are mainly stimulated by local dose deposition covering parts of the eye. Further analysis is in progress in order to find out whether substructures of the visual system causing the phosphenes can be identified.

REFERENCES

1. P.J. McNulty et al., Science 201 (1978) 341.
2. P.V. Gramenitsky and I.N. Fetisov, Radiobiologica 27 (1987) 133.
3. K.D. Steidley, Vision Res. 30 (1990) 1139.

ANALYSIS OF THE FACTORS THAT DISTURB DOSE CONCENTRATION IN CARBON BEAM THERAPY

Koichi Maruyama[1], Toru Kawabata[1], Kenki Mukai[1], Takatsugu Magara[2], Mitsutaka Kanazawa[3], Kazushige Maeda[3]

1) Graduate School of Medical Sciences, Kitasato University, Sagamihara, Japan
2) Department of Radiology, National Kanagawa Hospital, Hadano, Japan
3) National Institute of Radiological Sciences, Chiba, Japan
4) Graduate School of Science, Tohoku University, Sendai, Japan

Abstract **It is important for heavy ion therapy to evaluate the contribution from the fragmentation reactions. In the previous research, we established a method to identify fragmentation reactions on an event-by-event basis, and we improved this method to evaluate the following quantities: energy dependency of cross sections and the distribution of charged particle multiplicity in fragmentation reactions. The results are compared with Monte Carlo simulation calculations incorporating with two theoretical models (JQMD and Binary Cascade Model) of fragmentation reactions. The calculation reproduced experimental cross sections. The observed charged particle multiplicity distributions are not reproduced by the calculation. In order to apply this method to more realistic examples, we made two types of phantoms: a water phantom and a layered lung-cancer phantom. Measurements and calculations are compared in these cases.**

Introduction

Since 1994, clinical trials for carbon-beam therapy have been successfully carried out at HIMAC, Japan, and the Ministry of Health, Labor and Welfare approved a part of protocols as the advanced medical therapy in 2003. This treatment offers two advantages over conventional radiation therapy: better dose concentration due to the Bragg peak and higher RBE. However, there is the nuclear fragmentation reaction that might harm these advantages. These reactions cause the decrease of the number of incident carbon nuclei and they generate fragments that might be harmful to normal tissue. Therefore, it is necessary to estimate the effects accurately in the treatment planning. For the estimation, models that theoretically simulate fragmentation reactions are necessary.

While, the application of Monte Carlo simulation (Geant4[1]) to carbon beam therapy is in progress. In Geant4, there are two types of fragmentation models (Binary Cascade Model[2] and JQMD[3]), of which correctness are not yet established. The purpose of this study is to estimate the correctness of two types of models by evaluating these physical quantities experimentally and comparing them with calculations by the models.
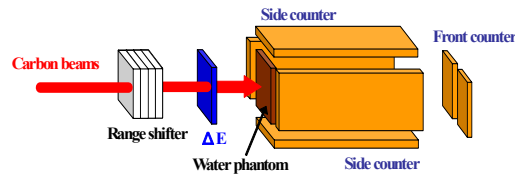
Fig.1 Schematic layout of detectors
The range shifter made of PMMA is to degrade incident energies by changing its thickness. ΔE identifies the type of incident particle. Six counters (four side counters and two front counters) surrounding the target are to detect charged particles generated by fragmentation reactions. Photomultipliers are

Otherwise, in the planning of treatment with carbon beam therapy, the dose distribution in the patient's body is calculated based on the data of the depth-dose distribution in water, and it does not take into account the beam attenuation in tissue other than water. There are few experimental methods for verifying the accuracy of the treatment plan.

Another purpose of this study is to establish an experimental method for evaluation of beam attenuation. We developed a detector system and inhomogeneous layered phantoms as a new method of verifying beam attenuation in body.

Materials and Method

1. Materials

The method to detects fragment-particles was performed by applying the method which the Kitasato University group established[4, 5]. Schematic layout of detectors shown in Fig. 1. In this method seven detectors surrounded the target. ΔE counter measure the stopping power and identify the type of incident particle. Another six counter are surrounding target (fragment detectors: four side counters, two front counters) detect charged particles generated by fragmentation reaction in target. If incident particles occur fragmentation reaction, charged particles hit into fragment detectors. On the other hand if incident particles don't occur fragmentation reaction, charged particles aren't generated and don't hit into fragment detectors. ΔE counter and side counters, front counters were composed by thin plastic scintillator (BC-400,BICRON) and photomultiplier tube (H6410,HAMAMATSU).

A. ΔE counter

Because the range shifter made of PMMA is to degrade incident energies its thickness at HIMAC, charged particles another ^{12}C mingle in incident beam. Therefore ΔE counter placed in front of target identifies incident particle by measuring its energy deposit and using difference of its stop energy(shown in Fig. 2).
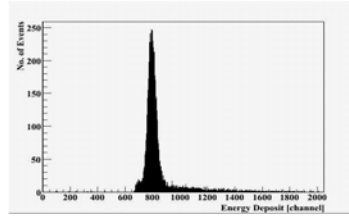
Fig. 2 Energy spectrum of ΔE counter

B. Fragment detectors

Fragmentation reactions in target cause a reduction in the energy deposit in target when the nuclei are fragmented into charged particles and neutral particles such as protons and neutrons. One can assume, however, that elastic scattering dose not change the total energy deposit. Among the fragment detectors, four side counters were used for the detection of large angle fragments, and two front counters for the detection of forward going particles. Based on a thickness of 5mm, we intended to measure not the neutrals but the charged fragments. Since neither hit positions nor injection angles were measured, only pulse height information.

C. Target

We used graphite(C), water (H_2O) and polyvinyl toluene ((C_9H_{10})$_n$) as target considering human composition ratio[6] in experiments of evaluations of cross section of fragmentation reaction and charge particle multiplicity produced.

We referred the number of registered patients to carbon beam therapy in National Institute of Radiological Science (NIRS) and selected lung-cancer: the number of registered patients is maximum in NIRS, prostate-cancer: the number of registered patients is maximum following lung-cancer. And we reproduce there cancer as four types phantoms using CT images: two lung-cancers (one with lung area, one without lung area) and two prostate-cancers (one with pelvis, one without pelvis) (shown Figs. 3 and 4) as target. The phantom consisted Tough-lung (Kyotokagaku, lung area), Tough-bone (Kyotokagaku : bone tissue) and acrylic (soft tissue) and the plates were stacked along the beam direction. The beam loss in the heterogeneous phantom was compared with that in water, which is used to verify the treatment planning.

①beam→ ΔE 0.5 soft tissue 3.0   ribs 0.5   lung area 9.0   cancer2.0 cm   total 14 cm

Carbon beam：200 [MeV/u]

②beam→ ΔE 0.5   soft tissue 5.0   ribs1.0   cancer2.0 cm   total 8 cm

Carbon beam：200 [MeV/u]
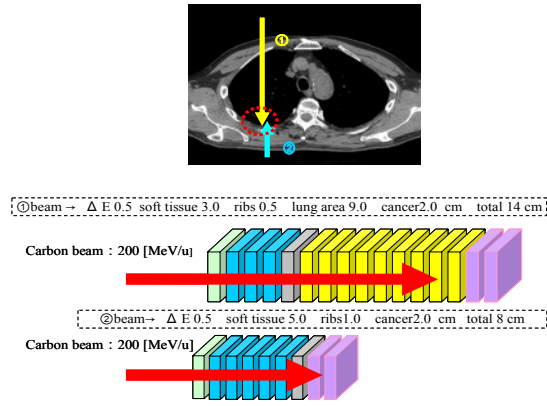
Fig. 3 Inhomogeneous layered phantom for lung-cancer.
Upper: A chest CT image. Beam1 achieves cancer (red circle) through soft tissue, ribs, and lung area. Beam2 achieves soft tissue, ribs. Middle: Schematic view of lung-cancer phantom (with lung area). Lower: Schematic view of lung-cancer phantom (without lung area).

③beam→ ΔE 0.5 soft tissue 4.5   pelvis2.0
          soft tissue 1.5   cancer & prostate 3.0 cm total 11 cm

Carbon beam：250 [MeV/u]

④beam→ ΔE 0.5   soft tissue 8.0   cancer & prostate 3.0 cm   total 11 cm

Carbon beam：250 [MeV/u]
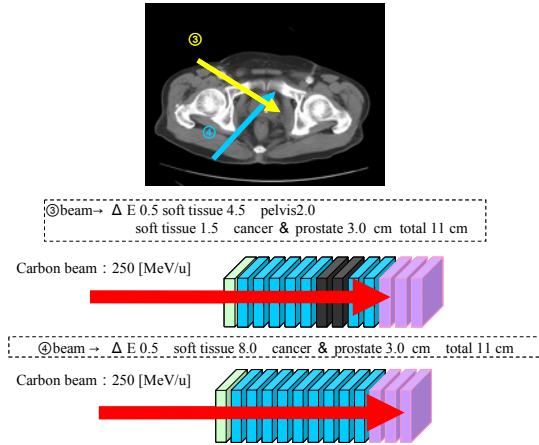
Fig. 4 Inhomogeneous layered phantom for prostate-cancer. Upper: A pelvis CT image. Beam3 achieves cancer through soft tissue, pelvis, and prostate. Beam2 achieves soft tissue and prostate. Middle: Schematic view of prostate-cancer phantom (with pelvis) Lower: Schematic view of prostate-cancer phantom (without pelvis).

2. Experiment

The experiment has done at secondary beam line in HIMAC (Heavy Ion Medical Accelerator in Chiba) at National Institute of Radiological Sciences, Japan. Carbon beam energy used the experiment was 100,150,200,300,350 MeV/u. These energies were coordinated by range shifter. The fragment produced at target detected by fragment detectors. The signal of each detectors obtained by NIM/CAMAC circuit. Data acquired analyzed to lead cross section of fragmentation reaction, attenuation using inhomogeneous layered phantom and charge particle multiplicity produced.

3. Simulation

 Simulation was operated to inspect its legitimacy by comparing results of experiments and simulation. Simulation code we used was Geant4 (Geometry and tracking version4). Gean4 is Monte Carlo calculation code used in field of high energy physics and applied in field of medicine in recent years. Theoretical models of fragmentation we used were two models: Binary Cascade (BC) and JAERI Quantum Molecular Dynamics (QMD) models. We installed Geant4 (Version 4.8.1) on Linux (SUSE Linux Version 9.1) in addition two theoretical models: Binary BC and QMD models was installed on Geant4. Simulation perpetrate on same condition of this experiment. The geometry reproduce by Geant4 is shown in Fig. 5. Results of Geant4 calculation compare with results of this experiment to inspect legitimacies of BC and QMD models. And to evaluate effect of fragment particle to dose distribution, we made dose distributions of every fragmented particles by BC and QMD models.
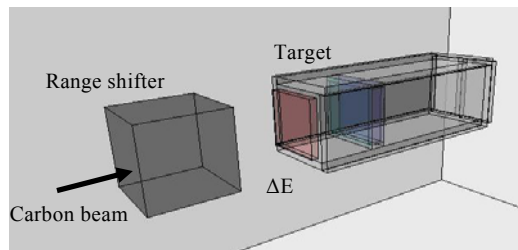
Fig.5 Geometry reproduced by Monte Carlo simulation

Results and Discussion

A. Cross section of fragmentation

  Fragmentation cross section of water is shown in Fig. 6. The cross section was constant in the high-energy range (200-300[MeV/u]), but grew large as energy became low. A similar tendency was provided in the other targets. Comparison of experiment and calculation of water is shown in Fig. 7. The calculated result by BC and QMD models agree with the experimental result within the error range. Therefore, the calculations reproduced measurements.
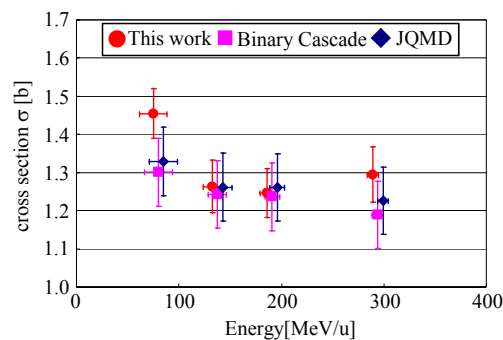
Fig. 6 Fragmentation cross section of water

The cross section was constant in the high energy range (200-300[MeV/u]), but grew large if energy became low.

Fig. 7 Comparison of experiment and calculation of water. The vertical axis divided a calculation result by an experiment result. The calculations reproduced measurements.

B. Charged particle multiplicity

In 150-300MeV/u, the calculation result by BC model reproduced an experiment result by an event of multiplicity 1-4, but did not reproduce an experiment result by an event of multiplicity 5-6 (shown in Fig. 8). QMD model reproduced an experiment result by an event of multiplicity 3, but did not reproduce an experiment result by the other events. The average numbers of H and He in an event are underestimated and that of Be is overestimated in Binary Cascade, while the average numbers of H and He in an event are overestimated and those of Be and C are underestimated in QMD model.
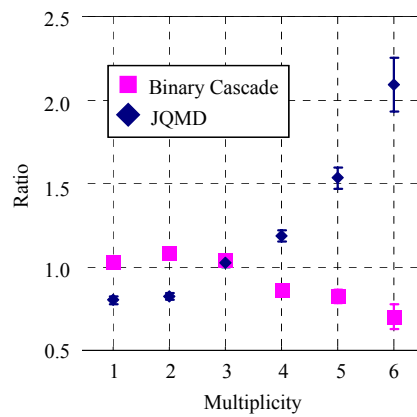
Fig. 8 Multiplicity in water (300MeV/u). The calculations reproduced only some multiplicity events of the experiment.

C. Dose Distributions of Fragmeted Particles

We calculated the dose distributions for each one of H, He, Be and C. As the result, it is shown that the contribution from H is negligibly small and those from He, Be and C are significant. As for He and Be, the contribution was big in the peak of the incident carbon particles, and, as for C, the contribution was big before several cm of the peak of the incident carbon particles. Therefore, the dose of the focus and normal tissue is underestimated or overestimated by the difference of the generation of He, Be and C.

D. Improve the Discrepancy

We discovered the discrepancy among experiment and Monte Carlo simulation.
It is required to improve Monte Carlo simulation models.

E. Inhomogeneous layered phantom

At lung-cancer phantom attenuation of water was 29.7±0.6％,lung-cancer with lung area was 31.7±0.6％,lung-cancer without lung area was 30.2±0.6％.At prostate-cancer phantom attenuation of water was 33.0±0.6％,prostate-cancer with pelvis was 32.2±0.6％,prostate-cancer without pelvis was 33.7±0.6％. Attenuation in water phantom and inhomogeneous layered phantom is shown in Fig. 9. In all phantoms incident beam attenuates about 30％ by fragmentation. The lung-cancer with lung area was higher than water about 2％(relatively 6.7％). Other phantoms correspond with water in error range. Fragmentation depends on atomic mass number. Atomic mass number of lung area is significant lower than it of water. Therefore attenuation in lung-cancer was underestimated. This difference between lung-cancer phantom with water means that the treatment planning using water underestimates the beam attenuation in lung cancer treatment.
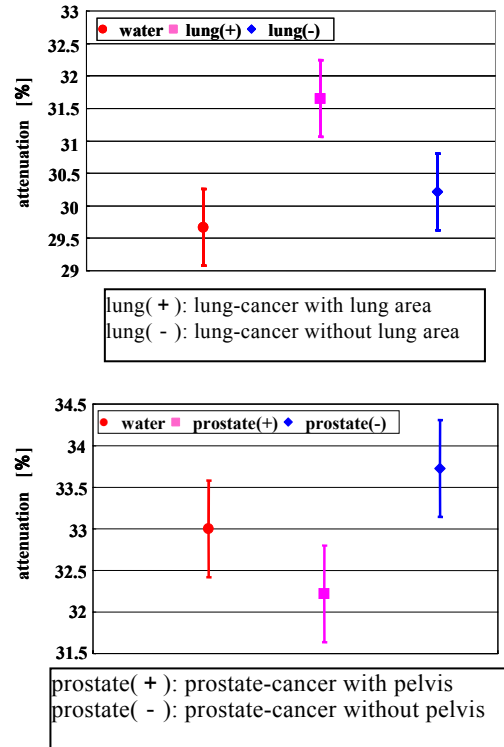
Fig. 9 Attenuation in water phantom and Inhomogeneous layered phantom. Upper is attenuation of using lung cancer phantom. The beam attenuation of lung(+) phantom of about 32 % is higher than the attenuation in water phantom. Lower is attenuation of using prostate cancer phantom. All phantoms correspond in error range.

Conclusions

  We succeeded in the test of the correctness of two types of models in cross section, charged particle multiplicity in fragmentation reactions and the evaluation of the carbon-beam attenuation and fragmentation cross sections in various materials by the method established by the Kitasato University group. The calculations reproduce measurements in cross sections of fragmentation. However, the calculations reproduced only a part of average multiplicities in an event for some type of fragmented nuclei. These should be taken into account for the dose calculation using Geant4 in the treatment planning.

  The beam attenuation in four heterogeneous layered phantoms was evaluated. The results show that it is more effective to verify the beam attenuation in the patient body using our phantom than the water, which is currently used in the treatment planning.

References

1) Agostinelli S, Amako K, Banerjee S et al.: GEANT4 - a simulation toolkit. Nucl. Instrum. Methods Phys. Res. Sect. **A 506**, 250-303, 2003.

2) G. Folger, V. N. Ivanchenko, J. P. Wellisch: The Binary Cascade. Eur. Phys. J. **A 21**: 407-417, 2004.

3) T. Koi, M. Asai, D. H. Wright et al.: Interfacing the JQMD and JAM Nuclear Reaction Codes to Geant4. *eConf* **C0303241**: THMT005, 1-4, 2003.

4) Koichi Maruyama et al.: A Method of Tagging the Nuclear Fragmentation Event Induced by ^{11}C for Cancer Therapy. *IEEE Trans.* **NS 53**(1): 346-350, 2006.

5) Magara et al.: Evaluation of Therapeutic Carbon-Beam Attenuation in Inhomogeneous Layered Phantoms. *Jpn. J. Med. Phys*. **26 Sup. 4**: 173-186, 2007 (in Japanese).

6) International Commission on Radiation Units and Measurements (ICRU): Tissue Substitutes in Radiation Dosimetry and Measurement, ICRU Report **44**, Bethesda, MD, 1989.

DIAMOND DETECTORS FOR HEAVY-ION BEAMS DOSIMETRY

M. Rebisz[*], B. Voss, A. Heinz, M. Ciobanu, M. Kis
Gesellschaft für Schwerionenforschung mbH, Planckstr. 1, 64291 Darmstadt, Germany

We present investigations on the performance of poly-crystalline CVD (pc-CVD) and single-crystal CVD (sc-CVD) diamond based beam-monitors operated as single-particle counters. Synthetic Chemical Vapour Deposition diamond detectors were tested in heavily ionizing ion beams at GSI. At the UNILAC accelerator, ions with energies near the Bragg-Peak have been stopped inside the material whereas at the heavy-ion therapy facility of GSI these detectors are operated in transmission mode and have been studied in a carbon beam from SIS with energies ranging from 80 to 430 MeV/u. In both energy regimes high-bandwidth electronics have been used to count the number of impinging particles. A counting efficiency of $100\pm7\%$ was established. Furthermore, the thermoluminescence (TL) response of synthetic-diamond dosimeters to heavily ionizing particles has been studied.

INTRODUCTION

The treatment of patients in the framework of the heavy-ion particle therapy at GSI is controlled by a set of large area ionization chambers [1]. In order to avoid the need for a daily calibration of these gaseous detectors in terms of 'particles per monitor unit' one could measure the intensity and structure of the pencil-like beam by counting the individual particles. By making these detectors position sensitive one could moreover replace the commonly used multi-wire proportional chambers measuring the position and shape of the sweeping beam in the same time.

The same argumentation applies as well to many other applications, e.g. the irradiation of biological probes at the UNILAC where one has to cope with particle energies in the Bragg-peak region and the fact that the irradiation is done in a fixed field setup.

At both sites, the beam delivery falls into two tasks: control and verification. The first one is an 'online' task the second one may be done 'offline' e.g. by passive detectors such as Thermo Luminescent Detectors (TLD). They are irradiated and afterwards heated emitting light, the intensity of which is proportional to the absorbed dose.

Diamonds have been formerly used in dosimetry as active devices integrating the charge produced by various radiations [2] or as passive thermoluminescent (TL) detectors [3].

One concept which could perform the non-integrating tasks could be to use CVD diamond material in order to count the number of impinging particles in the GHz/channel region. In this way one would profit from the extreme high counting capability which results from the high mobility of the charge carriers [4]. High radiation hardness and a low nuclear charge of the material as well as low thicknesses are required. The detectors have to stay in the beam during the irradiations without degrading the beam quality e.g. by nuclear reactions in the detector material or straggling effects. The most challenging task is then to achieve a sufficiently large signal from detectors with thicknesses of a few 100 μm only.

We present investigations on the performance of beam-monitors based on poly-crystalline CVD (pc-CVD) and single-crystal CVD (sc-CVD) diamond operated as single-particle counters.

For the passive detector application, the favourable properties of diamonds, such as tissue-equivalence, resistivity to radiation, chemical inertness and multiple exposure-readout capability make them attractive to clinical dosimetry applications. The studies on the response of TLD 700 thermoluminescent detectors to heavy charged particles have shown a strong decrease of the TL response if compared to sparsely ionizing radiation [5]. Here we present results on the TL response of pc-CVD diamonds and TLD 100 LiF:Mg,Ti detectors to carbon particles in the energy range of 88-430 MeV/u as used for cancer therapy.

MATHERIAL AND METHODS

For the first 'active' measurements an unpolished 'detector grade' pc-CVD diamond sample called 'D2' was used for online beam monitoring. Further experiments have been performed with sc-CVD diamonds named 'B1' and 'T3'. The characteristics of all diamonds used for the active measurements are presented in Table 1. Before sputtering of the multilayer electrodes the samples were boiled in a solution of KNO_3 in H_2SO_4 aiming for oxidized surfaces decreasing the resistivity of the film

Table 1. Characteristics of the diamond samples used for on-line counting.

Sample	Size [mm^2]	Number of pixels	Pixel area [mm^2]	Contacts
pc-CVD 'D2'	10×10×0.5	1	2.01	Ti / Pt / Au
sc-CVD 'B1'	4×4×0.5	1	6.87	Ti / Pt / Au
sc-CVD 'T3'	3.5×3.5×0.1	3	1.2	Cr / Au

Layers of Chromium (50 nm) / Gold (100 nm) or Titanium (20 nm) / Platinum (30 nm) / Gold (100 nm) form the contacts in parallel plate geometry on opposite surfaces of the detector. The samples were annealed for 15 minutes at 500 °C in an argon atmosphere directly after the metallization.

   Thermoluminescent measurements were performed with commercial '(PC) mechanical grade' pc-CVD diamonds. Before each irradiation a 15 minutes annealing at 510 °C was performed in air in order to reset the samples. They were then stored and irradiated simultaneously in a light-tight box. Read-outs were performed directly after irradiation in a darkroom with a RA'94 TL reader/analyzer equipped with a photomultiplier with bialkali photocathode. A linear heating rate of 5 °C/s was applied from 50 °C to 400 °C.

   Measurements at the UNILAC and SIS facilities of GSI Darmstadt were performed with different ion species, energies and fluencies. Here we show the thermoluminescence TL response of the pc-CVD diamond detectors to high-energy therapeutic carbon beams (88 - 430 MeV/u).

RESULTS

Online counting

To process the signals obtained from the active diamond detectors, an electronic based on a discrete high-bandwidth amplifier (DBA) [6] and alternatively a specially designed ASIC [7] amplified the current signals from the detectors. A 300 MHz Phillips discriminator together with a 225 MHz Phillips scaler served to count the number of detected particles. We tested unipolar as well as bipolar readout chains. Due to the better signal-to-noise ratio, the bipolar electronics based on the ASIC has been finally chosen.

As a result of the online beam-monitoring we achieved a counting efficiency of 95 % for carbon ions with initial energies of 89 MeV/u as shown in fig. 1. At this energy, the mean generated charge is 120 fC from which only 10 to 30 % (depending on the sample) is collected. The electronic threshold was fixed to 8 fC covering 95 % of the collected-charge distribution. The efficiency of the measurement decreases with increasing energy and thus decreasing amount of charges generated inside the diamond samples. In this way, for a fixed setting of the electronic threshold of the ASIC, some of the particles generate a too low signal in the pc-CVD diamond to be detected. For the higher signals obtained at UNILAC (several 100 fC) this problem is not so pronounced. In this place, the multi-hit problematic is the dominating factor that spoils the counting efficiency.

*Corresponding author: M.Rebisz@gsi.de
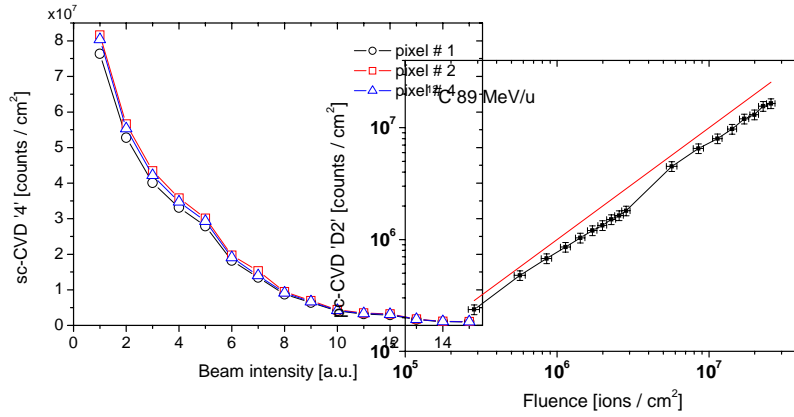
Figure 1: Efficiency of the pc-CVD diamond detector 'D2' for high-energetic carbon ions with initial energies of 89 MeV/u The expected gradient (straight line) is also given. A counting efficiency of only 95 ± 5 % was achieved.
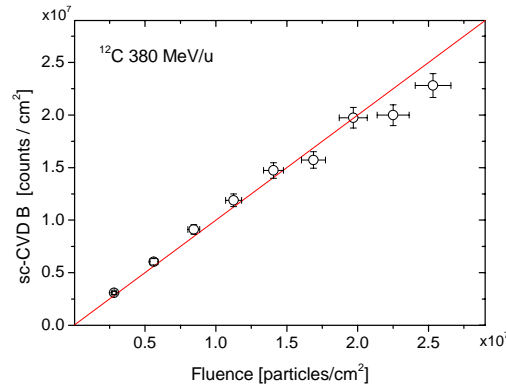
Figure 2: Efficiency of the sc-CVD diamond detector for carbon ions with an initial energy of 380 MeV/u. The linear fit reveals a counting efficiency of 100 ± 7 %.

Due to the smaller amount of internal charge trapping 'sc'-type material offers better charge collection efficiency (CCE), which is the ratio of the charge collected at the electrodes to the charge generated by the traversing particles in the material. Moreover, the pulse-height/-area distributions are more narrow, thus the signal-to-noise (S/N) ratios are better. As a result, improved detection efficiency may be obtained also if compared to poly-crystalline CVD material. Figure 2 shows the relation between the counted and the delivered numbers of particles for carbon ions with an initial energy of 380 MeV/u traversing a detector based on a 483 μm thick sc-CVD diamond. The signal was processed by the NINO ASIC. With this set-up an efficiency of 100 ± 7 % was achieved for a single read-out channel.

In order to be able to adopt the relevant features of the electronics to the requirements of the various experimental surroundings, a dedicated ASIC named PADI was developed [8]. A first prototype of this chip was tested in the framework of the cancer therapy the results are shown in fig. 3. The comparison of the integrated number of counts for 3 pixels on a sc-CVD diamond recorded by PADI for a ^{12}C beam with energy of 88 MeV/u and varying intensity show a difference below 2 %. This uncertainty can be explained by the general accuracy achieved with the irradiation method.

Figure 3: Comparison of the counts from 3 pixels on a sc-CVD diamond detector irradiated with carbon ions with an initial energy of 88 MeV/u with constant focus and varying beam intensity.

Offline TL dosimetry

The response of 60 commercially available synthetic polycrystalline diamonds (pc-CVD) and standard LiF Thermo-Luminescent Dosimeters to heavy-ions was investigated. In figure 4 the glow curve of the 'PC' diamond sample together with that of LiF:Mg,Ti (TLD 100 and TLD 700) detectors obtained after irradiation with C ions with an energy of 430 MeV/u to a dose of 2 Gy is shown.
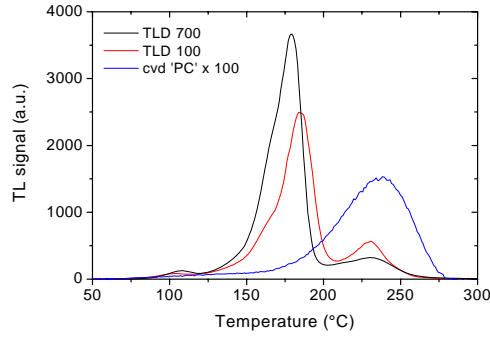
Figure 4: Typical TL glow curve of a diamond detector (scaled up by a factor 100) and LiF:Mg,Ti detectors.

Systematically recorded dose-response curves for high-energetic carbon beams (88 - 430 MeV/u) allowed to determine the relative TL efficiency of dosimeters. This quantity is defined as the ratio of the TL signal per unit dose and unit mass for heavy charged particles to the signal for sparsely ionizing radiation [9].

$$\eta = \frac{\left(TL/D\right)_{HI}}{\left(TL/D\right)_{ref}}$$

Measurements with a reference-radiation source have been done with ^{60}Co and an X-rays lamp. Figure 5 presents the relative efficiency of mechanical grade 'PC' diamonds and LiF dosimeters to carbon ions.
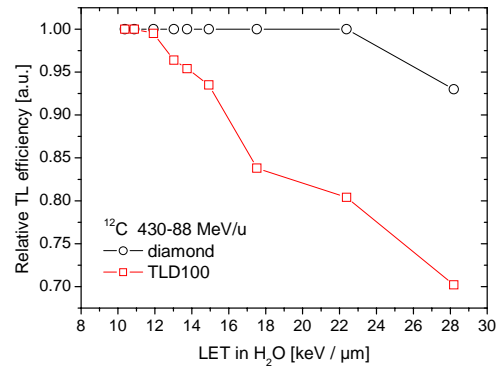
Figure 5: Experimental relative TL efficiency (η) for the pc-CVD diamond and LiF dosimeters as a function of the calculated LET in water.

The decrease of the relative TL efficiency with increasing Linear Energy Transfer (LET) is known for LiF detectors. It is less pronounced for diamond detectors [10]. For irradiations with high-energetic ^{12}C particles (100 – 430 MeV/u) we obtained 100 % efficiency for the pc-CVD detectors. In case of LiF detectors the efficiency decreases to 70 % with decreasing energy to 88 MeV/u and thus increasing deposited energy. This is explained as a saturation effect due to the very high local dose around the ions paths.

There are many instances in medical dosimetry where spatial (3D or 2D) dose distributions need to be measured. For the quality control of the therapeutic-beam parameters online measurements of intensity and profile of the pencil beam are not sufficient and the determination of the resulting dose distribution in phantoms is also necessary to obtain. The measurements of the TL signals of the pc-CVD diamonds and TLD 100 dosimeters for various depth in a phantom made of a stack of 60 PMMA slabs each with 5 mm thickness for the scanning ^{12}C beam are presented. Figure 6 illustrates the depth-dose distribution profiles as the results of two measurements performed with carbon ions with initial energies of 307 MeV/u and 354 MeV/u, for a dose of 1 Gy in the plateau region of the Bragg-curve. The detectors were calibrated with a carbon beam with an energy of 430 MeV/u.
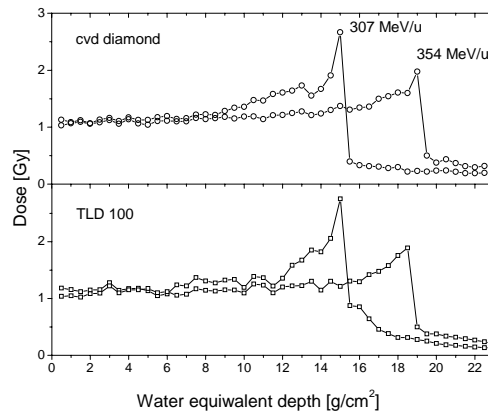
Figure 6: Depth-dose distributions for the 307 MeV/u and 354 MeV/u carbon beams measured with pc-CVD diamond material and TLD 100 LiF detectors.

For both dosimeters tested the Bragg-Peak with its steep fall off is clearly visible. The precision of the dose evaluation suffers from the imperfect positioning of the individual detectors in the phantom along the ions paths. Moreover, the Bragg-Peak is not always recorded with the required accuracy because of the granularity in depth.

CONCLUSIONS

Measurements at the UNILAC and SIS facilities were performed with different ion species, energies and fluencies.

Using sc-CVD diamond for the online counting has been proven to increase the sensitivity and efficiency if compared to pc-CVD material. The counting efficiency of 100 ± 7 % for carbon ions with energies of 88-430 MeV/u was achieved. The newly developed PADI ASIC seems to be a solution for multi-channel readout without the problem of cross-talk between the channels. However, the accuracy of theses measurements has still to be improved in order to cope with the needs of medical devices.

In order to overcome the problems concerning the calibration procedures, measurements with traversing particles and a beam spot size smaller than the active detector area will be performed.

Polycrystalline CVD diamonds were used for the investigation of their TL characteristics after irradiation with heavy ions. Generally pc-CVD shows a stable and reproducible signal with a higher efficiency for heavy-ions but with lower integral output if compared to standard LiF dosimeters. The

first results obtained for TL dosimeters recording beam depth-profiles in a phantom support the potential use of diamonds for 2D and 3D passive dosimetry in future applications.

The two different methods of dose determination require material with different, partially contradictory properties. Thus, depending on the application, the appropriate diamond material has to be chosen.

REFERENCES

1. Kraft G., Nucl. Instr. and Meth. in Phys. Res. A 454 (2000) 1-10.
2. Sakama M., Kanai T., Kase Y., Kamori M, Fukumura A., Kohno T., Phys. Med. Biol. 50 (2005) 2275-2289.
3. Guerrero M.J., Tromson D., Rebisz M., Mer C., Bazain B., Bergonzo P., Diamond Relat. Mater. 13 (2004) 2046-2051.
4. Pomorski M., Berdermann E., de Boer W., Furgeri A., Sander C., Morse J., Diamond Relat. Mater, Vol. 16 (2007), Issues 4-7, 1066-1069.
5. Geiß O.B., Krämer M., Kraft G., Nucl. Instr. and Meth. 142 (1998) 596-598.
6. Moritz P., Berdermann E., Blasche K., Stelzer H., Voss B., Diamond Relat. Mater. 10 (2001), Issues 9-10, 1765-1769.
7. F. Anghinolfi et al., Nucl. Instr. and Meth. in Phys. Res. A, Vol. 533 (2004), Issues 1-2, 183-187.
8. M.Ciobanu http://www.gsi.de/documents/DOC-2007-Mar-64-1.pdf
9. Horowitz Y.S., Avila O., Rodriguez-Villafuerte M., Nucl. Instr. and Methods Phys. Res. B 184 (2001) 85-112.
10.Rebisz M., Voss B., The response of thermally stimulated luminescence in CVD diamonds to heavy charged particles, Radiat. Meas., Feb. 2007, online, in press.

TECHNICAL IMPROVEMENTS OF THE 3D-ONLINE MOTION COMPENSATION SYSTEM FOR SCANNED ION BEAM THERAPY

N. Saito[1,*], N. Chaudhri[1], C. Bert[1], A. Schmidt[1], D. Schardt[1], and E. Rietzel[1,2]

[1]Abt. Biophysik, Gesellschaft für Schwerionenforschung (GSI), Planckstr. 1, 64291 Darmstadt, Germany

[2]Siemens Medical Solutions, Particle Therapy, Hofmannstr. 26, 91052 Erlangen, Germany

An integrated three dimensional on-line motion compensation (3DOMC) system is being developed at GSI to treat moving tumors with scanned ion beams. In comparison to the 3DOMC system of an initial feasibility study [1] major improvements regarding performance, i.e. speed, and reliability of the system have been implemented. We present technical details of the upgraded and integrated 3DOMC system. This includes measurements concerning (i) communication delay, i.e. the time between motion detection and beam adaptation, (ii) accuracy of longitudinal compensation, and (iii) acceleration studies of the linear motor of the longitudinal compensation sub-system.

INRODUCTION

Since 1997 more than 350 patients were treated with carbon ions at GSI using the rasterscanning technique [2]. Excellent dose conformity to the target volume has been achieved in the head, neck, and pelvis. In order to treat also intra-fractionally moving tumors, GSI develops a three dimensional online motion compensation (3DOMC) system to track moving targets with the pencil beam. A feasibility study has been performed [1,3], and basic functionality has been proven for lateral and longitudinal compensation [1,4,5]. The prototype 3DOMC system employs the rasterscanner for lateral target motion compensation and a range shifter to adapt the Bragg peak position longitudinally [1,6].

Recently, the prototype system was upgraded and integrated in the therapy control system (TCS). An overview of the performance of the upgraded system including experimental results with radiographic films, ionization chambers, and biological samples as detectors are presented at this workshop by Bert et al. and Schmidt et al. In the present work, technical details of the upgraded 3DOMC system are reported.

SYSTEM COMPONENTS

The integrated 3DOMC system consists of three sub-systems which are controlled by a CPU installed in the VME crate of the TCS: motion detection, lateral compensation, and longitudinal compensation. A schematic drawing of these components and the data flow are shown in fig. 1. Apart from these essential components a forth subsystem was included to monitor the compensation performance which is essential for technical developments and improvements. The following sections describe the details of each sub-system.

Motion detection

We have two motion detection systems available: a camera based solution and a laser position sensor.

The camera based solution tracks an infrared-light emitting diode (LED) attached to the moving target with a maximum frame-rate of 40 fps. It is read out by a PC, image coordinates are calibrated to room coordinates. The LED position in the image is extracted and sent via a PCI-VME-memory link [5] to the TCS.

The laser position sensor (SICK OD 100-35P840) measures distances at a rate of up to 1 kHz with a resolution of 150 µm. The position signal is encoded in analog voltage. An analogue-to-digital converter (ADC) in the VME crate is used to transfer the motion information to the TCS.

Since the laser sensor can be read out more often and allows more reliable time deterministic data processing than the camera based solution, the laser sensor is used for motion detection and the

---

*Corresponding author: n.saito@gsi.de

camera is mainly as part of the monitoring sub-system.

Lateral compensation

Lateral beam adaptation to the moving target is performed with the scanning magnets by applying an offset (dx, dy) to the nominal beam positions [1,4]. The previous version of the 3DOMC system used a PC to calculate the offset. The values were sent to the TCS via network connection (TCP/IP). The current system uses a dedicated CPU located in the TCS's VME crate. The offset values can thus be communicated to the scanning control unit via VME bus. This upgrade led to significant improvements of data transfer time and therefore stability of lateral compensation. Before the upgrade the system delay for lateral compensation was more than 40 ms [1,4,5]. It was therefore necessary to predict target motion. For the current system the delay time is negligible and motion prediction is no longer needed.
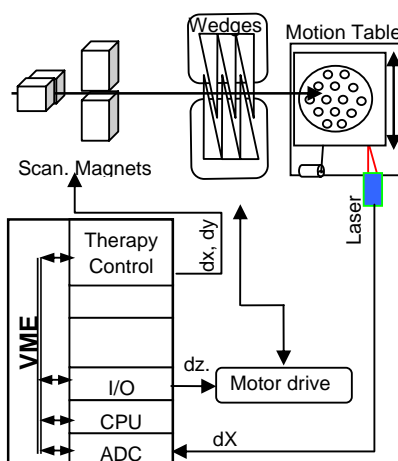
Figure 1: Schematic drawing of the 3DOMC system. The laser sensor measures the motion of a sliding table. Within the VME crate the analogue signal from the sensor is digitalized and processed in the CPU to generate lateral and longitudinal compensation parameters. The lateral beam adaptation parameters, dx and dy, are transfered to the scanning magnet controller within the TCS via VME shared memory. The longitudinal compensation parameter, dz, is sent to the linear motor drive of the range shifter encoded in a bit pattern generated in a digital IO card installed in the VME crate. The bit pattern is transformed to wedge position settings in embedded software on the motor drive.

Longitudinal compensation

Adaptation of the longitudinal Bragg peak position is more challenging than lateral compensation for various reasons. First, the accelerator is currently not suited for fast (i.e. milliseconds) beam energy modulation. We therefore use a passive modulation system installed between beam exit and isocenter. The system reacts slower than the magnetic deflection for lateral motion compensation because the wedge shaped absorbers are moved mechanically. In addition, the amount of depth correction can change remarkably even for adjacent raster points (grid spacing 2-3 mm) whereas lateral adaptation typically follows the smooth target motion.

Range shifter

The prototype 3DOMC system employs a range shifter consisting of two sets of Lucite wedges mounted on linear motors [1,6]. Fig. 2 shows a photograph of wedges and motors. Each set consists of five wedges which are mounted on the linear motors. By overlapping the two sets, the double wedge system currently provides an area of 8 x 15 cm^2 of homogeneous water-equivalent thickness. Details regarding the currently used Lucite wedges are reported in [1]. The range of the traversing ion beams is modulated by moving the wedges apart or together. When the two wedges are moved apart (together) along the linear motor axis, the total amount of absorber material traversed by the ion beams

decreases (increases) which leads to an increased (decreased) range within the target. Maximum range compensation of the current system is ± 50 mm water-equivalence.

Recently, the two linear motors were upgraded by fast servo linear motors (PASIM SB120) with digital servo drives (Elmo Tuba A12/230Q). As can be seen in fig. 2, the motors are mounted on a single linear axis on a granite stone for noise absorption together with linear encoders (Heidenhain LC481). The amount of longitudinal range compensation is calculated in the VME CPU depending on the motion state of the target and sent to the motor drives via logic inputs. Software running on the CPU embedded in the drives converts the compensation parameters in linear motor positions.
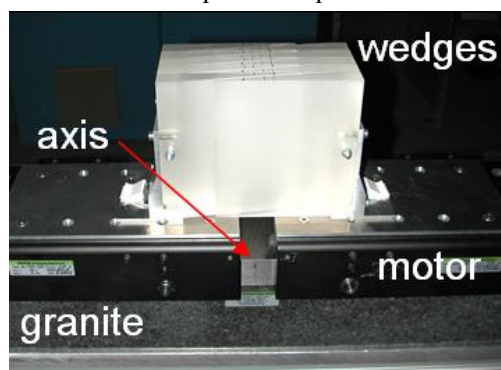
Figure 2: Photograph of the double wedge range shifter system. The Lucite wedges are mounted on linear motors. The motor axis is placed on a granite stone for noise absorption.

Compensation speed

At GSI the typical irradiation time for a raster point is on the order of several milliseconds which defines the timeframe for longitudinal compensation. Before the upgrade, the time to change the thickness was greater than 60 ms independent of the requested range change due to the performance of linear motors and motion controller. By upgrading the linear motors, the acceleration of the motor was improved from 0.6 g to 4 g, where g is the gravitational constant. In water-equivalent units this corresponds to a change from 1 g to 7 g. As an example a depth correction of 5 mm water-equivalence takes about 15 ms with the current range shifter system. Fig. 3 shows a comparison of nominal and measured linear motor positions. A delay of approximately 25 ms including the processing time at the motor drive was observed. This delay is currently mitigated by motion prediction in the calculation process of longitudinal compensation on the VME CPU.
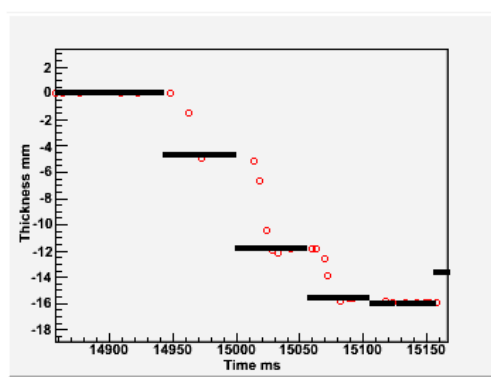
Figure 3: A typical plot of wedge thickness change relative to the reference wedge thickness deduced from measured motor positions (open circles) and nominal positions (lines). For 5 mm water-equivalent range changes delays of 25 ms are observed.

Calibration

Wedge thickness was calibrated with a carbon ion beam by measuring Bragg curves with a range telescope consisting of a water column with variable thickness and ionization chambers at entrance

and exit window [7]. The thickness was measured for five different linear motor settings. The results show good linearity between linear motor setting and measured thickness. A calibration factor from water-equivalence to motor settings was derived for the software embedded in the motor drive.

Homogeneity of the wedge thickness within the 8 x 15 cm^2 compensation area was checked with the range telescope by measurements at five different positions. With the current calibration, a maximum range deviation of approximately 0.7 mm has been observed.

Finally, Bragg curve measurements have been performed for both motion compensated and stationary scenarios to study the accuracy of the 3DOMC system. A maximum range deviation of 0.7 mm in the tail of the Bragg curve was observed. A plot of these measurements is presented by Bert et al at this workshop. Although the range calibration is currently acceptable further improvements are expected.

System monitoring

The purpose of system monitoring is temporally correlated data collection from all other sub-systems, the TCS, and optionally additional devices like motion detection by camera. Since most of the sub-systems have been improved during the upgrade, system monitoring was also required to be updated.

The TCS stores information like measured beam positions and particle deposition for each raster point. The VME CPU dedicated to motion compensation stores motion parameters such as the measured target position and the resulting beam adaptation parameters for each raster point. The linear motor drive records data of motor settings, nominal thickness from the VME CPU, and target position. The data from the motor drive are read out via CANOpen in millisecond intervals by an in-house developed LabVIEW 8.2 application on a PC. This high measurement rate allows recording of the fast wedge movement which can be combined with target motion measurements by the LED/camera motion detection system.

If information of all monitoring devices is combined offline, a detailed and precise analysis of data flow, timing, and compensation precision in the lateral or longitudinal direction can be performed. This is essential for system development, debugging, and further improvements and can be exploited for online monitoring in the future.

CONCLUSION

The 3DOMC system was recently upgraded by replacing most of the sub-systems by dedicated state of the art devices. The communication among the components is sufficiently fast and reliable to perform real time motion compensation in 3D. System performance monitoring has also been improved. It is stable and fast enough to check data for each raster point. Further improvements are currently in progress to provide motion tracking capabilities for more complex and realistic scenarios.

REFERENCES

1. Grözinger, Ph.D. Thesis, TU Darmstadt, Germany (2004)
2. Kraft, Prog. Part. Nucl. Phys. 45 (2000) 473
3. Li et al., Phys. Med. Biol. 49 (2004) 3029
4. Bert, Ph.D. Thesis, TU Darmstadt, Germany (2006)
5. Saito et al, GSI Sci. Rep. 2006 (2007) 360
6. Weber et al., Phys. Med. Biol. 45 (2000) 3627
7. Sihver et al, Jpn. J. Med. Phys. 18 (1998) 1

Poster: Radiobiology 1

CELL SURVIVAL MEASUREMENTS IN THE PRESENCE OF TARGET MOTION

A.Schmidt[1,*], Ch.Bert[1], N.Saito[1], N.Chaudhri[1], G.Iancu[1], C.v.Neubeck[1], E.Rietzel[1,2], W.K.Weyrather[1], G.Kraft[1]

[1]Abt. Biophysik, GSI Darmstadt, Planckstr. 1, 64291 Darmstadt, Germany
[2]Particle Therapy, Siemens Medical Solutions, Hofmannstr. 26, 91052 Erlangen, Germany

A scanned carbon ion beam is used at GSI for treatment of patients with tumors in head and neck, along the spinal cord and in the pelvic region. Tumors which are subject to respiratory motion can currently not be treated because organ motion and scanner motion interplay with each other producing deteriorated dose distributions. Possible motion mitigation techniques are rescanning, gating, and tracking. GSI favors tracking, i.e. an online adaptation of the beam positions to the patient's movement using a recently upgraded 3D-online motion compensation system (see Saito et al. and Bert et al., this workshop). In our experiments the online correction was tested for the first time using a biological detector. Chinese Hamster Ovary cells were seated in MicroWell™ plates which were put into a medium-filled container in upright position. This set-up allows for cell survival measurements at two different depths of the extended Bragg peak in planes perpendicular to the beam direction. A sliding table was used to sinusoidally move the set-up left-right in beam's eye view. Three irradiation scenarios were used. First, and used as reference, cell survival rates were measured with a non-moving, stationary set-up. Second, the set-up was moved but the beam positions were not adapted. Finally, the moving set-up was irradiated with 3D-online motion compensation. The measured survival levels of the compensated irradiation were compared to the results of the stationary reference. In addition, all measurements were compared to the calculations with our treatment planning software TRiP that was recently extended to calculate the biologically effective dose and cell survival in the presence of motion, either with or without 3D-online motion compensation. Our experiments demonstrate that the homogeneous reference survival distribution (scenario 1) was distorted if the beam positions were not adapted (scenario 2). Motion compensation experiments (scenario 3) worked successful, i.e. the reference survival distribution was restored. All measured survival rate distributions were in good agreement with the corresponding calculations.

INTRODUCTION

More than 350 patients mainly with head and neck tumors and lesions along the spinal cord were successfully treated with carbon ions at GSI [1]. The ions are delivered using the raster scanning technique [2]. Tumors which are subject to respiratory motion cannot be treated by simply adding additional margins to account for motion because scanned beam and organ motion interplay. GSI aims to mitigate motion effects by 3D online motion compensation [3,4]. In irradiations with 3D online motion compensation the position of the Bragg peak is adapted in 3D according to the target's motion state relative to a reference position. GSI built a prototype motion compensation system ([3] and Bert et al, Saito et al, this workshop). Cell survival measurements were conducted to validate the performance of the system with a radiobiological detector.

MATERIALS & METHODS

Cell handling

Chinese Hamster Ovary (CHO) cells were used to measure clonogenic survival. The cells were seeded in MicroWell™ plates and placed into a medium filled container under sterile conditions. Survival was measured at selected positions which were chosen prior to the cell analyzing procedure.

---

*Corresponding author: a.schmidt@gsi.de
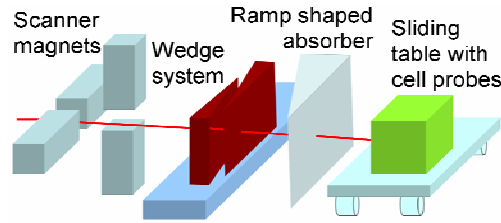
Figure 1: Schematic view of the set-up. As the table moves left-right the lateral beam position is adapted by the scanner magnets. In addition, the beam range has to be adapted by the wedge system, since the laterally adapted beam passes more (or less) material in the stationary ramp shaped absorber.

Set-up

The container was placed on a sliding table which sinusoidally (peak-to-peak amplitude: 4cm, period: 5s) moved left-right in beam's eye view. Because of the stationary ramp shaped absorber placed proximally to the table, lateral motion compensation results in range deviations which have to be adapted simultaneously by the wedge system (see fig. 1). .
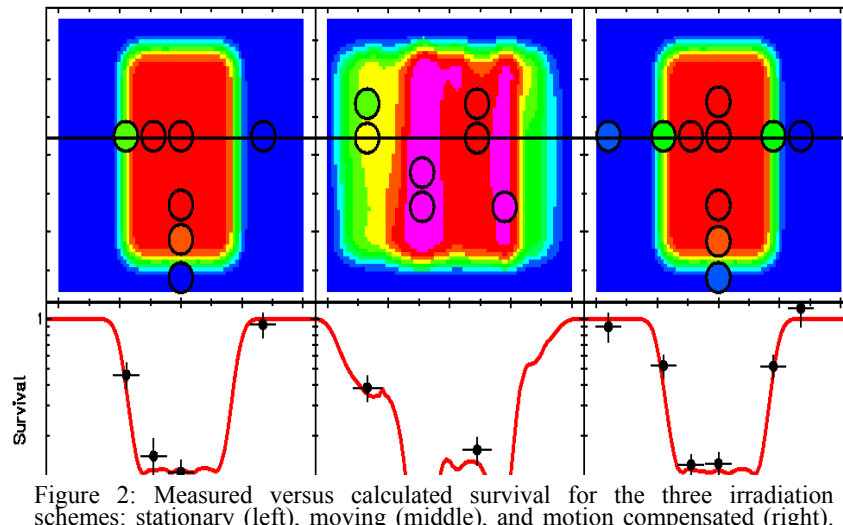
Figure 2: Measured versus calculated survival for the three irradiation schemes: stationary (left), moving (middle), and motion compensated (right). The upper panel shows the calculated 2D survival distribution (blue: high survival purple: low survival). The circles depict position and size of the wells which were analyzed for survival. The color within the circles reflects the measured survival level. The lower panel shows line profiles through the wells as indicated by the black line above. The red line shows the calculated survival level, the data points the measurements. Vertical error bars denote the processing uncertainties of the biological samples. Horizontal error bars denote the size of the wells and the positioning uncertainty.

Experimental procedure

For all experiments a treatment plan was optimized with our in-house planning software treatment planning for particles (TRiP) [5] which uses the local effect model [6] to calculate cell survival. The target area covered a volume of 28 x 45 mm^2 laterally and 23 mm longitudinally.

   With the cell container in the target volume, the plan was applied in three irradiation schemes:

(1) Stationary target: No motion
(2) Non-compensated beam application: The target was moved but the beam position was not adapted.

(3) <u>Compensated beam application</u>: The movement of the table and the resulting depth changes were compensated by the 3D online motion compensation system.

After irradiation, clonogenic cell survival was analyzed for each irradiation scheme. Measurements were also compared to calculations of our treatment planning software TRiP which was extended by 4D functionalities [7] and the possibility to calculate cell survival in the presence of motion. The variation of the relative biological effectiveness at the well positions varies between 1.6 and 2 for both the stationary and the compensated scenario and between 1.5 and 2.6 for the non-compensated irradiation.

RESULTS

All experiments showed good agreement to the calculations (see fig. 2). Motion compensation was successful. The measured survival levels in the compensated irradiation scheme indicate that the dose pattern which was totally distorted in the non-compensated irradiation can be restored with our compensation system. The deviation between calculated and measured survival is comparable to the precision which is achievable with our biological detector system. The experimental data are consistent with measurements of the absorbed dose (see Bert et al, this workshop).

REFERENCES

1. Schulz-Ertner et al., Int.J.Radiat.Oncol.Biol.Phys. (2007) 68
2. Haberer et al., Nucl. Instr. Meth. Phys. Res. A, (1993) 330
3. Grözinger et al., Radiother Oncol. (2004) 73
4. Grözinger et al., Phys. Med. Biol. (2006) 51
5. Krämer & Scholz, Phys. Med. Biol. (2000) 45
6. Scholz et al, Radiat. Environ. Biophys. (1997) 36
7. Bert & Rietzel, Radiat Oncol. (2007) 24

POSSIBLE IMPLICATION OF P53 IN HUMAN TUMOUR CELLS EXPOSED TO ACCELERATED BORON AND NITROGEN IONS

J. Torudd[*], M. R. Edgren, A. R.-M. Jernberg and A. E. Meijer

Departament of Oncology-Pathology, Medical Radiation Physics, Cancer Centre Karolinska, Karolinska Institutet-Stockholm University, P.O. Box 260, SE- 171 76 Stockholm, Sweden

High linear energy transfer (LET) charged particles induce cellular damage that are more severe than damage induced by low LET radiation. Therefore, high LET radiation normally has an increased relative biological effectiveness (RBE) for cell killing.

The damage induced by high LET radiation occur in clusters and give rise to biological signaling that have been shown to induce faster response and progression of apoptosis than low LET. Also, it has been reported that a variety of charged particles are more effective in inducing apoptosis than low LET in cells with different origin and gene status, although there are some conflicting reports on such LET effects.

In general, low LET radiation is a rather poor inducer of apoptosis in tumor cells. One possible explanation of this could be that more than 50% of all tumors have a tumor protein p53 gene mutation, which inhibits cell cycle arrest and apoptosis. However, there are several reports on that accelerated ions with high LET induce apoptosis independently of the p53 gene status of the cell, but there are also some results suggesting the involvement of p53 in high LET radiation-induced responses.

In order to further investigate these contradictive results we are using the established cell lines AA, a melanoma cell line with wild type p53, and a small lung cancer cell line, U-1690, with a mutated p53. The cells were exposed to accelerated boron ($^{10}B^{5+}$, 40, 80, 125 and 160 keV/µm) and nitrogen ($^{14}N^{7+}$, 80 and 140 keV/µm) ions. Samples were collected at different post-irradiation time-points (0, 30 min, 1, 3, 6, 9, 24, 48, 72 and 144 h) following exposures to 1, 2, and 4 Gy. The p53 responses are under investigation using ELISA analysis and the results from these investigations will be presented at the meeting.

CONCOMITANT RADIOBIOLOGICAL EXPERIMENTS FOR HEAVY ION PROSTATE CANCER THERAPY

C. von Neubeck[*], C. Schicker, G. Iancu, W. K. Weyrather

GSI Darmstadt Germany

The risk to come down with prostate cancer increases remarkable with age. More than 90% of the patients are older than 60 years [1]. The cancer therapy with heavy ions seems to be an effective alternative to the conventional radiation therapy in medical treatment of prostate cancer. In this study we started to establish an in vitro model for prostate cancer and the surrounding tissue.

In connection with the on going study on prostate cancer irradiation the cell survival and the cellular response of the affected cell types after exposure to x-ray and carbon ions will be measured.

CELL LINES

The rat prostate cancer cell line R 3327 AT-1 was chosen [2]. The use of this cell line in a parallel animal study allows an in vivo / in vitro comparison. For the normal tissue, which is co-irradiated during the treatment, the small intestine epithelial cell line of the rats (IEC-6) is an accepted model [3].

RESULTS AND OUTLOOK

In the first phase of the project the radiosensitivity of the two cell lines to 250 kV x-ray and carbon ions from UNILAC and SIS are determined. Concomitantly the analytical focus was fixed on numerical chromosomal aberrations in long-term cultivation as well as apoptosis and cell cycle effects. In a next step the two cell lines will be combined in a co-cultivation in order to simulate the border between the normal tissue and the tumour. In addition to the cellular survival of the co-culture after x-ray and carbon radiation, the analytic interest will be focussed on selected cytokines and apoptotic markers.

REFERENCES

1. Volker Rohde, Jürgen Wasem, Alexander Katalinic, Prostataerkrankungen, Gesundheitsberichterstattung des Bundes, Heft 36, Robert Koch Institut, Januar 2007
2. John T. Isaacs, William B. Isaacs, Wouter F.J. Feitz, Jack Scheres, Establishment and Characterization of Seven Dunning Rat Prostatic Cancer Cell Lines and Their Use in Developing Methods for Predicting Metastatic Abilities of Prostatic Cancer, The Prostate 9:261-281 (1986)
3. Andrea Quaroni, Jack Wands, Robert L. Trelstad, Kurt J. Isselbacher, Epitheloid Cell Cultures From Rat Small Intestine – Characterization by Morphological and Immunological Criteria, J. Cell Biology, Volume 80, February 1979, 248-265

SIRNA INCREASES THE RADIOSENSITIVITY OF HUMAN HEPATOMA SMMC-7721 CELLS TO HIGH-LET CARBON IONS

Xiao-Dong Jin[1,2], Li Gong[3], Qiang Li[1,*], Ji-Fang Hao[1], Feng-Tao Su[1,2], Zhong-Ying Dai[1,2], Ping Li[1]

[1]Institute of Modern Physics, Chinese Academy of Sciences, Lanzhou 730000, China

[2]Graduate School of Chinese Academy of Science, Beijing 100039, China

[3]School of Life Sciences, Lanzhou University, Lanzhou, 730000, China

1. Introduction

Survivin is a member of the inhibitor of apoptosis (IAP) protein family that interferes with post-mitochondiral events including activation of caspases[1-3]. Previous studies show that survivin plays a direct role in mediating radiation resistance to X-ray[4,5]. In this study, short interfering RNA molecules were used to decrease survivin expression in radioresistant human hepatoma SMMC-7721 cells, and the radiosensitivity of the cells treated with the siRNA to high-LET carbon ions was investigated.

2. Materials and Methods

Human hepatoma SMMC-7721 cells were maintained routinely in RPMI1640 medium supplemented with 10% (v/v) fetal calf serum. Cells were transfected with survivin-specific siRNA (5'-TGT GCT ATT CTG TGA ATT-3') or mispairing sequence (5'-TAAGC-TGTTCTATGTGTT-3') 24 hours before irradiation. The cells were irradiated with carbon ions (energy: 68MeV/u, LET: 35keV/μm) at doses of 2, 4 and 6Gy, respectively, in the Heavy Ion Research Facility in Lanzhou (HIRFL) at the Institute of Modern Physics (IMP), Chinese Academy of Sciences.

The cellular radiosensitivity was determined using colony forming assay. After irradiation, cells were incubated for 24, 48 or 72 hours. Survivin mRNA expression was measured with real-time PCR (RT-PCR). Cell cycle distribution of SMMC-7721 cells after the combined treatment was detected with FCM, and Annexin V assay was used to determine apoptotic rate.

3. Results

Compared with the un- or mis-transfected cells, there was a significant decrease in survivin expression at mRNA level at 24 hours after irradiation for the transfected cells, which increased again at 48 and 72 hours (see Fig.1). A dose-dependent decrease in survivin mRNA expression was also observed at 24 hours after irradiation. G2/M arrest data were similar to those derived from RT-PCR (see Fig.2). An obvious G2/M arrest at 24 hours after irradiation is shown. However, this G2/M arrest disappeared at 72 hours. Moreover, an increased percentage of apoptotic cells (see Fig.3) and reduced clonogenic survival (see Fig.4) were observed as well.

4. Discussion

In this work, whether survivin also plays a direct role in radio-resistant cell line SMMC-7721 to high-LET carbon ions was investigated. We showed that the attenuation of survivin mRNA expression by siRNA treatment resulted in an increased rate of radiation-induced apoptosis. Transfection with survivin siRNA induced a G2/M arrest, and finally caused an increased radiosensitivity as determined with the clonogenic assay.

These results indicate that the transfection with survivin siRNA could increase the radiosensitivity of SMMC-7721 cells to high-LET carbon ion irradiation.
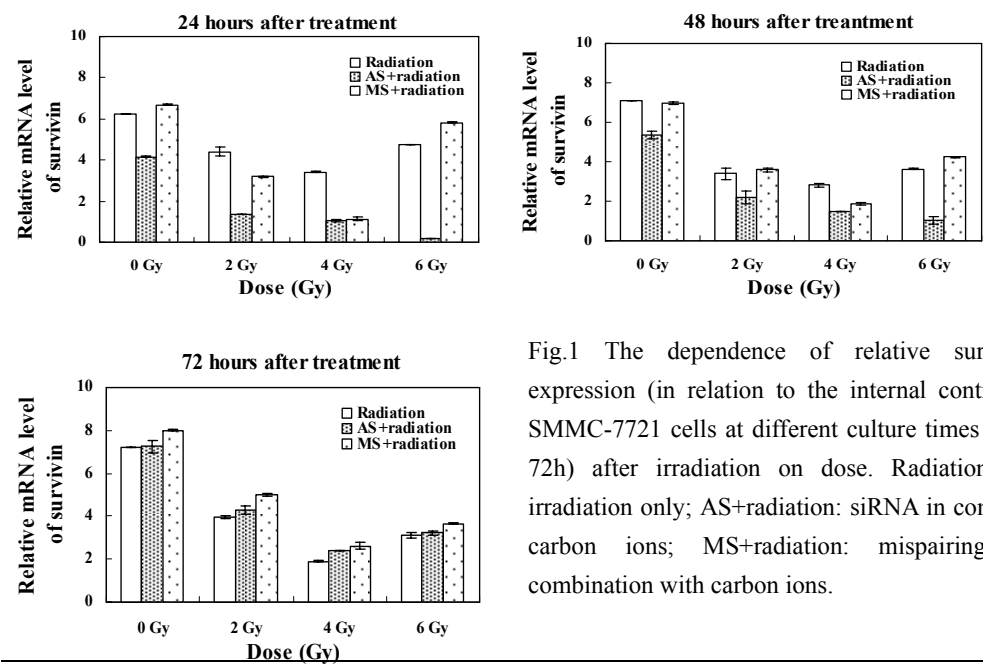
Fig.1 The dependence of relative survivin mRNA expression (in relation to the internal control β-actin) in SMMC-7721 cells at different culture times (24h, 48h and 72h) after irradiation on dose. Radiation: carbon ion irradiation only; AS+radiation: siRNA in combination with carbon ions; MS+radiation: mispairing siRNA in combination with carbon ions.

* Corresponding author: liqiang@impcas.ac.cn

24 h after radiation

48 h after radiation

72 hours after radiation
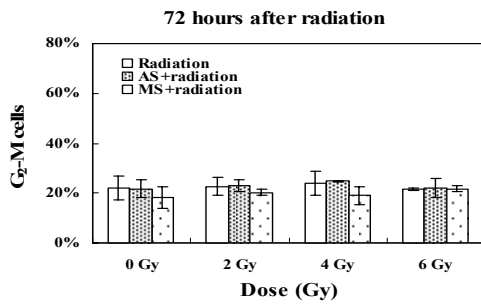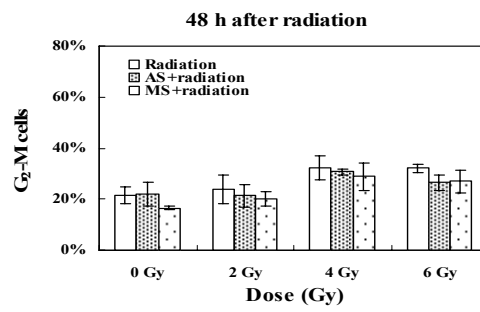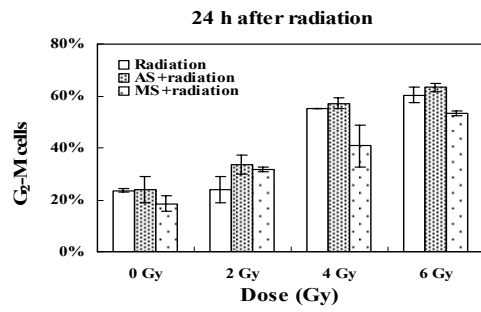
Fig.2 The G_2/M phase percentage of cells treated differently (radiation, AS+radiation, MS+radiation) at various culture times after irradiation (24h, 48h, 72h).

24 hour after radiation

48 hours after radiation

72 hours after radiation
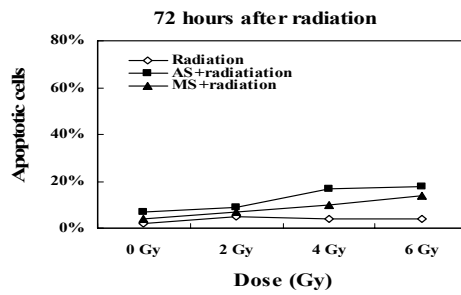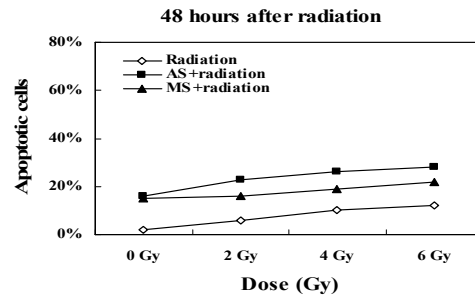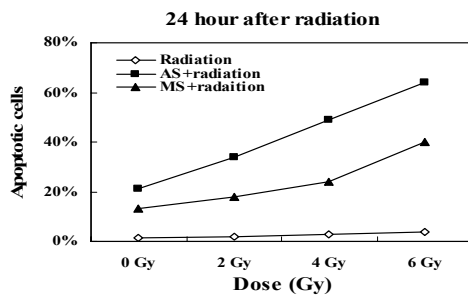
Fig.3 The dependence of the apoptotic rate (compared with the whole cells) of SMMC-7721 cells at different culture times after irradiation on dose.
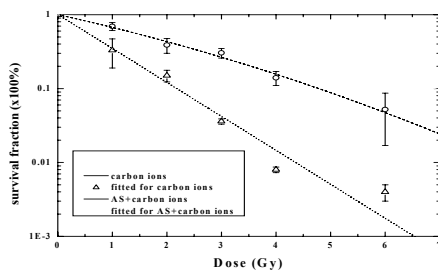
Fig.4 Survival curves of SMMC-7721 cells exposed to carbon ions determined by the clonogenic assay. Cells transfected with the antisense oligonucleotides (AS) show more sensitive to the carbon ion beam.

References

[1] G. Ambrosini, C. Adida, D.C. Altieri, A novel anti-apoptosis gene, survivin, expressed in cancer and lymphoma, Nat. Med. 3 (1997) 917-921.

[2] F. Li, D.C. Altieri, Transcriptional analysis of human survivin gene expression. Biochem J. 344 (1999) 305-311.

[3] G.S. Salvesen, C.S. Duckett. IAP proteins:Blocking the road to death's door. Nat Rev Mol Cell Biol. 2002, 3(6): 401-410

[4] R Claus , H Joachim , G Anke , et al. Spontaneous and Radiation-induced apoptosis in colorectal carcinoma cells with different intrinsic radiosensitivities:surviving as a radioresistance factor. Int. J. Radiat. Oncol. Biol. Phys. 2003, 55(5): 1341-1347

[5] F. Rodel, J. Hoffmann, L. Distel, et al. Survivin as a Radioresistance Factor, and Prognostic and Therapeutic Target for Radiotherapy. Cancer Res. 2005, 65(11): 4881-4887

SMALL DNA FRAGMENTS INDUCED IN HUMAN FIBROBLASTS BY 56FE IONS: EXPERIMENTAL DATA AND MC SIMULATIONS

D. Alloni[a], F. Antonelli[b], F. Ballarini[a], M. Belli[b], A. Campa[b], V. Dini[b], G. Esposito[b], W. Friedland[c], M. Liotta[d], A. Ottolenghi[a], H. G. Paretzke[c], G. Simone[b], E. Sorrentino[b], M. A. Tabocchini[b]

[a] Nuclear and Theoretical Physics Department, Università degli Studi di Pavia, and INFN Sezione di Pavia,Italy

[b] Health and Technology Department, Istituto Superiore di Sanità, and INFN Sezione di Roma1, Gruppo Collegato Sanità, Roma, Italy

[c] GSF, Institute of Radiation Protection, Ingolstädter Landstrasse 1, 85764 Neuherberg, Germany

[d] Physics Department, Università degli Studi di Milano, and INFN Sezione di Pavia, Italy

DNA double strand breaks (DSB) are considered as cellular critical lesions in the processes that, starting from the initial energy deposition by radiation, lead to the formation of relevant biological endpoints such as gene mutations, chromosome aberrations and cell death. The hypothesis that the cellular endpoints are strongly affected by the DSB distribution along the genome, and not only by the total number of DSB, is also widely supported; in fact, the spatial correlation of DSB, in particular the presence of several DSB close to each other, is thought to affect the ability of the cell to repair them. This distribution is in turn determined by the chromatin conformation and by the radiation track structure. High LET radiation is expected to lead to DSB distributions that can considerably differ from those induced by low LET radiation, with important consequences on both radiation protection and radiotherapy.

The DSB distribution can be studied by the evaluation of the DNA fragments that are induced by radiation. In this work we have studied the pattern of DNA fragmentation induced in human fibroblasts by iron ion beams of two different energies: 115 MeV/u and 414 MeV/u. Experimental data have been obtained for fragments belonging to the size range 1-5700 kilo-base-pairs (kbp). Monte Carlo simulations have been performed with the PARTRAC code. We present a comparison, between experimental and simulated data, for the number of fragments produced in four different size ranges: 1-9 kbp, 9-23 kbp, 23-1000 kbp and 1000-5700 kbp. The agreement can be considered satisfactory for both radiation qualities. The other type of result that we present is the evaluation of the RBE for DSB production. For this computation we have used the experimental data (again in the size range 1-5700 kbp) and the simulation results concerning fragments induced by γ-rays. The Monte Carlo simulations give the possibility to count also fragments outside the experimental range; while the number of fragments larger than 5700 kbp is negligible, at the doses considered, the number of fragments smaller than 1 kbp is large for the high LET radiations. As a consequence, we can compute different RBEs, depending on the size range considered for the fragment counting. The PARTRAC evaluation takes into account fragments of all sizes, while the evaluation from the experimental data can consider only the fragments in the range 1-5700 kbp. To further put in evidence the importance of small sizes, we have computed, from the experimental data, also the RBE resulting from the fragment counting limited to the range 23-5700 kbp.

Radiobiology 2

BIOLOGICAL ASPECTS OF ION BEAM THERAPY

M. Scholz[1,*]
[1]Gesellschaft für Schwerionenforschung (GSI) / Biophysik, Planckstraße 1, D-64291 Darmstadt

Besides the high degree of dose conformation to the tumor, the increased relative biological effectiveness (RBE) represents a major rationale for the application of ion beams in radiotherapy. For the biological optimization in treatment planning, the knowledge about the increased effectiveness has to be taken into account as precise as possible. Therefore, methods have to be developed to transfer the knowledge extracted from experimental data *in-vitro* and *in-vivo* to the clinical situation.

The major determinants of RBE are (1,2):

Ion species and energy: In general, RBE increases with LET. As a consequence, RBE is increased in particular in the region of the Bragg peak, whereas at high energies in the entrance channel the RBE is close to one. Furthermore, the increase of RBE in the Bragg peak region is more pronounced for heavier particles like carbon as compared to light particles like protons or helium ions. However, for particles heavier than carbon saturation effects occur in the Bragg peak region and thus lead to a reduction of RBE, diminishing the therapeutic ratio between RBE in the tumour region and RBE in the entrance channel.

Dose level: The increase of RBE towards higher LET values is accompanied by a change of the shape of the dose response curves. Whereas for high energetic particles and lower LET the survival curves are characterized by a linear-quadratic shape similar to that of photon radiation, at high LET value survival curves become more linear. As a consequence, the RBE also depends on the dose level and in general decreases with increasing dose.

Cell / tissue type: RBE also significantly depends on the cell / tissue type and biological endpoint under consideration. In general, repair-proficient cells show higher RBE than repair deficient cells, and similarly different tissues are characterized by different RBE values.

Oxygen effect: Whereas for conventional photon radiation the oxygen status has significant impact on radiosensitivity and hypoxic cells require 3fold higher doses to achieve the same effect as in oxic cells, this difference vanishes or at least is largely reduced for high-LET radiation. Thus, up to three times higher RBE values can be expected for hypoxic cells as compared to oxic conditions.

All parameters substantially vary within a field typically used for ion beam treatment, and thus RBE correspondingly varies and depends on the position in the field. Therefore, strategies have to be developed how to include these dependencies in treatment planning. In principle, two approaches can be followed: an experimental approach and a modeling approach. For the experimental approach, the systematics of RBE has to be measured with high accuracy for a countless number of different irradiation conditions. Therefore, it will be impossible to represent all clinically relevant conditions with respect to beam energies, size of the target volume, dose levels etc. Thus, interpolation or extrapolation of the data is required. Moreover, since only for in-vitro systems the systematics can be measured with sufficient precision, procedures have to be defined how to derive clinical RBE values for more complex tissue systems from the measured in-vitro data.

The second approach is based on biophysical modeling (3,4,5). The goal is to develop a model which should be able to predict the response to charged particle radiation for all clinically relevant situations. These include clonogenic survival as the major determinant of tumor control as well as more complex endpoints like normal tissue complications. The model could be based either on first principles or on a restricted set of input data, for which the model could represent a tool for the extrapolation to the more

general case. If e.g. the photon dose response curve is used as input for the model, it would ultimately allow to link the treatment planning for charged particle beams to the clinical experience with photon radiation. The criteria relevant for implementation of a model in the treatment planning procedure will be discussed.

1. Weyrather,WK et al., Int. J. Radiat. Biol. 75 (1999), 1357
2. Furusawa, Y. et al., Rad. Res 54.(2000), 485
3. Scholz M et al. , Radiat. Environ. Biophys. 36 (1997), 59
4. Elsässer T and Scholz M., Rad. Res. 167 (2007), 319
5. Scholz M and Elsässer T., Adv. Space Res. (2007)

*Corresponding author: m.scholz@gsi.de

Poster: Radiobiology 2

HIGH-LET ION BEAMS ACTIVATE THE TRANSCRIPTION FACTOR NF-κB IN HUMAN CELLS

C.E. Hellweg[1*], C. Baumstark-Khan[1], L.F. Spitta[1], R. Ruscher[1], A. Arenz[1], P. Lau[1], M.M. Meier[1], I. Testard[2], G. Reitz[1]

[1]Institute of Aerospace Medicine, German Aerospace Center (DLR), Linder Höhe, 51147 Köln, Germany

[2]Laboratoire d'Accueil en Radiobiologie avec les Ions Accélérés (LARIA), CIRIL – GANIL, Caen, France

Assessment of health risks for astronauts exposed to cosmic radiation during long-term space missions remains an open question. Knowledge of the cellular response to space radiation components can reduce the uncertainty. Apoptosis plays a major role in cancer induction and in acute responses to high radiation doses. In this work, the involvement of the transcription factor Nuclear Factor κB (NF-κB), which can be antiapoptotic, in the response to high LET ion beams was examined by means of a recombinant reporter cell line. Accelerated argon ions (95 MeV/A, LET 232 keV/μm) activate NF-κB dependent gene expression already at low fluences. This could favor the survival of cells with damaged DNA.

Within the next decades, an increasing number of human beings will be brought into space to accomplish technical and scientific tasks. During space missions, astronauts are exposed to not only greater amounts of natural radiation than they receive on Earth but also to a differing radiation quality, which can result in immediate and long-term risks. In the complex cellular radiation response, the interaction of pro- and antiapoptotic factors plays an important role in acute reactions to high radiation doses and in the development of possible late effects such as cancer after prolonged low dose exposure. The transcription factor nuclear factor κB (NF-κB) is generally regarded as an antiapoptotic factor.[1] As such, if activated in human cells by ion beam exposure, it could influence the cancer risk of astronauts exposed to cosmic radiation or the outcome of ion therapy. In this work, activation of NF-κB by high linear energy transfer (LET) ions was assessed using a stably transfected reporter cell line which expresses the destabilized variant of Enhanced Green Fluorescent Protein (d2EGFP) under control of a promoter containing four NF-κB binding sites.[2]

MATERIALS AND METHODS

The stably transfected human embryonic kidney cells (HEK-pNF-κB-d2EGFP/Neo)[2] were exposed at the French heavy ion accelerator GANIL to argon and carbon ions of different linear energy transfer (LET) as described earlier.[3] The time course of d2EGFP expression and thereby activation of NF-κB dependent gene expression was measured after heavy ion exposure using flow cytometry.

RESULTS

Accelerated argon ions (36Ar, 95 MeV/u, LET 232 keV/μm) activate the NF-κB pathway already at low particle densities (1-2 particle hits per nucleus), which result in as less as 5-50 induced double strand breaks per cell. Accelerated carbon ions (13C, 75 MeV/u, LET 30 keV/μm) induce NF-κB-dependent gene expression at higher particle densities (50-500 particle hits per nucleus), but to a lower extent than the argon ions. Sparsely ionizing radiation such as X-rays activates the NF-κB pathway at high doses (> 4 Gy).[4]

DISCUSSION

These results suggest a LET dependency of NF-κB activation: high LET radiation activates NF-κB more efficiently than low LET radiation. This may favour survival of cells with DNA damage, especially after low doses of densely ionising radiation. Furthermore, by upregulation of inflammatory

target genes such as cyclooxygenase-2 (COX-2), interleukin-6 (IL-6), tumour necrosis factor α (TNF-α), intercellular adhesion molecule 1 (ICAM-1) and vascular cell adhesion molecule 1 (VCAM-1), its radiation-induced activation could promote inflammatory responses and fibrotic changes in the irradiated tissues.

REFERENCES

1. Baichwal VR and Baeuerle PA (1997) Activate NF-kappa B or die? Curr.Biol., 7:R94-R96
2. Hellweg CE, Baumstark-Khan C, and Horneck G (2003) Generation of Stably Transfected Mammalian Cell Lines as Fluorescent NF-κB Activation Reporter Assay. J Biomol Screen 8(5), 511-521
3. Baumstark-Khan C, Hellweg CE, Arenz A, and Meier MM (2005) Cellular Monitoring of the Nuclear Factor kappaB Pathway for the Assessment of Space Environmental Radiation. Rad Res 164, 527–530.
4. Hellweg CE, Arenz A, Meier MM, Baumstark-Khan C (2005) Cellular monitoring systems for the assessment of space environmental factors. Adv Space Res 36, 1673–1679

*Corresponding author: christine.hellweg@dlr.de

HEAVY ION RADIOBIOLOGICAL STUDIES IN THE BRAGG PEAK REGION

J.Czub[1,*], D.Banaś[1,2], A.Błaszczyk[3], J.Braziewicz[1,2], I.Buraczewska[4], J.Choiński[5], U.Górak[6], M.Jaskóła[7], A.Korman[7], A.Lankoff[8], H.Lisowska[8], A.Łukaszek[6,9], Z.Szefliński[6], A.Wójcik[4,8]

[1] Institute of Physics, Świętokrzyska Academy, ul. Świętokrzyska 15, 25-406 Kielce, Poland

[2] Holycross Cancer Center, ul. Świętokrzyska 15, 25-406 Kielce, Poland

[3] Faculty of Physics, Astronomy and Informatics, Nicolaus Copernicus University, Grudziądzka 5, 87-100 Toruń, Poland

[4] Institute of Nuclear Chemistry and Technology , ul. Dorodna 16, 03-195 Warsaw, Poland

[5] Heavy Ion Laboratory, Warsaw University, ul. Pasteura 5A, 02-093 Warsaw, Poland

[6] Institute of Experimental Physics, Warsaw University, ul. Hoża 69, 00-681 Warsaw, Poland

[7] The Andrzej Soltan Institute for Nuclear Studies, 05-400 Otwock-Świerk, Poland

[8] Institute of Biology, Świętokrzyska Academy, ul. Świętokrzyska 15, 25-406 Kielce, Poland

[9] The Main School of Fire Service, ul. Słowackiego 52/54, 01-629 Warsaw, Poland

External ^{12}C and ^{20}Ne ion beams of energies of maximum linear energy transfer (LET) were used for radiobiological studies for cell line CHO-K1. A facility with a horizontal beam line has been designed and constructed at the Heavy Ion Laboratory in Warsaw University. In radiobiological experiments the cell survival of Chinese hamster ovary cells exposed to high LET of ^{12}C and ^{20}Ne beams and to low LET of γ-rays in the dose range 0 – 6Gy were measured. Relative biological effectiveness (RBE) values have been measured in dependence of LET.

The radiobiological effects of charged particles on cellular and molecular level are of fundamental importance in the field of biomedical applications, especially in hadron therapy and space radiation biology [1]. In the both fields the relative biological effectiveness describes the biological response in a tissue volume and therefore has to be known for different types of cells and radiations in a wide range of LET.

In the paper we present the technical instrumentation of a dedicated horizontal beam line together with the irradiation resolution. The results of the dosimetric studies and the measured RBE for CHO-K1 cell line as a function of LET value for ^{12}C and ^{20}Ne ions are presented.

IRRADIATION FACILITY

The facility of the Heavy Ion Laboratory of Warsaw University has been designed for irradiation process of biological samples under physiological conditions by various ions at a wide range of LET [2]. To achieve a homogeneous radiation field over the area of 1*1 cm^2 of the exit window the beams are passively spread out by a scattering foils of high atomic number material with appropriate thickness.

The beam monitoring factors describing the ratio of the ion intensity measured through the exit window to the intensity detected by silicon detectors placed at 15° or 20° were separately examined for different ion types and scattering foils using a removable diagnosis system. Typical relative beam intensity distribution of ^{12}C fitted to measured data over 1*1 cm^2 of exit window by principal component analysis (PCA) in Matlab is shown at figure 1.

*Corresponding author: czub@pu.kielce.pl
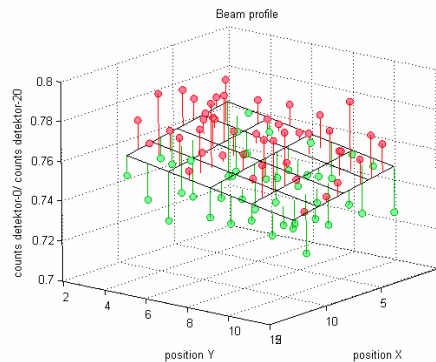
Figure 1. Measured two dimensional intensity distribution of the ^{12}C ions intensity scattered over the 1×1 cm^2 exit window at the cell container position normalized to the intensity of the elastically scattered ions at the 20° silicon detector together with the fitted plane.

Combining scattering of the beam with mechanical displacement of the remotely controlled x-y-z system of Petri dish holder, the beam uniformity of 2.5% over an area of 6×6 cm^2 was obtained.

CELL LINE AND RESULTS

Chinese hamster cells have been used as a suitable biological system for our radiobiological studies. The used cell line is characterized by genetical stability, the ability to form colonies, a relatively rapid growth rate with a cell cycle of 12-14 hours and a karyotype of 22±2 chromosomes.

A special CHO-K1 subclones of Chinese hamster ovary cells were cultured in 5A McCoy (Gibco,USA) medium, containing 10% fetal bovine serum (FBS), 1% penicillin and streptomycin and incubated in humidified atmosphere at 37°C with 5% CO_2.

The CHO-K1 cells were grown as a monolayer culture in specially designed Petri dishes (48 mm in diameter with thin Mylar bottom) in the time 12-24h before irradiation. For the experiments a suitable number of cells were plated. At the time of irradiation (1-5 min) the cells stayed in the medium in room temperature and were protected from the environment by a special Mylar foil located at a top of Petri dish.

Finally, during the work, CHO-K1 cells were exposed to very high LET at the Bragg peak, i.e. for 440-830 keV/μm for ^{12}C ions and for 930-1600 keV/μm for ^{20}Ne ions. In the ion energy region the variation of LET value with the depth of cell penetration is as large as 7-20% for ^{12}C and 6-40% for ^{20}Ne.
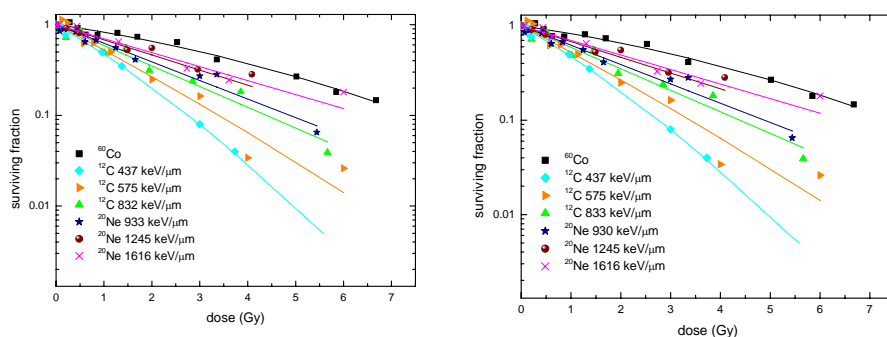
Figure 2. Survival curves of CHO-K1 cells as function of dose for ^{12}C and ^{20}Ne and for γ-rays.

The beam dosimetry is based on the single-particle counting. The calculated effective dose takes into account the increase of the dE/dx value with the depth of cell penetration by an ion. We estimated that dose determination has an overall error of 5%.

Survival data for the CHO-K1 cell line at different energies of ^{12}C and ^{20}Ne ions in dependence on the dose (Gy) are shown in figure 2. The data were fitted by the nonlinear least squares using Trust-Region algorithm implemented in software of Matlab 7.1 to the linear quadratic model $SF(D)=exp(-\alpha D-\beta D^2)$ where SF is the survival at dose D.

The RBE values at established value of surviving fraction for ^{12}C and ^{20}Ne of different energies, i.e. for different values of the LET were obtained using γ-rays from ^{60}Co as a reference. The tendency for changes in RBE is mostly clearly seen in the ratio of the initial slopes of surviving fractions, i.e $\alpha_{ion}/\alpha_{\gamma}=RBE_M$, which may be regarded as the maximum RBE and which is especially important for clinically relevant doses. The dependence of RBE_M on high LET values of ^{12}C and ^{20}Ne ions is shown in figure 3.
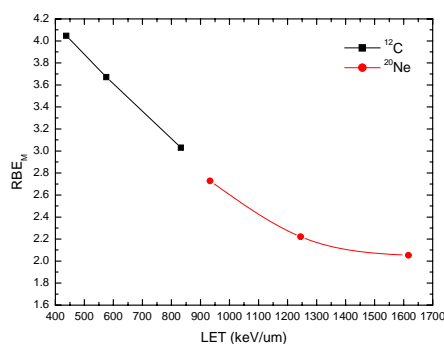
Figure 3. Maximum RBE derived from the ^{12}C and ^{20}Ne survival curves and the γ-ray survival curve in dependence on values of projectile LET.

Concluding, two beams ^{12}C and ^{20}Ne uniformly distributed in the irradiation plane to ±3% over 1×1 cm^2 were produced. On-line dose determination setup was implemented. Survival curves of cell lines irradiated with ^{12}C and ^{20}Ne beams for both irradiations were calculated.

REFERENCES

1. Kraft G.
Prog. tumor therapy with heavy charged particles. Part. Nucl. Phys. 45, 473–544 (2000).
2. Czub J., Banaś D., Braziewicz J., Choiński J., Jaskóła M., Korman A., Szefliński Z., Wójcik A
An irradiation facitity with a horizontal beam for radiobiological studies.
Radiat Prot Dosimetry, doi:10.1093/rpd/ncl518

FATE OF HUMAN FIBROBLASTS FOLLOWING EXPOSURE TO LOW AND HIGH LET IRRADIATION: SENESCENCE OR GENETIC INSTABILITY?

Claudia Fournier[1,*], Marcus Winter[1], Sebastian Zahnreich[1], Sylwester Sommer[1], Larissa Melnikova[1,2], Elena Nasonova[1,2] and Sylvia Ritter[1]
[1]GSI, Darmstadt, Germany
[2]JINR, Dubna, Russia.

Cellular and molecular changes ascribed to differentiation and senescence were investigated in irradiated and unexposed control populations up to the end of their respective life span. Special attention was paid on the link between senescence related changes and the formation of chromosome aberrations and genetic instability in cells, which re-entered the cell cycle days or even weeks after a radiation-induced arrest.

.
For this study, four fibroblast strains originating from different tissues were cultured over more than 6 months. At the onset of the experiment, cells from one strain (AG 1522) were exposed to X-rays or carbon ions (LET 150 keV/μm). A high dose of X-rays was administered as a single and a fractionated dose. The cell cycle distribution after exposure was measured by flow cytometry (FACS). The proliferation index was determined by BrdU uptake. The levels of cell cycle- (p53, p21) and senescence-related proteins (p16) were assessed by Western Blot analysis. The activity of senescence related (SA-) β-galactosidase was measured according to (1). The differentiation pattern (morphological features) was assessed at regular intervals according to (2). Structural and numerical aberrations as well as the frequency of single or complex translocations were analysed in metaphase cells (Giemsa and multiplex fluorescence in situ hybridisation (m-FISH) staining).
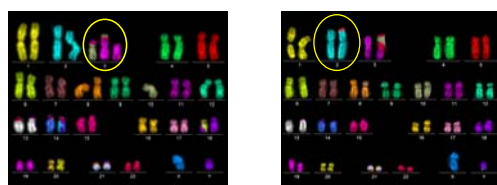
Figure 1. mFISH analysis of clonal translocations (circles) in AG1522 cells, occuring at different passage numbers after exposure in control cells (left) as well as in the progeny of irradiated cells (right, here shown for 8 x 2 Gy X-rays).

The fraction of cells arrested after irradiation in the initial G1-phase increased with dose and LET. Accordingly, enhanced protein levels of the cell cycle regulators p53 (only immediately after exposure), p21 (persisting over 2 to 3 passages after exposure) and p16 (slight, 3 passages after exposure) were detected. In parallel, enhanced activity of β-galactosidase and premature differentiation were observed (3). Then, the described changes were no more detectable. However, compared to the initial levels, the frequency of transmissible aberrations was elevated in all populations. This effect was more pronounced in the progeny of cells exposed to a high dose of X-rays and regardless of a fractionation (8 x 2 Gy, 16 Gy). Some of the aberrations were clonal, either expanding or regressing (figure 1).

---

*Corresponding author: c.fournier@gsi.de
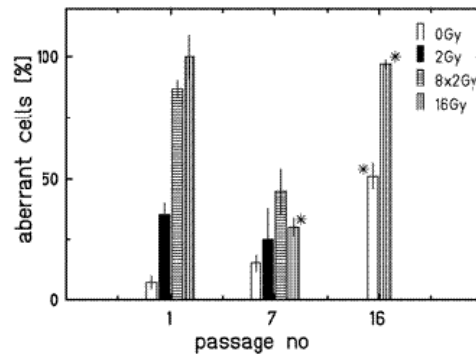
Figure 2. Analysis of non-transmissible aberrations (1, 7 and 16 passages after X-exposure) in AG1522 cells by Giemsa staining.* data obtained in a separate experiment.

As shown in figure 2, the frequencies of non-transmissible aberrations (dicentrics, rings, chromatid type aberrations and chromosome breaks) were also elevated in the descendents of exposed cells during this period of time (passage no. 7), but to a less extend than in the cells of the first passage after exposure. Up to the same period of time, the number of aberrant control cells had increased slightly compared to the initial values.

However, at around 10 passages post-irradiation, the cellular and molecular changes associated to a senescent stage appeared again in the previously irradiated populations and persisted, i.e. higher levels of cell cycle- and senescence- related proteins compared to the control cells. This is exemplarily shown for one out of 3 experiments in figure 3.
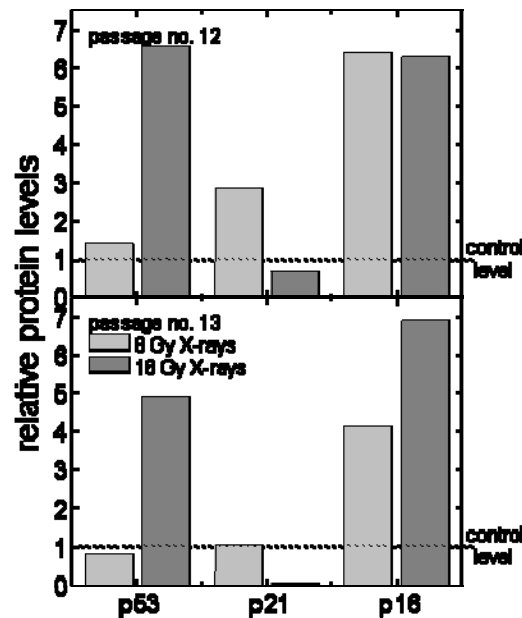
Figure 3. Western Blot analysis of the expression of cell cycle- and senescence-related proteins in AG1522 cells at 12 and 13 passages after exposure to X-rays (0, 8 and 16 Gy). The expression pattern for the progeny of 8 Gy irradiated cells indicates a higher level for all proteins compared to control cells, whereas the patter in the progeny of 16 Gy irradiated cells is different: the p53 protein level is very high and the p21 expression is low (passage no. 12) and by a later time point no more detectable (passage no. 13).

The descendents of 8 Gy irradiated cells displayed the described pattern, whereas the progeny of 16 Gy irradiated cells were different in this particular experiment. In this population, the level of p53

protein was more than 6 fold increased, the level of p21 was low and later (passage no. 13) no more detectable. At the same time, a very pronounced expansion of the clonal aberrations was observed in the descendents of cells exposed to high doses of X-rays (8x2 Gy, 16 Gy). In addition, newly formed translocations (figure 2, passage no.16), aneuploidy and an enhanced proliferation activity (not shown) were detected.

In repeated experiments, other deviations from the pattern of senescence-related protein expression, associated with genetic instability, were detected. Surprisingly, they occurred sometimes also in control cells, and for fibroblasts originating from all tissues assessed (foreskin, skin, lung; not shown). It was also a general observation, that the yield of de novo formed untransmissible aberrations increased at the very end of the life span in all populations and regardless of radiation exposure and radiation quality (shown in figure 2 for 0 Gy, passage no.16).

The lately occurring changes related to senescence, i.e. the elevated expression levels of cell cycle inhibiting proteins, are considered as a prerequisite for the maintenance of the genomic integrity in fibroblasts. The results presented here confirm this, mainly in that genetic instability, but no transformation was observed.

The factors determining the fate of fibroblasts are likely to be single events in terms of transmissible mutations or chromosomal aberrations, bearing an advantage for survival for the respective progeny. Such a constellation is reflected by an impaired cell cycle arrest among the progeny of irradiated cells or in aging controls. The probability of the formation and expansion of such persisting aberrations increases with the dose initially delivered, but the quality of the effect is not correlated to dose and radiation type.

REFERENCES

1. Dimri GP, Lee X, Basile G, Acosta M, Scott G, Roskelley C, Medrano EE, Linskens M, Rubelj I , Pereira-Smith O et al., A biomarker that identifies senescent human cells in culture and in aging cells in vivo. Proceedings of the national academy of sciences 1995; 92 :9363-9367.
2. Fournier C, Scholz M, Weyrather WK, Rodemann HP and Kraft G, Changes of fibrosis-related parameters after high and low LET irradiation of fibroblasts. International Journal of Radiation Biology 2001; 77:713-722.
3. Fournier C, Winter M, Zahnreich S, Nasonova E, Melnikova L and Ritter S, Interrelation amongst differentiation, senescence and genetic instability in long-term cultures of fibroblasts exposed to different radiation qualities. Radiotherapy and Oncology 2007; 83: 277-282.

EARLY CELLULAR SIGNALLING AFTER EXPOSURE TO PARTICLES OF HIGH LINEAR ENERGY TRANSFER (LET)

C. Fürweger[1,2,*], M. Hajek[1], N. Vana[1], R. Kodym[3] and R. Okayasu[4]

[1]Atomic Institute of the Austrian Universities, Vienna Technical University, Stadionallee 2, 1020 Vienna, Austria

[2]Clinic for Radiotherapy and Radiobiology, Medical University of Vienna, Währinger Straße 18-20, 1090 Vienna, Austria

[3]Division of Molecular Radiation Biology, Department of Radiation Oncology, University of Texas, Southwestern Medical Center, 2201 Inwood Rd., Dallas, TX 75390-9187, USA

[4]Heavy-Ion Radiobiology Research Group, Research Center for Charged Particle Therapy, National Institute of Radiological Sciences, 4-9-1 Anagawa, Inage-ku, Chiba-shi, 263-8555, Japan

In order to obtain a deeper insight into the cellular response to DNA damage induced by high energy charged particle radiation, we assessed early cellular signal transduction events after exposure as a function of particle LET and recovery time. Therefore, human skin fibroblasts were exposed to 60 mGy of high energy ions incident in perpendicular direction to the cell layers. Different LET values of 13 (^{12}C), 31 (^{20}Ne), 56 (^{28}Si) and 198 (^{56}Fe) keV/μm H_2O were selected. For three time points (20', 1h, 2h) after irradiation, the formation of pATM (S1981) and pDNA-PKcs (T2609) foci was visualized via immunofluorescence.

We found that at the 20' time point, the number of pATM- and pDNA-PKcs-foci per fibroblast nucleus was highest in cells irradiated with ^{28}Si ions. Furthermore, for samples exposed to the ^{56}Fe beam, the number of detected pATM- and pDNA-PKcs-foci was very close to the calculated number of nuclear particle traversals, suggesting a high efficiency for single high-LET particles to initialize a cellular signalling response. Interestingly, whereas ^{56}Fe ions initially yielded fewer foci than lower LET ^{28}Si and ^{20}Ne particles, only the ^{56}Fe-exposed cultures exhibited no decrease in the number of foci until two hours after exposure, thus exceeding cells exposed to lower-LET beams at that time point. These results indicate that the microdosimetric aspect of energy deposition strongly modulates the early cellular response to radiation.

High energy charged particle radiation is known to cause specific damage patterns in biologic tissue because of the radiation energy being deposited along the particle tracks in a highly localized manner. We therefore investigated the induction of two key events in DNA double strand break (DSB)-induced cellular signalling, the formation of pATM (S1981) and pDNA-PKcs (T2609) foci, which are known to greatly modulate DSB repair and cell cycle transition. By focusing on low radiation doses, the LET-dependence of the cellular response to a localized deposition of radiation energy is explored.

MATERIALS AND METHODS

Cell Culture and Exposure

Human foreskin fibroblasts (kindly provided by the Children's Cancer Research Institute St. Anna, Vienna, Austria) were grown in RPMI 1640 supplemented with 10% foetal calf serum, 100 U/ml penicillin and 100 μg/ml streptomycin and maintained in a humidified atmosphere of 95% air and 5% CO2 at 37°C. At about 60% confluence, cell layers were exposed to 60 mGy of different particles (table 1) incident in perpendicular direction or mock-irradiated at the Heavy Ion Medical Accelerator (HIMAC) facility of the National Institute of Radiological Sciences (Chiba, Japan). Cells were left to recover at 37°C for 20', 1 or 2 h. The fraction of hit nuclei was determined from particle fluences measured with a scintillation counter. Calculated dose and LET values were verified by simultaneous exposure of thermoluminescence detectors (LiF:Mg,Ti), which were evaluated according to the High

*Corresponding author:
christoph.fuerweger@meduniwien.ac.at

Temperature Ratio (HTR) method (1).

Table 1. Selected particles and their distribution on the cell-layer level at 60 mGy.

Ion	Energy [MeV/n]	LET [keV/μm H$_2$O]	% hit nuclei
^{12}C	290	13.0	>99
^{20}Ne	400	30.9	93
^{28}Si	490	56.0	77
^{56}Fe	500	197.8	35

Immunofluorescence and Sample Analysis

Immunofluorescence was carried out as published recently (2) using phospho-specific antibodies for pATM (S1981) and pDNA-PKcs (T2609) obtained from Rockland Immunochemicals. Rhodamine Red-X- and Cy2-tagged secondary antibodies were purchased from Jackson Immuno Research. For determination of the absolute number of foci, digital microscopic images were captured and an intensity cut-off value was applied for distinction of focal areas from background.

RESULTS AND DISCUSSION

Figure 1. ATM phosphorylation (S1981) as a function of time after irradiation with particles of different LET. Results are means of 4 to 6 samples ± s.e..

The numbers of pATM- and pDNA-PKcs-foci per 100 fibroblasts have been determined for different particle beams and are illustrated in figures 1 and 2 as functions of time after irradiation. We found that at the earliest time point (20'), the number of both foci types was highest in cells irradiated with ^{28}Si-ions. Furthermore, whereas foci induced by the lower-LET ^{12}C-, ^{20}Ne- and ^{28}Si-particles are rapidly resolved until two hours after irradiation, the number of foci stays at a constant level in ^{56}Fe-exposed samples during the same period. As a consequence, at the 2h time point, ATM and DNA-PKcs phosphorylation are observed to be highest in cells treated with ^{56}Fe ions. Furthermore, the number of foci due to ^{56}Fe irradiation exceeding the level of mock-irradiated control samples is found to concur very well with the calculated number of ^{56}Fe particles traversing nuclear areas. This finding supports the view that single particles of sufficiently high lineal energy are able to trigger cellular signal transduction mechanisms.

   In comparison to ATM activation, the absolute number of pDNA-PKcs foci is found to be slightly lower in all samples. This may be attributed to the specific function of DNA-PKcs phosphorylation in

non-homologous end joining and the chosen cell density of 60% confluence, where a smaller fraction of DSBs is expectedly treated via the DNA-PKcs-independent homologous recombination pathway.
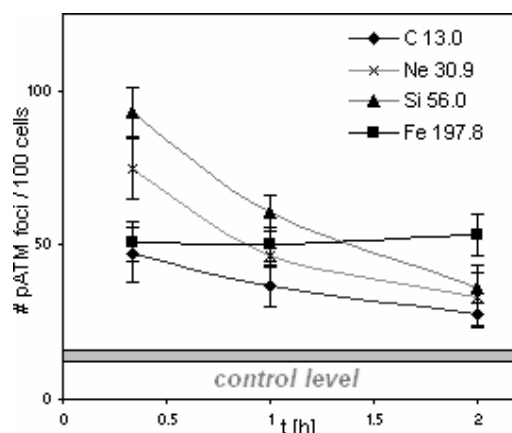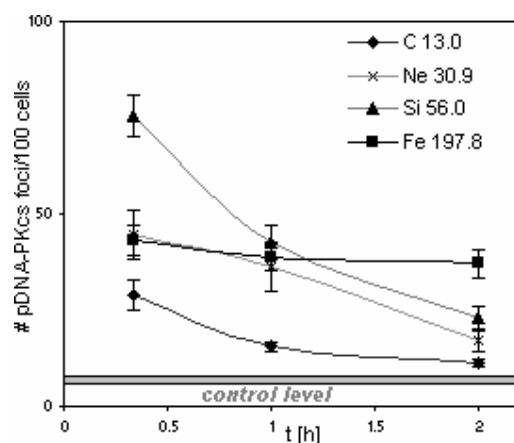

Figure 2. DNA-PKcs phosphorylation (T2609) as a function of time after exposure to particles of different LET. Results are means of 4 to 6 samples ± s.e..

Since both pATM and pDNA-PKcs are known to be associated with DSBs, our data indicates that whereas DNA damage induced by lower-LET radiation may be found distributed across a higher number of sites, increased ATM and DNA-PKcs phosphorylation persists over a longer time period in cells exposed to higher-LET particles, arguing for less efficient repair of induced DNA damage.

Overall, we were able to demonstrate that in the low dose range, the time-dependent cellular response to low dose particle radiation is modulated by the energy deposition of single particles. The specific behaviour in the formation and persistence of pATM (S1981) and pDNA-PKcs (T2609) foci induced by different particle beams illustrate that both the initial extent of radiation-induced damage and repair kinetics are greatly depending on radiation quality.

REFERENCES

1. Schöner W, Vana N, Fugger M. The LET-dependence of LiF:Mg,Ti-dosemeters and its application for LET-measurements in mixed fields. Radiat Prot Dosim. 1999;85(1-4):263-6.
2. Fürweger C, Hajek M, Vana N, Kodym R, Okayasu R. Cellular signal transduction events as a function of linear energy transfer (LET). Radiat Prot Dosim. 2007 Jun 18; [Epub ahead of print]

ANALYSIS OF REPAIR PROCESSES IN DIFFERENT HAMSTER CELL LINES EXPOSED TO CARBON IRRADIATION

Hana Hromčíková, Miloš Lokajíček, Pavel Kundrát

Institute of Physics, Academy of Sciences of the Czech Republic,

Na Slovance 2, 182 21 Prague 8, Czech Republic

Abstract

The response of cells to ionizing radiation depends not only on the radiation quality, i.e. physical parameters, but also on biological characteristics of the cells. In particular, the repair capacities play an important role. E.g. large differences have been observed in survival after carbon irradiation of three Chinese hamster cell lines, wild-type V79 and CHO-K1 cells and repair-deficient CHO mutant xrs5 [Weyrather et al 1999]. These data sets, measured for carbon beams with energies covering the whole range of interest in radiotherapy, have been analyzed on the basis of the probabilistic two-stage model [Kundrát et al 2005]. This model enables to distinguish and describe various types of lesions caused by ionizing particles as well as the outcome of cellular repair processes. In agreement with experimental evidence, we have assumed that the variations in the induction of DNA damage between the three cell lines are only minor and that the main source of differences among cells in their response to a given radiation is their repair capacity. From the given data, detailed characteristics of damage induction and repair-success probabilities will be quantified. The reported studies suggest the need of explicitly involving the repair processes in radiobiological models.

Radiobiological model

To represent the damage induction and repair processes in cells, the probabilistic two-stage model [Kundrát et al 2005, Kundrát 2006] has been used.

The cell survival at dose D can be described as

$$s(D) = \sum_k P_k(D)\, q_k \tag{1}$$

where q_k stands for survival of cells traversed by k tracks.

$$P_k(D) = (hD^k / k!)\exp(-hD) \tag{2}$$

is the distribution of tracks over cell nucleus, given by Poisson statistics with the mean number $h = C\sigma/L$, where σ represents the area of the cell nucleus and L stands for LET value (conversion constant $C = 6.24$ keV Gy^{-1} μm^{-3}). Survival probability q_k of cells traversed by k tracks is

$$q_k = \sum_{i=0}^{k}\binom{k}{i} a^i (1-a)^{k-i} \sum_{j=0}^{k-i}\binom{k-i}{j} b_j (1-a)^{k-i-j} R_a R_b \tag{3}$$

here a stands for the average probability that a single track induces lethal damage to DNA, b is the probability that a less severe lesion has been created. The b-type damage must combine with at least two events to kill the cell and R_a, R_b represent repair success probabilities for both damage types. In this approach, repair R_a and R_b is a constant specific for each cell line. Damage induction probabilities depend on transferred energy, approximated by LET value L. The detailed biophysical interpretation of equation (3) and damage classification is discussed in [Kundrát et al 2005, Kundrát et Stewart 2005].

Analysis of experimental data

Survival curves for Chinese hamster cells xrs5 and CHO-K1 irradiated by carbon ions of different LET values measured by [Weyrather et al 1999] have been used. In accordance with [Dikomey et al 1977] we have supposed that these cell lines did not vary in the number of induced strand breaks, and difference in radiation response is due to their different repair capacities. Model representations of these survival curves for both cell lines are presented in Figure 1. The derived damage induction probabilities (equal for both cell lines) are not shown.
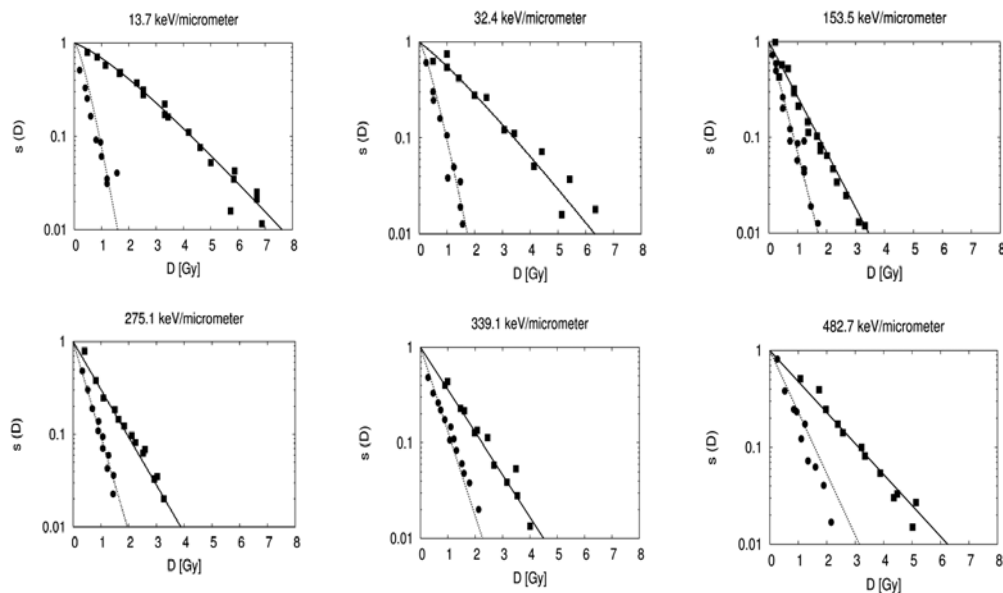
Figure 1. Theoretical curves (lines) in comparison with measured survival data for CHO-K1 (squares) and xrs5 cells (circles).

Discussion and conclusion

The results have validated the hypothesis that the differences in radiation response between different cell lines rise from differences in their repair capability. In present analysis, only the effective damage yields have been reflected, the effects of repair processes common for both cell lines have been implicitly included in the damage induction itself. Therefore, for the radiosensitive mutant xrs5 it has been possible to neglect the repair success probability at all. The wild-type line CHO-K1 succeeds in repairing relatively large amounts of DNA damage. The present results indicated that the further development of detailed radiobiological models including repair processes is needed.

References

Dikomey E, Dahm-Daphi J, Brammer I, Martensen R, Kaina B. *Correlation between cellular radiosensitivity and non/repaired double/strand breaks studied in nine mammalian cell lines.* Int. J. Radiat Biol 73 (1997) 269-278.

Kundrát P., *Detailed analysis of the cell-inactivation mechanism by accelerated protons and light ions*. Phys. Med. Biol. 51, 1185-1199 (2006).

Kundrát P, Lokajíček M, Hromčíková H, *Probabilistic two-stage model of cell inactivation by ionizing particles;* Physics in Medicine and Biology, 50 (2005) 1433–1447.

Kundrát P., Stewart R. D. *On the biophysical interpretation of lethal DNA lesions induced by ionizing radiation*. Radiat Prot Dosimetry.2006; 122: 169-172

Weyrather WK, Ritter S, Scholz M, et al., *RBE for carbon track-segment irradiation in cell lines of differing repair capacity;* . Int. J. Radiat Biol 75 (1999) 1357-1364.

EFFECT OF OXYGEN ON DNA DAMAGE CAUSED BY IONIZING RADIATION OF DIFFERENT QUALITY

M. DAVÍDKOVÁ[1], V. ŠTĚPÁN[1,2]

[1]Dept. of Radiation Dosimetry, Nuclear Physics Institute AS CR, Prague, Czech Republic
[2]Faculty of Nuclear Sciences and Physical Engineering, Czech Technical University, Prague, Czech Republic

Local hypoxia-induced radiation resistance is one of the major problems in current radiation therapy of solid tumors. Hypoxic cells are two to three times more resistant to a single fraction of ionizing radiation than those with normal levels of oxygen. Concentration of diluted oxygen is not uniform within tumor volume and changes during the course of radiotherapy. Presence of oxygen within living cells can influence mainly i) the extent of radical attack to DNA by scavenging radical species produced by radiation, ii) the yields and types of DNA damages due to reactions with chemically modified sites within macromolecule. The goal of the presented study is to estimate the effect of oxygen on the yield of primary DNA damage caused by ionizing radiation of different quality.

Theoretical modeling approach based on Monte Carlo technique was used for this purpose. DNA oligomer was described at the atomic level. Energetically minimized spatial conformations of 100 bp DNA fragments were obtained using Amber 7 molecular dynamics package (Pearlman, D.A. *et al.* 1995, Comp. Phys. Commun. 91, 1). Track structures of the ionizing particles were obtained by Monte Carlo code TRIOL (Bigildeev, E.A., Michalik, V., 1996, Radiat. Phys. Chem. 47, 197). Both unscavengeable and scavengeable damage was followed. Unscavengeable damage results from direct energy deposition on DNA macromolecule or into the bound water. Scavengeable damage involves DNA damage caused by radiolytic species produced by energy depositions outside the bound water region. Water radiolysis was simulated using program STOCHECO (Michalik, V., Běgusová, M. and Bigildeev, E.A., 1998, Radiat. Res. 149, 224). Radical diffusion motion in random directions was followed together with 21 chemical reactions of radiolytic species and reactions of dissolved O_2 with e_{aq}^-, $H^.$ and O^-.

Yields of particular types of simple and complex DNA damages and the ratio of scavengeable to unscavengeable DNA damage in dependence on oxygen concentration ranging from anoxic to normal conditions will be presented and discussed for electrons, protons and alpha particles with LET in range 0.41-160 keV/μm.

ESTIMATING THE GENOTOXIC EFFECTS OF FE-IONS: IMPACT OF CELL CYCLE EFFECTS, APOPTOSIS AND INTRA-INDIVIDUAL VARIABILITY

Ryonfa Lee[1], Sylwester Sommer[1] and Elena Nasonova[1,2] and Sylvia Ritter[1]
[1]Gesellschaft für Schwerionenforschung, Darmstadt, Germany
[2] Joint Institutes for Nuclear Research, Dubna, Russia

Health hazards of charged particles, in particular Fe-ions, are of major concern for the planning of manned space explorations. Among the health effects carcinogenesis is currently considered to be the main risk factor for astronauts. To estimate the cancer risk, chromosome aberration frequencies are generally measured in peripheral blood lymphocytes. Cells are cultivated for about 48h in vitro. Then, the aberration yield is determined in first cycle cells. Since our preceding studies using hamster cells and human fibroblasts have shown that heavy particles induce dramatic cell cycle delays and that these delays are related to the aberration burden of a cell, we analysed in detail the time-course of aberrations in human lymphocytes after Fe-ion exposure. Additionally, factors that might confound the aberration yield were examined. In the experiments, lymphocytes from a healthy volunteer were exposed to either Fe-ions with differing linear energy transfer (LET) or X-rays. Lymphocytes were harvested at multiple times and aberrations were determined in 1st cycle metaphases and prematurely condensed G2-cells. Furthermore, cell cycle effects (e.g. S-phase labelling, G2-delay), apoptosis and intra-individual variations in the cytogenetic response were recorded. Our data reveal a pronounced increase in the aberration yield with sampling time after Fe-ion exposure. This increase was about threefold for LET=150 keV/μm, sevenfold for LET=400 keV/μm and tenfold for LET=3160 keV/μm. In contrast, a stable aberration yield was found after X-ray exposure. As a consequence, RBEs derived from late sampling times were significantly higher than those obtained at early sampling times. A similar picture was found for G2-phase cells. However, the increase was less pronounced than that observed in metaphase samples. Furthermore, with increasing LET the number of lymphocytes capable of entering the cell cycle decreased, while the number of cells undergoing apoptosis increased indicating a rapid removal of heavily damaged cells from the population. Finally, marked intra-individual variations in the cytogenetic response were observed. The significance of these observations for estimating health risks associated with high LET exposure will be discussed and alternative research strategies will be presented.

Poster:
Radiobiology 3

CROSS-TALK BETWEEN NON-HOMOLOGOUS ENDJOINING, SINGLE-STRAND ANNEALING AND GENE CONVERSION FOR REPAIRING CHROMOSOMAL DSB IN MAMMALIAN CELLS

Mansour W. Y.[1]; **Schumacher, S.**[1]; **Rhein, T.**[1]; **Rosskopf, R.**[1]; **Schmidt-Petersen, F.**[1]; **Gatzemeier, F.**[1]; **Haag, F.**[2]; **Borgmann, K.**[1], **Dahm-Daphi, J.**[1]

[1] Laboratory of Radiobiology & Experimental Radiation Oncology, Department of Radiotherapy and Radiation Oncology, [2] Institute of Immunology, University Medical School Hamburg-Eppendorf, Martinistreet 52, D-20246 Hamburg, Germany

Double-strand breaks (DSBs) are the critical DNA lesions which determine cell killing and mutagenesis after ionizing radiation. In mammalian cells DNA double-strand breaks (DSB) are repaired by three mechanistically distinct pathways, nonhomologous end-joining (NHEJ), gene conversion (GC) and single-strand-annealing (SSA). The aim of this study is to understand the network between these pathways and how they may compete for repairing a single DSB. We employed novel reporters constructs that monitor the repair of a single I-SceI-induced DSB specifically by NHEJ (pEJ), GC (pGC) and alternatively by NHEJ/SSA (pEJSSA). The DSB ends created are non-compatible and require end processing, thereby in part mimicking radiation induced DSB. The reporters have been integrated into CHO K1 and xrs5 cells (Ku80-deficient). Repair events were analysed by PCR and sequencing.

Our results revealed a decrease in NHEJ efficiency as well as an increase in the deletion length in Ku80-deficient cells compared to wild-type. The decrease in NHEJ efficiency is compensated by an increase in SSA. In addition, GC was 6-times increased in xrs5 compared to CHOK1 cells. The phenotype of xrs5 is completely reverted after complementation with hKu80. In contrast to the Ku80-defect, suppression of Rad51 did not enhance NHEJ. As a novel function, we found that Rad51 regulates the competition between NHEJ and SSA in favour of NHEJ.

Together, we could characterize an intimate crosstalk between the three DSB repair pathways whereby functional Ku80/NHEJ acts as a principal restricting the use of both SSA and GC for repairing a single DSB. Ku80 and Rad51 together have regulatory role on deleterious SSA. If NHEJ or GC fails cells may use SSA as a rescue pathway which however increases the mutagenic potential of DSBs.

CHARACTERIZATION OF CELL DEATH INDUCED BY HIGH LET IRRADIATION IN SQUAMOUS CELL CARCINOMAS FOR FUTURE CLINICAL APPLICATION IN HADRONTHERAPY

MAALOUF M[1*], ALPHONSE G[1], FOURNIER C[2], TAUCHER-SCHOLZ G[2] and RODRIGUEZ-LAFRASSE C[1]

[1] Department of Cellular and Molecular Radiobiology, EA3738, Lyon-Sud Medical School, Lyon, France
[2] GSI, Darmstadt, Germany

Increased interest in the biological effects of high-LET carbon irradiation lies in the emerging development of hadrontherapy. However a number of molecular issues regarding the mechanisms of action of carbon ions remain to be clarified. We initiated studies on the mechanisms of cell death in two p53-mutated head and neck squamous carcinoma cell lines (HNSCC) with different radiosensitivity, since recent clinical trials (1) had shown that the local treatment of the HNSCC by carbon hadrontherapy is much less efficient than in other radioresistant cancer.

To date, hadrontherapy has been used to target traditionally difficult-to-operate tumors. Treatment currently focuses on deep-seated tumors, or tumors close to sensitive organs, as head and neck tumors. Our project aims to analyze the specific molecular signature of carbon irradiation in tumor cells. These studies will participate to the comprehension of the mechanisms leading to resistance to conventional radiotherapy and will precise the elective indications of hadrontherapy. This point is crucial in order to determine the best treatment for certain types of tumors and to direct the patients towards hadron- or conventional radio-therapy.

In this context and in order to verify the cellular basis of the high RBE levels, studies on the mechanisms of cell death were initiated in two p53-mutated head and neck squamous carcinoma cell lines (HNSCC) with different radiosensitivity, SCC61 (radiosensitive to x-rays) and SQ20B (radioresistant to x-rays).

We first found that low energy carbon ions (9.8MeV/u) induce a higher level of clonogenic cell death than carbon ions of the medium energy range (75MeV/u) and X-rays, for both cell lines. Although, SQ20B were systematically less sensitive than SCC61 cells.

As shown in figure 1, in response to high LET ions the radiosensitive cell line, SCC61, undergoes apoptosis in a time dependent manner. Four to 240 hours after irradiation the adherent and floating cells were pelleted and fixed for apoptosis quantification using propidium iodide labeling. Analysis was performed by flow cytometry. The percentage of cells in sub-G1 phase, taken as an index of apoptosis, was more pronounced in response to low energy carbon ions compared to carbon ions of the medium energy range, reaching 80 % at 72h and 95 % at 240h.

We have previously demonstrated (2), in the radiosensitive cell line SCC61, a direct relationship between apoptosis and ceramide production after X-ray irradiation. In response to carbon ion irradiation, an increase in ceramide levels occurred in parallel to that of apoptosis (data not shown).

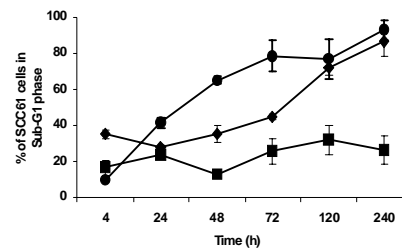*Corresponding author: m.maalouf@gsi.de

Figure 1: Kinetics for radiation-induced apoptosis (sub-G1 phase) in SCC61, after carbon ion exposure ■ 0Gy, ♦ 10Gy-C75MeV/n, ● 10Gy C-9.8MeV/n

In contrast, SQ20B cells (radioresistant to x-rays) did not show any induction of apoptosis during 120h following X-ray or carbon irradiation. In addition, no changes in the production of ceramide were detected. Only a moderate increase of apoptosis and ceramide levels was noticed at 240h after carbon irradiation.

However, in response to x-rays, SQ20B showed a transient arrest in G2 phase at 24h. This G2 arrest was even more pronounced and maintained 5 days after irradiation by carbon ions (9.8MeV/n) (figure 2). We also demonstrated that the G2 arrest was related to a high expression of Chk1-P, a major checkpoint kinase mainly responsible for the G2/M checkpoint.

In addition, from 5 days post-irradiation, a significant percentage of cells showed an enlarged and flat morphology and an enhanced activity of senescence-like related β-galactosidase (SA β-gal) (data not shown).
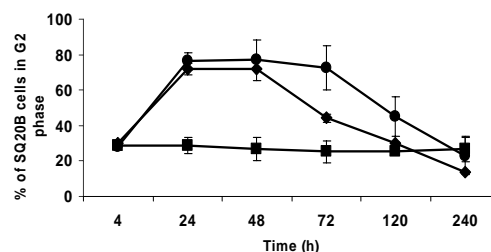
Figure 2: Percentage of SQ20B cells in G2 phase after carbon ion exposure ■ 0Gy, ♦ 10Gy-C75MeV/n, ● 10Gy C-9.8MeV/n.

In both cell lines, carbon ion irradiation does not modify the type of cell death induced, but amplifies it, compared to the same doses of x-rays irradiation.

In the radiosensitive SCC61 cell line, the ceramide p53-independent apoptotic pathway is involved following photon and carbon ions exposure. The high efficiency of carbon irradiation in radioresistant SQ20B cells could not be explained by the induction of apoptosis but by a persistence of the cell cycle arrest during several days after exposure. These results may explain the moderate tumor control observed in HNSCC patients treated by carbon hadrontherapy compared to the results obtained for other tumor entities and need to be further investigated.

References
1. Jun-etsu Mizoe *et al.,* Int J Rad Oncol Biol Phys 2004, 60: 358-364
2. Alphonse G *et al*., Int. J. Rad Biol 2002, 78: 821-835

APOPTOTIC AND CELL CYCLE RESPONSES IN THE SMALL CELL LUNG CANCER CELL LINE U-1690 FOLLOWING EXPOSURE TO DIFFERENT LET OF BORON AND NITROGEN IONS

A. E. Meijer[1,*], W.-C. Kim[1, 2], M. R. Edgren[1] and A. Brahme[1]

[1]Departament of Oncology-Pathology, Medical Radiation Physics, Cancer Centre Karolinska, Karolinska Institutet-Stockholm University, P.O. Box 260, SE- 171 76 Stockholm, Sweden
[2]Inha University, Department of Radiation Oncology, Medical Collage, Incheon, Korea

High linear energy transfer (LET) radiation has several advantages compared to conventional photons in terms of higher biological effectiveness, independence of oxygen status, less variation in cell cycle radiosensitivity etc. Previously published results on the effects of boron and nitrogen ion radiations on the apoptotic response in the human melanoma cell line AA (wt TP53) and the human glioblastoma cell lines M059J (DNA-PK$_{CS}$ deficient) and M059K (DNA-PK$_{CS}$ proficient), showed that high LET radiation-induced apoptosis varied in a dose and time-dependent manner from cell line to cell line.

In this study we investigated if the type of ion or LET have any influence on the apoptotic and cell cycle responses. The human small cell lung cancer cell line (SCLC) U-1690 (mut TP53) was exposed *in vitro* to 2 Gy of accelerated boron ions (40, 80 and 125 eV/nm), nitrogen ions (80 and 140 eV/nm) or photons (0.2 eV/nm). The induction of apoptosis was measured up to seven days after irradiation using morphological characterisation of apoptotic cells and bodies. In parallel, measurements of cell-cycle distribution, monitored by DNA flow cytometry were performed.
Both low LET photons and high LET accelerated ions induced apoptosis in the human SCLC U-1690 in a time-dependent manner. The maximum inductions were reached at 48, 72-96 and >72 h for boron, nitrogen and photons, respectively. The maximum induction of apoptosis for boron ions (48 h) were around 25%, 20% and 15% for 40, 80 and 125 eV/nm, respectively. For nitrogen ion the maximum levels (72-96 h) were 20% and 15-22% for 80 and 140 eV/nm, respectively, and for photons 3% (>72 h). There were no significant differences in the level of apoptosis within the different high LET exposures neither for boron nor nitrogen ions. However, in comparison with low LET photons both boron and nitrogen ions induced significantly elevated levels of apoptosis at 48 and 72-96 h, respectively. These apoptotic responses occurred after the release of accumulated cells in S- and/or G2/M phase of the cell cycle.

STUDIES ON BYSTANDER EFFECT USING THE GSI HEAVY ION MICROBEAM

T. Pouthier[a], C. Fournier[a], Ph. Barberet[b], K. O. Voss[b], G. Becker[a], C. Sieben[a], B. E. Fischer[b], G. Taucher-Scholz[a]

[a]*Biophysics and* [b]*Materials Research, Gesellschaft für Schwerionenforschung (GSI), 64291 Darmstadt, Germany*

Beams of heavy charged particles, especially carbon ions, represent an optimized tool for the treatment of deep-seated tumors. Tumor cells can be irradiated effectively with a minimal exposure of the surrounding tissue. This type of ionizing irradiation has been shown to induce DNA-damage in the targeted cells thereby causing cell death. However, more and more studies provide evidence that irradiated cells affect their unirradiated neighbours, so that they in turn display cellular responses typically associated with direct radiation exposure, a phenomenon called bystander effect.

To study the bystander effect in human fibroblasts, the existing focusing heavy-ion microprobe at the Gesellschaft für Schwerionenforschung in Darmstadt (Germany) was used to perform targeted irradiation of single selected cells with a defined number of ions. The aim was to investigate a bystander response after microbeam irradiation, with respect to following endpoints: induction of the cell cycle regulator CDKN1A (p21) and the formation of γ-H2AX foci and micronuclei.

In various studies, the CDKN1A protein has been reported to be involved in bystander effects after low-LET and alpha irradiations. In our experiment transient bystander responses were obtained for the induction of CDKN1A (p21) after microbeam irradiation with carbon particles. Comparing to the control cells, bystander cells show a slight but reproducible overall increase of the protein expression level of CDKN1A (p21), but no clusters of cells with elevated p21 protein levels were observed in the neighbourhood of the traversed cells up to a radial distance of 200 μm (Fournier *et al*., 2007).

In addition, we investigated DNA damage as a potential basis for the effects on CDKN1A induction in bystander cells. Using development of image processing techniques allowing automatic detection and counting of the foci, the formation of γ-H2AX foci (indicating DNA double strand-breaks) was quantified in irradiated and bystander cells. First results did not show significant differences between bystander and control cells. In addition, micronuclei as an indicator of DNA damage at the chromosomal level damage were scored in bi-nucleated bystander cells after microbeam or broadbeam irradiation, on synchronous or asynchronous cells. Our data after carbon and uranium irradiation suggest that the formation of micronuclei is not enhanced in bystander cells.

DEVELOPMENT OF A SYSTEM FOR OER MEASUREMENTS

C.Schicker, G.Iancu, C.von Neubeck, W.K.Weyrather
GSI Biophysik, Darmstadt

Radioresistant hypoxic cells are often the reason for recurrent tumours in radiotherapy. To measure the influence of cell hypoxia for carbon ion irradiation and to test ways to include it into treatment planning, a system has been established, that enables the irradiation of an extended volume under defined oxygen conditions.

Hypoxic cells are often the reason for recurrent tumours in radiotherapy. On the one hand, they are more resistant to irradiation, on the other hand hypoxia enhances malignant progression. High LET (linear energy transfer) irradiation offers the possibility to reduce this radio-resistance, as the OER (oxygen enhancement ratio) is strongly LET dependent.

To measure the influence of cell hypoxia for carbon ion   irradiation and to test ways to include it into treatment planning, a system has been established, that enables the irradiation of an extended volume under defined oxygen conditions. Cells have been cultivated on gas-permeable foil which was stuck on a plastic ring. Gas of a predefined composition has been flushed through the system. Acute hypoxia was achieved by flushing the system with 100% nitrogen. Cells have been gassed 1-2 hours before irradiation. For chronic hypoxia cells have been cultivated several hours under specific conditions (5% CO_2, 0,5% O_2, 94,5% nitrogen). Survival has been determined by a colony formation assay.

Test measurements have been performed with Chinese hamster ovary cells (CHO-K1) and results are compared to x-ray irradiation of oxic and hypoxic cells. Furthermore, differences between acute hypoxia and chronic hypoxia, leading to a change in the proteome, have been investigated. In the future, the influence of hypoxia-regulated p53 will be on particular interest. As a tumour suppressor p53 affects radio-resistance in some cancer cell lines.

The experimental system will be used for the rat prostate cancer cell line R 3327-AT-1 which is also used in an animal model. Thus, it is possible to mimic in a better way the irradiation of prostate cancer.

In a next step, the system will be further developed. Finally, it should allow the simulation of complex tumours with oxic and hypoxic regions. So interaction between these two different cell populations can be investigated *in-vitro*.

REFERENCES

1. Furusawa, Y., Fukutsu, K., Aoki, M., Itsukaichi, H., Eguchi- Kasai, K., Ohara, H., Yatagai, F., Kanai, T. and Ando, K.: Inactivation of Aerobic and Hypoxic Cells from Three Different Cell Lines by Accelerated ^{3}He-, ^{12}C- and ^{20}Ne-Ion Beams.
Radiat. Res. 154, 485–496 (2000).

2. Zhang L, Subarsky P, Hill RP.: Hypoxia-regulated p53 and its effect on radiosensitivity in cancer cells.
Int. J. Radiat. Biol. 83(7), 443-56 (July 2007).

DECREASED VARIATION IN CELL SURVIVAL AFTER PHOTON COMPARED TO NITROGEN ION RADIATION IN NORMAL AND TUMOUR CELLS

A. R.-M. Jernberg[*], A. E. Meijer and M. R. Edgren
Departament of Oncology-Pathology, Medical Radiation Physics, Cancer Centre Karolinska,
Karolinska Institutet-Stockholm University, P.O. Box 260, SE- 171 76 Stockholm, Sweden

The purpose with this study was to investigate and compare the radiosensitivity of different human cells after exposure to photons (low linear energy transfer, LET, radiatio) and accelerated nitrogen ions (high LET radiation).

Normal fibroblasts (glutathione proficient, $GSH^{+/+}$, and deficient, $GSH^{-/-}$), a melanoma cell line (AA), a small cell lung carcinoma cell line (U-1690) and glioma cells deficient (M059J) and proficient (M059K) in the catalytic subunit of the DNA-dependent protein kinase ($DNA-PK_{CS}$) which is involved in the repair of DNA double strand breaks, respectively, were exposed to photons (0.2 keV/µm) or accelerated nitrogen ions (140 keV/µm). The radiosensitivity was measured as clonogenic cell survival. The surviving fraction at 2 Gy (SF2) and the relative biological effectiveness (RBE) values at different survival levels were calculated using the survival.

The SF2 varied from 0.02 to 0.72 for the γ irradiations, and from 0.02 to 0.08 for the nitrogen ion beam irradiations. The RBE values were in the range 1.1-4.5 for 10% survival level and 1.1-8.5 for 75% survival level.

The large variation in sensitivity to photon radiation of human normal and tumour cells were highly reduced after accelerated nitrogen ion radiation, with clonogenic cell survival values being nearly the same after high LET exposures. The RBE values are higher and more dependent on the survival level for tumour cells compared to the normal cells. Therefore the impact to kill γ-radioresistant tumour cells with high LET radiation is very pronounced.

Treatment Planning

MEASUREMENT OF RELATIVE BIOLOGICAL EFFECTIVENESS (RBE) AND FRACTIONATION RATIOS (α/β) AFTER SINGLE AND FRACTIONATED DOSES OF CARBON IONS TO THE SPINAL CORD OF THE RAT

C.P. Karger[1], P. Peschke[2], M. Scholz[3], J. Debus[4]
[1] Dept. of Medical Physics in Radiation Oncology, DKFZ Heidelberg, Germany
[2] Clinical Cooperation Unit Radiation Oncology, DKFZ Heidelberg, Germany
[3] Dept. of Biophysics, GSI Darmstadt, Germany
[4] Dept. of Clinical Radiology, University of Heidelberg, Germany

Abstract The depth dose profile of ions (Bragg curve) allows for a high degree of dose conformation to the Tumor [1]. Heavy charged particles such as Carbon ions additionally show an increased relative biological effectiveness in the Bragg peak relative to the plateau region. The increased RBE has to be considered in treatment planning by incorporating the RBE. At GSI (Germany), the RBE is calculated at each point within the treatment field using the local effect model (LEM) [2]. Dose response curves for the endpoint paresis °II was measured in a rat model using 1, 2, 6 and 18 fractions of photons and Carbon ions (Bragg-peak and plateau), respectively, and the resulting RBE-values were compared with predictions of the LEM [3,4]. In addition, values for the α/β-parameter of the linear-quadratic model were derived. In the experiment, the LEM overestimated the RBE in the plateau and underestimated the RBE in the Bragg-peak region. A significant fractionation effect was only found for the plateau region. The experimental data contribute to the validation of the LEM and quantify the involved uncertainties.

INTRODUCTION

The tolerance of the rat spinal cord to photon and Carbon ion irradiations was investigated to determine the relative biological effectiveness (RBE) of carbon ions (^{12}C) in the plateau region and in a spread-out Bragg-peak.

METHODS AND MATERIALS

The cranial part of the spinal cord of the rat was irradiated with 1, 2, 6 or 18 fractions of photons or ^{12}C-ions, respectively. Plateau irradiations were performed in the entrance region of a 270 MeV/u Bragg-peak, while for the peak irradiations a 10 mm spread-out-Bragg-Peak of 140 MeV/u. was used. Animals were followed up for 300 days after irradiation for the onset of paresis grade II. Dose response curves were calculated for each irradiation experiment and D_{50}-values (dose at 50% complication probability) were determined.. Based on these D_{50}-values, the RBE and the α/β-parameters were calculated. The RBE-values were compared with predictions of the local effect model (LEM).
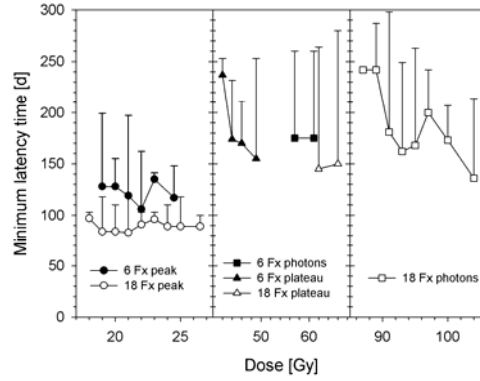
Fig. 1. Latency time after irradiation (reprinted from [4] with permission from Elsevier)

RESULTS

The experimentally determined RBE-values for 1, 2, 6 and 18 fractions were 1.44±0.08, 1.37±0.05, 1.33±0.02 and 1.42±0.02 for the plateau- and 1.77±0.06, 2.17±0.06, 2.97±0.05, and 5.04±0.08 for the peak-irradiations. The respective predictions by the LEM were 1.14, 1.19, 1.37, and 1.72 for the plateau- and 1.28, 1.61, 2.35, and 3.80 for the peak irradiations. The measured α/β-values were 2.8±0.4 Gy for photons, 2.1±0.4 Gy for the plateau and 37.0±5.3 Gy for the peak-irradiations, respectively.

Fig. 1. Dependence of the relative biological effectiveness (RBE) on fraction number (a) and dose (b). (reprinted from [4] with permission from Elsevier)

CONCLUSIONS

Carbon ion irradiations of the spinal cord are significantly more effective in the peak than in the plateau region. A significant fractionation effect was only found for the plateau-irradiations. For the peak irradiations, the LEM correctly describes the dose dependence of the RBE, although it generally underestimates the RBE by 25%. In the plateau region, overestimations o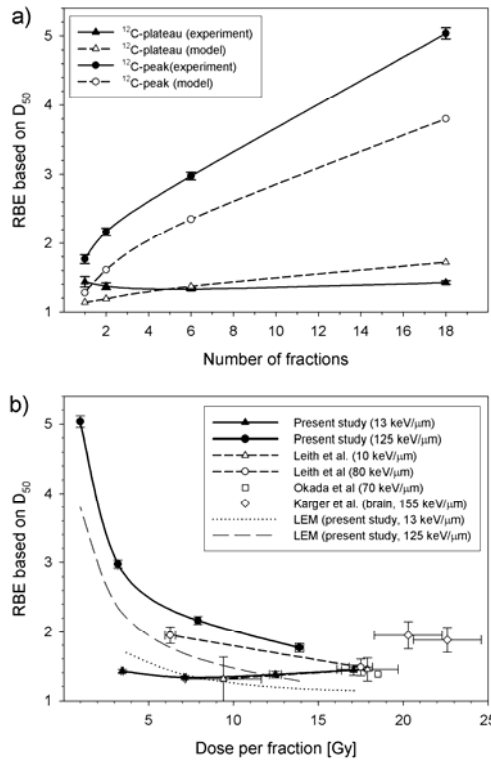f up to 20% were found for the clinically applied low doses per fraction. The experimental data contribute to the validation of the LEM and quantify the involved uncertainties.

REFERENCES

1. Karger C.P., Jäkel O.: Current status and new developments in ion therapy. Strahlentherapie und Onkologie 183, 295-300, 2007
2. Scholz M., Kellerer A.M., Kraft-Weyrather W., Kraft G. Computation of cell survival in heavy ion beams for therapy. The model and its approximation. Radiat. Environ. Biophys.;36, 59-66, 1997.
3. Debus J., Scholz M., Haberer T., Peschke P., Jäkel O., Karger C.P., Wannenmacher M.: Radiation tolerance of the rat spinal cord after single and split doses of photons and carbon ions. Radiation Research 160, 536-542, 2003
4. Karger C.P., Peschke P., Sanchez-Brandelik R., Scholz M., Debus J.: Radiation tolerance of the rat spinal cord after 6 and 18 fractions of photons and carbon ions: experimental results and clinical implications. International Journal of Radiation Oncology, Biology, Physics 66, 1488-1497, 2006

*Corresponding author: c.karger@dkfz.de

DEPENDENCE OF CELL SURVIVAL AFTER CARBON IRRADIATION ON THE α/β−RATIO FOR PHOTON IRRADIATION- IMPLICATIONS OF THE LOCAL EFFECT MODEL

Th. Elsässer[*], M. Scholz

Gesellschaft für Schwerionenforschung (GSI) mbH, Planckstr. 1, 64291 Darmstadt, Germany

The prediction of the relative biological effectiveness (RBE) of swift ions for different tissues is a crucial task for biophysical modelling in heavy ion therapy. The Local Effect Model (LEM) has been proven to provide good estimates in order to assess cell inactivation related to tumor control probability as well as normal tissue complications. Based on a systematic dependency of the RBE on the α/β− ratio of the corresponding photon irradiation, it is shown that the LEM can predict the biological response for a large range of α/β− ratios. Here, the improvement of the recently introduced cluster extension of the model is discussed. Furthermore comparisons of the modified LEM to experimental *in vivo* data are presented.

INTRODUCTION

The treatment of tumors with heavy ions requires a biophysical model in order to predict the relative biological effectiveness (RBE) at each position in the irradiation field. Since, in general, the RBE depends on the energy and LET of the primary beam and all its fragments, the tissue under consideration, the dose level and the biological endpoint, it basically varies from voxel to voxel in the irradiation field. For an application in treatment planning the dependence on different biological endpoints such as tumor control probability (TCP) and normal tissue complication probability (NTCP) is of special interest.

The Local Effect Model (LEM) (*1*) developed at GSI is currently the only model, which is implemented in treatment planning and takes these dependences into account. It calculates the RBE for different ions and cell lines starting from the corresponding experimental photon data and an amorphous track structure model. A key feature of the model is that it uses the experimental data obtained by photon irradiation as input to predict the biological response following ion irradiation by assessing the ion-induced *local* damage.

CLUSTER EXTENSION

Here, we analyze an extension of the model (*2*) which takes cluster effects of single strand breaks at the nanometer scale into account. In line with the main idea of the LEM, we take the yield of single (SSB) and double strand breaks (DSB) from experimental photon data and use a Monte-Carlo method to distribute them onto the DNA. We score clusters of SSBs where individual SSBs on different strands are separated by less than 25 bp as additional DSBs. Assuming that the number of DSBs is a measure for cell lethality, we derive a modified cell survival curve for photons which takes these cluster effects into account. Additionally we improved the representation of the radial dose distribution by explicitly considering radical diffusion. Therefore, we use a Gaussian function in two dimensions to disperse the energy with a spread of 4 nm representing the radical diffusion length in mammalian cells.

COMPARISON WITH CELL EXPERIMENTS

We compare this extended version of the LEM to various experimental *in vitro* data and find a better agreement of the RBE than for the original model (*2*). The key feature of the extension is an increased ratio of RBE values for high-LET particles of several hundred keV/μm with respect to low-LET particles. However, an observable overestimation of the RBE values for low-LET particles remained although the improvements due to the modified version was significant. Additionally, we tested our improved model with cell inactivation experiments mimicking a clinical situation, where cells are

placed in a phantom which is comprised of a u-shaped tumor embracing an organ-at-risk (*3*). We find a better agreement with experimental data especially in the tumor region, where high-LET particles are most important, whereas in the entrance channel, the calculated survival levels were systematically lower than the measured data.

DEPENDENCE ON THE α/β−RATIO

We use the modified version of the LEM in order to investigate the RBE dependence of carbon ion irradiation on the α/β-ratio of the corresponding photon survival curve. The extensive data base of Suzuki et al. (*4*) is ideally suited for a meaningful analysis, since the photon survival curve together with a low- and high-LET survival curve is measured for 16 different human cell lines. We show that the LEM gives good results for the entire range of ratios and the improvement of the modified version of the LEM is specifically demonstrated at large α/β-ratios, where the original LEM underestimates the RBE for high-LET irradiation. Generally, the decrease of maximum RBE values for increasing α/β-ratios is nicely reproduced. In an earlier publication (*5*) we showed that the model predictions for the RBE depend more strongly on this ratio than on the absolute values for the linear and quadratic component of the photon dose response curve. Therefore, the LEM can be applied to a large range of different tissues if the dose response after photon irradiation parameterized by the α/β-ratio is known.

NORMAL TISSUE COMPLICATIONS

Before heavy ion treatments started at GSI, the RBE for normal tissue complication in the skin of minipigs was predicted by the LEM and compared to experimental data (*6*). This comparison showed a nice agreement between simulation and experiment demonstrating the capability of the LEM to provide reasonable RBE values. In a different set of experiments, the RBE for the radiation tolerance of the rat spinal cord was measured for four different fractionation schemes (*7*). It was shown that the LEM can predict the general behavior of the dose dependence. However, a deviation from the experimental data up to 30% for low doses in a spread-out Bragg peak was observed. The cluster modification of the LEM yields better agreement especially at low doses, although the difference between experimental and simulated data exceeds 15%.

SUMMARY

It was demonstrated, that the modified version of the LEM significantly improves the RBE predictions and shows good agreement with a large set of experimental results. Especially the improvement of the dependence of RBE on the radiosensitivity after photon irradiation expressed by the linear-quadratic model parameters, makes the cluster extension favorable for application in heavy ion tumor treatment planning. In future, the discrepancy between measurements and predictions for low-LET particles will be addressed.

REFERENCES

1. M. Scholz and G. Kraft, Calculation of heavy ion inactivation probability based on track structure, x-ray sensitivity and target size. Radiat. Prot. Dosim. 52, 29-33 (1994).
2. Th. Elsässer and M. Scholz, Cluster Effects within the Local Effect Model. Radiat. Res. 167, 319-329 (2007).
3. A. Schmidt, M. Krämer, C. von Neubeck, and W. Weyrather, Multiple field optimization and biological dosimetry of a 2D-treatment plan. GSI Report, (2005).
4. M. Suzuki, Y. Kase, H. Yamaguchi, T. Kanai, and K. Ando, Relative biological effectiveness for cell-killing effect on various human cell lines irradiated with heavy-ion medical accelerator in Chiba (HIMAC) carbon-ion beams. Int. J. Radiat. Oncol. Biol. Phys. 48, 241-250 (2000).
5. M. Scholz and T. Elsässer, Biophysical Models in Ion Beam Therapy. *Adv. Space Res.* doi:10.1016/j.asr.2007.02.066 , (2007).
6. T. Zacharias and others, Acute response of pig skin to irradiation with 12C-ions or 200 kV X-rays. Acta Oncol. 36, 637-642 (1997).
7. C. P. Karger, P. Peschke, R. Sanchez-Brandelik, M. Scholz, and J. Debus, Radiation tolerance of the rat spinal cord after 6 and 18 fractions of photons and carbon ions: experimental results and clinical implications. Int. J. Radiat. Oncol. Biol. Phys. 66, 1488-1497 (2006).

THEORETICAL LIMITS OF LEM

M. Beuve[1,2], A. Colliaux[1,2], E. Testa [1]
[1] IPNL, université Lyon 1, CNRS UMR5822, Villeurbanne, F-69622, France. Université de Lyon, Lyon, F-69003, France
[2] LIRIS, université Lyon 1, CNRS UMR5205, Villeurbanne, F-69622, France. Université de Lyon, Lyon, F-69003, France

Abstract: As a complement to the evaluation of Local Effect Model (LEM) by facing its predictions to experimental data, we undertook a theoretical analysis of its main assumptions. In this paper, we focused on the notion of locality and on the expression that links the local effects to the local dose. With a Monte-Carlo simulation we demonstrated this expression, which mixes macroscopic scale and microscopic scale, is inconsistent. We also showed that describing the local effect by a simple function of the local dose does not allow to reproduce the shoulder that can be observed in cell survival to X-rays.

A INTRODUCTION

Cell survival to ionizing radiation is an interesting biological endpoint for the planning of treatment by radiotherapy since it can be linked to the probability to control tumor. Generally cell survival is estimated by in-vitro measurements. Cell are seeded in flasks and irradiated with a uniform dose covering the whole sample. Counting the formed colonies gives access to rate of cells that survived to the irradiation. Survival curves give the survival probability expressed as a function of the dose delivered by the irradiation facility. To be inserted in treatment planning systems, experimental data has to be accurately reproduced by a model, which allows to get survival value at any dose. Within conventional radiotherapy, survival is directly linked to the physical dose. Consequently an interpolation with a mathematical expression for which the parameters are fitted to the experimental data is convenient. Thus, LQ model allows rather faithful predictions with only two free parameters. In the field of radiotherapy with light ions, survival depends on the physical dose, but also on the ion nature and the ion energy. This dependency is attributed to the high level of heterogeneity of the dose deposition. Indeed, along the path of the ion, the density of ionized and excited molecules may be very huge for high-LET ions. As a consequence they may induce complex damage as double strand break or clusters of damage sites in DNA. Such defects are very difficult to repair for the cell. Among possible evolutions, they may induce cell death.

To predict cell survival, Local Effect Model (LEM) [1-4], considers cell killing stems from the induction of lethal events by the ionizing radiation. Assuming the number of lethal events obeys a Poisson distribution, the probability for the cell to survive reads:

$$S = e^{-N_{lethal}} \qquad (1)$$

where N_{lethal} is the mean number of lethal events induced in the cell. The first key point of LEM is to consider that the lethal events are local events generated by the local dose deposited by the radiation. Then, the number of lethal events in the cell is the summation, over the cell sensitive volume, of the local lethal events density:

$$N_{lethal} = \iiint\limits_{Sensitive Volume} \rho_{lethal}(r)d\mathbf{r} \qquad (2)$$

where the density of lethal events is a simple function of the local dose d(**r**):

$$\rho_{lethal}(r) = f(d(r)) \qquad (3)$$

In LEM, the sensitive volume is assumed to be homogeneously sensitive and it is restricted to nucleus. The second key point of LEM is to extract the relation between the density of lethal events and the local dose from survival measurements performed with X-ray radiation. Indeed, since the dose deposited by X-ray radiation is considered to be homogeneous,

$$d(r) \approx D \qquad (4)$$

the relation between the density of lethal events and the dose can be deduced from the number of lethal events in the cell:

$$N_{lethal}(D) = \iiint\limits_{Sensitive\,Volume} f(D)d\mathbf{r} \qquad (5)$$

i.e.

$$N_{lethal}(D) = f(D)\iiint\limits_{Sensitive\,Volume} d\mathbf{r} \qquad (6)$$

Here D is the dose delivered in the sample by the X-ray source. According to Equation (1), the number of lethal events can be deduced from the survival curve. The average number of lethal events can then be calculated even for heterogeneous dose distribution provided that the local dose *d(r)* is known:

$$N_{lethal} = \iiint\limits_{Sensitive\,Volume} \frac{-\ln S_x(d(r))}{V} d\mathbf{r} \qquad (7)$$

where V is the nucleus volume.

Practically, a configuration of ion irradiation is generated randomly for an irradiation dose D_{ion}. For this configuration, the local dose is calculated by a track structure model. The average number of lethal events is then deduced from Equation (7), which gives the probability for the cell to survive $S(D_{ion})$ to the dose D_{ion} according to Equation (1). Because the ion irradiation is a very stochastic phenomenon, the process has to be reiterated many times to reduce statistical fluctuations on the predicted survival. By means of fitting one parameter describing the survival curve at high doses (> 10 Grays), LEM predicts the main tendencies that are observed experimentally and for some ions the agreement with the existing experimental data is quite satisfactory. Nevertheless as mentioned by LEM authors [5], the model still has to be improved.

The best way to evaluate models such as LEM is to face their predictions to experimental data. It is all the more true that the main goal of LEM is to supply predictions for clinical applications. However, the set of available experimental data is still non exhaustive in particular because access to ion-beam facilities is a limiting factor. As a complementary approach, theoretical analysis could help in evaluating some of the LEM assumptions by proving them or drawing some limits of application. Moreover such analysis can suggest directions to improve the quality of the predictions. In this paper, we focus on the relation between the density of local lethal events and the local dose. As mentioned above, this relation is based on the extrapolation to local scale of the relation between the X-ray dose and the average number lethal events. This extraction is supported by the idea that X-ray radiation is homogeneous (even at local scale). The aim of the present work is to evaluate to which extend the local dose deposited by X-ray can be assumed to be homogeneous.

B MATERIAL AND METHODS

To quantify the level of heterogeneity of the local dose we built a histogram of local dose. Practically, we meshed a water sample with cubes and simulated the irradiation with a Monte-Carlo Code. The simulation consists in following the incident particles and all the electrons of the induced electronic cascades. The results of the simulation is a spatial distribution of low-energy electrons (< meV), ionized and exited water molecules. The dose of each cube is calculated by summing the energy of all the species standing in the cube at the end of the simulation. We calculated histograms of local dose for X-ray irradiation but also ion irradiation. For ion irradiation we applied a simulation for which details can be found in [6-7]. For X-ray irradiation, we simulated the irradiation of 1.3 MeV photons, which matches with the γ-rays generated by a ^{60}Co source. At this energy, Compton interaction dominates and most of the photon interactions eject Compton electrons. We followed the ejected electrons with the code used for ion irradiation. In both modalities of irradiation, we applied to the sample periodical boundary conditions to avoid edge effects and to ensure the equilibrium of charged particle. The sample was chosen large enough to avoid any significant correlation effects and to reduce statistical errors in histograms.

The choice of the cube size is crucial since it defines the level of locality. Papers describing LEM model do not definitely fixed the scale of locality. But, in principle, it cannot be higher than the lethal-event spatial extension. Double strand break extension is said to be less than 20 pairs of bases (~6 nm). If one considers that damage may be induced by indirect actions, one may add 4 nm to take into

account the diffusion of radicals. Finally, we chose 10 nm for the cube size. The sample size was typically 50x50x10um³, which is challenging on the side of computer-memory management.

C RESULTS

We performed simulations for an irradiation of 1 Gray with γ -ray, H[10MeV] and C[10MeV/n] (fig. 1) and of 5 Grays (fig. 2). We first observed that more than 99% of the cubes do not receive any dose even for X-ray irradiation. We can then conclude that, even for X--ray irradiation, the local dose is far from been homogeneously spread within the target.
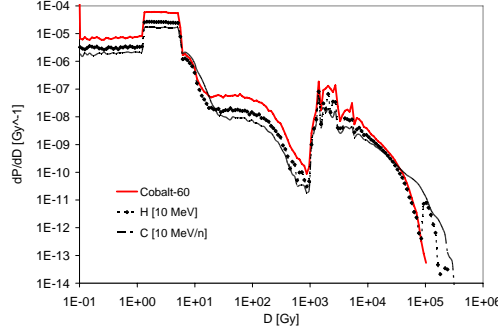

Figure 1. Histogram of local dose calculated in a sample of 50x50x10 um³ irradiated with a dose of 1 Gray at equilibrium of charged particles. The mesh resolution is 10 nm.

The second observation we made concerns now the distribution of local dose for the nonempty cubes. According to fig. 1 local dose varies from 0.1Gray to 10^5 Grays for X-ray. Moreover below 10^4 Grays, the histogram features are similar for all particles. The peaks in the histograms have to be attributed to the energy threshold for rotation, vibration, excitation and ionization of water molecules. The amplitude of the histogram depends on the particle. The lower the LET, the larger the proportion of cube that received energy. Differences in features can be reported beyond 30 kGrays for H[10MeV] and 80 kGrays for C[10MeV/n]. These features may probably be attributed to the events in the very core of the tracks.

Summarizing these observations, we conclude that, not only the local dose deposited by X-ray is strongly heterogeneous, but it ranges from 0.1Grays to 100 kGrays. As a consequence, as for ion radiation, the number of lethal events is a complex function of the distribution of local dose and therefore the relation between the local dose and the density of lethal events cannot be simply set as:

$$f(d(r)) = \frac{-\ln S_X(d(r))}{V} \qquad (8)$$

The local dose has to be classified among microscopic phenomena. It is defined at the scale of nanometers and it is deposited in less than microsecond (most of the electronic cascades are achieved within 10^{-15}s). Instead the dose in the survival curve has to be classified among macroscopic phenomena. It is generally deposited within minutes and uniformity is ensured at a scale of 0.1mm. Finally from this analysis we can conclude the method to insert in LEM the experimental data obtained with X-ray radiation is not consistent since it mixes two different levels of scale.

To go further we wanted to know, if however, it was possible to find out any local function f(d) for which the parameters could be fitted to get predictions in agreement with experimental data for X-ray. Such a function could then be applied for ion radiation to deduce survival to high-LET radiation. Considering the cubic mesh, Equation (2) and (3) gives:

$$N_{lethal} = \sum_{Sensitive\,Volume} f(d_i)\Delta V \qquad (9)$$

where d_i is the local dose in the cube i and ΔV is the cube volume. Gathering the local dose allows to introduce the histogram of local dose according to:

$$N_{lethal} = \sum_k h(d_k)f(d_k)\Delta V \qquad (10)$$

To simulate the irradiation of a cell nucleus, we reduce the sample size to 10x10x10 um^3. Again the conditions of irradiation were set to ensure the equilibrium of charged particles. Fig. 2 compares the results for an X-ray irradiation of 1 Grays and one of 5 Grays.
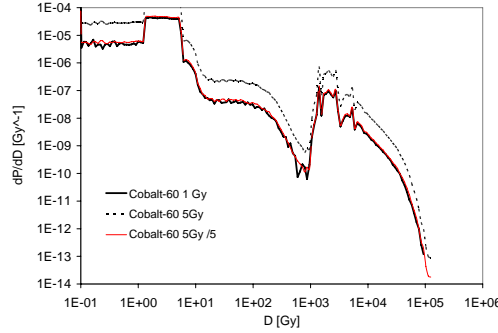

Figure 2.   Histogram of local dose calculated in a sample of 10x10x10 um^3 irradiated with a dose of 1 Gray and 5 Gray at equilibrium of charged particles. The mesh resolution is 10 nm. The curve labeled with "Cobalt 60 5Gy/5" represents the histogram calculated for 5 Grays and divided by a factor 5.

We observe that after normalization to the irradiation dose, the histogram for 5 Grays matches with the histogram for 1 Gray (for the non empty cubes). Consequently, for dose D of X-rays lower than 5 Gray, one has:

$$h_D(d_k) = h_1(d_k).D \quad \forall d_k \neq 0 \ (11)$$

where h_D (resp. h_1) is the histogram of local dose for an irradiation dose of D (resp. 1 Gray). In other words, at local scale, two photons cannot contribute to the same site. In fact, increasing the dose simply increases the number of hit cubes. It is now interesting to inject Equation(11) in Equation (10). It reads:

$$N_{lethal}(D) = D.\sum_k h_1(d_k) f(d_k) \Delta V \ (12)$$

Defining the constant α_X by:

$$\alpha = N_{lethal}(D=1\,Gy) \qquad (13)$$

we can deduce from Equation (1) that the cell survival to an X-ray irradiation of dose D obeys:

$$S_X(D) = e^{-\alpha D} \qquad (14)$$

These calculations show that a description of a radiobiological endpoint by a simple function of the local dose $f(d_k)$ gives a linear relation for cell survival to X-rays. In particular the shoulder, which can be observed experimentally, cannot be reproduced. In this aspect, LEM is not fully consistent since by inserting as input data the survival to X-ray, one should expect the survival to X-ray to be reproduced. This observation may explain the difficulty for LEM to "perfectly" predict survival for both high-LET and low-LET ion at a time.

All the mentioned conclusions are quite robust. For instance, we verified that Equation (12), which is necessarily valid for cube length lower than 10 nm, is still valid for cube length as high as 100 nm. As it is presented, LEM is not fully consistent. However, considering the relevant results of this model when facing its predictions to experimental data, we suggest that some "non local effects" may be already included somewhere in the model but no clearly visible thought its description. Finding in which way these effects are included may open LEM to improvement.

C CONCLUSIONS

To evaluate one of the main assumptions of LEM, we calculated within a Monte Carlo simulation the distribution of local dose deposited by the irradiation of water samples with ions and X-rays. To this aim we meshed the samples with cubes of length 10 nm and calculated the energy deposited in each cube. This resolution was chosen because it may correspond to the spatial extension of lethal events such as double strand break or cluster of damage sites. However decreasing the length or increasing it to 100 nm does not change the main conclusions. We first observed that at local scale, X-ray radiation is far from been homogeneous. Indeed, more than 99% of the space does not receive any local dose. Moreover, the local varies from 0.1 Gray to 10^5 Grays, even if the radiation field is uniform. As a

consequence, the relation between the dose and lethal events generated in a cell cannot be extended to local effects as it is assumed in LEM. This extension is equivalent to mix *microscopic scale*, in which dose is strongly heterogonous and is deposited in a time period lower than microseconds, and *macroscopic scale*, in which the dose is generally deposited within minutes and defined with a resolution not more accurate than 0.1 mm. To go further we focused on a possible description of biological endpoints by a simple function of local dose. We concluded that a simple function cannot describe biological effects such as the shoulder that can be observed in curves of cell survival to X-ray radiation. It seems therefore necessary to include non local effect. However, the relevant of LEM predictions suggests that such "non local effect" might be already included in this model. Clarifying this point might help to improve LEM.

REFERENCES

1. Scholz M., Kraft G. "Track structure and the calculation of biological effects of heavy charged particles"; Adv Space Res. 18 (1-2):5-14 (1996)
2. Scholz, M, Kellerer, AM, Kraft-Weyrather, W, Kraft, G. "Computation of cell survival in heavy ion beams for therapy - the model and its approximation"; Radiat. Environ. Biophys. 36, 59–66 . (1997)
3. Scholz M & Kraft G 2004 Rad. Res. 161, 612 – 620.
4. Kramer M and Scholz M "Treatment planning for heavy ion radiotherapy: calculation and optimization of. biologically effective dose"; Phys. Med. Biol, 45/11, 3319 – 3330 (2000)
5. Scholz, M., Kellerer, A. M.; "Improvement of the local effect model (LEM)—implications of clustered DNA damage" ; Radiat Prot Dosimetry.2006; 122: 475-477
6. Gervais B, Beuve M, Olivera G H & Galassi M E; "Numerical simulation of multiple ionization and high LET effects in liquid water radiolysis"; Radiation Physics and Chemistry 75, 493–513 (2006).
7. Gervais B, Beuve M, Olivera G H, Galassi M E & Rivarola R D ;"Production of HO[2] and O[2] by multiple ionization in water radiolysis by swift carbon ions" ; Chemical Physics Letters 410(4-6), 330–334 (2006).

TREATMENT PLANNING FOR ION BEAMS

O. Jäkel [1,*], M. Ellerbrock[1], M. Krämer[2], J. Debus[3]

[1]Department of Medical Physics in Radiation Oncology, German Cancer Research Center (DKFZ), Im Neuenheimer Feld 280, D-69121 Heidelberg, Germany
[2]Department of Biophysics, Gesellschaft für Schwerionenforschung (GSI), Darmstadt, Germany
[3]Department of Radiation Oncology, University Heidelberg, Heidelberg, Germany

Radiotherapy with a scanned ion beam puts some special demands on the treatment planning process. An overview over some technical aspects and their implication on the treatment planning system are reported. This includes the aspects of an active beam scanning system, as well as patient positioning, target definition and the question of dose prescription. Especially, the approach followed at GSI and Heidelberg, for the biological optimization in treatment planning is discussed.

Introduction: Ion Beam Therapy in Germany

Within the last two decades particle therapy with protons and heavy ion beams has gained increasing interest. Currently the availability of heavy ion RT is limited, as worldwide only 3 facilities offer carbon ion RT: two hospital based facilities in Japan (HIMAC/Chiba and HIBMC/Hyogo) and a physics research facility at GSI, Darmstadt in Germany. There is, however, an increasing interest in ion radiotherapy especially in Europe, where new facilities are being built in Germany [4] and Italy or are in an advanced planning phase like in Austria and France.

At the research laboratory Gesellschaft für Schwerionenforschung (GSI) in Darmstadt, a therapy unit began its clinical operation in 1997 [2]. Until mid 2007, about 370 patients have been treated with carbon ions. In the meantime a hospital based ion beam facility was built in Heidelberg and will start clinical operation in 2008.

Both facilities are equipped with a 3D beam scanning system, which can deliver highly conformal dose distributions to arbitrarily shaped volumes with a spatial resolution of 1-2mm in all three directions. Using a magnetic deflection system, the intensity controlled raster scanner can deliver a monoenergetic pencil beam over an arbitrarily shaped area. To do so, a beam of 4-10mm full-width half-maximum is scanned over a regular grid of points with typically 2-3mm spacing. After completion of a scan, the accelerator energy can be switched from pulse to pulse and another scan can be performed with a different radiological depth. In total, 252 accelerator energies are available [3].

A feedback loop from the intensity control moves the beam to the next beam spot, when a predefined number of particles is reached. An online monitoring of the beam position and a feedback loop to the scanner is used to keep the beam extremely stable at each scan spot.

Implications of the beam delivery system

Passive beam shaping still is most commonly used in proton and heavy ion therapy. Modulators, range shifters, compensators, collimators and a double scattering system is typically introduced in the beam, in order to shape the individual fields of a treatment plan.

This has several disadvantages: first, the depth dose can only be tailored to the distal end of the target, but not to the proximal end. A considerable amount of the high dose region (and high LET region) is therefore located in the normal tissue. Secondly, the amount of material in the beam line leads to an increase in nuclear fragments produced by nuclear interactions with the material of the beam modifiers. Finally, a large number of patient specific beam modifiers have to be manufactured like

*Corresponding author: o.jaekel@dkfz.de

compensator and collimator for each treatment field and various modulators, which have to be exchanged for different patients.

Using the passive depth dose shaping system at HIMAC, the depth dose profile is fixed by the modulator hardware throughout the irradiation field and no further optimization is necessary. The modulators were designed in order to achieve a prescribed homogeneous biological effective dose for a single field. The design of the modulators reflects the fixed dependence of the RBE with depth for a certain dose level [7], which was optimized for a certain fractionation scheme and dose per fraction. The TPS can thus rely on measured depth dose data and a detailed modeling of nuclear fragmentation is not mandatory.

In contrast, active beam shaping takes advantage of the possibility of scanning the beam over the treatment field. Moreover, the energy from a synchrotron can be switched from pulse to pulse in order to adapt the range of the particles in tissue. This way, a target volume can be scanned in three dimensions and the dose distribution can be tailored to any irregular shape without any passive absorbers or patient specific devices, like compensators or collimators. Therefore, the high dose region can also be conformed to the proximal end of the target volume and the integral dose as well as the volume receiving high LET radiation is minimized.

There is, however, considerable effort necessary in order to monitor on-line the position and intensity of the beam and to enable a safe and accurate delivery of dose to the patient.

For an active beam shaping system for ions a research TPS was developed for the GSI facility. The system is a combination of a graphical user interface for RT planning (Virtuos [1]) and the program TRiP for all ion specific tasks [9,10,6]. TRiP handles the optimization of absorbed as well as biological effective dose and the optimization of the machine control data. The TPS and its development are subject to a concise quality assurance system [5].

While a modulator for passive beam shaping is designed to achieve a prescribed homogeneous biological effective dose for a single field, a 3D scanning system, however, can produce nearly arbitrary shapes of the spread out Bragg peak (SOBP). The shape of the SOBP therefore has to be optimized separately for every scan point in the irradiation field.

The new demands on the TPS are:

- The beam intensity, energy and position of each scan point have to be optimized to obtain a homogeneous biological effect.
- The capability for intensity modulated radiotherapy with ions should be taken into account.
- All fields of a treatment plan are applied at the same day (in contrast to passive systems).
- The dose per fraction should be variable for every patient.

The dose calculation for active beam shaping systems also relies on measured data. Instead of the measured depth dose data for the SOBPs resulting from the modulators, data for the single energies are needed. If the applied dose is variable, it is necessary to base the calculation of absorbed dose on absolute particle numbers rather than on relative values.

Concerning the biological effectiveness, a biological model is needed, which takes into account the variation of beam parameters for each scan spot. Such a model was developed e.g. at GSI [11]. The model takes into account the different energy deposition patterns of different ions and is thus able to model their biological effect. A prerequisite for this is the knowledge of the number of fragments produced as well as their energy spectrum. The calculated RBE shows a dependence on the dose level and cell type, if the underlying photon survival data for this respective cell type are known. In the TPS, a prescribed biological effective dose within the target volume is then optimized [9,6]. The dose dependence of the RBE demands the use of absolute dose values during optimization.

Aspects of patient positioning

Due to the high spatial accuracy that is achievable with ion beams, patient fixation and positioning require special attention. Patient fixation is currently achieved with an individually prepared mask systems developed at DKFZ. This system allows only very small movements of the skull within the mask of 1-2mm. A high accuracy during the initial positioning is achieved by the use of stereotactical imaging and positioning techniques. Prior to every fraction the position is verified using X-ray imaging in treatment position. The comparison of the X-ray images against digitally reconstructed radiographs obtained from the treatment planning CT allows the detection and correction of deviations

in the patient position in the order of 1mm [8]. For the Heidelberg facility a robotic controlled digital X-ray system will be available to obtain accurate position verification.

For the treatment of tumors in the pelvic region a cast system of the same material as for the head mask is used to fix the bony structures of the pelvis. In addition a modified head mask is used to limit movements of the patient in craniocaudal direction. In combination with the X-ray position verification, the accuracy of the position of bony structures in the pelvis is less than 3mm.

Target definition and dose prescription

For the treatment of skull base tumors the PTV is defined by adding a margin of 1-2mm around the CTV. The margin accounts for target movement, uncertainties in the set-up during the treatment course and uncertainties in the beam delivery and range calculation.

Setup errors in the direction longitudinal to the beam are not very important, as the scanned ion beam has a very small divergence (about 1 milli-steradian) and can be considered parallel. This is due to the fact that the virtual source point is about 8m upstream of the isocenter. Lateral setup errors are much more important.

The uncertainty due to the scanning beam delivery system amounts to approximately 0.5mm in lateral direction. This is ensured by the online monitoring of the beam position used to control the scanning magnets. The uncertainty in the beam energy is extremely small since the SIS synchrotron represents a very efficient spectrometer. Range uncertainties due to energy variations can therefore be neglected. The calculation of ion ranges in tissue, however, is the largest source of uncertainty. It depends strongly on the type and homogeneity of the traversed tissue. For a beam path through cranial bone and brain tissue without large inhomogeneities the uncertainty is around 1mm. For a beam path through the auditory channel or paranasal cavities range uncertainties of up to 5mm may occur.

For tumors in the neck region or paraspinal tumors larger setup errors are expected and the margin has to be increased to 3mm for extracranial tumor sites. Moreover, in critical cases the robustness of the treatment plan is assessed by simulating various setup errors and their effect on the dose distribution.

The quantity used for optimization is always the biological effective dose, i.e. in the TPS the absorbed dose is optimized so that the product of dose and relative biological effectiveness is homogeneous throughout the target volume.

It is intended that the whole target volume is covered with at least 90% of the prescribed dose. The homogeneity of dose distributions is typically much better than in conventional therapy or IMRT.

Typically, for a fully fractionated treatment, 20 fractions are delivered on 20 consecutive days. Only the fraction dose enters the TPS, as complete repair is assumed to take place in one day. For a fully fractionated treatment, a sequential boost is delivered typically during the last 5 days of the treatment course. This is obtained by optimization of a second treatment plan optimized for the PTVII (the GTV plus a 1-2mm safety margin), usually with the same dose per fraction as the treatment of PTVI.

When defining the prescribed dose per fraction, it is important to specify also the endpoint for which the RBE has to be optimized. With the biological model used at GSI, it is the α- and β-values that have to be specified in order to allow for an optimization of the RBE. Since the applied doses in most cases are limited by the surrounding normal tissues, it is the α- and β-values for late effects in the normal tissues that are used for the optimization of RBE. If α- and β-values for the dose limiting toxicity and for the tumor are assumed to differ substantially, the biological treatment optimization is done separately using the α/β-ratios for both, the OAR and the tumor, respectively.

Planning of combination therapies

In case of adenoidcystic carcinoma and pelvic tumors, the carbon ion treatment is currently delivered as a boost treatment given in addition to a conventional 3D conformal RT or an IMRT treatment. Typically a carbon boost of six fractions is given on six consecutive days prior to the IMRT treatment. Both treatment modalities are planned using the same patient CT data and volume definitions and are integrated in the treatment planning platform VIRTUOS.

First the carbon ion treatment plan is optimized to yield a homogeneous biological effective dose to the PTVII. The calculated carbon ion dose distribution is assessed in the TPS in order to derive the

constraints for the OARs for the IMRT optimization. The KonRad software is used for the optimization of the photon dose distribution.

The weighted sum of the resulting photon dose and carbon ion dose distribution is then calculated on a voxel by voxel basis. Before the summation, the IMRT treatment plan is normalized to the median dose. The carbon dose may not be normalized since it is optimized to an absolute value of absorbed dose, or absolute particle numbers. Then both dose distributions are added up using the fraction of dose delivered with each modality.

Intensity modulated ion therapy

Although any treatment field applied with the beam scanning method is intrinsically modulated in intensity, intensity modulation (IM) is usually referred to as a simultaneous optimization of several treatment fields, each delivering an inhomogeneous dose to the target. A first prototype allowing the optimization of a homogeneous biological effective dose for 2 or 3 fields of carbon ions is available and is currently being evaluated. The necessary modifications of TRiP are described in the abstract by M. Krämer et al. The questions connected to its clinical use are discussed in the abstract by M. Ellerbrock and O. Jäkel.

Conclusion and Outlook

The treatment planning system developed for the GSI pilot project is capable of optimizing the biological effective dose of a beam of carbon ions applied with the active beam scanning system. An example of the highly conformal dose distribution that is achievable with the beam scanning system is shown in figure 1.

In the meantime, the algorithms of the TPS prototype were incorporated in a commercial treatment planning software by OCS Siemens, which will be used in the Heidelberg ion facility. The research platform of the TPS will be used, however, for a continuous development of the TPS, like improvements of the biological modeling and the fragmentation models as well as developments for the treatment of moving organs using beam tracking.

References

1. Bendl R, Pross J, Schlegel W (1993) VIRTUOS - A program for VIRTUal radiotherapy Simulation. In: Lemke HU, Inamura K, Jaffe CC, Felix R (eds.) Computer Assisted Radiology - Proceedings of the International Symposium CAR 93. Springer, Heidelberg, pp 676-682.
2. Debus J, Haberer T, Schulz-Ertner D et al. (2000) Fractionated Carbon Ion Irradiation of Skull Base Tumours at GSI. First Clinical Results and Future Perspectives. Strahlenther. Onkol. 176: 211-216.
3. Haberer T, Becher W, Schardt D, Kraft G (1993) Magnetic scanning system for heavy ion therapy. Nucl. Instrum. Meth. A330: 296-305.
4. Heeg P, Eickhoff H, Haberer T (2004) Die Konzeption der Heidelberger Ionentherapieanlage HICAT. Z. Med. Phys. 14: 17-24.
5. Jäkel O, Hartmann GH, Karger CP, Heeg P, Rassow J (2000) Quality assurance for a treatment planning system in scanned ion beam therapy. Med. Phys. 27: 1588-1600.
6. Jäkel O, Krämer M, Karger CP, Debus J (2001) Treatment planning for heavy ion radio-therapy: clinical implementation and application. Phys. Med. Biol. 46: 1101-1116.
7. Kanai T, Endo M, Minohara S et al. (1999) Biophysical characteristics of HIMAC clinical irradiation system for heavy-ion radiation therapy. Int. J. Radiat. Oncol. Biol. Phys. 44: 201-210.
8. Karger C. P., Jäkel O., Debus J., Kuhn S., Hartmann G. H. (2001) Threedimensional accuracy and interfractional reproducibility of patient fixation and positioning using a stereotactic head mask system. Int. J. Radiat. Oncol. Biol. Phys. 49/5 (2001) 1223-1234.
9. Krämer M, Scholz M (2000) Treatment planning for heavy ion radiotherapy: calculation and optimization of biologically effective dose. Phys. Med. Biol. 45: 3319-3330.
10. Krämer M, Jäkel O, Haberer T, Kraft G, Schardt D, Weber U (2000) Treatment planning for heavy ion radiotherapy: physical beam model and dose optimization. Phys. Med. Biol. 45: 3299-3317.

11. Scholz, M, Kellerer, AM, Kraft-Weyrather, W: Computation of cell survival in heavy ion beams for therapy - the model and its approximation. Rad Environ Biophysics 36: 59-66, 1997

Fig.1 : Example of a treatment plan for a patient with a skull base chordoma. The contours refer to the PTV(red), brain stem (blue), optical nerves (green, purple) and eyes (purple, light blue), respectively. Isodose lines of 10%, 30%, 50%, 70% and 90% of the prescribed dose are shown.
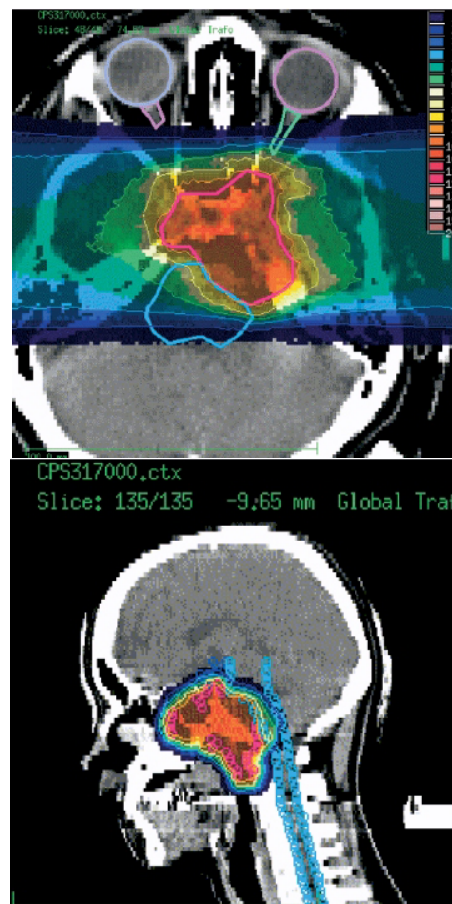
BIOLOGICAL TREATMENT PLANNING FOR ION BEAMS: STATUS AND DEVELOPMENTS

M. Krämer

GSI Biophysics, Planckstr. 1, D-64291 Darmstadt, Germany

1 Introduction

Charged particles like protons or heavier ions are becoming increasingly attractive tools for cancer radiotherapy, as can be seen from the increasing number of facilities currently in operation or being built in Germany (HIT, RKA Marburg), Europe (CNAO, Austron, Etoile), and Japan (NIRS, Hyogo) [1]. One reason is the good physical selectivity of ion beams, i.e. their inverted dose profile, and their reduced or negligible lateral scattering. Moreover, charged particles offer the possibility of active dose shaping via energy variation and magnetic deflection. This allows a much better dose conformation to arbitrary shapes of target volumes than conventional photon irradiation or ion irradiation with beam degraders. Consequently, all european ion radiotherapy sites are or will be equipped with magnetic scanning devices.

The other advantage, in particular for heavier ions such as carbon, is their relative biological effectiveness (RBE) increasing with penetration depth. Thus the maximum of radiobiological effect is in the vicinity of - or even coincides with - the maximum of energy absorption. Moreover, different inherent radiosensitivity of different tissues can be exploited to increase the probability of killing tumour cells whilst sparing healthy tissue. This offers the opportunity of sophisticated dose optimization procedures.

2 RBE

RBE, or, more precisely, radiobiological effect depends on a multitude of different parameters [2]. In view of its definition via dose-effect curves the most prominent dependency is on particle type and energy. Densely ionizing radiation, i.e. high-Z low-energy particles are expected to cause the highest biological effect. Clearly, RBE depends also on the type of tissue under consideration. The radiosensitivity of a particular cell type is dominated by the efficiency of its repair mechanism. Repair-deficient mutants of an otherwise repair-efficient cell line may exhibit an entirely different dose response, although the radiation physics is almost the same. For the purposes of treatment planning the dependency on absorbed dose - or particle fluence - is extremely important. This follows already from the definition of RBE via dose-effect curves. Since these are linear-quadratic for a particle of given charge and energy, simple linear addition of biological dose values is not possible. This nonlinearity is one of the challenges for treatment planning involving complex radiation fields in three or even four dimensions.

The multiple parameter dependency of biological effects in ion radiotherapy makes it impossible to rely on empirical data alone. It is not conceivable to obtain experimental patient-related data for all combinations of absorbed dose levels, particle types and energies, and tissue species. Likewise it is - at least for the foreseeable future - not feasible to perform ab-initio calculations starting at the DNA level, which would lead to results of any practical therapeutical relevance.

3 Models

Ion radiotherapy of the past and present relies on pragmatic approaches to safely incorporate radiobiological effects into treatment planning. First clinical experience with treatment planning for heavy ions has been collected at the Lawrence Berkeley Laboratory (LBL, Berkeley/USA) and later at the National Institute for Radiological Science (NIRS, Chiba/Japan) At the LBL the RBE was described as a function of dose-averaged LET to estimate the biologically effective dose [3], using a Linear-Quadratic (LQ) model to calculate a uniform biological effect across the spread-out-Bragg peak. At NIRS biological treatment planning is based on cell survival levels which are calculated using a LQ model as well [4]. Starting from mono-energetic beams the dose-averaged coefficients α

and β for a mixed beam are calculated. The model has been verified with V79 cells. For patient planning Human Salivary Gland (HSG) tumour cells are used to obtain the RBE distribution as a function of depth. Based on the position in the spread-out Bragg peak (SOBP) showing the same RBE for cell survival as neutrons, all RBE values are then rescaled according to the RBE observed in clinical studies with neutrons.

For proton irradiations, the RBE in extended fields is assumed to be close to 1, and hence is usually neglected.

While these approaches work well for passive irradiation systems, single field irradiations and fixed dose levels, they are not appropriate for current and future scanning systems, multiple field optimizations and true three-dimensional dose distributions involving all dose levels.

For scanning systems with their unique capabilities of dose shaping a radiobiological model must

- be able to treat all ion species (at least protons to oxygen),
- work at all absorbed dose levels, i.e. particle fluences ,
- be able to handle all tissues, even if no empirical patient data are available for ions or neutrons,
- allow for experimental verification via biological dosimetry,
- interface smoothly with absorbed dose calculation to allow three-dimensional CT based dose calculation and optimization,
- be computational efficient to allow complete patient planning within hours or even minutes on a single CPU without sacrificing accuracy.

So far the above requirements are met only by the Local Effect Model (LEM) [5]. It uses the microscopic dose distribution around an ion track together with the - empirical - dose-effect relation curve obtained from photon irradiations. The basic idea is, that the locally deposited dose within a cell nucleus determines the biological endpoint, regardless whether the radiation damage is inflicted by photons or charged particles. Recent improvements include the effects of single strand break clustering as well [6].

With the LEM approach it is possible to generate a set of base data for all particle charges and energies for each tissue type and biological endpoint. These data sets represent a tissue's response under track segment conditions for single particles. They do not depend on the actual absorbed dose level or composition of the radiation field. Complex fields at various dose levels have to be handled by the treatment planning system, as it is implemented in GSI's TRiP98 code.

A requisite for both, the NIRS as well as the GSI approach, is sufficient knowledge of the physical composition of the radiation field as a function of depth. At NIRS, this is provided by the HIBRAC code (or its derivatives) [7], at GSI the physical beam model (YIELD with semi-empirical adaptions) is integrated into the TRiP98 TPS [8].

4 Treatment Planning for Scanning Systems

Magnetic scanning systems like those realized at GSI, PSI and soon also at HIT deliver dose distributions by superposition of several ten thousands of individual pencil beams [9, 10]. Even for irradiations from a single direction this leads to rather complex radiation fields comprising particles of different charges and very different energies. The situation becomes even more complex if - as usual - two or more treatment fields from different directions are superimposed. With the algorithms specified by the LEM model, however, the resulting biological effects (RBE) can be calculated correctly on a voxel-by-voxel basis from the local particle distribution [11]. This is especially important if not only forward dose calculation is desired but also dose optimization by inverse planning. The main task of treatment planning for scanning systems actually is the determination of the particle numbers in the individual pencil beams. This is not trivial because the biological dose distribution depends non-linearly on the particle numbers and hence this task can only be solved by iterative methods. The validity of this approach has been verified experimentally by means of biological dosimetry of model systems set up and planned under patient-like conditions [12].

The application of the "classical" LEM algorithms is rather time consuming since they require the interpolation of four-dimensional particle distributions and repeated sampling of two-dimensional

histograms for each voxel under consideration. In the pilot project, jointly performed by GSI, DKFZ and Radiological Clinic Uni Heidelberg [13], where on the average about two new patients have to be planned per day, it was nevertheless possible to perform the full calculations on a set of about a dozen IBM Power CPUs.

For higher throughputs, however, and more sophisticated treatment scenarios like e.g. simultaneous optimization of multiple fields under healthy tissue constraints, the algorithmic efficiency had to be improved significantly. Consequently, a much faster but nevertheless accurate "low-dose" (LD) approximation for dose levels up to 10 GyE has been developed. LD still implements all current and future benefits of the LEM model, but is about 100 times faster than the classical method. Thus biological dose distributions can be calculated in a "survey mode" in a few seconds for an entire CT, and sophisticated multifield optimizations are feasible within less than an hour or even within minutes, depending on the size of the target volume. Again, the method has been verified experimentally by means of biological dosimetry.

5 Future

Biological multifield optimization under constraints has recently been put into clinical use in the GSI pilot project. The method appears to be very promising, although there is still room for refinement, in particular in the definition and implementation of tissue constraints, but also as far as convergence speed is concerned.

In the past twenty years biological treatment planning has gone from one dimension (past) to three dimensions (present). With the ongoing developments concerning irradiation of moving targets, four-dimensional biological treatment planning will become important in the future. Promising experimental as well as calculational results have already been obtained at GSI [15, 16]. Consequently, TRiP98 will be enhanced by a 4D-version.

References

[1]   G. Kraft: Schwere Geschütze gegen den Krebs Physik Journal **6**, 29-35, (2007).

[2]   M. Krämer, W. K. Weyrather, M. Scholz The Increased Biological Effectiveness of Heavy Charged Particles: From Radiobiology to Treatment Planning Technology in Cancer Research & Treatment **2/5**, 427-436 (2003).

[3]   Petti P L, Lyman J T, Castro J R: Sensitivity of helium beam-modulator design to uncertainties in biological data Med. Phys. **18(3)**, 506-512, (1991).

[4]   Kanai T, Furusawa Y, Fukutsu K, Itsukaichi H, Eguchi-Kasai K and Ohara H: Irradiation of Mixed Beam and Design of Spread-Out Bragg Peak for Heavy-Ion Radiotherapy Radiat. Res. **147**, 78-85, (1997).

[5]   M. Scholz, A.M. Kellerer, W. Kraft-Weyrather, G. Kraft: Computation of cell survival in heavy ion beams for therapy - the model and its approximation Rad. Environ. Biophysics **36**, 59-66 (1997).

[6]   T. Elsässer, M. Scholz: Cluster Effects within the Local Effect Model Rad. Res. **167**, 319-329 (2007).

[7]   L. Sihver, D. Schardt and T. Kanai: Depth-Dose Distributions of High-Energy Carbon, Oxygen and Neon Beams in Water. Jpn. J. Med. Phys, **18/1**, (1998).

[8]   M. Krämer, O. Jäkel, T. Haberer, G. Kraft, D. Schardt and U. Weber: Treatment planning for heavy-ion radiotherapy: physical beam model and dose optimization Phys. Med. Biol. **45**, 3299 (2000).

[9]   Jäkel O, Krämer M, Karger CP, Debus J. Treatment planning for heavy ion radio-therapy: clinical implementation and application. Phys. Med. Biol. **46**, 1101-1116 (2001).

[10]   Jäkel O, this workshop.

[11]   M. Krämer, M. Scholz: Treatment planning for heavy-ion radiotherapy:calculation and optimization of biologically effective dose Phys. Med. Biol. **45**, 3319 (2000).

[12]   M. Krämer, J.F. Wang, W. Weyrather: Biological dosimetry of complex ion radiation fields

Phys. Med. Biol. **48**, 2060 (2003).

[13]   Schulz-Ertner D, Nikoghosyan A, Thilmann C, Haberer Th, Jäkel O, Karger C, Kraft G, Wannenmacher M, Debus: Results of carbon ion radiotherapy in 152 patients Int. J. Radiat. Oncol. Biol. Phys. **58(2)**, 631-540 (2004).

[14]   M. Krämer, M.Scholz: Rapid calculation of biological effects in ion radiotherapy Phys. Med. Biol. **51**, 1959-1970 (2006).

[15]   C. Bert, E. Rietzel: 4D treatment planning for scanned ion beams Radiation Oncology **2**, 24 (2007).

[16]   C. Bert, A. Schmidt, N. Saito: this workshop.

COMPARISON OF ANALYTICAL AND MONTE CARLO CALCULATIONS OF CLINICAL DOSE DISTRIBUTIONS IN PROTON AND CARBON ION THERAPY

S. Brons[1], K. Parodi[1], F. Cerutti[2], A. Ferrari[2], E. Gadioli[3], F. Sommerer[4], A. Mairani[5]

[1] Heidelberg Ion Therapy Center, Heidelberg, Germany,

[2] CERN, Geneva, Switzerland

[3] University of Milano and INFN, Section of Milano, Milano, Italy,

[4] Atominstitut of the Austrian Universities, Vienna, Austria,

[5] University of Pavia and INFN, Section of Pavia, Pavia, Italy

Currently, dedicated or commercial treatment planning systems (TPSs) for ion therapy are essentially analytical codes based on fast performing one dimensional pencil-beam algorithms. However, Monte Carlo (MC) statistical methods are increasingly considered powerful tools for accurate calculations of dose deposition, since they are assumed to provide a more realistic representation of the physical interactions undergone by the primary beam and the resulting secondaries. Moreover MC methods include naturally mixed field capabilities and three dimensional spread of the particle fluence.

Although the long computing time prevents their use in clinical routine, MC tools can be very useful for verification, and in certain cases improvement, of the dose calculations performed by the analytical treatment planning engines. In fact, they allow the dose evaluation for every real situation, taking into account the realistic patient anatomy instead of the water-equivalent approach, and in all the cases for which the experimental dosimetric verification is impossible.

MC codes can be particularly advantageous in situations sensitive to lateral scattering (especially for protons), nuclear fragmentation (especially for heavier ions), and in the presence of large inhomogeneities, e.g., due to metallic implants. Furthermore, MC simulations can provide accurate physical databases to be input into TPSs.

Thanks to the recent efforts made by the FLUKA Collaboration in order to produce reliable nucleus-nucleus event generators in the energy range of therapeutic relevance, the FLUKA Monte Carlo code nowadays represents a valuable choice for accurate CT-based calculations of dose not only in proton therapy but also for the entire spectrum of heavier ions of therapeutic relevance. In this presentation, FLUKA MC simulations are compared with the results of the analytical treatment planning codes Focus/XiO (Computerised Medical Systems Inc.) and TRiP (TReatment Planning for Particle), which are used in clinical routine for proton and carbon ion therapy at MGH Boston and GSI, respectively. In general, MC dose distributions are found in good agreement with the analytical calculations, except few cases e.g. in the presence of metallic implants and air/tissue interfaces.

Clinical Results
of Particle Therapy

CLINICAL RESULTS OF CARBON ION RADIOTHERAPY IN JAPAN

Hirohiko Tsujii

Research Center for Charged Particle Therapy, National Institute of Radiological Sciences, Chiba, JAPAN

Currently, there are two operating facilities for carbon ion radiotherapy in Japan, including the National Institute of Radiological Sciences (NIRS) in Chiba and the Hyogo Ion Beam Medical Center (IHIBM) in Hyogo. More than 3,100 patients have been treated at NIRS since 1994, and more than 150 patients have undergone carbon ion therapy in Hyogo since 2002. At IHIBM, proton therapy is also available and so far more than 1,200 patients have been treated with proton beams.

NIRS was the first facility in the world to carry out full-scale carbon ion radiotherapy and was successful in obtaining approval from the Ministry of Health, Welfare and Labor for its "Highly Advanced Medical Technology" in October 2003. This means that heavy particle radiotherapy has achieved for itself a solid place in general practice in Japan after clinical experiences of a whole ten years. Carbon ion therapy at NIRS has been available mainly for those tumors of the brain, head and neck, lung, liver, prostate, bone/ soft-tissue, uterine cervix, and pelvis (post-ope pelvic recurrences of rectal cancer). On the other hand, the indication at IHIBM has been limited to the tumors of the head and neck, lung, liver and bone/soft tissue.

In the first instance at NIRS, phase I/II trials were carried out in order to confirm the safety and obtain data about the anti-tumor effect of carbon ion therapy. Based on this evidence, the recommended dose was established by fixing both the fraction number and treatment time for each disease and escalating the total dose in successive increments of 5 to 10% at a time. Experiences to date indicate that carbon ion radiotherapy is advantageous for the following types of tumors: By histological type, adenocarcinoma, adenoid cystic carcinoma and sarcoma; by primary tumor site, head and neck, lung, liver, prostate, bone and soft tissue, pelvis, etc. Tumors that originate in the digestive tract itself or infiltrate in the digestive tract, however, are difficult to control with carbon ions alone.

Regarding dose-fractionations employed, it has been possible to complete the treatment in a short time. For example, stage 1 lung cancer and liver cancer can now be treated with only one or two irradiation sessions. Even for prostate cancer and bone and soft-tissue tumors requiring a relatively long course of radiotherapy, only 16 to 20 sessions have been sufficient, roughly half the number of fractions required in the case of standard radiotherapy. This means that the facility can be operated more efficiently, offering treatment for a larger number of patients than is possible with other modalities over the same period of time.

CLINICAL RESULTS OF CARBON ION RT AT GSI

D. Schulz-Ertner[1,*], A. Nikoghosyan[1], B. Didinger[1], H. Hof[1], S.E. Combs[1], O. Jäkel[2], C.P. Karger[2], M. Scholz[3], M. Krämer[3] and J. Debus[1]
[1]Dept. of Radiation Oncology, University of Heidelberg, Germany
[2]Division of Physics in Medicine, German Cancer Research Center, Heidelberg, Germany
[3]Dept. of Biophysics, GSI, Darmstadt, Germany

Since 1997, almost 400 patients have been treated with carbon ions at the physics based particle therapy facility at GSI Darmstadt. Treatments were carried out in three treatment blocks of 3 weeks each year. Carbon ion RT was delivered actively using the raster scan technique developed at GSI in the 90ies. Treatment planning included biologic plan optimization using a biologic model also developed at GSI. Most patients have been treated within clinical phase I/II trials investigating feasibility and toxicity of carbon ion RT. Clinical phase I/II trials were initiated for patients with skull base chordomas and chondrosarcomas, locally advanced adenoid cystic carcinomas, extracranial chordomas and chondrosarcomas and for locally advanced prostate cancer. All trials except the prostate trial have been completed in the meanwhile. Based on the favourable results observed in these trials, carbon ion RT is considered the standard of care in Germany in patients with skull base chordomas and chondrosarcomas as well as in patients with locally advanced adenoid cystic carcinomas of the skull base. A subsequent trial is planned to be initiated in 2008 to investigate carbon ion RT alone for extracranial chordomas, since local control was found to be unsatisfactory after photon RT with a carbon ion boost in the interim analysis of the data obtained in the phase I/II trial. The clinical phase I/II trial investigating combined photon IMRT plus carbon ion boost in locally advanced prostate cancer, which was initiated in 2006, is still recruiting. This manuscript reviews the clinical results of carbon ion RT at GSI obtained so far.

INTRODUCTION

Carbon ion beams offer the physical advantage of a finite range with a steep dose fall-off after the so called Bragg peak, thus limiting toxicity to healthy normal tissue behind the Bragg peak. Carbon ions also prohibit biologic advantages by means of higher relative biological effectiveness within the Bragg peak as compared to the entrance region. These properties make carbon ion RT a promising approach for the treatment of tumors which are less sensitive against conventional RT in critical location. Chordomas, chondrosarcomas, locally advanced adenoid cystic carcinomas and prostate cancer are considered potential indications for carbon ion RT.

MATERIAL AND METHODS

Chordomas and chondrosarcomas of the skull base

Between November 1998 and September 2005, 96 patients with chordomas and 54 patients with low and intermediate grade chondrosarcomas of the skull base have been treated with carbon ion RT at GSI. All patients had gross tumor residuals after surgery. Median tumor dose was 60 CGE (range 60–70 CGE) delivered in 20 fractions within 3 weeks. Treatment planning included biologic plan optimization using the local effect model (LEM) by Scholz (1). The α/ß value was assumed to be 2 Gy for chordoma cells and the endpoint late toxicity in normal brain tissue (dose-limiting toxicity). Taking into account fractionation, biologically equivalent doses (BED) between 75 and 96.25 CGE were reached. Positron emission tomography (PET) was used for online beam verification. For detailed information see also (2, 3).

---

*Corresponding author: Daniela.Ertner@fdk.info

Locally advanced adenoid cystic carcinoma

Between 1998 and September 2003, 29 patients with locally advanced adenoid cystic carcinoma of the skull base have been included into a clincal phase I/II trial investigating combined photon IMRT or fractionated stereotactic RT with static fields plus carbon ion RT as a boost. Only patients with macroscopic tumors without history of a former irradiation were accepted. Photon IMRT was delivered to the CTV which covered the macroscopic tumor and a generous margin along the typical tumor spread. We applied 54 Gy of photon RT in a weekly fractionation of 5 x 1.8 Gy. The macroscopic tumor was treated additionally with carbon ion RT. The boost dose was 18 CGE given in 6 fractions prior to the initiation of the photon RT. In 8/29 patients perineural spread was present. Prior to RT partial tumor resection was performed in 22 patients, 7 patients had a biopsy only. For detailed information see also Schulz-Ertner et al. (4).

Extracranial chordomas and chondrosarcomas

Between 2001 and August 2005, 20 patients with extracranial chordomas and chondrosarcomas have been treated with combined photon and carbon ion RT at GSI and the University of Heidelberg within a clinical phase I/II trial. We included 13 chordomas of the sacrum and 4 chordomas of the spine. One patient was treated for spinal chondrosarcoma and 2 for sacral chondrosarcomas. Carbon ion RT was delivered as a boost to the macroscopic tumor, while photon RT was applied to the CTV. Patients without residual tumors after surgery were not eligible for the study. Most patients had very large and inoperable tumors. Median GTV was 519 mL (range 70 – 3321mL). We applied 50.4 Gy with photon RT with a weekly fractionation of 5 x 1.8 Gy. The photon dose was reduced to 36 Gy and 48.6 Gy in two patients with very large tumors. A carbon ion boost with 18 CGE was given in 6 fractions to the GTV in all patients.

Phase I/II trial of combined photon IMRT plus carbon ion boost in locally advanced prostate cancer

The study investigates feasibility and toxicity of photon IMRT (60 Gy, weekly fractionation 5 x 2.0 Gy) plus carbon ion boost (18 CGE, weekly fractionation 6 x 3.0 CGE) to the prostate in intermediate risk prostate cancer patients. Eligibility criteria are: Pre treatment PSA between 10 and 20 ng/ml and at least one unfavourable factor (stage > T2a, Gleason Score > 6). Exclusion criteria are as follows: KPS < 70% positive lymph nodes, distant metastases, history of a former course of RT to the pelvis or prostatectomy.

Statistical analysis

All studies were performed as clinical phase I/II trials investigating feasibility and toxicity of carbon ion RT as main endpoint. Local tumor control and overall survival rates were determined as secondary endpoints. Patients had follow-up examinations including MRI in regular intervals. Toxicity was assessed and scored according to the Common Terminology Criteria and the RTOG/EORTC score. Any enlargement of the tumor on subsequent control MRI scans was considered a local recurrence. Locally controlled patients were censored at the time of their last follow-up or death, whichever occurred first. Overall survival was calculated from the initiation of carbon ion irradiation until death or last follow-up. Local control and overall survival rates were calculated according to the Kaplan Meier method.

RESULTS

Chordomas and chondrosarcomas of the skull base

Median follow up was 31 months for chondorsarcoma patients and 33 months for chordoma patients, respectively.

Local recurrences were observed in 15 out of 96 chordoma patients and in 2 out ouf 54 chondrosarcoma patients. It is noteworthy, that only patients with macroscopic tumors were included into the trials. Both patients who developed recurrences of their chondrosarcoma had Grade 2 histology. Five-year local control rates were 70% and 89.8% for chordomas and chondrosarcomas, respectively. Chordoma patients with primary tumors had significantly higher local control probability as compared to patients irradiated for recurrent tumors (p=0.001, log-rank). Gender did not influence outcome in chordoma patients (p=0.244, log-rank). Two out of 96 patients with chordoma developed distant metastases (3).

In chondrosarcoma patients we did not observe any distant metastases (4). Overall survival rates at 5 years were 88.5% for chordomas and 98.2% for chondrosarcomas (3, 4). Severe acute effects > CTC grade 2 were observed in less than 5% of the patients. Late toxicity included optic nerve neuropathy grade 3 in less than 5% of the patients in both patient series. No patient developed toxicity to the brain stem so far. Minor temporal lobe injury by means of new contrast enhancement after RT occurred in 3.5% of the chordoma patients treated with biologically equivalent doses of 75 CGE and in 33.3% of the patients who received tumor doses in excess of 75 CGE up to 96 CGE. Most of the patients were asymptomatic, in only two patients temporal lobe lesions were associated with a perifocal edema and neurologic sequelae necessitating steroid medication (RTOG/EORTC grade 2) (3).

Locally advanced adenoid cystic carcinoma of the skull base

Median follow-up was 16 months (range 2-60 months). During the observation period 4 patients developed locoregional recurrences. Three of the recurrences were located within the carbon ion treatment fields, one recurrence occurred within the CTV outside the GTV. The 4-year locoregional control rate was 77%. Four patients developed distant metastases. The overall survival rate was 75.8% at 4 years. Two patients died of distant metastases and one patient died of locoregional disease progression. Toxicity was acceptable. Only one patient developed recurrent bacterial infections requiring subsequent surgery, which was classified as Grade 4 late reaction. Acute toxicity was mild (4).

Extracranial chordoma and chondrosarcoma

The follow-up period is still short. The aim of the interim analysis performed most recenty was mainly to assess toxicity. However, local control seems to be unsatisfactory, since 10 out of 20 patients developed a locoregional recurrence. Toxicity was very mild. We did not observe any severe acute or late toxicity.

Locally advanced prostate cancer

The trial is still recruiting. So far, 6 patients have been treated with combined photon IMRT plus carbon ion boost. We did not observe any toxicity to the rectum. Genitourinary toxicity was very mild in the first 6 patients. No patient developed toxicity > CTC grade 2 so far.

*Corresponding author: Daniela.Ertner@fdk.info

DISCUSSION

Chordomas and chondrosarcomas are rare tumors occurring frequently in the skull base region. Since complete oncological resection is rarely achieved, postoperative radiotherapy is an important treatment component. With conventional RT, however, local control probability is low, because the radiation dose is limited by the close vicinity of radiosensitive organs at risk such as optic apparatus and brain stem. In the past, particle therapy with protons was therefore considered the optimal RT modality for these tumors, allowing high doses to the tumor while adhering to the tolerance doses of the organs at risk nearby. 5-year local control rates of almost 60% and between 75 and 98% have been reported after proton RT of chordomas and chondrosarcomas, respectively (5, 6, 7). Late toxicity was acceptable in these series, occurring in 5 to 10% of the patients.

Given the slow growth pattern of these tumors together with their low radioresponsiveness, these patients are considered ideal candidates for carbon ion RT as well. The hypothesis of an enhanced relative biological effectiveness in carbon ion RT was investigated for these tumors within clinical phase I/II trials at GSI. It could be shown, that carbon ion RT given with biologically equivalent doses between 75 and 96 CGE yields high 5-year local control rates of 70% and 89.8% for skull base chordomas and chondrosarcomas, respectively. Severe late effects occurred in less than 5% of the patients.

Taking together the available data for proton RT and carbon ion RT, a clear dose-response-relationship can be demonstrated at least for chordomas (2).

Currently, there is no data comparing prospectively proton RT and carbon ion RT in the treatment of these tumors. Prospective randomized phase III trials would be necessary to determine the optimal particle RT modality.

It can, however, be concluded from the data available in the literature, that particle therapy with protons or carbon ions should be considered the standard of care, because the required high tumors doses can not be reached with photons.

Postoperative RT is the standard treatment in adenoid cystic carcinomas. While local control rates are in excess of 90% with moderate doses after complete resection, local control rates remain unsatisfactory with conventional RT after incomplete resection of adenoid cystic carcinomas. Tumor doses in excess of 70 Gy are considered necessary to control gross tumors. In the past, neutron RT has been found to improve control rates in locally advanced gross residual tumors, as compared to photons. A randomized clinical phase III study proved the superiority of neutrons over photons (8). These data support the finding of Batterman that neutrons show a higher relative biological effectiveness in adenoid cystic carcinoma cells (9). The disadvantage of neutrons is their poor depth dose distribution, leading to unacceptable toxicity in a number of patients. This problem is most pronounced in the skull base region where the temporal lobes are at high risk for radiation induced necrosis.

Carbon ions can be focussed much better to the tumor, especially if active beam delivery is used for application. Therefore, the high LET effect can be restricted to the tumor, while normal tissue surrounding the tumor is spared much better.

Using a combination of photon IMRT to the clinical target volume and a carbon ion boost to the gross tumor residual in locally advanced adenoid cystic carcinoma of the skull base, high locoregional control rates could be observed. While local control was 77%, overall survival was 75.8% at 4 years (4). This data is comparable to the historic neutron data, if similar patient collectives are compared. Control rates after carbon ion RT are, however, better than those found in a historic control group treated with photon RT alone in Heidelberg. Combined photon IMRT plus carbon ion RT seems to be superior to photon IMRT alone, although the difference did not yet reach statistical significance in a non-randomized retrospective comparison of both collectives (4).

Patients with extracranial chordomas and chondrosarcomas did not show a satisfactory tumor control after combined photon IMRT with carbon ion boost in the prospective clinical phase I/II study

*Corresponding author: Daniela.Ertner@fdk.info

completed in summer 2005. We did, however, not observe any unexpected acute or late toxicity. The feasibility and safety of carbon ion RT in extracranial tumors could therefore be demonstrated. One of the reasons for the low local control rate might be the fact, that only 25% of the dose had been delivered with carbon ions while 75% of the dose was given as photon RT. Taking into account the favourable results observed after fully fractionated carbon ion RT in skull base chordomas at GSI and more recent data from Chiba, where high control rates in excess of 90% could be found for sacral chordoma patients treated with carbon ion RT alone, a prospective trial investigating carbon ion RT alone in sacral chordomas is warranted.

REFERENCES

1. Scholz M, Kellerer AM, Kraft-Weyrather W. Computation of cell survival in heavy ion beams for therapy. The model and its approximation. Radiat Environ Biophys 36:59-66, 1997
2. Schulz-Ertner D, Karger CP, Feuerhake A et al. Effectiveness of carbon ion radiotherapy in the treatment of skull-base chordomas. Int J Radiat Oncol Biol Phys 68(2):449-457, 2007
3. Schulz-Ertner D, Nikoghosyan A, Hof H et al. Carbon ion radiotherapy of skull base chondrosarcomas. Int J Radiat Oncol Biol Phys 6781):171-177, 2007
4. Schulz-Ertner D, Nikoghosyan A, Didinger B, et al. Therapy strategies for locally advanced adenoid cystic carcinomas using modern radiation therapy techniques. Cancer 104(2):338-344, 2005
5. Terahara A, Niemierko A, Goitein M et al. Analysis of the relationship between tumor dose inhomogeneity and local control in patients with skull base chordoma. Int J Radiat Oncol Biol Phys 45(2):351-358, 1999
6. Hug EB, Loredo LN, Slater JD et al. Proton radiation therapy for chordomas and chondrosarcomas of the skull base. J Neurosurg 91(3):432-439, 1999
7. Rosenberg AE, Nielsen GP, Keel SB et al. Chondrosarcoma of the base of the skull: a clnicopathologic study of 200 cases with emphasis on its distinction from chordoma. Am J Surg Pathol 23(11):1370-1378, 1999
8. Laramore GE, Krall JM, Griffin TW et al. Neutron versus photon irradiation for unresectable salivary gland tumors: final report of an RTOG-MRC randomized clinical trial. Radiation Therapy Oncology Group. Medical Research Council. Int J Radiat Oncol Biol Phys 27(2):235-240, 1993
9. Batterman JJ, Breur K, Hart GA et al. Observations on pulmonary metastases in patients after single doses and multiple fractions of fast neutrons and cobalt-60 gamma rays. Eur J Cancer 17:539-548, 1981

Poster:
Therapy Planning

GATING WITH SCANNED CARBON BEAMS

Ch. Bert[1], E. Rietzel[1,2], A. Schmidt[1], N. Saito[1], S. Brons[3], Th. Haberer[3], D. Schardt[1]

[1]Gesellschaft für Schwerionenforschung (GSI), Darmstadt, Germany
[2]Siemens Medical Solutions, Particle Therapy, Erlangen, Germany
[3]Heidelberger Ionentherapie (HIT) Heidelberg, Germany

Scanned particle beam application to moving tumors can result in deterioration of the delivered dose distribution due to interplay effects. Techniques such as gating and tracking can be employed to mitigate these interplay effects. GSI and HIT plan to use tracking (see Bert et al this workshop) and as an intermediate solution gating to treat tumors that are subject to respiratory motion.

In simulations we determined suitable parameter combinations for beam spot size and raster grid spacing with different residual motion amplitudes within the gating window. A series of corresponding experiments was started with so called knock-out (KO) extraction from the synchrotron. KO extraction allows suspending and resuming beam delivery within a beam pulse based on a gating signal. It is available in an experimental mode at GSI but will be standard at HIT. Radiographic films were used as detectors. The films were placed on a sliding table that moved periodically left-right in beam's eye view with peak-to-peak amplitude of 4 cm and a period of ~5 s. Detector motion was monitored via an IR-LED attached to the moving table, a CCD-camera, and a PC for image processing.

Motion traces were analyzed online on the PC, gating windows were set, and resulting gating signals were transmitted to the treatment delivery system via a digital IO-interface. Experiments were performed with beam spot sizes of ~15 mm FWHM, constant raster grid spacing, varying magnitudes of residual motion within the gating window, and two different irradiation patterns (treatment plans). Experimental results in the presence of motion were compared to irradiations of stationary films.

Simulations showed that the overlap of individual beam spots (i.e. the combination of grid spacing and spot size) has to be increased with increasing residual motion within the gating window. In the experiments, beams of ~15 mm FWHM allowed adequate dose delivery to the moving detector for gating windows of up to 7 mm residual motion.

Analysis was based on visual inspection of film responses, dose profiles in comparison to irradiation of stationary films, and the homogeneity within the irradiated field.

In conclusion: Gated treatment delivery of a scanned carbon pencil beam was implemented at GSI. Experiments with ~15 mm FWHM spot size at 2 mm grid spacing resulted in dose distributions that were not degraded in comparison to irradiations of stationary detectors for rather large residual motion amplitudes of up to 7 mm.

THE ROBUSTNESS OF INTENSITY MODULATED CARBON ION TREATMENT PLANS

M. Ellerbrock[1,*], O. Jäkel[1]

[1]Department of Medical Physics in Radiation Oncology, German Cancer Research Center (DKFZ), Im Neuenheimer Feld 280, D-69121 Heidelberg, Germany

The robustness of intensity modulated carbon ion treatment plans is investigated concerning patient positioning and ion range uncertainties. A planning study indicates that treatment plans obtained using simultaneous multiple field dose optimization are superior to conventional plans optimized separately for individual fields in terms of dose distribution and robustness concerning treatment plan application.

Purpose/Objective

Intensity modulated particle therapy (IMPT) is currently implemented in clinical heavy ion therapy. Patients are treated with carbon ions at the GSI since 1997, using a raster scanning technique with active energy variation. So far, individual treatment fields are optimized separately and thus exhibit homogeneous dose distributions. An advanced version of the treatment planning software, TRiP98BEAM, allows the simultaneous dose optimization of multiple fields to further improve the sparing of organs at risk and to enhance the conformity of the target volume. The focus of this presentation is directed to the robustness of IMPT treatment plans concerning inter- and intra-fractional patient movements and ion range uncertainties.

Materials/Methods

A planning study is performed using actual patient data of skull base tumours close to critical structures. Dose distributions are compared for single and multiple field optimization using dose volume statistics for the target volume and organs at risk. The robustness of IMPT plans concerning patient positioning and range uncertainties is investigated and compared to conventional therapy. For this purpose, the dose distributions of treatment plans are recalculated using shifted target coordinates, setup angles and look-up tables for the conversion of CT Hounsfield units to ion ranges.

Results

Comparisons with conventional plans demonstrate the big advantage of the IMPT technique with respect to target dose conformity and sparing of critical organs, especially for complicated target volume locations demanding e.g. for field patching methods so far. Concerning positioning and range uncertainties, the robustness of IMPT plans is comparable with conventional plans of homogeneous individual fields. At worst, the originally beneficial IMPT plans get as critical as the conventional ones.

Conclusions

Multiple field dose optimization as implemented in TRiP98BEAM provides improved treatment plans. The dose distributions are superior to conventional plans, and positioning and range uncertainties at worst may compensate this benefit. IMPT in carbon ion therapy thus is ready for clinical use. In addition, the IMPT technique may allow to extend heavy ion therapy to patients with metal implants close to the target volume who are excluded so far.

*Corresponding author: M.Ellerbrock@dkfz.de

OPTIMIZATION OF ACCEPTANCE CRITERIA FOR THE GAMMA-INDEX IN SCANNED HEAVY ION THERAPY

S. Lahrmann, O. Jäkel and C. P. Karger

Department of Medical Physics in Radiation Oncology, German Cancer Research Center (DKFZ), Heidelberg, Germany

The gamma index has been implemented into the dose verification system for scanned carbon ion beams used at GSI. Gamma index calculation has been performed on 40 treatment fields. Acceptance criteria suitable for scanned heavy ion beams have been derived and compared to currently applied criteria. The gamma index tool has the potential to improve dose verification for carbon ions and can be used for other heavy ions as well.

Introduction

The gamma-index is a routinely used comparison tool for measured and calculated dose distributions for dose verification in photon IMRT. Here, 3% of the maximum dose and 3mm for the distance to agreement (DTA) are well established acceptance criteria [1]. The gamma index was implemented into the dose verification system for scanned ion beams and different acceptance criteria were investigated. Due to the more inhomogeneous dose distributions produced by scanned beams modified acceptance criteria may be required.

Materials and Methods

In carbon-ion therapy at GSI (Darmstadt, Germany) dose verification is performed using an array of 24 ionization chambers [2]. Current acceptance criteria comprise 5% for the mean deviation as well as for the standard deviation of deviations between measured and calculated dose considering only measurement positions with moderate dose gradients. Now, a tool for calculation of the gamma-index in 3 dimensions has been developed. The dose is calculated with a spatial resolution of 1mm*1mm*2mm and linear interpolation of the calculated dose is done using 16*16*32 subvoxels per voxel. The gamma-index was calculated for 40 treatment fields verified and accepted at GSI. The analyzed treatment fields were subdivided into groups with the center of the array positioned at a depth of

(A) <7.5 cm
(B) 7.5-12.5 cm

We applied acceptance criteria of

(C) 3%/3mm

(D) 5%/2mm

(E) 6%/1mm

(F) 7%/2mm

Results

Group (A) exhibited a mean dose deviation of (-2.1±5.1)% (1 SD) where 90% of the individual measurement positions showed deviations below 9.0%. When measurement points in large dose gradients are not taken into account, this changes to (-2.2±4.5)% (1 SD) with 90% below 8.2%. Figure 1 shows the individual mean dose deviations calculated according to our criteria.

*Corresponding author: s.lahrmann@dkfz-heidelberg.de
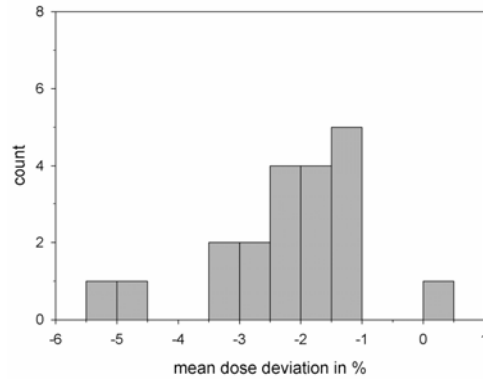
Figure 1. Histogram of mean dose deviations
per field with array center <7.5cm

In group (B) the mean deviation was (-3.5±4.8)% (1 SD) with 90% showing deviations below 9.8%. For the currently evaluated measurement positions this reduces to (-3.2±4.1)% (1 SD) with 90% below 8.9%.

The range of the mean gamma-indices for individual patients was in (A) 0.29–1.12 for (a), 0.27–0.95 for (b), 0.27-0.96 for (c) and 0.21–0.74 (d)(see figure 2).
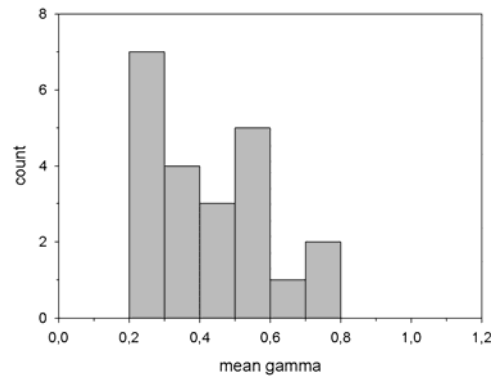
Figure 2. Histogram of mean gamma per field
with array center < 7.5cm and acceptance
criteria 7%/2mm

In group (B) the corresponding results were 0.24–1.12 for (a), 0.25–0.95 for (b), 0.24-0.94 for (c) and 0.19–0.74 (d). In (A) a fraction of (a) 0.81, (b) 0.85, (c) 0.83 and (d) 0.90 of all measurement positions in all fields yielded a gamma-index below 1. In (B), the fractions were (a) 0.82, (b) 0.84, (c) 0.82 and (d) 0.89.

Conclusion

The gamma-index is a useful tool in dose verification for scanned ion beams. Although the gamma-values at single measurement positions were larger than 1, the mean gamma-index for the criteria (b), (c) and (d) was below 1 for all investigated fields. The lowest values were obtained with criteria (d). Histograms of group (A) have been investigated exemplarily. Comparing the mean dose deviation per field (figure 1), as currently used in verification, to the mean gamma index per field (figure 2), as obtained with acceptance criteria of 7% dose and 2mm DTA, one observes an accumulation at small gamma values and small deviations, respectively, and larger values are less frequent in both cases.

This suggests that the mean gamma-index yields similar results with respect to the acceptance as the currently applied criteria. Nevertheless, rather than using the mean value alone for validation, we suggest to set additional limits on the maximal fraction of measurement positions per field being allowed to exceed 1. The selection of adequate criteria, however, is complicated by the systematic negative deviations generally found in dose verification measurements.

REFERENCES

1. D. A. Low, W. B. Harms, S. Mutic, and J. A. Purdy, Int. J. Radiat. Oncol., Med. Phys. **25**, 656-661 (1998).
2. C. P. Karger, O. Jäkel, and G. H. Hartmann, Med. Phys. **26**, 2125-2132 (1999).

ANALYSIS OF THE MULTIPLE SCATTERING IMPLEMENTATION IN TRIP *

G. Iancu[1] and M. Krämer[1]
1GSI, Darmstadt, Germany

TReatment plannIng for Particles[1] is the software successfully used at GSI for therapy planning. In calculating the angular distribution of the beam ions suffering multiple scattering a corrected form of the Moliere[2] distribution is used. Nevertheless, for therapy purposes the spatial distribution of the beam particles, needed to calculate the local dose, is of primary interest. To calculate this spatial distribution of the beam, departing from the Moliere angular distribution, the formulas of Lewis[3] are employed. These formulas give an exact analytical form for the mean value of lateral displacement and that of the correlation between output angle and lateral displacement. An improvement in speed is to be observed.

One of the main goals of any therapy treatment planning is the delivery of a conformal dose distribution in the target tissue while sparing the near seated critical ones. The multiple scattering is one of the important aspects that play a role in the modelling of the beam parameters.

TRIP

Dose calculation algorithms, used in TRiP, are designed for reasonable speed and acceptable accuracy. Monte Carlo algorithms, such as those used for simulation in particle physics, might provide higher accuracy in exceptional cases, but are in general too time consuming for clinical practice and moreover lack proper treatment of biological effects and support of dose optimization by inverse planning. To shortcut this overhead TRiP is using a dose distribution database. This database is calculated for different ions in water and practically used energies (for 12 C 50-500 AMeV).

MULTIPLE SCATTERING

For calculating the multiple scattering the Highland[2] parameterised form of the Moliere[3] scattering is used. This is found to be suitable in the case of small angles [4].
The procedure used follows:
(1) for each energy a Monte Carlo simulation is used to build an ensemble of beam particles
(2) using the Highland parameterisation each ensemble is then propagated through the target material. The momentum change is accounted using the Morrisey[5] formula
(3) the angle distribution obtained is then transformed in a spatial distribution and fitted through a double Gaussian

The new calculation algorithm is using the advantage of Lewis[7] formulas which are giving the exact analytical form for the spatial distribution as well as the correlation between output angle and lateral displacement.
The calculation will then be calibrated with the available measurements of angular distribution as an effect of multiple scattering and nuclear reaction.
In a next step the beam convergence will also be implemented.

REFERENCES

1. M. Krämer et al. , "Treatment planning for heavy ion radiotherapy: physical beam model and dose optimisation", Phys. Med. Biol. 45 (2000) 3299-317.
2. V. L. Highland, "Some practical remarks on multiple scattering", Nucl. Instr. and Meth. 129 (1975) p.497 and 161 (1979) p.171
3. G. Moliere, "Theorie der Sreuung schneller geladener Teilchen", Z. Naturforschung 3a (1948) p. 78
4. B. Gottschalk et al., "Multiple coulomb scattering of 160 MeV protons", Nucl. Instr. and Meth. B74 (1993) p. 467-490
5. D.J. Morrisey, Phys. Rev. C39 (1989) p.460
6. U. Weber , Doctoral thesis, Uni Kassel (1996)
7. H.W. Lewis, Multiple Scattering in an Infinite Medium, Phys. Rev. 78 (1950) p. 526

REQUIREMENTS TOWARDS REAL TIME AND IN-SITU DOSE DELIVERY CONTROL IN HADRONTHERAPY

Madjid Boutemeur, Université de Savoie, Laboratoire SYMME et IPNL Lyon, Polytech'Savoie, 5 Chemin de Bellevue - BP 80439, 74944 Annecy Le Vieux Cedex

Madjid.Boutemeur@cern.ch

It has been demonstrated that PET (Positron Emission Tomography) information can be used successfully for the monitoring of particle range as well as for dose quantification in both proton and carbon therapy (hadrontherapy). The monitoring results are obtained only after the full dose delivery, i.e. the execution of the treatment plan and are taken into account for the following session. For a real time control, a PET scanner alone would not suffice. Unlike photons in conventional radiotherapy where the non-scattered fraction of the incoming flux can be used for in-situ imaging, hadrons are totally stopped in the target material. However, a sizeable fraction of the incoming hadrons undergoes nuclear interaction with the target nuclei. As a result, light nuclear fragments are produced. In one hand and for the therapy purpose, these fragments contribute to the dose delocalisation and might be a serious obstacle against the application of hadrontherapy, particularly for small target volumes. In the other hand, PET monitoring was possible thanks to the produced β^+ emitter fragments like ^{11}C, ^{10}C or ^{15}O. In our approach, we propose an experimental setup that would add to the PET scanner data all the information carried out by the light fragments escaping the target volume. These are the prompt nuclear photons, the protons and the neutrons. Preliminary test beam results as well as Monte-Carlo simulations indicated that correlating the outgoing flux from the target to the incoming primary beam flux, at a level of a single particle, is a major step towards real time control of the 3D-distribution of the dose delivery. Here we present our scenario for an experimental setup dedicated to real time control as well as our preliminary results.

Status Reports

PROGRESS IN HEAVY-ION CANCER THERAPY AT IMP-CAS

Q. Li[1,*]
[1]Institute of Modern Physics, Chinese Academy of Sciences, Lanzhou 730000, China

Basic research related to heavy ion cancer therapy has been conducted at the Institute of Modern Physics (IMP), Chinese Academy of Sciences (CAS) since 1995. Now a plan of patient treatment with heavy ions has been launched at IMP-CAS. First, superficially-placed tumor treatment with carbon ions is expected in the therapy terminal at the Heavy Ion Research Facility in Lanzhou (HIRFL), where carbon ion beam with energy up to 100MeV/u can be supplied. After the commissioning of a newly-built synchrotron HIRFL-Cooling Storage Ring (HIRFL-CSR), high-energy carbon ion beams will be applied to treat tumors anywhere in the bodies in the planned therapy terminal at HIRFL-CSR. A passive beam delivery system has been developed and installed in the superficially-placed tumor therapy terminal at HIRFL. Two- and three-dimensional conformal irradiations to target volumes can be performed with the passive system at the earlier therapy terminal. Both the conformal irradiation methods have been verified experimentally in phantoms and a clinical trial of superficially-placed tumor patient treatment with carbon ions has been started at IMP-CAS since November 2006. Up to now, 27 patients have been treated and encouraging clinical results have been preliminarily obtained.

Due to the favorite characteristics of heavy ion beam such as inverted depth-dose distribution as well as high relative biological effectiveness (RBE), heavy-ion cancer therapy is attracting growing interest all over the world [1]. Based on the accelerators available, the Institute of Modern Physics (IMP), Chinese Academy of Sciences (CAS) plans to realize heavy-ion cancer therapy in a manner of two steps, that is the treatment for superficially-placed tumors with intermediate energy ($\leq$100MeV/u) carbon-ion beam at the existing Heavy Ion Research Facility in Lanzhou (HIRFL) at first and then for deep-seated tumors with high-energy carbon ions at the newly-built HIRFL-Cooling Storage Ring (CSR). In fact, basic research related to heavy-ion cancer therapy has been carried out at IMP since 1995. Fruitful achievements have been obtained in the aspects of radiation physics, radiobiology and therapeutic technique [2]. For the first step, a therapy terminal has been constructed underground the experimental hall of the HIRFL complex, where a vertical beam line is equipped as shown in Fig.1.
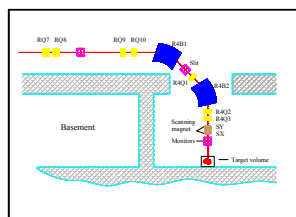
Figure 1. The vertical beam line in the therapy terminal at HIRFL for the treatment of superficially-placed tumors with heavy ions.

BEAM DELIVERY SYSTEM

At the earlier stage a passive beam delivery system has been developed and installed in the therapy terminal at HIRFL due to its simplicity and easy implementation. The passive system includes two orthogonal beam-scanning dipole magnets, which continuously scan pencil beams laterally and generate a broad and uniform irradiation field at the iso-center, a range modulator (ridge filter or ripple filter, depending on 2D or 3D conformal irradiation), a motor-driven energy degrader (range shifter) and a multi-leaf collimator. The first scanning magnet driven by a zigzag periodic current with a high frequency (50~150Hz) is for the fast scan in the x direction and the second driven by another zigzag periodic current with a low frequency (15~50Hz) instead is for the slow scan in the y direction. In this

---

way, the magnetic scanning system guides a focused beam to paint a target volume located at the isocenter of the therapy terminal with a Lissajous- or raster-like pattern, depending on the difference between fast and slow frequencies. Due to the limited space of the basement where the therapy terminal situated, only an 8cm×8cm square uniform field at the isocenter can be formed by the beam scanning system when the fast magnet is driven by a current with the maximum amplitude of 160A. Two types of range modulator, ridge filter and ripple filter, are adopted to spread out the thickness of the Bragg-peak dose region of a heavy ion beam in order to cover the extent of a solid tumor in depth. Ridge filter is used to obtain a full spread-out Bragg peak (SOBP) for a mono-energetic ion beam to stack throughout the depth of the target volume. However, the sharp Bragg peak is slightly spread out by ripple filter to form a mini SOBP.

CONFORMAL IRRADIATIONS

Based on the passive beam delivery system described above, 2D and 3D layer-stacking conformal irradiations can be easily performed. In 2D conformal irradiation, a ridge filter is selected among the optional ridge filters, depending on the SOBP width and the thickness of the planned target volume in depth. The multi-leaf collimator is set by use of a foam block, which is made according to the maximum contour of the target volume projected on the plane perpendicular to the beam line with the aid of our preliminary treatment planning system. In 3D conformal irradiation, a ripple filter is used instead of a ridge filter. The target volume is divided into several 2mm water-equivalent thick layers along the beam direction, and scanned layer by layer with the mini SOBP by changing the residual range of the beam with the range shifter. For irradiating each layer, the multi-leaf collimator is adjusted to shape an irradiation field according to the projected maximum contour of the corresponding layer. Clearly, compared with the 2D conformal method, the 3D conformal irradiation increases the degree of conformity so as to spare the normal tissue proximal to a target volume as much as possible. In practice, the option of 2D or 3D conformal irradiation relies on the clinical status of the patient.

TREATMENT PLANNING SYSTEM

A preliminary treatment planning system (TPS), which is anticipated to serve the heavy ion therapy project at IMP-CAS, is being developed. 3D reconstruction of CT slice images and dose calculation based on CT images and the code of HIBRAC [3] can be done with the preliminary TPS. Nevertheless, more developments of the TPS, for example dose calculation based on more accurate beam and RBE models, are needed. At present, biological effective dose are calculated based on the RBE data obtained in our *in vitro* cell radiobiological experiments.

EXPERIMENTAL VERIFICATION

To examine the passive beam delivery system and the conformal irradiation methods, a carbon-ion beam of 80.55MeV/u was provided for testing in the therapy terminal at HIRFL. After passing the vacuum window and air gap in the beam line, the energy of the beam was reduced to 75.82MeV/u at the isocenter. Correspondingly, the residual range of the beam is about 15.8mm in water. The uniformity of the irradiation fields generated by the beam scanning system with different fast and slow scanning frequency combinations was measured to be around 93%, which is considered to be good enough to treat superficially-placed tumors at the earlier stage. The modulating effect by the range modulators and the range changeability by the range shifter were also verified with the testing carbon beam. A 3D conformal irradiation to a target volume was simulated by irradiating phantoms, which consisted of a stack of CR39 slices. The dose-visualization results by the CR39 slices qualitatively illustrate that the beam delivery system in the earlier therapy terminal at HIRFL allowed the 3D conformal irradiation.

PATIENT TREATMENT

A clinical trial has been started at IMP-CAS since November 2006. Up to now, 27 patients with superficially-placed tumors have been treated with carbon ions (80~100MeV/n) in the therapy terminal at HIRFL. Different prescribed doses given in 7~10 fractions in a manner of continuous days

were applied to the patients. Preliminary clinical results show our treatments with carbon ions to these patients were successful.

REFERENCES

1. Amaldi U, Kraft G. Recent applications of synchrotrons in cancer therapy with carbon ions. Europhys News. 2005, 4: 114-118.
2. Li Q. Biomedical research with heavy ions at the IMP accelerators. Adv Space Res. 2007, doi: 10.1016/j.asr.2007. 03.096.
3. Sihver L, Schardt D, Kanai T. Depth-dose distributions of high-energy carbon, oxygen and neon beams in water. Jpn J Med Phys. 1998, 18: 1-21

THE PARTICLE THERAPY CENTRE OF RHÖN KLINIKUM AG AT THE UNIVERSITY HOSPITAL MARBURG

U.Weber et al.

RHÖN-KLINIKUM AG, c/o Universitätsklinikum Gießen und Marburg GmbH, Standort Marburg, Baldingerstraße, 35043 Marburg

Abstract:
The Rhön-Klinikum AG (RKA) builds a combined proton and ion beam therapy facility at the University Hospital of Marburg. The facility comprises four treatment rooms. The treatment of patients will start in 2010.

Intending to offer a highly effective radiotherapy for its patients in future, Rhön-Klinikum AG (RKA) has designed a combined proton and ion beam therapy (= particle therapy) facility. RKA will install this facility at the University Hospital Marburg, one of the two sites of the new "Universitätsklinikum Gießen und Marburg GmbH", a subsidiary of RKA. The facility comprises four treatment rooms, three with a fixed horizontal beam line and one with an oblique (45°) fixed beam-line instead of a gantry.

The layout of the facility has been carefully designed in order to yield high patient throughout and a minimum distance between treatment rooms and preparation rooms at the same time.

Project Schedule

Preparation of building site	01.03.07✓
Start of construction	01.08.07✓
Start installation of accelerator	01.08.08
Start installation of med. equipment	03.11.08
First beam in treatment room	01.07.09
Begin of clinical operation	31.08.10

The constructor of the technical part of the facility is the Siemens AG (Particle Therapy group). Important technical properties are listed below:

Accelerator:
  Synchrotron (design with 12 dipoles) , Linac (GSI-design)
Particles :
  Protons 50 –220 MeV , Carbons 85 – 430 MeV/u
Beam application:
  Raster Scanning with active energy variation by synchrotron
Treatment field size :
  20 x 20 cm^2
Treatment rooms :
  4 fixed beam (3 horizontal and 1 oblique with 45°)

The Rhön-Klinikum AG is the biggest German hospital company. 45 hospitals at 34 sites with altogether approximately 15.000 beds belong to RKA.
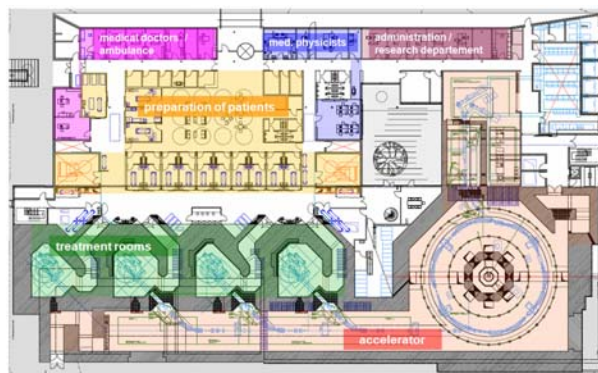
Fig 1. Layout of the facility

Fig 2. Front view of the facility (simulation)

Index of authors

Publikationen des Fachverbandes für Strahlenschutz e. V.

FS-05-130-AKNIR **Leitfaden Sonnenstrahlung,** Stand: 25. Januar 2006

FS-05-131-AKNIR **Leitfaden Ultraviolettstrahlung künstlicher Quellen;** Stand: 25. Februar 2005

FS-05-132-AKNIR **Leitfaden Sichtbare und infrarote Strahlung;** Stand: 25. Februar 2005

FS-05-133-AKNIR **Leitfaden Laserstrahlung,** Stand: 25. Februar 2005

FS-05-134-AKNIR **Leitfaden Lichteinwirkung auf die Nachbarschaft,** Stand: 25. Februar 2005

FS-05-135-AKNIR **Leitfaden Elektromagnetische Felder,** Stand: 25. Februar 2005

FS-05-136-AKNIR **Leitfaden Infraschall,** Stand: 25. Februar 2005

FS-05-137-AKNIR **Leitfaden Ultraschall**, Stand: 5. April.2005

*FS-05-138-AKE **Leitfaden für die praktische Umsetzung des § 29 StrlSchV,** (Freigabeleitfaden), Ausgabe 3, Arbeitskreis Entsorgung, Hrsg.: A. Bertram-Berg u. a., Stand: 8. Dezember 2005, TÜV-Verlag GmbH, Köln, oder Download unter www.fs.de

*FS-05-139-T **Strahlenschutz-Aspekte bei der Entsorgung radioaktiver Stoffe,** 37. Jahrestagung des Fachverbandes für Strahlenschutz e. V., 5. Gemeinsame Jahrestagung mit dem Österreichischen Verband für Strahlenschutz, 20.–23. September 2005 in Basel, Bandhrsg.: A. Zuberbühler, M. Baggenstos, N. Zoubek, A. Janett, TÜV-Verlag GmbH, Köln

FS-06-140/CD **Chronik 1966–2006 – Daten, Fakten und Notizen zur 40-jährigen Geschichte des FS,** Juni 2006, Redaktion: Dietrich E. Becker, Hans H. Brunner, Klaus Henrichs, Rupprecht Maushart

*FS-06-141-T **Strahlenschutz-Aspekte bei natürlicher Radioaktivität,** 38. Jahrestagung des Fachverbandes für Strahlenschutz e. V., 19.–22. September 2006 in Dresden, Bandhrsg.: E. Ettenhuber, R. Giessing, E. Beier, A. Bayer, TÜV Media GmbH, Köln

*FS-07-142-AKN **Vorkehrungen und Maßnahmen bei radiologischen Ereignissen,** 5. Seminar des Arbeitskreises Notfallschutz, 25.–27. April 2007 in Augsburg, Hrsg.: A. Bayer, H. Faleschini, S. Krüger, Chr. Strobl, TÜV Media GmbH, Köln

*FS-07-143-AKNAT **Optimierung der Auswahl von Messmethoden zur Bestimmung natürlicher Radionuklide,** Arbeitskreis natürliche Radioaktivität, Hrsg.: T. Heinrich, L. Funke, M. Köhler, U.-K. Schkade, F. Ullrich, W. Löbner, J. Höpner, D. Weiß, TÜV Media GmbH, Köln 2007

*FS-07-144-T **Ion Beams in Biology and Medicine,** 39. Annual Conference of the German-Swiss Association for Radiation Protection and 11th Workshop of Heavy Charged Particles in Biology and Medicine, 26.–29. September 2007 in Heidelberg, Bandhrsg.: J. Debus, K. Henrichs, G. Kraft, TÜV Media GmbH, Köln

Mit * oder ** bezeichnete Publikationen sind über den Buchhandel zu beziehen, die übrigen bei den im Sigel angegebenen Arbeitskreisen.

StrahlenschutzPRAXIS, die Vierteljahres-Fachzeitschrift des Fachverbandes für Strahlenschutz e. V. – aktuell, interessant, informativ!
TÜV Media GmbH, Köln, www.tuev-media.de

=► Die vollständige Liste finden Sie unter unter www.fs-ev.de!